

MODELLING THE NANOSCALE PROPERTIES
OF CALCIUM SILICATE HYDRATE AND ICE

Amy Romaniuk

Department of Civil and Environmental Engineering

University of Strathclyde

Glasgow, U.K.

September 2018

This thesis is submitted to the University of Strathclyde for the
degree of Doctor of Philosophy in the Faculty of Engineering.

This thesis is the result of the author's original research. It has been composed by the author and has not been previously submitted for examination which has led to the award of a degree.

The copyright of this thesis belongs to the author under the terms of the United Kingdom Copyright Acts as qualified by University of Strathclyde Regulation 3.50. Due acknowledgement must always be made of the use of any material in, or derived from, this thesis.

Signed:

Date:

“Life’s tough. But I’m tougher.”

Mr. T

Acknowledgements

First and foremost, I would like to thank my supervisors, Dr Shangtong Yang and Dr Leo Lue. If it were not for their support, this research would not have been possible. I am eternally grateful for your guidance - I have learned so much from you.

The support of the Archie-West team was critical in completing this work and their training and guidance helped facilitate this research. Similarly, I would like to thank Darren Grant for his continual IT support and assistance throughout the past 4 years.

I would like to thank my parents for keeping me grounded throughout this journey and for your continued support with everything. You taught me how to grit my teeth and get on with it.

There are many friends who I would like to thank. First and foremost, Greg Anderson - it has been a long time now since we embarked on our chemistry degree and who knew we would make it so far - I am so grateful of your support. Jack Hawkins and Nicola Masey, thank you for being such good friends. If it were not for the many pizza nights and cakes I would never have survived. Thank you to Hazel Snelling, even though you are all the way in Australia, you were always available to chat on the phone when times were tough. Thank you to Ding Fan, Chris Wong and Ronnie Turner, we started this PhD journey together and fingers crossed we finish it together! Riccardo Maddalena - I am so grateful for all of the fun times throughout our time as PhD students. Also thank you to Pieter Bots for all of your geochemistry help and for keeping the faith.

Finally, I would like to thank Robert Walker. Genuinely without your support, especially over the past few months, I would never have made it this far.

Abbreviations

AFM	Atomic force microscopy
BMEoS	Birch-Murnaghan equation of state
Ca/Si	Calcium to silicate ratio
c_{ij}	Elastic constant relating direction i to j
C-S-H	Calcium silicate hydrate
DFT	Density functional theory
E	Young's modulus/elastic modulus
EoS	Equation of state
FEM	Finite element modelling
FWEoS	Fiestel and Wagner equation of state
G	Shear modulus
G_R	Reuss averaged shear modulus
G_V	Voigt averaged shear modulus
H ₂ O/Si	water to silicate ratio
HD	High density calcium silicate hydrate
K	Bulk modulus
K_R	Reuss averaged bulk modulus
K_V	Voigt averaged bulk modulus
LAMMPS	Large-scale Atomic/Molecular Massively Parallel Simulator
LD	Low density calcium silicate hydrate
MCL	Mean chain length
mC-S-H	Natural mineral calcium silicate hydrate
(m)C-S-H	Natural mineral and synthetic calcium silicate hydrate
MD	Molecular dynamics
N	Number of particles
NMR	Nuclear magnetic resonance
OPC	Ordinary Portland Cement
p	Pressure
PCB	Periodic boundary conditions
PDF	Pair distribution function
r	Distance
RDF	Radial distribution function
ρ	Density
T	Temperature
TBOD	Total bond order density
V	Volume
VMD	Visual Molecular Dynamics
XRD	X-ray diffraction

Abstract

Cement is the most widely used construction material in the world. It can sustain substantial load due to its high compressive strength but is vulnerable to cracks due to its quasi-brittle nature. Calcium silicate hydrate, the origin of strength in cement, is a complex, nano-crystalline material. An understanding of the structure-property relationships of calcium silicate hydrate at the nanoscale is of great importance in order to modify the structure for improved mechanical properties.

Molecular dynamics simulation studies are often used to investigate nanoscale materials and rely upon an accurate chemical structure and force field bonding description of the system. For cementitious materials, however, there is no established force field. ReaxFF, a reactive force field which can account for the creation and breaking of chemical bonds, has shown promise in the literature for simulation of the mechanical properties of calcium silicate hydrates. However, little evidence of validation of the force field for describing calcium silicate hydrates has been seen in the literature. Furthermore, the lack of experimental data for comparison makes validation of the simulation methods difficult.

One material which has been studied extensively both experimentally and in simulations, and is also of engineering importance, is ice Ih. In this work, ReaxFF is shown to make excellent predictions of the structure and physical properties of ice Ih and makes reasonable comparisons to experimentally measured elastic constants. A fracture simulation protocol has been designed and produces realistic values of fracture toughness and fracture speeds of ice Ih showing improvements over existing simulation studies. By employing methods validated using ice Ih, this thesis goes on to predict the structure-property relationships of calcium silicate hydrate. It is revealed that the structure-property relationship is strongly correlated to chemical composition and therefore altering the ratio of the starting products in cement has the potential to lead to a product with tailor-made mechanical properties. Additionally, this thesis gives an insight into the tensile failure of calcium silicate hydrate at the nanoscale and highlights the challenges in simulating fracture such as the very high strain rate which must be adopted in simulations or the inability to model polycrystalline structures.

Contents

1	Introduction	2
2	A Review of the Chemical Structure and Properties of Cementitious Calcium Silicate Hydrates	7
2.1	Overview	7
2.2	Multiscale Modelling of Cementitious Materials	8
2.3	General Cement Chemistry	11
2.3.1	Production of C-S-H from Hydration of OPC	12
2.3.2	Production of Synthetic C-S-H	14
2.4	Experimental Characterisation of C-S-H	14
2.4.1	The Layered Structure of C-S-H and Natural Analogues	15
2.4.2	Influence of Ca/Si Ratio on the Structure of C-S-H	16
2.4.3	Influence of Water on the Structure of C-S-H	17
2.4.4	Influence of Silicate Chain Length on the Structure of C-S-H	18
2.4.5	Mechanical properties of C-S-H	18
2.5	Molecular Simulations of Calcium Silicate Hydrate	20
2.5.1	Computational Models of C-S-H	20
2.5.2	Force Fields for Molecular Dynamics Simulations	23

2.5.3	Previous Work on Structure Property Relationships for C-S-H	24
2.6	Summary	26
3	A Review of the Chemical Structure and Properties of Ice	27
3.1	Overview	27
3.2	The Structure and Properties of Water Ice	28
3.2.1	The Structure of Ice Ih	28
3.2.2	The Phase Diagram of Ice	30
3.2.3	The Polycrystalline Structure of Ice Ih	31
3.2.4	Mechanical Properties of Ice	32
3.3	Molecular Simulations of Ice	34
3.3.1	Force fields	34
3.3.2	Mechanical Properties of Ice at the Nanoscale	36
3.4	Justification for using Ice Ih for validation of methods	37
3.5	Summary	38
4	The Methodology of Molecular Simulations for Calculating Structure-property Relationships	39
4.1	Overview	39
4.2	Molecular Dynamics	40
4.3	Force Fields	44
4.3.1	ReaxFF	45
4.4	Choosing an Appropriate Time Step	48
4.5	Calculating Elasticity from Molecular Simulation	50
4.5.1	Voigt-Reuss-Hill Averaging	52
4.6	Fracture Simulations	52

4.7	Summary	55
5	Equilibrium Simulations of Ice Ih	56
5.1	Overview	56
5.2	Introduction	57
5.3	Methods	60
5.4	Results and Discussion	62
5.4.1	Unit Cell Predictions and EoS	62
5.4.2	Heat Capacity Calculations	69
5.4.3	Elasticity	70
5.5	Conclusions	78
6	Fracture Simulations of the ice Ih Phase of Water	79
6.1	Overview	79
6.2	Introduction	81
6.3	Methods	84
6.3.1	System Preparation	84
6.3.2	The Tensile Fracture Method	87
6.4	Results and Discussion	89
6.4.1	Simulating Fracture Under Plane Strain Conditions	90
6.4.2	Effect of initial crack size	92
6.4.3	Failure of Ice Ih Under Tension at Different Strain Rates	97
6.4.4	Effect of Temperature on the Fracture Properties of Ice Ih	101
6.4.5	Direction of Loading	104
6.4.6	Measurement of the Crack Speed of Ice Ih	106
6.4.7	Crack tip analysis	109

6.5	Conclusions	111
7	Equilibrium Simulations of Calcium Silicate Hydrates - Validation of ReaxFF	113
7.1	Overview	113
7.2	Introduction and Review of Previous Work	114
7.3	Simulation details	118
7.3.1	Measuring the Radial Distribution Function	121
7.4	Structures studied	122
7.4.1	β Wollastonite	123
7.4.2	The Tobermorite Family	124
7.4.3	Jennite	130
7.4.4	Rejmak Structures	132
7.5	Validating ReaxFF using tobermorite 14 Å and jennite	143
7.5.1	Variation of Lattice Parameters with Temperature for (m)C-S-H	144
7.5.2	Heat Capacity	148
7.5.3	Thermal Expansion Coefficient	150
7.6	Conclusions	150
8	Elastic Properties of Calcium Silicate Hydrates	152
8.1	Overview	152
8.2	Introduction	153
8.3	Simulation Details	155
8.4	Results and Discussion	156
8.4.1	System Size Effects in the Elasticity Calculation	157

8.4.2	Comparing ReaxFF predicted elastic properties of tobermorite and jennite to Available Data	158
8.4.3	Predicted Elastic Constants of Mineral Calcium Silicate Hydrates	161
8.4.4	Predicted Elastic Constants for Hypothetical Calcium Silicate Hydrates	163
8.4.5	Overall Analysis of Mechanical Properties for mC-S-H and C-S-H	164
8.4.6	Isothermal Equation of State of Calcium Silicate Hydrates	168
8.4.7	Anisotropy in Calcium Silicate Hydrates	184
8.5	Summary	188
9	Nanoscale Fracture Processes of Calcium Silicate Hydrates	189
9.1	Overview	189
9.2	Introduction	190
9.3	Methods	192
9.3.1	System Preparation	193
9.3.2	The Tensile Fracture Method	194
9.4	Results and Discussion	195
9.5	Conclusions	201
10	Conclusions and Future Work	202
10.1	Key Findings	203
10.2	Limitations of this Work	204
10.3	Conclusions and Future Work	205
	Bibliography	208

List of Tables

2.1	Summary of common clinker phases in OPC	12
2.2	Experimental elastic modulus and hardness at different Ca/Si ratio and density for low density (LD), high density (HD), inner product and outer product	19
5.1	Comparison of the predicted density of ice Ih for a number of water potentials at 250 K and 0 bar pressure	67
5.2	Elastic constants ReaxFF, SPC/E compared to theoretical and experimental results	72
5.3	Bulk modulus K and shear modulus G of ReaxFF and SPC/E compared to experiment.	73
6.1	Dimensions of initial crack sizes	94
6.2	Tensile strength at different initial crack sizes	96
6.3	Fracture toughness and tensile strength data measured under different strain rates at 200 K.	101
6.4	Fracture toughness and tensile strength data measured under different temperatures at a strain rate of $5 \times 10^{-6} \text{ fs}^{-1}$	103
6.5	Fracture toughness and tensile strength data measured under different temperatures at a strain rate of $5 \times 10^6 \text{ fs}^{-1}$	105
7.1	System sizes for ReaxFF simulations	120

7.2	Lattice parameters for ReaxFF compared to experiment	143
7.3	Average Bond Distances for tob 14 Å and jennite	144
7.4	Heat capacities of mC-S-H and C-S-H at 298 K	149
7.5	Thermal Expansion coefficients of mC-S-H and C-S-H at 298 K .	150
8.1	Comparison of Voigt-Reuss-Hill averaged elastic moduli for tobermorite 14 Å at different system sizes	158
8.2	Comparison of ReaxFF Voigt-Reuss-Hill Bulk Modulus K , Shear Modulus G and Young's Modulus E	159
8.3	Voigt-Reuss-Hill Bulk modulus K , Shear modulus G and Young's modulus E averages for mC-S-H structures Structure	162
8.4	Voigt-Reuss-Hill Bulk Modulus K , Young's Modulus E and Shear Modulus G and Young's Modulus E averages for C-S-H	164
8.5	Nanoindentation Hardness H and Modulus M data of synthetic C-S-H	164
8.6	Variation of K with Ca/Si ratio for C-S-H in High Pressure XRD experiments	165
8.7	Measurable Physical Properties of mC-S-H and C-S-H by simulation	168
8.8	Voigt-Reuss-Hill Bulk Modulus K and Shear Modulus G for C-S-H and mC-S-H structures	169
8.9	Comparison of BMEoS at zero temperature elastic constant method mC-S-H and C-S-H structures	184
8.10	Percentage compression at 4.8 GPa for mC-S-H and C-S-H structures	187
9.1	Fracture properties from simulation studies in the literature of Pel-lenq's C-S-H model	191
9.2	Dimensions of Simulation Cells and Initial Cracks for T2Ca1 and T5Ca1	194
9.3	Fracture properties measured by ReaxFF for Rejmak structures .	200

List of Figures

2.1	Computational modelling techniques and their corresponding scale.	10
2.2	Number of publications per year for studies involving C-S-H and MD.	11
2.3	Tobermorite 14 Å - an example of a layered calcium silicate hydrate structure	15
2.4	Bridging tetrahedra in calcium silicate chains.	22
3.1	Structure of a single water molecule.	28
3.2	Structure of Ice Ih.	29
3.3	Defects in Ice Ih which lead to hydrogen disorder.	30
3.4	Phase Diagram of Water	31
4.1	Timeline of ReaxFF	46
4.2	Calculation of Potential Energy of a typical ReaxFF system [125].	47
4.3	Energy convergence of tobermorite 14 Å at different time steps with ReaxFF	49
4.4	Principle stresses of a cubic crystal	51
5.1	Types of water models	58
5.2	Structure of hexagonal ice Ih.	63

5.3	Comparison of thermal expansion of lattice constants and volume of ice Ih as predicted by ReaxFF.	64
5.5	Dependence of thermal expansion coefficient with T for common water potentials.	68
5.6	Comparison of dependence of density on pressure for common water potentials.	69
5.7	Change in C_p with temperature for Ice Ih.	70
5.8	Comparison of Expt., SPC/E, ReaxFF and TIP4P elastic constants prediction.	72
5.9	Temperature dependence on ice Ih elastic constants as predicted by ReaxFF at 0 kbar.	74
5.10	Temperature dependence of bulk modulus K and shear modulus G for ReaxFF.	75
5.11	Pressure dependence C_{ij} ice Ih 0.5–1.51 kbar at 237 K.	76
5.12	Comparison of ReaxFF and experimental pressure dependence on bulk and shear modulus at 237 K.	77
6.1	Variation of compressive strength and tensile strength with temperature.	82
6.2	Variation of compressive strength and tensile strength with strain rate at 263 K.	82
6.3	Illustration of ice Ih tensile test set-up.	86
6.4	Relation of fracture toughness, K_{IC} to thickness, B	91
6.5	Fracture test carried out with and without PBC.	92
6.6	Fracture propagation using small initial crack.	94
6.7	Fracture propagation using medium initial crack.	94
6.8	Fracture propagation using large initial crack	95
6.9	Stress strain curve for different initial crack sizes.	97

6.10	Stress strain curve for normal structure at different strain rates.	98
6.11	Visual of extreme brittle fracture and deformation at strain rate 5×10 ⁻⁵ , x-direction, 200K.	99
6.12	Stress strain curve for fracture tests at different temperatures. 200 K	103
6.13	Effect of pulling direction on stress-strain curve.	105
6.14	Speed time curve for ice Ih at different strain rates.	108
6.15	Speed time curve for ice Ih at different temperatures.	109
6.16	Crack tip shapes of ice Ih, strain rate 5×10 ⁻⁶ , x-direction, 200K.	111
7.1	Measurement of the radial distribution function	122
7.2	Crystal structure of β wollastonite.	124
7.3	Radial distribution function of β wollastonite	125
7.4	Crystal structure of tobermorite 14 Å	127
7.5	Radial distribution function of tobermorite 14 Å	128
7.6	Crystal structure of tobermorite 9 Å	129
7.7	Radial distribution function of tobermorite 9 Å	130
7.8	Crystal structure of jennite.	131
7.9	Radial distribution function of jennite.	132
7.10	Crystal structure of T5Ca1.	134
7.11	T5Ca1 radial distribution function.	135
7.12	Crystal structure of T5-H1.	137
7.13	T5H1 radial distribution function.	138
7.14	Crystal structure of T2Ca1.	139
7.15	T2Ca1 radial distribution function.	140
7.16	Crystal structure of T2H1.	141
7.17	T2H1 radial distribution function.	142

7.18	Dependence of lattice parameters on temperature at temperatures ranging from 273-323 K for C-S-H structures.	146
7.19	Dependence of lattice parameters on temperature at temperatures ranging from 273-323 K for mC-S-H structures.	146
7.20	Dependence of density on temperature at temperatures ranging from 273-323 K for C-S-H structures.	147
7.21	Dependence of density on temperature at temperatures ranging from 273-323 K for mC-S-H structures.	147
8.1	Simulated values of bulk modulus for T14 from the recent literature compared to high pressure XRD experimental value	155
8.2	Elastic constants (C_{ij}) for tobermorite 14 Å at different system sizes	158
8.3	Elastic constants (C_{ij}) for tobermorite 14 Å and jennite as predicted by ReaxFF compared to other simulation studies.	160
8.4	Elastic constants (C_{ij}) for mCSH structures	162
8.5	Elastic constants (C_{ij}) for C-S-H	163
8.6	Variation of K with Ca/Si ratio	166
8.7	Variation of Elastic Moduli with TBOD ratio	167
8.8	Variation of elastic moduli K , G and E for mC-S-H and C-S-H using ReaxFF	167
8.9	Variation of elastic moduli with measurable physical properties using ReaxFF	169
8.10	Tobermorite 14 Å BMEoS comparison of experimental and simulation.	172
8.11	RDF of tobermorite 14Å at 0 GPa and 4.8 GPa	173
8.12	Comparison of crystal interlayer of tobermorite 14Å at 0 GPa and 4.8 GPa	173

8.13	Jennite BMEoS comparison of experimental, ReaxFF simulation and DFT simulations.	174
8.14	RDF of jennite at 0 GPa and 4.8 GPa	175
8.15	Comparison of crystal interlayer of jennite at 0 GPa and 4.8 GPa pressure.	175
8.16	mC-S-H Birch-Murnaghan BMEoS, tobermorite 14Å tobermorite 9Å jennite	176
8.17	RDF of tobermorite 9Å at 0 GPa and 4.8 GPa.	177
8.18	Comparison of crystal interlayer of tobermorite 9 Å at 0 GPa and 4.8 GPa pressure.	177
8.19	C-S-H BMEoS	178
8.20	RDF of T5Ca1 at 0 GPa and 4.8 GPa.	179
8.21	Comparison of crystal interlayer of T5Ca1 at 0 GPa and 4.8 GPa pressure.	180
8.22	RDF of T2Ca1 at 0 GPa and 4.8 GPa.	181
8.23	Comparison of crystal interlayer of T2Ca1 at 0 GPa and 4.8 GPa pressure.	181
8.24	RDF of T5H1 at 0 GPa and 4.8 GPa.	182
8.25	RDF of T2H1 at 0 GPa and 4.8 GPa.	183
8.26	Comparison of crystal interlayer of T2H1 at 0 GPa and 4.8 GPa pressure.	184
8.27	Comparison of crystal interlayer of T5H1 at 0 GPa and 4.8 GPa pressure.	184
8.28	Lattice constant (normalised) dependence on pressure for C-S-H.	186
8.29	Lattice constant dependence on pressure for mC-S-H.	187
9.1	Tensile pulling directions.	194
9.2	Effect of loading direction on stress-strain curve of T5Ca1.	197

9.3	Deformation of T5Ca1 in the z-direction	198
9.4	Deformation of T5Ca1 in the y-direction	199
9.5	Comparison of stress-strain curve for T2Ca1 and T5Ca1.	200

Chapter 1

Introduction

It is estimated that around 5-7% of Global CO₂ emissions are caused by cement production alone[1]. Improving the mechanical properties of cementitious material can help increase the durability of cement, thus reduce the demand for production and in turn reducing the CO₂ emissions associated with production. However, improving the mechanical properties of cement requires an understanding of the relationship between the structure and the mechanical properties. The primary composition of Portland cements at the nanoscale is calcium silicate hydrate (C-S-H), a major product of cement hydration. C-S-H consists of a porous network of calcium silicate chains and is responsible for the engineering properties of cement. C-S-H is poorly crystalline with limited long range order, and as a result, traditional solid state characterisation methods such as X-ray diffraction (XRD) has been unable to define a crystal structure due to the broad diffraction peaks associated with nanocrystalline and amorphous materials. The composition of C-S-H varies from sample to sample, furthering complications in characterisation. In an effort to overcome these complications and produce a single phase C-S-H, synthetic C-S-H has been developed in the lab and after extensive structural probing, some aspects of the structure are now known[2,3]. The structure is thought to form a polymer made up of a repeating unit of 3 components, also known as dreirketten chains, and resembles a disordered form of the naturally occurring mineral tobermorite; the chains are sandwiched between layers of water and calcium ions with an interlayer spacing of around 11 Å .

The lack of characterisation of the crystal structure of C-S-H means that structure-property determination by experiment alone remains a significant challenge. Research to understand the structure-property relationships of C-S-H using molecular simulations is a rapidly growing area. Molecular dynamics (MD) simulations can provide a vast amount of information on physical, thermodynamic and mechanical properties of a material and, when coupled with a reactive force field potential, can give an indication of how the material behaves when deformed to the point of failure at the nanoscale. Since the exact chemical structure of C-S-H has yet to be determined, crystal-solved natural mineral analogues are often employed. However, molecular simulations in this area are still at an early stage. As a result, accurate bonding descriptions for MD, known as force fields, are underdeveloped for C-S-H type structures.

One force field which is showing promise in the literature for simulation of C-S-H materials is known as ReaxFF, a reactive force field based upon bond order. Not only is this force field easy to implement and is transferable across a range of structures, it is capable of modelling deformation processes, such as fracture, due to the unique ability to model bond breaking and bond making processes — something which traditional MD force fields cannot achieve. ReaxFF, however, has not been parametrised specifically for C-S-H materials; therefore, appropriate validation must be carried out to allow realistic predictions to be made. This non-specific force field development, combined with the lack of experimental data for even resolved mineral C-S-H (mC-S-H) structures, makes validation of force fields and simulation methods extremely difficult. Without a rigorous validation protocol, the accuracy and usefulness of predictions cannot be determined.

Water is known to influence the structure and properties of C-S-H and is one of the most simulated materials in the world, largely due to its importance for life. The overall structure of water and its condensed phases is reasonably well understood and there are well over 100 force fields in the literature[2]. The solid phase of water which is the form found on Earth is known as ice Ih, where I indicates that it was the first ice structure discovered and h represents the hexagonal structure which it adopts, and is a suitable structure to validate simulation protocols using ReaxFF for a number of reasons. Firstly, there is a significant amount of experimental physical and mechanical experimental data available, for

ice (and water), for comparison to simulation data. Secondly, the large number of force fields has resulted in a huge amount of available simulation data in the literature to compare to. Thirdly, both ice Ih and C-S-H show viscoelastic behaviour and have different physical and mechanical properties depending on the scale in which they are studied as a result of the complex systems adopted at each scale. Finally, since water is known to have significant influence over the structural and mechanical properties of C-S-H, studying water in the solid form may give insight into the behaviour of water in C-S-H. Furthermore, as a standalone material, the mechanical properties of ice are also of major engineering importance in cold climate engineering and ship design, making validation of the force field and methods on ice Ih a worthwhile venture.

The main aim of this thesis is to determine the physical and mechanical properties of C-S-H at the nanoscale. To address this aim, in this thesis, the specific objectives are presented. Firstly, it is required to critically and thoroughly review the state-of-the-art of the nanostructure of C-S-H, modelling methods, atomic structures, and the structure-property relationship. A proof of concept study will take place using ice Ih where the ReaxFF will be used to validate the simulation methods for the mechanical property testing with available experimental data. Validation of the existing atomic structures for C-S-H and ReaxFF force field using MD will be carried out by comparing the results from simulated equilibrium simulations with the available experimental data. This will be followed by an investigation into the elastic behaviour and determination of the elastic constants of C-S-H. The final objective is to apply the fracture protocol to simulate the fracture of C-S-H and obtain the fracture properties of C-S-H.

The remainder of this thesis is structured as follows. In Chapter 2, general cement chemistry and multiscale modelling is introduced and the structure of C-S-H is discussed providing details of the most recent structural models of cement. The chapter then reviews the state of the art of molecular simulations and evaluates prior work highlighting the difficulty in modelling C-S-H.

Chapter 3 introduces the structure of ice Ih and demonstrates the suitability of the material for use in validating the simulation methods. This chapter includes a review of the mechanical properties of ice and demonstrates the abundance of

existing simulation and experimental data for verification of the force field and methods.

In Chapter 4 the method of MD is presented and the force fields used in this work are described. The chapter also gives details on the theory of elasticity and how it can be used in a simulation environment. Following on from this, molecular scale fracture and mechanical properties are discussed and the method for producing a stress strain curve at the atomic level is described.

The validation of structure and physical properties of ice Ih for use with ReaxFF is given in Chapter 5 by analysing and comparing the structure, density and thermodynamic properties to experimental measurements and by comparing to other force field predictions. This chapter also evaluates the ability of molecular simulations to predict the elastic properties of ice and compares the results to experimental data.

In Chapter 6, the reader is guided through the design and considerations of the fracture molecular simulation method using ice Ih as a validation material. The capabilities and limitations of the method are discussed in detail and the results are compared with available experimental and simulation data in the literature.

Following on from the method validation chapters, Chapter 7 applies the methods to C-S-H. In this chapter, ReaxFF is used to simulate a number of crystalline C-S-H materials with known crystal structures before going on to predict the physical and structural properties of C-S-H, comparing to experimental data where possible. This chapter gives insights into the chemical structure of C-S-H that cannot be determined by experiment alone.

Chapter 8 applies the elasticity simulation method validated in Chapter 5 to C-S-H. This chapter begins the first attempt to determine structure-property relationships of C-S-H by studying a number of structurally solved mineral C-S-H phases and hypothetical C-S-H structures comparing them to other simulation methods in the literature.

The final results chapter, Chapter 9, applies the fracture method devised in Chapter 6 to C-S-H and some preliminary data is presented. The limitations of this method to predict the fracture properties of C-S-H is discussed and the plan for

further development of the method is detailed.

Finally, Chapter 10 concludes the research in this thesis and outlines future work which could be carried out to complement and build upon the work carried out in this thesis.

As the employment of molecular simulations in the cement industry is still immature, this thesis as a whole takes a critical and thorough approach to validation of methods to ensure that the best molecular predictions can be made. Although molecular simulations are not without their limitations, this thesis aims to evaluate the structure-property relationships in the most appropriate way and demonstrate the value that can be gained from molecular simulations.

Chapter 2

A Review of the Chemical Structure and Properties of Cementitious Calcium Silicate Hydrates

2.1 Overview

The field of materials science relates the structure of a material to its properties, bringing together chemistry and engineering. This encompasses the physical and chemical properties, characterisation of the structure, processing and assessing the performance of the materials. In materials like cementitious calcium silicate hydrate (C-S-H) where the chemical structure is complex or poorly understood, establishing the link between the structure and properties can be challenging. The complex, nanocrystalline structure of C-S-H has yet to be fully characterised and therefore, determining structure-property relationships by experiment alone is a major challenge facing the cement industry. By incorporating molecular simulation tools, useful predictions of experimental data can be made by modelling C-S-H structures, however, this relies upon the development of accurate simulation protocols.

The aim of this chapter is to introduce the background information relating to general cement chemistry and the viewpoints on current structural models and mechanical properties of the C-S-H and to review the literature relating to the simulation of cementitious C-S-H. This chapter begins with a short introduction to the field of materials modelling, before going on to describe general cement chemistry. The structure of cementitious C-S-H is discussed, followed by a short overview of the nanoscale experimental mechanical properties. Lastly, a review of current simulation work is presented which includes force fields, characterisation and mechanical properties.

2.2 Multiscale Modelling of Cementitious Materials

Concrete is the most widely used construction and building material in the world and is produced by mixing aggregate, cement, sand and water[3]. When mixed with water, the cement undergoes a chemical reaction, known as hydration, and the material begins to set, forming a solid material. As the chemical reaction proceeds, the material increases in strength, and it is this structural property that makes it an ideal building material. A lack of sustainability in production however has led to intense research to develop new, more sustainable, cement and specifically target the durability of common cement[4–7]. Concrete is renowned for its strength and durability, however, it has negative attributes, one of which is the formation of fracture under tensile loading[8]. Improving resistance to fracture and other mechanical properties requires an understanding of the chemical products and their properties at a small scale. Recent estimates say that 5-7% of the Global CO₂ emissions worldwide are due to cement production[9]. It is predicted that the significant development and maintenance of infrastructure worldwide will only increase the demand for cement[7, 9]. There are two ways in which global emissions related to cement can be reduced (i) tackling the cement production process directly to reduce emissions at every stage from production to transportation or (ii) by targeting the chemical make-up to produce cement which is less likely to fracture or have reduced mechanical properties, thus pro-

ducing a longer lasting, more durable cement. It is the latter that this work will focus on.

Modelling of cement is frequently used alongside experimental testing to give an insight where experiments are lacking. Cementitious materials consist of a complex hierarchical structure where the material components and mechanical properties change depending on the scale under study. According to Wittman, three distinct levels should be considered for multi-scale modelling approaches[10]. The first of these levels considers the macroscale where the material is predominantly concrete and consists of sand, aggregate and hydrated cement paste. At this scale the cement is considered to be homogeneous. In the second level, pores, inclusions and cracks exist and is known as the mesoscale. The third level deals with the microscale and is related to the microscopic structure of cement paste. Recently however, cement-based research has turned to a fourth level of study to understand the origin of strength. This level, the nanoscale, is predominantly made up of calcium silicate hydrate gel, and to get an accurate representation of structure-property relationships, the influence of nanoscale properties on macroscale behaviour must be understood.

Nano-engineering refers to the modification, alteration and development of materials at the nanoscale to produce desired properties based upon the materials chemical structure and composition. The bottom-up approach, first mentioned by Richard Feynman, demonstrated that complex material problems could be understood, and potentially solved by understanding the fundamentals which come into play at the nanoscale[11]. For the cement industry, computational nano-engineering is still a relatively new area of study with computations such as molecular dynamics (MD) not being used until the late 2000's. Popularity in molecular simulation tools is growing rapidly in the cement industry for structure-property relationships, however, lack of understanding of the crystal structure of calcium silicate hydrate and lack of force field development has limited progress in the field.

Multiscale modelling ranges from atomistic modelling of electron based methods at the nanometer scale such as density functional theory (DFT) to the micro and macroscale Finite Element Modelling (FEM). Figure 2.1 depicts where MD fits

into this scale relative to common engineering modelling such as FEM.

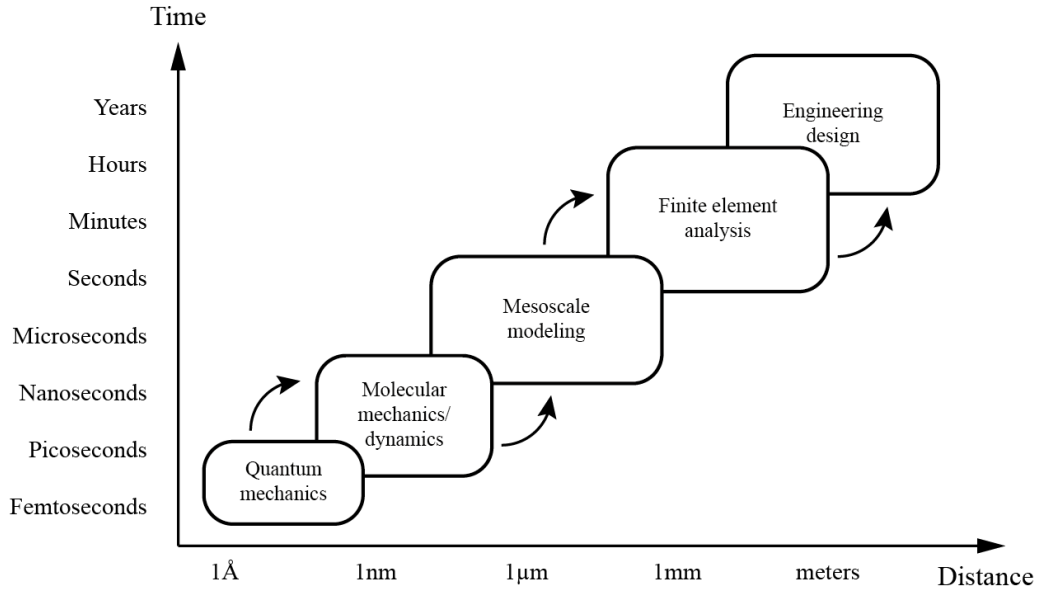


Figure 2.1: Computational modelling techniques and their corresponding scale.

While being a relatively new area of research within the cement industry, there has been a significant rise in the number of MD studies and a Web of Knowledge metrics search of *calcium silicate hydrates* and *molecular dynamics* demonstrates this trend as shown in Figure 2.2. The rise in the number of publications can be attributed to the advances in experimental data which gives more insight into the chemical structure of C-S-H. Most notably, solved crystal structures of C-S-H mineral analogues jennite and tobermorite were published in 2004 and 2005 respectively, the first atomic coordinates hypothetical structure of C-S-H was published in 2009, and a C-S-H specific force field was published in 2014[12–15]. These milestones have contributed to real advancements in the application of MD to solve cement chemistry problems and will be discussed in more depth later in this chapter.

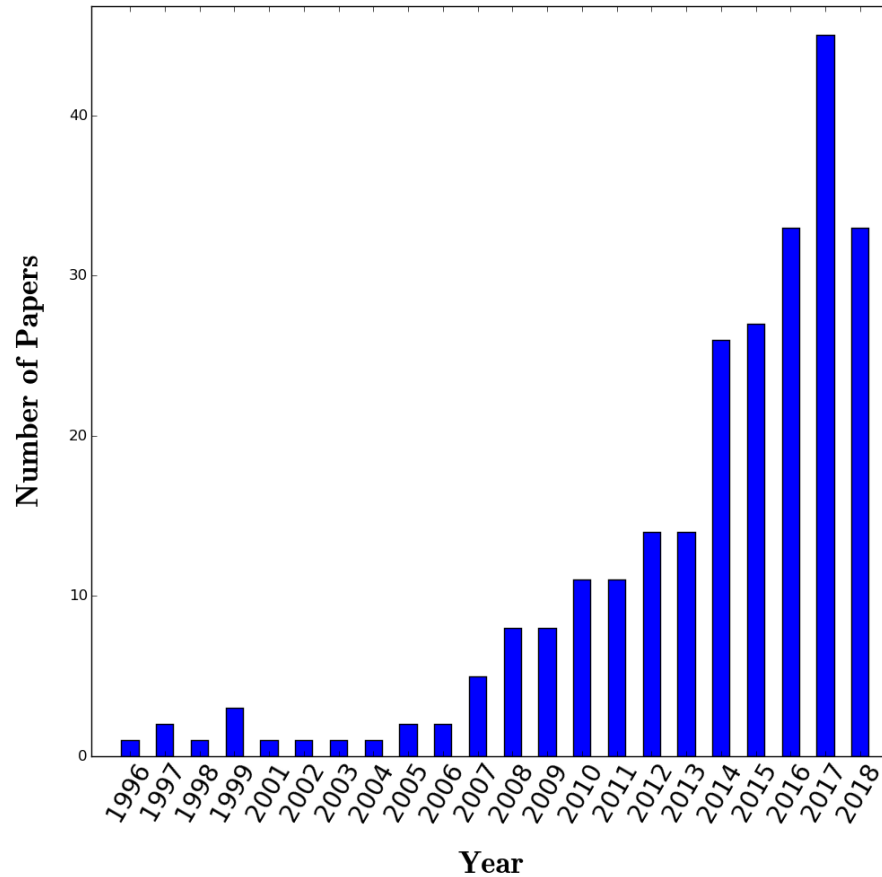


Figure 2.2: Number of publications per year for studies involving C-S-H and MD.

2.3 General Cement Chemistry

Ordinary Portland cement (OPC), is one of the most common cements and is produced at high temperature in a kiln from a quantifiable mixture of ground raw materials such as limestone, alumina and silica[3]. The product of this process is known as clinker and is formed from the reaction between lime, silica, alumina and iron oxide. It is this clinker phase which is ground and mixed with water to produce cement paste. Clinker consists of four products; alite, belite, aluminate and ferrite. Their chemical composition is found in Table 2.1

Table 2.1: Summary of common clinker phases in OPC

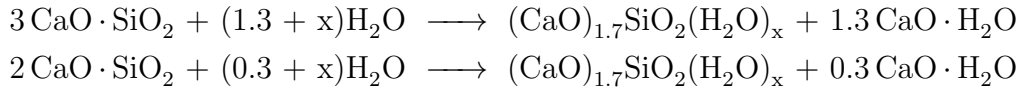
Clinker Phase	Chemical Name	Empirical Formula	Hydration Product
Alite	Tricalcium silicate	$3 \text{CaO} \cdot \text{SiO}_2$	C-S-H gel and calcium hydroxide
Belite	Dicalcium silicate	$2 \text{CaO} \cdot \text{SiO}_2$	C-S-H and calcium hydroxide
Aluminate	Tricalcium aluminate	$3 \text{CaO} \cdot \text{AlO}_3$	Calcium aluminate hydrate
Ferrite	Tetracalcium aluminoferrite	$4 \text{CaO} \cdot \text{Al}_2\text{O}_3 \cdot \text{Fe}_2\text{O}_3$	Ettringite and mono/trisulaluminates and iron substitutes of these

Alite is the most abundant mineral in clinker constituting approximately 65% of the total clinker phase and is found in the form of equidimensional grains[3]. Belite makes up around 15% and takes the form of rounded twinning grains[3]. Aluminate and Ferrite, along with some other minor components make up the rest of the clinker and comes in the form of rectangular crystals and solid solutions respectively. The components of cement include minor oxides which have some effect on the atomic arrangements, crystal form and properties of the silicates. Further compounds exist in traces (normally only 2% by mass) and include MgO, TiO₂, Mn₂O₃, K₂O and Na₂O. The latter two, also known as the alkalis can react with some aggregates and can affect the strain gain rate of concrete[3].

2.3.1 Production of C-S-H from Hydration of OPC

Hydration is the chemical reaction that occurs when water is added to cement. The major product of the hydration is C-S-H gel which stems from the hydration of alite and belite[3]. Calcium hydroxide is formed as a by-product of the hydration reaction of alite and belite and is commonly known by its mineral name portlandite. It is often found as a hexagonal flat crystal which is soluble in water and can lead to leaching problems in concrete structures when exposed to wet conditions, as the calcium hydroxide leaches, pores are created[3]. The following

scheme shows the chemical equation for the hydration reaction of alite and belite[3].



Hydration of alite is considered to be the fastest and most important hydration process as it provides early strength to the cement. The resulting cement paste is made up of around 50% by volume C-S-H gel which expands to a greater volume than the original cement grains. When alite and belite are hydrated on their own, their behaviour is remarkably similar to the behaviour of cement upon hydration, indicating that these are the most influential components of cement concerning their physical properties[3].

The overall strength of the cement is a result of the newly formed C-S-H binding to the particulates and holding them all together. One particular characteristic of C-S-H is the pore system - the volume expansion during hydration traps water in small pores within the gel. These pores are known as gel pores and result in variation in water content from one sample to another since the trapped water cannot carry out further hydration to produce more C-S-H gel. Similarly, the larger pores in the cement paste, known as capillary pores, become isolated, providing a resistance to permeability of water and ions throughout the C-S-H system.

The porous system also gives rise to high and low density C-S-H which are associated with inner product and outer product C-S-H. The high density C-S-H forms in cement particles whereas the low density C-S-H forms at particle edges and in between particles[16–18]. It has been observed that these high and low density products exhibit different mechanical properties and does not depend on water to cement ratio (W/C) or cement type, suggesting that density may play an important role in the mechanical behaviour of C-S-H[18–21].

2.3.2 Production of Synthetic C-S-H

Recently, research has focused on the development of synthetic calcium silicate hydrates as a means of increasing the sustainability of the production of C-S-H as well as producing pure C-S-H for structural characterisation. The most common preparation of synthetic C-S-H reacts stoichiometric amounts of $\text{Ca}(\text{OH})_2$ or CaO with amorphous silica or nanosilica to control the Ca/Si ratio[22–26]. CaO can be produced from CaCO_3 by heating to 1000°C for 5 hours. The preparation is normally carried out under nitrogen to minimise carbonation of the samples. These methods can be fine tuned to produce C-S-H with the desired Ca/Si ratio and allow for characterisation of single phase C-S-H(I) at low Ca/Si ratio i.e. without portlandite by controlling the stoichiometric ratios of the calcium and silica source. Recent work by Kumar et al. showed that high Ca/Si ratio C-S-H can be produced from the reaction of sodium silicate and calcium nitrate, under strictly controlled pH conditions and is free of portlandite[27]. This is a breakthrough in enabling investigation of the properties and structure of single phase C-S-H at high Ca/Si ratio.

2.4 Experimental Characterisation of C-S-H

There have been many attempts to determine the molecular structure of C-S-H, however, there are difficulties which need to be overcome. C-S-H is described as a gel due to the amorphous, poorly crystalline nature and as a result, traditional solid state analysis techniques such as X-ray diffraction cannot give an accurate sense of the chemical structure[28]. C-S-H crystals that do form in cement paste are incredibly small (nm in size) therefore structure probing is extremely difficult[29]. The structure of C-S-H is directly related to the Ca/Si ratio of the starting materials[28]. Despite the challenges in resolving the chemical structure, properties such as Ca/Si ratio variability, silicate polymer chain length shrinkage and porosity are accounted for reasonably well in modern models of C-S-H. The structure and composition will now be discussed, starting with the description of the structural analogues of C-S-H.

2.4.1 The Layered Structure of C-S-H and Natural Analogues

From XRD and NMR experiments, the structure of C-S-H is thought to be similar to the naturally occurring mineral calcium silicate hydrates such as tobermorite and jennite[12, 13, 30, 31]. The first chemical formula and density of cementitious C-S-H were measured by Allen et al. by neutron scattering experiments and was found to be $(\text{CaO})_{1.7}(\text{SiO}_2)(\text{H}_2\text{O})_{1.80}$ and 2.604 g/cm^3 respectively. The formula was an average and accounted for the considerable variation in chemical composition and structure that is typically associated with cementitious C-S-H[32]. Recent advancements in the experimental analysis have determined C-S-H to be nanocrystalline in structure with short to medium range order and has been described as turbostratic, meaning that the basal planes of the crystal are somewhat disordered and misaligned[6, 31]. These minerals consist of layers calcium silicate chains sandwiched between layers of water and calcium ions as illustrated in the example of tobermorite 14 \AA in Figure 2.3.

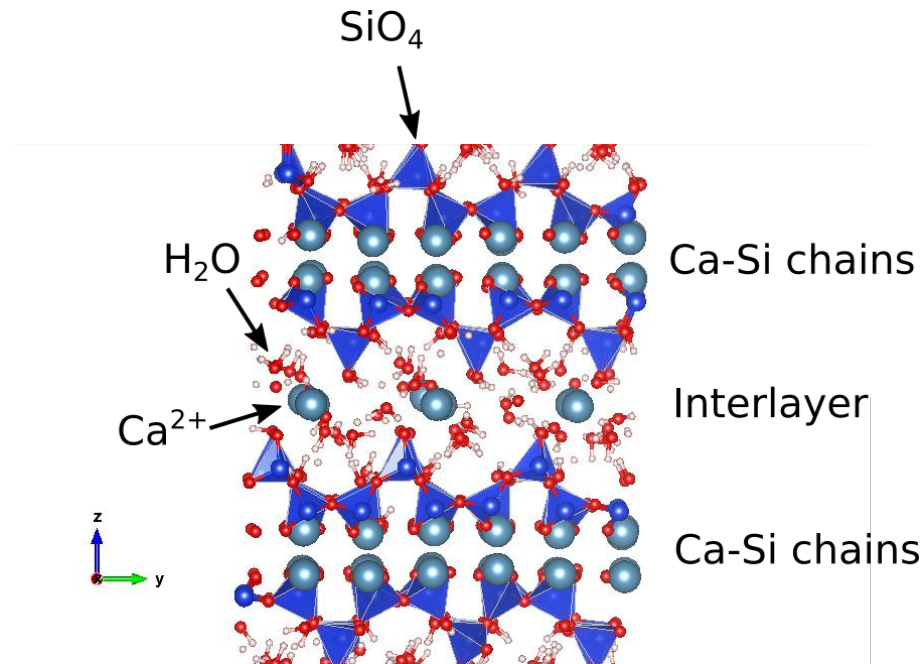


Figure 2.3: Tobermorite 14 \AA - an example of a layered calcium silicate hydrate structure

Tobermorite 14 Å is considered to be one of the main structural analogues of C-S-H. Structural refinements via synchrotron XRD and has concluded an average chemical formula of $\text{Ca}_5\text{Si}_6\text{O}_{16}(\text{OH})_2 \cdot 7\text{H}_2\text{O}$, and as the name suggests, a basal spacing of 14 Å[13]. The structure is formed of alternating layers of single chains which are known to be similar in structure to the calcium-silicate chains of the mineral wollastonite[13]. Water resides between these silicate chains and is coordinated to Ca^{2+} cations in an octahedral arrangement. Silanol groups can be found in four instances per unit cell and five water molecules reside in the zeolitic cavities. For C-S-H, like tobermorite, the Si is tetrahedrally coordinated to four oxygens, and these oxygens form part of a bridge. In contrast to the infinitely long silicate chains found in tobermorite, the silicate chains tend to be of a finite length and have been reported to be in the range of two to fifteen Si tetrahedral units[28]. Ca^{2+} is coordinated to six or seven oxygen atoms and flanks the silicate chains. The basal spacing is found to be shorter than in tobermorite and is on average 11 Å. The short range order does not exceed 3.5 nm in C-S-H, hence the difficulty in refining the structure by XRD [24]. The cementitious C-S-H found in cement paste (as opposed to synthetic C-S-H produced in a controlled environment in the lab) tends to have a greater water content than tobermorite and has a higher calcium to silicate (Ca/Si) ratio, where Ca/Si ratio is the ratio of CaO to SiO_2)[32]. To quantify, the $\text{H}_2\text{O}/\text{Si}$ ratio measured in OPC by Allen et al. is 1.80 compared to 1.16 in tobermorite 14Å and the Ca/Si ratio is 1.7 in OPC compared to 0.83 in tobermorite 14Å [32].

2.4.2 Influence of Ca/Si Ratio on the Structure of C-S-H

The Ca/Si ratio is believed to influence both the structural and mechanical properties of C-S-H[5, 15, 28]. The Ca/Si ratio is naturally variable in C-S-H throughout the structure, however, as mentioned in the previous section, Allen et al. measured average Ca/Si ratio of OPC to be 1.7[32]. In synthetic pastes, the Ca/Si ratio can be controlled under strict experimental conditions[27]. The work of Taylor and Howsin suggested that a high Ca/Si ratio is associated with the presence of shorter silicate chains, and is in effect an equivalent to removal of bridging tetrahedra and balancing residual charge with Ca^{2+} ions[33, 34]. Further

research by Richardson and Groves described two different types of C-S-H — one with a high Ca/Si ratio where the chemical structure was similar to the natural mineral jennite, and another where a low Ca/Si ratio resulted in a tobermorite-like structure[35]. More recent work has related the Ca/Si ratio to the polymer chain length — at very low Ca/Si ratios, highly polymerized chains approaching infinity are observed and as the Ca/Si ratio is increased, depolymerisation of the silicate chains occurs, supporting earlier hypotheses of Taylor and Howsin[28, 33].

The Ca/Si ratio has been shown to affect the Ca-O coordination reducing it from approximately seven to six at high Ca/Si ratios[22]. The same authors suggested that jennite exists at high Ca/Si ratios due to decreasing basal spacing however; this is in contrast to a number of other studies where jennite phases are not observed[6, 27, 31]. A decrease in the basal spacing with increasing Ca/Si ratio was observed by Rodriguez et al.[23].

2.4.3 Influence of Water on the Structure of C-S-H

The influence of water on physical, mechanical and thermodynamic data is still a widely debated area in the field. The water content of C-S-H has a large effect on the structure and comes in the form of interlayer water, capillary water and structural water[36]. Interlayer water resides in the layers between the silicate chains within the crystal structure[36]. Capillary water, or free water, is found at the microscale and can leave the pores without modification of the structure of C-S-H[36]. Lastly, gel water is found within the nanopores in C-S-H and can influence crystal properties due to shrinkage of the crystal unit cell[36]. The relative humidity of C-S-H is known to affect the cohesion between C-S-H grains, and in turn, the distance between C-S-H grains. This is an important consideration for the application of C-S-H in extreme temperature environments as this can affect structural and mechanical properties[37]. Furthermore, it was suggested that water adsorbed on the surface of such small crystals should be taken into account when considering how water affects the properties of C-S-H due to the small relative surface area to crystal size[38]. It can be noted that for molecular simulations, this need not be considered as free surfaces are not modelled due to the infinite repeating body, implemented by periodic boundary conditions.

2.4.4 Influence of Silicate Chain Length on the Structure of C-S-H

Silicate chain length varies in C-S-H and is often characterised by ^{29}Si NMR investigations[39–41]. In natural mineral C-S-H structures such as tobermorite and jennite, the silicate chains are of an infinite length, however, in cementitious C-S-H, the chains are much shorter and are linked to the Ca/Si ratio. Richardson demonstrated that the mean silicate chain length (MCL) increases exponentially as the Ca/Si ratio decreases and that at Ca/Si ratios around 0.8, the MCL was greater than 11[28]. As the Ca/Si ratio is increased to 1.0, the MCL drops to around 5. Further increasing the Ca/Si ratio to 1.2 drops the MCL to around 3. Increasing the Ca/Si ratio beyond 1.2 causes no further decrease, and the MCL stabilises 2-3 suggesting that monomers are not present[28].

MCL is known to be influenced by the length of the curing time and the humidity[41]. Postovgar et al., through NMR studies of hydration of C-S-H, showed that within the first few hours of the hydration, the C-S-H is predominantly dimeric[41]. After 10 hours hydration, the MCL is predominantly >2 , and after 1.5 months, 44% of the C-S-H was found to be octameric, 7% pentameric, 42% dimeric, 5% monomeric and only 2% was found to be unhydrated suggesting that well hydrated C-S-H was predominantly octameric and dimeric. Samples cured at low relative humidity have been found to have a greater degree of polymerisation than those cured at higher humidities[42].

2.4.5 Mechanical properties of C-S-H

The lack of crystal structure of C-S-H ultimately means it is difficult to fully understand the mechanical properties and structure-property relationships from experiment. Nonetheless, Atomic Force Microscopy (AFM) and nanoindentation have been valuable tools in determining elastic modulus and hardness of C-S-H samples. Plassard et al. concluded that the elastic modulus increased with increasing Ca/Si ratio[43]. The elastic modulus of pure C-S-H was ≈ 40 GPa, however, when Ca/Si ratio was increased (as a result of the presence of CaOH) the elastic modulus increased to ≈ 280 GPa at a concentration of 18 mmol/L

Table 2.2: Experimental elastic modulus and hardness at different Ca/Si ratio and density for low density (LD), high density (HD), inner product and outer product

C-S-H Type	Ca/Si Ratio	Elastic Modulus (GPa)	Hardness (GPa)	Ref.
LD	-	21.7	0.8	[19]
HD	-	29.7	1.0	[45]
LD	-	18.2	0.45	[45]
HD	-	29.1	0.83	[46]
LD	<1	20.0	0.8	[46]
HD	>1	31.6	0.9	[46]
inner product	-	22.94	0.88	[47]
outer product	-	25.74	0.88	[47]
HD	1.85	22.97	0.88	[48]
LD	-	23.4	0.73	[48]
HD	-	31.4	1.27	[48]
LD	-	18.1	-	[18]
HD	-	31.0	-	[18]
LD	-	22	0.6	[49]
HD	-	32	0.9	[49]

of CaOH[43]. The Ca/Si ratio, however, was not measured. This work was in contrast with findings by Pelisser who found that increasing the Ca/Si ratio caused a decrease in elastic modulus e.g. with a Ca/Si ratio of 0.7, elastic modulus was ≈ 27 GPa, whereas at a Ca/Si ratio of 2.1, the elastic modulus fell to 15-20 GPa[44]. The elastic modulus was also measured by Constantinides et al. using nanoindentation techniques and measured the elastic modulus of C-S-H to be in the range of 18-36 GPa[19].

It can be seen in Table 2.2 that conclusions cannot be drawn about the effect of Ca/Si ratio on the elastic modulus and hardness due to the lack of Ca/Si ratio reporting. Additionally, few studies use portlandite free C-S-H for their work. As a result, there has yet to be a full understanding of the C-S-H structure at small scale, possibly due to the complex structural nature of the material. It can be concluded that there is a general trend that high density C-S-H has a greater elastic modulus and hardness than the low density C-S-H within the same study.

However, there is a gap in the literature which needs to be filled regarding small scale forces and mechanical properties which contribute to this and the effect in which Ca/Si has upon the elastic modulus and hardness.

2.5 Molecular Simulations of Calcium Silicate Hydrate

Since C-S-H is a component of cementitious building materials in the construction industry, it is unsurprising that the majority of the simulation work for C-S-H type structures have been aimed at determining mechanical properties[4, 14, 15, 39, 50, 51]. Numerous studies been carried out in the last four years with a focus on the elasticity, stress-strain relationship and fracture of calcium silicate hydrates and their analogues[4, 14, 15, 39, 50, 51]. MD simulations of C-S-H and the structural analogues are becoming more popular with the development of C-S-H specific force fields and since the determination of the crystal structure of tobermorite and jennite, making predictions of structure property relationships feasible[15, 52]. In addition to modelling mineral analogues, hypothetical structures have been generated to predict properties with varying compositions and structures. In the following sections, some hypothetical models are introduced before going on to discuss simulation predicted properties.

2.5.1 Computational Models of C-S-H

Since the exact crystal structure of C-S-H has yet to be found by means of experiment, a number of hypothetical computational models have been derived from mineral analogues primarily tobermorite and jennite. One of the first models was that by Pellenq et al. where a hypothetical C-S-H model was produced from an 11 Å tobermorite structure[14, 53]. The proposed model matched the Ca/Si ratio and density of C-S-H determined by Allen et al. and enabled simulation of C-S-H like structures for the first time. However, the model has been criticised in the literature due to some inconsistencies with experimental data. Firstly, the Ca environment of the model was unrealistic due to undercoordination of at least

half of the Ca^{2+} ions in the system[14, 28]. It is known that calcium ions are normally bound to between 6 and 8 other species however Pellenq's model has many calcium ions bound to only 5, 4 and even 3 other species[14]. Furthermore, work by Richardson has shown that dimeric silicate chains cannot be found in a starting model that is an ortho-tobermorite such as the starting model used in Pellenq's model[14, 28]. Nonetheless, despite inadequacies, the model allowed simulation of some C-S-H like structures which propelled the study of cement nano simulations.

Manzano et al. used tobermorite 14 Å and jennite as starting structures for producing a C-S-H model[5]. When silicate chains depolymerize, it is known that bridging tetrahedra are removed [28, 54]. Manzano et al. built pentameric, dimeric and octameric silicate chain C-S-H structures. When jennite was used as the starting structure, the process of producing C-S-H involved the removal of SiO_2 groups from the finite silicate chains, and in this case, no subsequent charge balance was required. With tobermorite as the starting structure, $\text{SiO}(\text{OH})$ groups are removed, and charge balance was achieved by adding protons or interlayer calcium ions on residual negative charges. After the bridging tetrahedra are removed, Manzano observed the interlayer Ca ions moving into the new unoccupied region during relaxation suggesting that Ca ions may be found in this site experimentally[5]. In jennite, the authors observed that the terminal oxygens left behind from bridging tetrahedra removal results in CaO coordination with the end chain oxygens but it is the silicate chains twist to accommodate this[5].

Rejmak et al. produced C-S-H models based on tobermorite 14 Å and jennite in a similar fashion to Manzano[39]. These models were developed specifically to identify differences in NMR results based on chain length variations, to aid in the experimental characterisation of the structure of C-S-H. With his models, Rejmak was able to show that, as the depolymerisation reduces the length of silicate chains, a movement of the chemical shift of ^{29}Si NMR to lower values is seen. In Rejmak's work, to obtain finite chains, $\text{SiO}(\text{OH})^+$ units remaining after removal of bridging tetrahedra (indicated in Figure 2.4) were charge balanced with protons, Ca^{2+} or $\text{Ca}(\text{OH})^+$. It is also worth noting that Rejmak carried out a stability study using DFT and found that removal of pairing tetrahedra, instead of bridging tetrahedra, lead the structure to be higher in energy and

therefore less stable. Before any DFT calculations were carried out, each model was optimised using the General Utility Lattice MD simulation tool (GULP) with a polarisable core-shell interatomic potential[55]. The study reinforced the work of Grangeon that jennite models are not found in C-S-H gels by demonstrating more similarity in NMR spectra obtained with tobermorite based models rather than jennite based models when compared to experimentally generated NMR spectra[31].

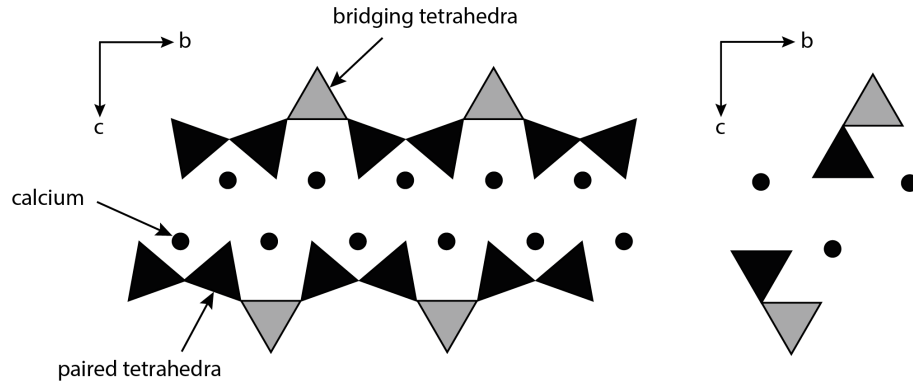


Figure 2.4: Bridging tetrahedra in calcium silicate chains

Richardson's models were derived from geochemical reasoning based upon analysis of 35 known calcium silicate hydrates[28, 56]. His models were made up of varying silicate chain lengths based on observed experimental results and were a mix of structures that had either 11 or 14 Å interlayer spacings, were derived from clino or ortho starting structures and that had varying silicate chain lengths. Even though no simulations were carried out using these structures by Richardson, the structures were compared to experimental characterisations of C-S-H where appropriate. The models were found to be consistent with many experimental trends observed for C-S-H. First of all, the models designed to display a shortening of interlayer spacing with increasing Ca/Si ratio which is consistent with experimental findings. The structures showed how low Ca/Si ratios could contain dimers which is consistent with Brunet et al. NMR data but this is inconsistent with a number of other theories where low Ca/Si ratio is thought to be made up of infinite chains at Ca/Si ratios as low as 0.9.[31, 57] Changes in the interlayer spacing of the models was found to be correlated to H_2O/Si ratio,

like in experiments. Lastly, calculated XRD patterns for the hypothetical models showed overlap for experimentally determined C-S-H.

2.5.2 Force Fields for Molecular Dynamics Simulations

MD uses a force field to describe the interactions and forces between atoms in a system. These force fields are often parameterised from experiment or *ab initio* simulations and describe the mean interaction between two atoms. The range of force fields for studying calcium silicate hydrate materials using molecular dynamics is narrow and historically has employed the classical force fields CLAYFF and COMPASS[58, 59]. The narrow range is most likely due to a low demand for force fields in this area thus there has been no drive for development. The COMPASS forcefield is a general forcefield developed to describe organic, inorganic and polymer materials via valence and non-interaction terms. CLAYFF is a general force field parameterised for studying clay-type minerals with complex layered structures[58]. CLAYFF uses a SPC model (a rigid model which has 3 interaction sites - one on each atom of water) to describe water for use in hydrated clays. In contrast to common classical potentials, the non-aqueous phases are described by non-bonded interactions. This not only makes implementation of the force field to molecular dynamics codes such as LAMMPS more straightforward as detailed bonding specifications are not required but also makes it easier to transfer between a number of mineral structures without deep modification of the input parameters. Pellenq et al. modified CLAYFF to be more akin to cementitious calcium silicate hydrate materials by more accurate parameterisation of the non-bonded parts leading to the development of the CSHFF[14].

One particular force field which has been rapidly increasing in popularity is ReaxFF, a reactive force field[60]. The ability of ReaxFF to carry out reactive processes means that non-equilibrium processes such as hydration and fracture can be studied at the nanoscale[50, 61–63]. Although ReaxFF has been used a number of times in the literature, it is evident that simple force field benchmarking has yet to take place. Similarly, as is the case with the CLAYFF and CSHFF, force field predictions of thermodynamic properties such as thermal expansion and heat capacity have not taken place - possibly due to the lack of

experimental data for comparison or due to the fact that the field has been more interested in modelling mechanical properties.

2.5.3 Previous Work on Structure Property Relationships for C-S-H

The models described above in Section 2.5.1 have enabled simulation of C-S-H structures in addition to mineral analogues. Over the past ten years, the number of molecular simulation studies has risen dramatically with the aim of linking the structure of C-S-H to its mechanical properties.

This quantifying of structure-property relationships has mainly been focused on elastic constants measured via molecular simulations. Elastic constants are relatively easy to calculate by simulation and they can be representative of large scale polycrystalline structure as their properties are averaged. Calculating the elastic constants by molecular simulation normally involves making small, reversible deformations in the simulation cell and measuring the resulting strain[64]. Another way is by increasing the length of the cell, applying a strain, and measuring the resulting stress. The elastic constants are often used to determine elastic moduli known as the bulk K , shear G and Young's modulus E through a method known as Voigt-Reuss-Hill averaging. Elastic constants can be calculated experimentally through methods such as Brillouin spectroscopy and bulk moduli can be calculated by high pressure XRD methods[65].

Work carried out by Manzano et al. showed that the indentation modulus increased with increasing silicate chain length indicating that long chain lengths result in a material with a higher stiffness and therefore, in this case, more desirable mechanical properties[4, 5]. The data was comparable to experimental nanoindentation work for C-S-H. The simulated indentation modulus was in the range of 12-22 GPa for simulations compared with 18 GPa for C-S-H gel concluding that the simulations were a reasonably accurate representation of experimental results[5]. Further work carried out by Pellenq et al. using models of varying Ca/Si ratio demonstrated that the Ca/Si ratio affected the trend in stiffness. The authors demonstrated that the indentation modulus decreased with

increasing Ca/Si ratio[15].

Recently, a small number of molecular fracture studies have been carried out on C-S-H using MD. Work by Hou et al. modelled fracture using Pellenq's C-S-H model with a circular central defect in which the fracture will propagate from and observed the tensile stress to be dependent on the direction of pull[66]. On the x-axis, where pull occurred in the direction parallel to the silicate chains, the tensile stress was found to be around 3.4 GPa, compared to 1.9 GPa in the direction perpendicular to the silicate chains i.e. equivalent to the crystal *c*-axis. It is expected that the crystal *c*-axis is the weakest layer since it does not involve breaking of covalent bonds and fracture would be associated with separation of the silicate chains through the water interlayer, which consists of weak hydrogen bonds[66]. Tensile stress in the x-direction fails at a higher strain compared to the z-direction (0.19 vs 0.35) further exemplifying the weakness in the z-direction. While this work backs up the hypothesis that C-S-H is most likely to fail in the crystal *c*-axis, the methodology was somewhat questionable. The work involved the use of CSHFF, a classical force field which does not have the ability to simulate the breaking and formation of bonds. It also observed that, during the tensile tests in the x and z-direction, the length of the box in the all directions is 138 Å with a central circular defect of 50 Å. This leaves 44 Å either side of the defect meaning that the defect is 6 Å larger than the length in which the fracture can propagate in the positive or negative direction. The authors did check the effect of the initial defect size and found that the tensile strength reduced from approximately 42 GPa to 26 GPa as the initial defect was reduced from 50 Å to 0 Å in diameter. While one aim of this simulation study was to assess the effect of the initial defect, or gel pore as it is referred to in the paper, the interaction of such a large crack with periodic images should have been considered. Additionally, it cannot be inferred from the information if a single crack was produced in cases other than the largest initial defect size.

Work by Bauchy et al. used a more appropriate force field where ReaxFF, a reactive force field capable of studying fracture, was employed and used the same C-S-H model by Pellenq using an elliptical initial defect[67]. A similar method to Hou et al. was used, however, the study was limited to pulling in the z-direction as this would be the most likely failure direction due to the weak bonding in the

interlayer compared to the covalent silicate chain bonding. The simulation size in this instance was around 2000 atoms which is considerably smaller than the 300,000 atoms in the simulations by Hou et al. The tensile strength measured by Bauchy et al. was 1.4 GPa, with a failure strain of 0.053. Despite the differences in method, force field and system sizes, this was close to the value of 1.9 GPa calculated by Hou et al. It can be concluded that the work of Bauchy et al. is more physically acceptable but the closeness in values is surprising. This raises questions regarding the simulation method however without usable experimental data to compare with, it is impossible to draw reasonable conclusions. There is now a need for validation of the general simulation and fracture method against sound experimental results using a well simulated material.

2.6 Summary

This chapter has provided an introduction to general cement chemistry including the formation of C-S-H in cement and the production of synthetic C-S-H. The current viewpoint on the structure was described and a review of the experimental characterisation was presented. The influence of Ca/Si ratio, H₂O/Si ratio and the MCL was discussed indicating that the fluctuation in composition is not fully understood. Additionally this chapter gave an overview of some hypothetical C-S-H models and their inclusion in MD simulations to measure the mechanical properties. Finally the chapter highlights the early stage at which MD simulations are at in the cement field and show that a more rigorous approach to future modelling research should be taken so that valid predictions can be made. To achieve this, any method should be designed and tested on a material which has been well characterised and one that has a range of mature force fields to benchmark simulation outputs. The next chapter introduces a material which can help to address this issue.

Chapter 3

A Review of the Chemical Structure and Properties of Ice

3.1 Overview

The lack of experimental and crystal data for C-S-H means that validation of molecular simulation methods against experimental results is challenging. In this thesis, ice Ih is used to validate the methods since the crystal structure, physical and mechanical properties are well known. In addition, water is one of the most simulated materials in the world and therefore the force field and the method can be compared with a vast amount of simulation data. This chapter introduces the structure and properties of ice Ih giving an overall description of ice Ih.

This chapter begins with an introduction to the chemical structure of ice Ih and its complex phase diagram. Both the single crystal and polycrystalline structure are discussed followed by a discussion of the mechanical properties of ice Ih. Finally, a selection of the most common force fields for modelling water and ice are introduced and a review of molecular simulations is carried out.

3.2 The Structure and Properties of Water Ice

Water is one of the most simulated materials due to its importance for life and interesting physical properties. It is the most heavily used liquid in industrial processes and is the only substance on Earth known to exist in all three states of matter[68]. Study into the structure-property relationships of ice Ih has attracted researchers spanning many fields including biological, planetary, atmospheric and geophysical sciences. While the properties of ice at the macro and microscale are reasonably well understood, many questions surrounding physical and chemical properties and processes at the nanoscale remain. In this section, the structure of the water molecule and how it forms a hexagonal ice structure in the solid phase is discussed.

3.2.1 The Structure of Ice Ih

Water is made up of two hydrogen atoms bonded to a central oxygen atom through an angle of 104.52° and a bond length of 0.9572 \AA as shown in Figure 3.1[69].

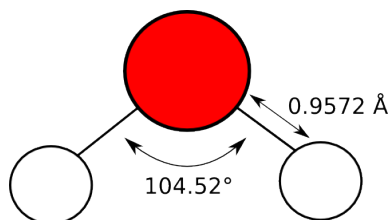


Figure 3.1: Structure of a single water molecule. Oxygen atom (red), hydrogen atom (white)

Although water is a relatively simple molecule containing only 3 atoms, the interatomic interactions in the liquid phase are complex and much has still to be discovered. Upon cooling to 273 K at ambient pressures, water condenses to form ordinary ice, also known as ice Ih, where I signifies that it was the first ice structure to be solved and the h refers to the hexagonal crystal structure in which it adopts. It is the form that is found naturally on earth, in sea ice, glaciers and

snow. Neutron diffraction studies have shown that the structure of ice Ih consists of a network of hydrogen bonded water molecules (see Figure 3.2 where the oxygen atoms are arranged in a tetrahedral geometry with an interatomic O-O-O hydrogen bond angle of 109.47° and an O-O equilibrium distance of 2.76 \AA [70]. The central oxygen atom forms a tetrahedral structure with 4 neighbouring oxygen atoms as depicted in Figure 3.2. The overall crystal structure is a hexagonal prism with an aspect ratio (length of c/a axis) is shorter than is normally seen with purely tetrahedral structures.

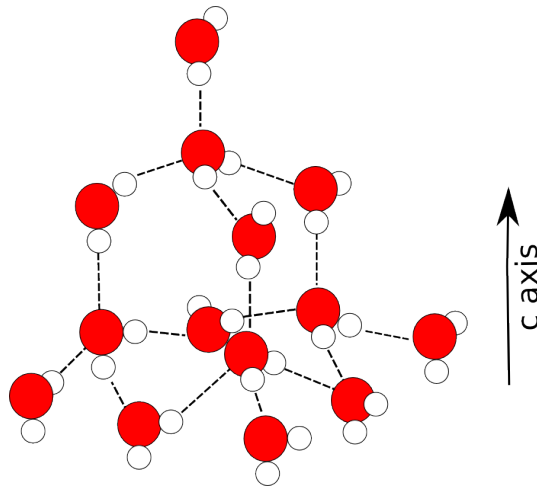


Figure 3.2: Structure of Ice Ih.

Each molecule in the network participates in four hydrogen bonds where it donates two hydrogen bonds and accepts two hydrogen bonds as illustrated in Figure 3.2 (two acceptor and two donor). While the oxygen atoms are strictly ordered, the water hydrogen atoms contain a degree of disorder as a result of natural crystal defects. The disorder of the ice Ih phase is associated with the ice structures which form a boundary on the phase diagram with liquid phases and arises from point defects in the crystal structure allowing movement of hydrogens from one molecule to the next through the large hydrogen bonded network. Figure 3.3 illustrates the type of defects that are thought to lead to hydrogen disordered phases in ice[71]. The first type of defects are known as Bjerrum defects and are associated with a water molecule being aligned in a way where one hydrogen from one water molecule meets another hydrogen from a different water molecular (D

defect) or where an oxygen meets another oxygen (L defect). In both cases, the defect results in a missing hydrogen bond[71]. The second type of defect are known as Ionic defects and exist when a hydronium or hydroxyl ion is found. When one defect is found the defects can easily migrate throughout the system.

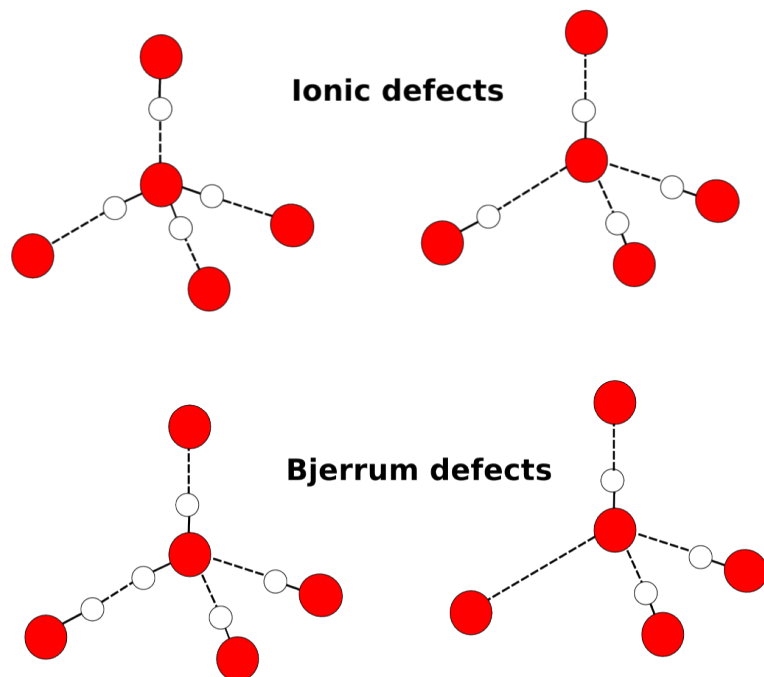


Figure 3.3: Defects in Ice Ih which lead to hydrogen disorder [71].

3.2.2 The Phase Diagram of Ice

While ice Ih is the common form of ice on Earth, it is in fact one of many phases of ice that exist and like C-S-H, ice is a dynamic structure in which the properties change depending on the temperature, pressure and time. Figure 3.4 shows the phase diagram of water across a range of temperatures and pressures. As can be seen in the figure, thirteen different phases of ice are shown, however, seventeen different phases are known including amorphous ice phases[71].

The hydrogen disorder described earlier which occurs for ice Ih is also found in a number of other phases of ice that make up the phase diagram. The disordered phases are those which share a border on the phase diagram with liquid wa-

ter. Research has shown that disordered phases can be transformed into ordered phases upon cooling[72].

The complex phase diagram of ice makes molecular simulation challenging if working close to a phase boundary and work has shown that the majority of water potentials do not transfer well to ice[73, 74]. Vega and co-workers have demonstrated that many water models incorrectly predict the melting point and other key characteristics[73, 74]. Therefore careful considerations must be taken before using a water model for ice.

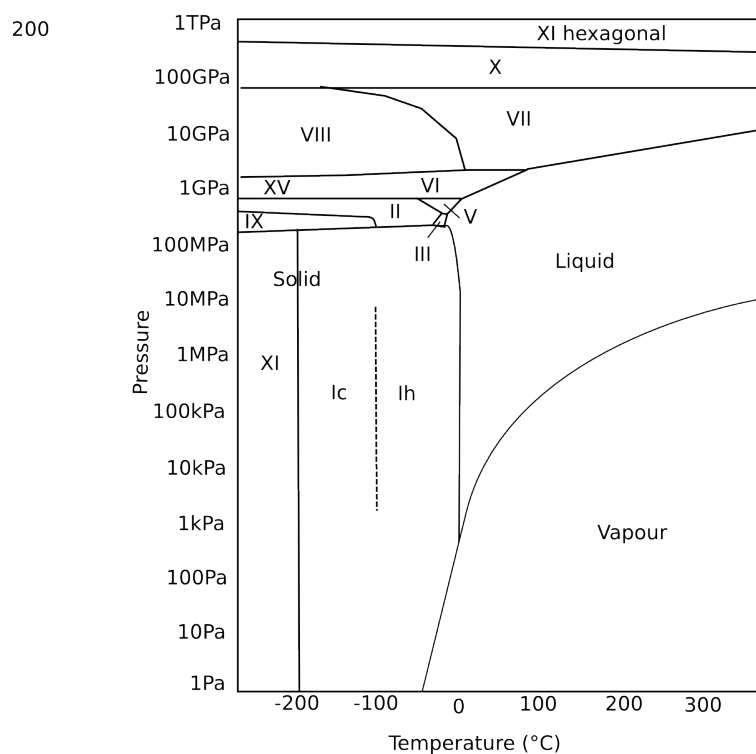


Figure 3.4: Phase Diagram of Water

3.2.3 The Polycrystalline Structure of Ice Ih

Naturally formed ice such as sea ice, snow or glacial ice normally takes the form of polycrystals. Ice polycrystals consist of an agglomeration of single crystals and can be 1 mm to 20 mm in size[75]. The polycrystal grains can be visualised under a microscope with cross polarized light and as a result, much is known about the

polycrystalline ice structure.

The grain boundaries which naturally occur in polycrystalline ice are particularly interesting and contribute to the chemical and physical processes. As ice approaches the melting temperature, liquid layers form at the grain interface[76]. Over time, the grain size increases as a result of single crystals merging under stress, and in doing so, the crystals align their c axis[76]. Phase changes occur at the crystal grain boundary therefore a number of simulation studies have researched into this area. Recent work has shown the relevance of the surface to the frictional properties of ice. In particular, activities such as skiing and skating are enabled specifically due to the surface liquid properties[77].

3.2.4 Mechanical Properties of Ice

Ice is a viscoelastic material, like C-S-H and as such, the mechanical response varies by the load and the rate of loading resulting in brittle and ductile behaviour[78, 79]. Some early work focused on determining the elastic constants of a variety of different natural ice forms[80, 81]. Using Brillouin spectroscopy, a method which uses inelastic scattering to determine the elastic moduli, Gammon et al. found that the local elastic properties of ice were the same regardless of the type of ice being measured i.e. lab grown ice, glacier ice or lake ice however the bulk elastic properties were affected by the presence of air bubbles, particulates and grain size[80]. Gagnon et al. demonstrated a pressure dependence on the elastic constants of single crystal ice showing that the value of the individual elastic constants increased with increasing pressure. At 0 kbar $C_{11}=144.8$ kbar, $C_{12}=73.5$ kbar, $C_{13}=59.7$ kbar, $C_{33}=156.3$ kbar and $C_{44}=31.5$ kbar with a bulk modulus of 92.4 kbar. At 2.80 kbar pressure the elastic constants are $C_{11}=157.1$ kbar, $C_{12}=88.8$ kbar, $C_{13}=73.1$ kbar, $C_{33}=168.9$ kbar and $C_{44}=30.2$ kbar with a bulk modulus of 105.9 kbar. The data shows that each elastic constant, with the exception of C_{44} , increases with increasing pressure suggesting that ice becomes more stiff with increasing pressure. This is reflected in the density which increases from 0.9228 g/cm³ to 0.9500 g/cm³ upon increasing the pressure to 2.80 kbar. This could be a result of the hydrogen bonds shortening within the ice network due to the applied pressure, increasing their attraction and creating a more com-

pact structure with more resistance to compression. The C_{44} elastic constant is a shearing modulus and therefore the lowering of this value may be a result of the increases pressure restricting the ability to withstand shear in this direction. The elastic constants determined from single crystals in the work by Gagnon et al. were indifferent to the polycrystalline work by Gammon et al. indicating that the elastic properties are not affected by the nature of the ice[80, 81]. Gagnon et al. reported the Young's modulus of ice to be 93.32 kbar and the bulk modulus to be 88.99 kbar[81].

The tensile strength of ice was found to be in the range of 0.7 MPa to 3.1 MPa measured over a temperature range of 253-263 K. Tensile failure of ice commonly occurs when thermal fractures are created, in floating Arctic sea ice, by the hulls of ice breaker ships and when crevasses form in glaciers[82–84]. Experimentally it has been reported that ice fails after straining of 0.01-0.1% via a transgranular cleavage and it was demonstrated that the tensile strength is independent of the strain rate and has a small dependence on temperature[85, 86]. Linear elastic fracture mechanics is often used to describe ice undergoing brittle failure as the crack speeds occur so quickly to avoid any sort of creep behaviour; however, a brittle to ductile transition does occurs at low strain rates[87].

Fracture of ice is more complex and is dependant upon the nature of the ice being studied i.e. single crystal or polycrystal. There is a great deal of interest in studying fracture in ice as it relates to glacial melts and the effect of embedded carbon dioxide or sediments is crucial to understanding how Arctic ice will deform over time. Tensile failure for single crystal ice has been observed to be independent of temperature and strain rate. It is, however, dependent on the direction of tensile stress relative to the crystal c axis and has been found to be in the range of 4 MPa and 6 MPa at 0° and 90° respectively with basal plane fracture being the most likely scenario at 263 K[88]. Single crystal ice is generally stronger with respect to brittle tensile failure than polycrystalline ice which is in the range of 0.5 MPa to 2 MPa. Experimentally it has been reported that polycrystalline ice fails after straining of 0.01-0.1% via a transgranular cleavage and it was demonstrated that the tensile strength is independent of the strain rate and has a small dependence on temperature[85, 86] In polycrystalline ice, temperature is known to reduce the tensile stress by around 10% when the temperature is dropped from 273 K to

243 K. The strain rate has negligible influence on polycrystalline ice tensile stress over the range of 10^{-7} s^{-1} to 10^{-1} s^{-1} [88]. At much higher strain rates, polycrystalline ice can withstand a tensile stress up to around 50 MPa at 10^4 s^{-1} [88]. By using a critical stress intensity factor to capture when fracture propagation occurs, the fracture toughness has been calculated to be between 0.05 and 0.40 $\text{MPa}^{1/2}$ [84, 88]. The toughness is independent of ice temperature but is directly related to porosity and density.

3.3 Molecular Simulations of Ice

Molecular simulations are critical to understanding the behaviour of ice at the nanoscale. Since the first simulations of liquid water by Watts and Barker, and Rahman and Stillinger, the number of simulation studies have boomed due to the importance of water to life and climate[89, 90]. One of the most important considerations when modelling the solid phases of water is to choose an appropriate force field potential. The number of force fields for describing water is well over a hundred however despite the vast array to choose from, the models are not capable of describing the whole phase diagram and many struggle to describe the properties of ice[2, 91]. In the following section, a short review of the force fields which have been used to study ice Ih will be discussed.

3.3.1 Force fields

Water models are parametrised by fitting to *ab initio* simulations or by fitting to experimentally measured properties[74]. Many of the water potentials are based on non-polarisable, rigid models where the H-O-H angle and O-H bond lengths are fixed and rely solely on an intermolecular bonding description[74]. The rigid water models often employ an algorithm known as the shake algorithm which restricts movement of the molecule, keeping the bond rigid[92, 93]. The simple rigid models are hugely advantageous when running large systems as their simplicity means that the computational expense associated with their simulation is relatively low. These rigid models include the widely used 3-point interaction

models like SPC and SPC/E and TIP3P, 4-point interaction models TIP4P/ice and TIP4P and 5-point interaction models such as TIP5P[94–99]. Drawbacks of such rigid force fields include the inability to simulate vibrational properties where bending and stretching modes play an important role. As a result, a number of flexible models for the study of ice such as the flexible SPC model and TIP4P/2005f were developed from their rigid counterparts[100, 101].

The simplest models are the 3 point models and are made up of rigid intramolecular bonds and fixed H-O-H angle. Instead, only intermolecular interactions are used. The models are based upon Lennard Jones interactions and despite being far from the real situation, they provide a cost effective model with reasonable predictions[73].

One of the biggest difficulties when finding an appropriate force field for water is finding one which predicts the correct melting point. Melting points are easily calculated by experiment however in a simulation, the task is much more involved. Melting points can be calculated using molecular dynamics by using free energy methods, coexistence simulations or thermodynamic integration[102]. Another method recently proposed by Vega et al. is the free surface method which involves simple temperature runs with the absence of super-heating[103]. For SPC and SPC/E, the melting temperatures fall substantially below the experimental value of 273 K. SPC predicts a melting point at 190.5 K whereas SPC/E predicts a melting point of 215 K[104]. The TIP4P water models show an improvement in the prediction of melting points with TIP4P, TIP4P/Ew determining melting points at 232.0 and 245.5 respectively. TIP4P/ice is by far one of the best predictions of 272.2 K[104]. Similarly, TIP5P predicts a melting point of 273.9 K[104]. The difference in melting points is directly related to parametrisation of the individual force field. For example, SPC, SPC/E, TIP3P and TIP4P were parametrised to reproduce the properties of liquid water at ambient pressures and temperatures. In the case of TIP5P, the peak density, at 4 °C, was used to fit the parametrisation and in TIP4P/ice, the melting temperature of ice was used to fit the parameters. As a result, naturally, the resulting melting points will vary.

Furthermore, no one water model has been able to describe the entire phase diagram of water. Work by Vega et al. has shown that SPC/E and TIP5P fail

to produce the correct phase diagram whereas TIP4P produces the correct shape but precision is far from the experimental data[105]. TIP4P/ice on the other hand accurately reproduces the correct phase diagram for water and predicts the correct densities for all phases of ice[105].

3.3.2 Mechanical Properties of Ice at the Nanoscale

Despite the vast field of research relating to the simulation of ice, only a few simulations studies exist where mechanical properties have been determined indicating a gap in the literature. Two studies have been reported in the literature investigating fracture of ice Ih using MD[106, 107]. The studies have focused on the effect of embedded CO₂ on the fracture properties of ice Ih using ReaxFF. One study simulated a 50 Å × 20 Å × 20 Å system which was made up of 2592 atoms and found that the tensile stress decreased with increasing CO₂ concentration[106]. The tensile stress was found to be 4.4 GPa as pure ice and 3.9 GPa with the presence of 10 CO₂ molecules. This decrease in mechanical properties was thought to be related to the CO₂ molecules disrupting the hydrogen bond network and thus weakening the structure. This tensile stress of pure ice as stated earlier is 4-6 MPa which is three orders of magnitude smaller than the simulated tensile stress by Cranford. The work by Qin et al. determined the tensile stress to be around 0.3 GPa at 200 K for pure ice using a system of 40 Å × 40 Å × 40 Å, and although this value is still somewhat larger than that seen by experiment, it is an order of magnitude closer. It is also likely that the size difference of the simulation cells will have an effect. Qin et al. measured the fracture toughness of ice for the first time using ReaxFF and MD and found the value to be 19 kPam^{1/2}[107]. The authors compared to an experimental value of 22 kPam^{1/2} at 250 K, however, other experimental reports have been higher in value (100-140kPam^{1/2} at 250 K[108] and 80-110 kPam^{1/2} at 263 K in another study[109]). This demonstrates the difficult nature of investigating fracture properties in experiment and via simulation.

3.4 Justification for using Ice Ih for validation of methods

The significance of using ice Ih as a validation material is primarily due to the fact that for ice Ih, vast amounts of experimental and simulation data is available for comparison.[73, 84, 88, 110] This means that when developing and checking force fields, there are plenty of other force field data to compare to. Furthermore, and of equal importance, the results gained from any methods implemented or developed can be compared directly to the available data whether the data is physical, thermodynamic or mechanical[81, 84, 109, 111]. This gives confidence that the methods which are then applied to C-S-H, which is heavily lacking in experimental data, can at least reproduce data for another material, in this case ice Ih.

With respect to mechanical behaviour, ice Ih has some similarities to C-S-H which makes it an appropriate validation material, in addition to the vast array of available data for comparison. First of all, ice Ih is made up entirely of hydrogen bonding intermolecular interactions. In C-S-H, it has been shown recently that much of the mechanical behaviour stems from the hydrogen bonded network resulting from the bound and pore water which resides in the interlayer between the silicate chains[15, 62]. Some authors in the past have used silicon as a validation material when attempting to understand the mechanical behaviour of C-S-H[67], however, the bonding structure of silicon consists entirely of covalent bonds. Whilst C-S-H contains covalently bonded silicate chains, the covalent bonds in C-S-H are unlikely to break due to the strength of covalent bonds compared to hydrogen bonding. It has already been shown by some authors that the hydrogen bonded network in C-S-H is the driver of failure[15, 61, 62] and therefore, the view point of this thesis is that ice Ih makes a more suitable validation material than silicon due to the hydrogen bond network. Silicon is known to have a brittle failure mechanism[112] where ice Ih is known to have time dependent failure, much in the same way which C-S-H fails[113].

Lastly, like C-S-H, ice Ih is viscoelastic[114]. At low strain rates, for example glaciers under the strain of gravity, creep deformation results similar to the creep

deformation as seen in cement. This similarity in small strain failure mechanisms adds to the usefulness of ice Ih for validating simulation methods of C-S-H. [115, 116]

To conclude, while ice Ih in composition is different from C-S-H, the hydrogen bonded network failure mechanisms have some similarities. Furthermore, the large amount of simulation and experimental data available for comparison to the work in this thesis adds confidence to the realistic nature of the methods developed in this thesis. Therefore, this thesis proposes ice Ih as a validation material.

3.5 Summary

In this chapter, the structure and properties of ice Ih were introduced. It was shown that ice Ih has well characterised experimental physical and mechanical properties which can be used as a comparison to simulation studies. The main force fields commonly used for ice Ih were presented and it was highlighted that little is known about the mechanical properties of ice Ih at the nanoscale. This exemplifies the need and double significance of using ice Ih as a proof of concept study for developing MD mechanical property methods – it is useful to study ice Ih as the experimental data available for comparison is plentiful and well advanced, and secondly, there is a gap in the literature which should be filled regarding the nanoscale mechanical properties of ice. This work is not only important to the fields of civil engineering for advancing nanoscale understanding of C-S-H, but will have have to the potential to impact on the fields of glaciology and planetary sciences.

Chapter 4

The Methodology of Molecular Simulations for Calculating Structure-property Relationships

4.1 Overview

Molecular simulation of amorphous and complex materials can often be critical in understanding structure-property relationships. Molecular simulations can be used to complement experimental results and can predict properties where experimental data is lacking. In this chapter, the core of molecular dynamics theory will be introduced and the form of the potential force field used will be described. Finally, the determination of mechanical properties from molecular simulations and how these properties can be compared to experimental data will be discussed.

4.2 Molecular Dynamics

The theories discussed in this section can be found in references [102, 117, 118]. MD is a technique which uses Newton's classical equations of motion to describe how a system behaves over time, allowing time dependent processes to be studied. The technique has broad applications ranging from protein studies and drug discovery to materials characterisation and prediction of nanoscale mechanical properties.

Molecular dynamics is based upon Newton's equations of motion which relates the force, F_i , applied to an object of mass, m , to the resulting acceleration:

$$\mathbf{F}_i = m_i a_i = m_i \cdot \frac{d\mathbf{v}_i}{dt} = m_i \cdot \frac{d^2 \mathbf{r}_i}{dt^2} \quad (4.1)$$

$$\mathbf{F}_i = -\nabla_i U \quad (4.2)$$

Where m , a , v , t and r are the mass, acceleration, velocity, time and coordinate of atom i respectively, and U is the potential energy function of the positions of all of the atoms. By calculating the force acting upon each atom of known mass, the acceleration can easily be determined. Over time, the integration of the acceleration can produce the atomic velocities and positions to produce a trajectory. From analysis of this trajectory, a wide range of properties can be calculated, for example; equation of state, melting points, dynamics of structural folding in proteins and molecular docking.

The atomic coordinates and bonding potentials are specified alongside the desired conditions such as temperature, time step and total runtime. Next, the starting velocities are specified. The forces acting on each particle in the system is calculated and the equations of motion described above in equation 4.1 are integrated. The forces are then recalculated and again, the equations of motion are integrated until the end of the simulation. From this simple set up, it is possible to gather a range of information from the simulation to compute ensemble averages such as volume, lattice parameters and thermodynamic data such as compressibility and heat capacity.

To perform a molecular dynamics simulation, a reasonable prediction of the atomic structure and bonding must be known, often in the form of an experimentally calculated crystal structure. This crystal structure can provide accurate information on atomic coordinates, bonding and symmetry. A potential description of bonding, also known as a force field, is then applied and the starting configuration of atoms are given an initial velocity. Parameters which make up a force field normally include a harmonic expression of the bond, the angle of the atomic bonds in a dihedral, and a cut off distance in the atoms are no longer accepted as being bonded. This cut off allows for less force calculations to be carried out during the course of the simulation and reduces the overall computational expense. The simulation begins and the forces between atoms in each frame are calculated and the equations of motion are integrated at each step for a specified length of time. From the resulting atomic trajectories many statistical physical and thermodynamic properties can be calculated.

It was mentioned earlier that at every step in the simulation the equations of motion must be integrated. An appropriate method should be one which is accurate, conserves energy and ideally has a high computational speed and small memory requirements. However, the force calculation is often the limiting factor in terms of computational speed. The Verlet algorithm is often used to perform time integration in MD and has been shown to be advantageous over other integration methods such as the Euler method which suffers from inaccuracies. Unlike the Euler method, the Verlet algorithm is reversible and therefore conservation of energy is achieved and the original starting point can be recovered.

A Taylor expansion is used to calculate the position of an atom in time:

$$\mathbf{r}(t + \Delta t) = \mathbf{r}(t) + \mathbf{v}(t)\Delta t + \frac{\mathbf{F}_i(t)}{2m}\Delta t^2 + \frac{\Delta t^3}{3!}\ddot{\mathbf{r}} + \mathcal{O}(\Delta t^4) \quad (4.3)$$

where t is the time step, m is the mass of atom i , r is the Cartesian atomic position and \mathcal{O} is order of approximation of t^4 . Reversible time integration can

be calculated by:

$$\mathbf{r}(t - \Delta t) = \mathbf{r}(t) - \mathbf{v}(t)\Delta t + \frac{\mathbf{f}(t)}{2m}\Delta t^2 - \frac{\Delta t^3}{3!}\ddot{\mathbf{r}} + \mathcal{O}(\Delta t^4) \quad (4.4)$$

By combining equations 4.3 and 4.4, the need to calculate the velocity at each time step is removed, allowing for a more accurate calculation of the atomic trajectory:

$$\mathbf{r}(t + \Delta t) + \mathbf{r}(t - \Delta t) = 2\mathbf{r}(t) + \frac{\mathbf{f}(t)}{m}\Delta t^2 + \mathcal{O}(\Delta t^4) \quad (4.5)$$

$$\mathbf{r}(t + \Delta t) \approx 2\mathbf{r}(t) - \mathbf{r}(t - \Delta t) + \frac{\mathbf{f}(t)}{m}\Delta t^2 + \mathcal{O}(\Delta t^4) \quad (4.6)$$

Atomic trajectories can be used to calculate particle velocities via:

$$\mathbf{r}(t + \Delta t) - \mathbf{r}(t - \Delta t) = 2\mathbf{r}(t)\Delta t + \mathcal{O}(\Delta t^3) \quad (4.7)$$

$$\mathbf{r}(t) = \frac{\mathbf{r}(t + \Delta t) - \mathbf{r}(t - \Delta t)}{2\Delta t} + \mathcal{O}(\Delta t^2) \quad (4.8)$$

Force fields are used to describe the harmonic interactions between particles and can be generated by quantum mechanical and *ab initio* calculations. These algorithms produce a potential energy surface which can be used to assess both ground and excited states and should be representative of the system in question.

A standard empirical force field takes the form of:

$$U = \sum_{bonds} \frac{k_b}{2}(r - r_0)^2 + \sum_{angles} \frac{k_a}{2}(\theta - \theta_0)^2 + \sum_{torsions} \frac{V_n}{2[1 + \cos(n\phi - \delta)]} + \sum_{improper} V_{imp} + \sum_{LJ} 4\epsilon_{ij} \left(\frac{\sigma_{ij}^{12}}{r_{ij}^{12}} \right) - \left(\frac{\sigma_{ij}^6}{r_{ij}^6} \right) + \sum_{elec} \frac{q_i q_j}{r_{ij}} \quad (4.9)$$

where k and r is the force and position of atom i respectively, ϕ is the angle

between atoms a and b , q is the charge on each atom of the bond, V_n corresponds to the energy barrier of the interaction, σ is the potential cut off distance, and ϵ is the potential well depth. The first four terms of equation 4.9 represent bonding, angles, torsional and improper terms respectively and are known as intramolecular terms. The last two terms are Lennard-Jones interaction potential and electrostatic terms, respectively. The bonding term is a harmonic approximation and fixes the length of a bond within a given range. The harmonic potential does not take into consideration the chemical nature of the species it is describing as bonds cannot be broken nor created when described by this potential.

The angle term describes the angle between three bodies and in this case is also described by a harmonic term however a trigonometric term can also be used. The torsion term is used to describe interactions between 4 bodies where rotation as well as bending can occur. This term is somewhat more important than the previous two as torsional effects are more likely to affect structural properties due to conformational influence. The final, improper term is used to describe molecules which lie in one plane such as sp^2 hybridized carbons. Although the torsional term works alongside this term, the improper term increases the energy when e.g. planar molecules move out of conformation.

When describing classical potentials in a system it is necessary to state a cut off radius and is normally equivalent to half of the periodic simulation box. This cut of radius is required to ensure the potentials only act where needed and can reduce the overall computational cost of the simulation. One of the simplest force field potentials is the Lennard-Jones Potential:

$$V(r_{ij}) = 4\epsilon \left(\frac{\sigma_{ij}}{r_{ij}} \right)^{12} - \left(\frac{\sigma_{ij}}{r_{ij}} \right)^6 \quad (4.10)$$

where ϵ is the potential well depth, σ is the potential cut off distance and r is the distance between atoms i and j .

4.3 Force Fields

Classical force fields enable the simulation of dynamic atomistic systems over time with reasonable computational expense. Due to the relatively low computational expense of a classical forcefield, simulations can be carried out for several nanoseconds and, in some cases, can contain up to one million atoms. The disadvantage of classical dynamical systems however is that electronically driven processes such as mapping reaction coordinates and transition states cannot be studied and these potentials are limited to non-reactive bonding descriptions where only hydrogen bonding, van der Waals and electrostatic forces come into play. To study electronic properties, quantum mechanical theories such as DFT or *ab initio* must be employed. These methods have a large computational expense and as a result, simulations are restricted to small system sizes of a few hundred atoms and very short time scales. To overcome these drawbacks and bridge between quantum and classical simulations, reactive empirical force fields have been developed such as COMB, Tersoff and ReaxFF potentials[119–121].

Developing force fields is a tricky, involved task and can take a substantial amount of time. This is further complicated when parametrising a force for complex, unsolved systems such C-S-H. As such, developing a new force field as part of this project would have been expensive both in real time and computational time. As a result, it was decided to implement existing force fields within this study as it is important to evaluate existing force fields for use before any force development should be attempted. Furthermore, from a research perspective, it is more interesting, and certainly more useful, to evaluate the fitness of existing force fields to find the capabilities and limits.

The principle force field used throughout this thesis is ReaxFF, a reactive force field with charge variability[122]. ReaxFF has been further developed from the original ReaxFF parameters in [122] and developments relevant to the work in this thesis will be discussed. The parameters used for both calcium silicate hydrates and water ices are found in [123]. The ReaxFF will now be introduced.

4.3.1 ReaxFF

First parametrised in 2001 for the modelling of hydrocarbons, ReaxFF is an empirical force field based on bond order theory and can be used for reactive and equilibrium molecular dynamics[122]. Unlike other classical force fields, ReaxFF has no explicit bonding configurations, instead it uses bond order determination from the instantaneous configurations by calculating interatomic distances to determine a bonding configuration. As such, the implementation of ReaxFF in classical molecular dynamics codes such as LAMMPS (Large-scale Atomic/Molecular Massively Parallel Simulator) is simple, straight forward and easily transferred from one system to another without the requirement of bond lists.

A number of parametrisations of ReaxFF exist and the background to their development varies. Figure 4.1 details the most important milestones in ReaxFF development and the origins in which the parameters used in this thesis have come about. The original ReaxFF development [122] was written to describe hydrocarbon systems. This system could not be directly transferred to Si bond descriptions and therefore was extended to describe Si systems as described in reference[121]. From 2005 onwards, the ReaxFF as produced by van Duin has remained relatively constant and as such, the standalone ReaxFF which can be found in a number of molecular dynamics codes such as LAMMPS. Detailed theory of ReaxFF descriptions can be found in [124].

Like many empirical force fields, the overall system energy of ReaxFF is described by a simple addition of the partial energy contributions as described:

$$E_{tot}^{REAXFF} = E_{bond} + E_{over} + E_{under} + E_{lp} + E_{val} + E_{pen} + E_{tors} + E_{conj} + E_{vdw} + E_{Coulomb} \quad (4.11)$$

Where E_{bond} describes the energy associated with bond order and bond energy, E_{over} and E_{under} is the energy associated with over and under coordination respectively, E_{lp} is an energy contribution from atoms which contain lone pairs, E_{val} is the energy from individual atomic valency, E_{pen} is the energy penalty associated with double bonded atomic valency, E_{tors} for torsional angles, E_{conj} for conjuga-

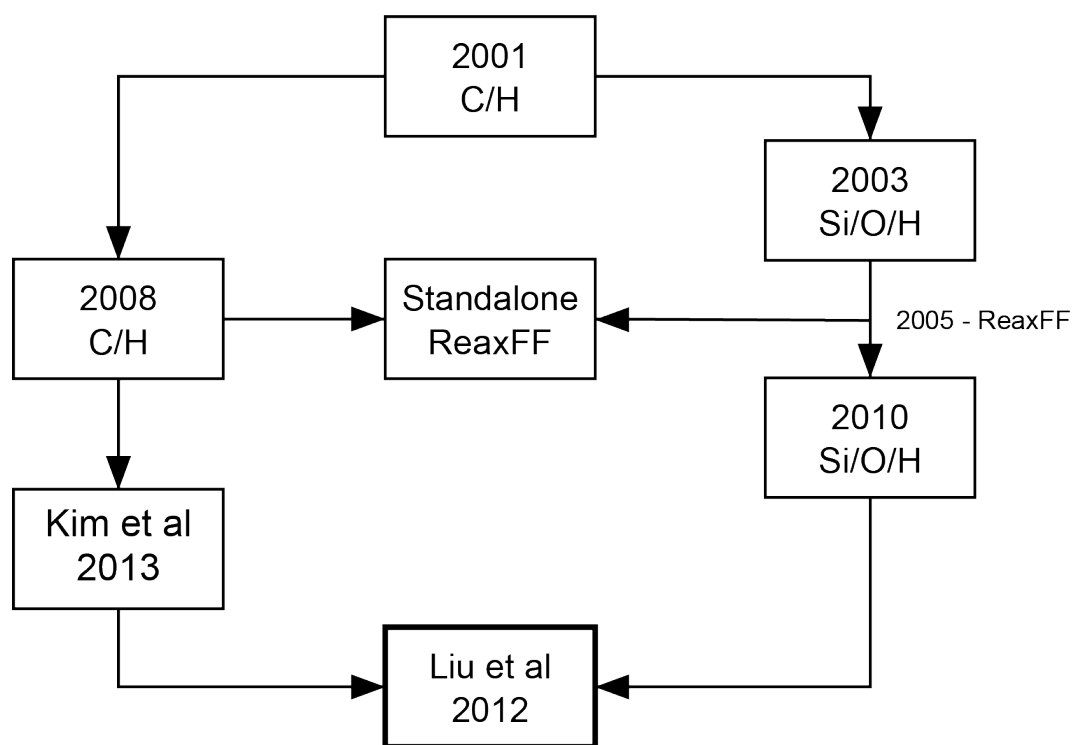


Figure 4.1: Timeline of ReaxFF

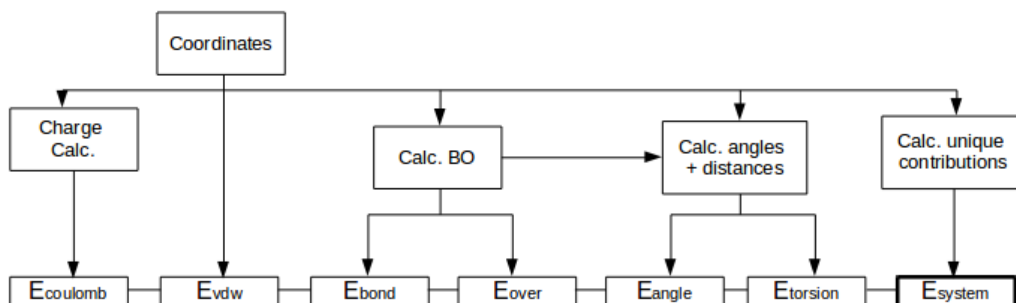


Figure 4.2: Calculation of Potential Energy of a typical ReaxFF system. [125]

tion, E_{vdw} van der Waals energy contribution and finally E_{Coulomb} for coulombic energy terms.

The procedure for calculating the total system energy is shown in Figure 4.2. Once atomic coordinates are read in, calculations of bonding contributions are divided into bonded and non-bonded interactions. Non-bonded interactions involve summing coulombic and van der Waals energies and the charge re-calculations are also carried out at this step. At the same instance, bond orders and angle contributions are calculated and corrected by inclusion of the energy penalty terms.

E_{bond} is entirely made up from bond order calculations and is described further in equation 4.12. The bond order is calculated based on the atomic coordinates and relative positions to each other. ReaxFF calculates the bond order of atoms i and j by considering the interatomic distances of the initial atomic coordinates to determine single, double and triple bonds. Interactions associated with bond connectivity such as hydrogen bonding and valency are kept realistic by incorporating a dependency on bond order.

$$BO_{ij} = \exp[p_{bo,1} \cdot (\frac{r_{ij}}{r_o})^{p_{bo,2}}] + \exp[p_{bo,3} \cdot (\frac{r_{ij}}{r_o})^{p_{bo,4}}] + \exp[p_{bo,5} \cdot (\frac{r_{ij}}{r_o})^{p_{bo,6}}] \quad (4.12)$$

Where p is the bonding term, r_{ij} is the distance between atom i and atom j , and r_o is the equilibrium distance of each bond type. Bonding terms and equilibrium distances are set to match quantum mechanical calculations. Single, double and triple bonds are described from the first, second and third term respectively in the Equation 4.12.

For hydrocarbon systems, the total bond energy of ReaxFF is simply a sum of the single, double and triple bond dissociation energies due to the gradual increase in bond strength associated with increasing bond orders. For Si systems, the bond dissociation energies (D_e) are somewhat different and as a result, additional bond order terms are required.

4.4 Choosing an Appropriate Time Step

The time step of a dynamic system is critical in capturing adequate sampling of a system over time. A time step which is too small will add unnecessary time onto the end of a simulation, however, a large time step may cause inappropriate sampling of the vibrational modes to take place. Ideally, to save on computing time, the largest possible time step should be used. For the ReaxFF system, rather small time steps are required due to the charge equilibration and re-calculation of bond order which must take place after each movement. The recommended time step for ReaxFF is in the range of 0.1 - 1.0 fs to account for such complex charge equilibrium calculations [124].

To determine the appropriate time step for the system in question, tobermorite 14 Å is used. The time step was chosen based on energy conservation of a micro-canonical ensemble (NVE) at 298 K and zero pressure using the tobermorite 14 Å 0.1 - 1.0 fs. Figure 4.3 displays the total energy captured by each time step.

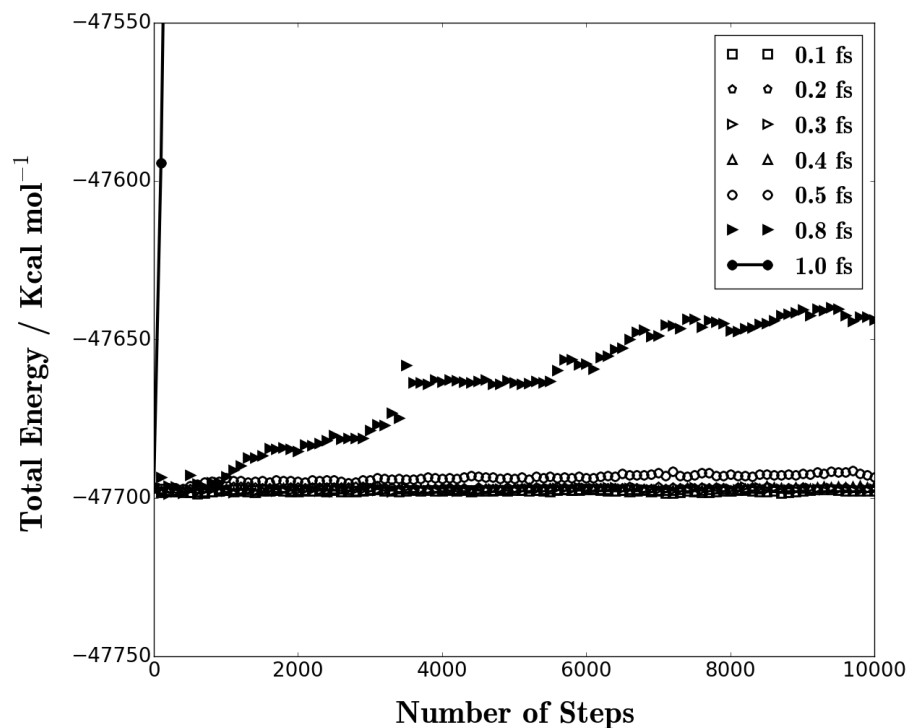


Figure 4.3: Energy convergence of tobermorite 14 Å at different time steps with ReaxFF

From Figure 4.3, it is clear that a time step greater than 0.4 fs affects the convergence of the total energy of the system. Choosing a time step as low as 0.1 fs will require additional computational time and as can be seen from Figure 4.3, the time step is not required to be so low. A time step of 0.2 fs is chosen as based on this convergence study, the total energy of the system converges well. While, based on the convergence study a larger time step of 0.3 or 0.4 fs could have been a more appropriate choice and would allow for a lower computational expense, this time step is chosen to allow for the best coverage of bond breaking and making processes which may be important for the study of fracture.

4.5 Calculating Elasticity from Molecular Simulation

The elasticity of a material can tell us how that material behaves under load and directly relates the structure of a material to its physical properties. It can give an idea of how bonding relates to strength, can give an indication of crystal elastic response and can aid in characterisation of mineral crystals and the study of their behaviour under high pressure. Elasticity describes the linear relationship between stress and strain to study reversible deformations where stress is defined as the applied force and the strain as being the resulting change in length or volume.

Stress, a second rank tensor, can be applied to a crystal hydrostatically (equally in all directions) or uniaxially (in one direction only). In the case of a cubic crystal, stress can be applied on each face and can be compressive stress or stress applied in tension. Normal stresses are those applied in the x, y or z direction and are equivalent to the force per unit area. Shear stresses are forces acting on a face in the direction perpendicular to that face. Each face of the cube in Figure 4.1 can have one normal stress and two shear stresses for example, σ_{11} represents the normal stress acting on the x face, σ_{12} and σ_{13} represent the stresses applied in the x-direction perpendicular to the face. Likewise, for each face in a cubic crystal, 3 strains exist and for every stress σ_{ij} , there is a resulting strain ϵ_{ij} . In an isotropic cubic crystal in equilibrium, the number of individual stresses or strains can be reduced to six. In the case of an anisotropic crystal where the properties are dependent on direction then the total number of stress components can be much greater.

Elastic constants relate stress to the resulting strain:

$$\sigma = C_{ij}\epsilon \quad (4.13)$$

Stress and strain are 3×3 matrices as seen in Figure 4.4. The elastic constants are written as a 6×6 matrix.

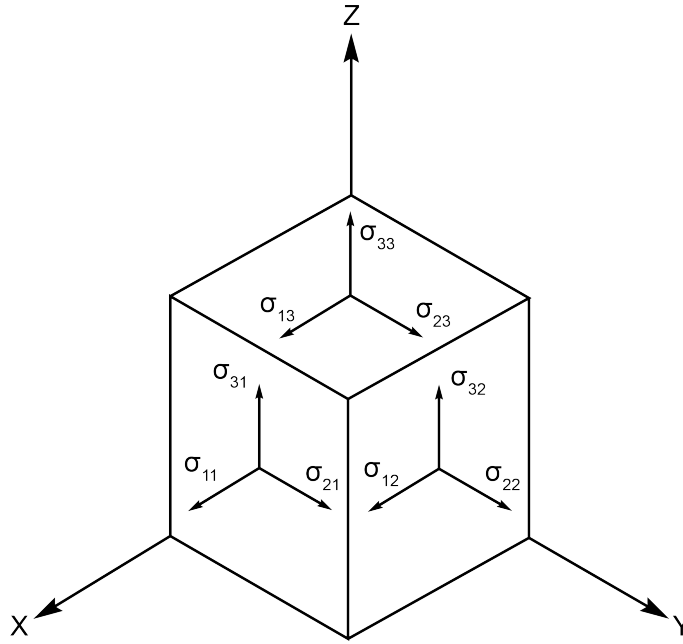


Figure 4.4: Principle stresses of a cubic crystal

$$\begin{pmatrix} \sigma_1 \\ \sigma_2 \\ \sigma_3 \\ \sigma_4 \\ \sigma_5 \\ \sigma_6 \end{pmatrix} = \begin{pmatrix} C_{1,1} & C_{1,2} & C_{1,3} & C_{1,4} & C_{1,5} & C_{1,6} \\ C_{2,1} & C_{2,2} & C_{2,3} & C_{2,4} & C_{2,5} & C_{2,6} \\ C_{3,1} & C_{3,2} & C_{3,3} & C_{3,4} & C_{3,5} & C_{3,6} \\ C_{4,1} & C_{4,2} & C_{4,3} & C_{4,4} & C_{4,5} & C_{4,6} \\ C_{5,1} & C_{5,2} & C_{5,3} & C_{5,4} & C_{5,5} & C_{5,6} \\ C_{6,1} & C_{6,2} & C_{6,3} & C_{6,4} & C_{6,5} & C_{6,6} \end{pmatrix} \cdot \begin{pmatrix} \epsilon_1 \\ \epsilon_2 \\ \epsilon_3 \\ \epsilon_4 \\ \epsilon_5 \\ \epsilon_6 \end{pmatrix}$$

A full elastic tensor of a crystal which is fully anisotropic is made up of 81 components due to there being 9 individual stress components and 9 individual strain components. It is possible to relate all of the stresses and strains through the compliance tensor, s_{ijkl} :

$$\epsilon_{ij} = s_{ij} \sigma_{kl} \quad (4.14)$$

The inverse of the compliance tensor is known as the stiffness tensor, c_{ij} and can be determined and compared for different materials.

In reality, only 36 independent stiffness or compliance tensors exist since only 6

individual components of stress and 6 individual components of strain exist i.e. σ_{12} and σ_{21} are equivalent. Furthermore the energy as a result of the summation of independent strains is:

$$\frac{1}{2} \sum_{ijkl} c_{ijkl} \epsilon_{ij} \epsilon_{kl} \quad (4.15)$$

where $c_{ijkl} = c_{klij}$ and as such, 36 is the maximum number of independent stiffness tensors.

4.5.1 Voigt-Reuss-Hill Averaging

From the individual compliance and stiffness tensors it is possible to calculate the bulk modulus K and shear modulus G . In anisotropic systems, the Voigt and Reuss represent the upper and lower limits of elasticity:

$$K_{Voigt} = \frac{c_{11} + c_{22} + c_{33} + 2(c_{12} + c_{23} + c_{13})}{9} \quad (4.16)$$

$$\frac{1}{K_{Reuss}} = s_{11} + s_{22} + s_{33} + 2(s_{12} + s_{23} + s_{13}) \quad (4.17)$$

$$G_{Voigt} = \frac{(c_{11} + c_{22} + c_{33}) - (c_{12} + c_{23} + c_{13}) + 3(c_{44} + c_{55} + c_{66})}{15} \quad (4.18)$$

$$\frac{15}{G_{Reuss}} = 4(s_{11} + s_{22} + s_{33}) - 4(s_{12} + s_{23} + s_{13}) + 3(s_{44} + s_{55} + s_{66}) \quad (4.19)$$

where c_{ij} is the elastic constant and s_{ij} is the compliance tensor.

4.6 Fracture Simulations

Fracture mechanics involves studying the fracture propagation through a material, often from an existing crack and aims to understand a materials resistance to fracture. Studying atomic scale fracture mechanics is a significant challenge as bulk scale fracture analysis such as Linear Elastic Fracture Mechanics, J-integral

evaluation or fictitious crack model are not appropriate for materials such as C-S-H at the nanoscale as these theories assume that the bulk is made up of an entirely homogeneous material. Instead, by using the energetic theory of fracture, it is possible to gain an understanding of how deformation occurs at the atomic level.

Fracture toughness is often measured by the stress intensity fracture, K_{Ic} , the total amount of stress a material can withstand before a fracture occurs[67]. The critical remote stress, σ , can be calculated by:

$$\sigma = \frac{K_{Ic}}{\sqrt{\pi c}} = \sqrt{\frac{EG_{Ic}}{\pi}} \quad (4.20)$$

where K_{Ic} is the critical stress intensity factor, c is the crack length, E is the modulus of elasticity, and G_{Ic} as the fracture energy also equivalent to 2 times the surface energy, γ .

The Griffith theory of fracture mechanics states that the surface energy resulting from the exposed material faces post fracture must be less than the reduction in strain energy due to the fracture production. Griffith's theory also states that the following conditions must be met:

- (i) bonds must be broken at the furthestmost crack tip for the fracture to propagate where the relation of stress to the ratio of crack tip radius to crack length and is directly linked to the stress concentration factor.
- (ii) For crack extension to occur, the strain energy released must be greater than or equal to that required for the surface energy of the two new crack faces.

This can also be described by the following equation:

$$\frac{dU_s}{dc} \geq \frac{dU_\gamma}{dc} \quad (4.21)$$

In this thesis we employ a combination of the theories proposed by [126] and [112]. By using periodic boundary conditions in all directions, a central notch is created, and by assuming that the temperature throughout the systems remains

constant, under applied load, the excess free energy in the system is converted to mechanical energy P by deformation of the solid or results in crack propagation and therefore fracture energy G_c is produced.

$$dF = dP + G_c dA \quad (4.22)$$

The fracture energy, G_c is related to fracture toughness by Irwin's formula:

$$K_{IC} = \sigma_f^2 \sqrt{\pi a} \quad (4.23)$$

For a brittle material, the surface energy is related to the critical energy release rate by:

$$G_c = 2\gamma \quad (4.24)$$

For a ductile material:

$$G_c \gg 2\gamma \quad (4.25)$$

G_c can be simulated using MD by integrating over a simulation under load:

$$G_c = \frac{\Delta F}{\Delta A} = \frac{L_x L_y}{\Delta A} \int_{L_{ymin}}^{L_{y0}} \sum dL_y \quad (4.26)$$

where A is the surface area of the fracture, L_x , L_y and L_z are the length of the cell in x , y and z direction, respectively. From this, the fracture toughness can easily be calculated using MD and the resistance of the material to fracture can be inferred.

4.7 Summary

In this chapter, the MD method has been introduced and the ReaxFF and SPC/E force fields which are employed in this work have been described. The overall method for generating the elastic constants has been presented and the Voigt-Reuss-Hill method for averaging the bulk and shear modulus have been given. Finally, fracture mechanics has been introduced and a method for calculating basic fracture properties from MD was shown. The following chapters will apply the methods described herein to simulate the properties of ice Ih and C-S-H.

Chapter 5

Equilibrium Simulations of Ice Ih

5.1 Overview

The understanding of ice phases of water can be enhanced by the use of molecular simulation. Many force field potentials for water are based upon rigid, non-polarisable models and, although they describe well many physical properties of liquid water, it is often the case that such potentials fail to transfer well to the ice phases. These models can be classified into three categories namely; three-point e.g. SPC/E, four-point e.g. TIP4P or five-point water models e.g. TIP5P. In this chapter, the the ability of ReaxFF, a flexible, reactive bond-order based potential, to describe the most common solid phase of water: ice Ih is investigated. Although the parametrization used was designed for studying liquid water, we show that there is promise for the force field in describing ice phases. Physical and thermodynamic properties such as the equation of state, heat capacity and elastic constants have been quantified under a range of equilibrium conditions using MD. Comparisons of a number water models including 4 point water models (TIP4P) are made. These water models are derived from slightly different parameters namely TIP4P/ice for ice specific descriptions, TIP4P/Ew using Ewald techniques, TIP4P/2005 which is one of the original TIP4P paramterisations and

TIP4PQ/2005, a path integral simulation potential. ReaxFF is found to provide an excellent description of the lattice constants of ice Ih ($< 1.2\%$ deviation from experiment) and predicts a similar density to the TIP4P/ice and TIP4P/Ew 4-point water models. In the temperature range of 0–200 K, ReaxFF has a poorer performance compared to TIP4PQ/2005 and TIP4P/2005 when attempting to reproduce the experimental heat capacity. Lastly, the elastic properties of ice Ih are calculated demonstrating that ReaxFF shows an improvement over the SPC/E potential. In this chapter it is shown that ReaxFF can be considered as a useful potential for the study of ice Ih and could give a theoretical insight into the physical properties of ice where rigid, non-polarisable potentials are lacking.

5.2 Introduction

Water is one of the most essential substances for life. Accurate computer simulation of water and aqueous substances is critical in understanding biological, atmospheric and planetary sciences. Furthermore, water makes up a large part of C-S-H and therefore will contribute to many of its physical and thermodynamic properties.

Since the first computer simulations of water by Barker and Watts[89], and Rahman and Stillinger[90], a vast number of potential models have been proposed for water. In a detailed review by Guillot in 2002, the number of independent water potentials was 46 - this number has since increased substantially to well over a hundred[2, 91]. Parametrisations of these models tend to come about by fitting to *ab initio* simulations or by fitting to experimentally measured properties[74]. Many of the water potentials are based on non-polarisable, rigid models where the H-O-H angle and O-H bond lengths are fixed and rely solely on an intermolecular bonding description[74]. These rigid models are normally associated with point charges to describe electrostatics, and Lennard-Jones interactions to describe Van der Waals interactions. These models of course deviate from reality due to the lack of polarisation, the lack of molecular vibration and the inability to simulate proton delocalisation and quantum effects, which influence the dynamics of water[127].

In the case of 3 point models interaction models like SPC and SPC/E the point charges are located on the oxygen and hydrogen atoms. For 4-point interaction models such as TIP4P/ice and TIP4P the point charges are located on the oxygen and hydrogens atoms and the last point charge is located on a dummy atom as indicated in Figure 5.1. Five point charge models 5-point interaction models such as TIP5P contain the same point charges as the 4-point models with an additional dummy atom as in Figure 5.1[94–99]. The drawbacks of these rigid force fields include the inability to simulate bond vibrational properties where bending and stretching modes play an important role. As a result, a number of flexible models for the study of ice, such as the flexible SPC model and TIP4P/2005f, developed from their rigid counterparts[100, 101].

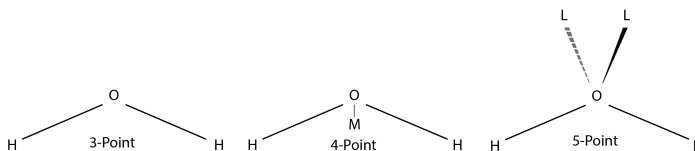


Figure 5.1: Types of water models

It is often the case that a model is developed to reproduce a particular property of interest and therefore, at times, can fail to describe other properties out-with that state. As a result, no single potential can be used to describe the entire phase diagram of water. In addition, many of the potentials were parametrized to describe the liquid properties of water and as a result do not transfer so well to the solid ice phases[74]. To add to the complexity, the phase diagram of water contains 17 solid ice phases alongside a number of triple points and amorphous phases, and therefore, creating a potential to accurately describe all of the phases presents a significant challenge. It has also been shown that the potentials mentioned above fail to describe parts of the phase diagram, for example, yielding low melting temperatures and predicting poor structural stability of some ice phases[105].

ReaxFF — a polarizable, flexible force field — was originally parametrised to study hydrocarbons but since then, additional parameters have been developed

to cover a broad range of elements within the periodic table and can model a wide range of materials for example inorganic catalysts, and energetic materials[122, 128, 129]. Unlike many other force fields, ReaxFF consists of single parameters for individual elements regardless of the speciation, making the force field easily transferable [50, 130]. The force field is part of a family of reactive force fields which has been developed by van Duin and co-workers and uses instantaneous bond order and bond distance. A water-specific ReaxFF parametrisation, water-2017, was developed and is capable of describing the Grotthus diffusion of hydroxide and hydronium ions however this particular version so far has only been used to describe liquid water[131]. ReaxFF has already been used to study ice nucleation in graphene, cosmic ice cluster impacts and CO₂ embedded ice; however, basic thermodynamic and physical comparisons of ReaxFF to other water models for both liquid and solid phases has yet to be carried out[107, 132–134]. In this chapter, ReaxFF predictions of bulk, thermodynamic and elastic properties of ice Ih are compared to previously published simulation and experimental work using the ReaxFF parametrisation found in reference [123].

The literature has shown that many water potentials fail to reproduce certain experimental characteristics of the ice phases of water, such as the density and the melting point. Vega et al. have carried out much work into the validation of water potentials against such physical properties and has demonstrated that TIP3P, SPC, SPC/E and TIP5P all melt well below the experimental melting point and that TIP3P and SPC/E fail to reproduce accurate experimental densities for ice Ih[73]. In spite of these shortcomings, their work has highlighted the effectiveness of the TIP4P class of water models in describing physical properties of water.

Few studies of the experimental and simulated elastic properties of the ice phases are present in the literature. Gammon et al. measured the elastic constants of polycrystalline natural and lab-made ice frozen from distilled water and Gagnon et al. measured the pressure dependence of the elasticity of a single crystal of ice Ih[80, 81].

In this work, the aim is to assess the ability of ReaxFF to describe the physical properties of ice Ih over a range of temperatures and pressures and compare

the performance of ReaxFF to existing experimental and simulation data. The remainder of this chapter is organised as follows — details of the methodology are given before going on to structurally validate ReaxFF by comparing unit cell predictions with experiment. Equation of state (EoS) predictions by ReaxFF are compared to other water potentials. Results of heat capacity (C_p) and thermal expansivity (α) is then carried out. Lastly, the performance of ReaxFF in predicting elastic properties of ice Ih is tested and compared to experimental data and simulations by the SPC/E water potential. By thorough checking of the force field in this manner, the simulation methods can be validated for ice Ih before applying the methods to C-S-H, which is less well studied.

5.3 Methods

As described in Chapter 4, ReaxFF is a reactive force field based upon bond order and bond distance, is employed in this work. ReaxFF is easy to implement across a range of different structures without the need for an explicit bonding description. Like many force fields, the overall system energy of ReaxFF is described by a simple addition of the partial energy contributions as described:

$$E_{tot}^{REAXFF} = E_{bond} + E_{over} + E_{under} + E_{lp} + E_{val} + E_{pen} + E_{tors} + E_{conj} + E_{vdw} + E_{Coulomb} \quad (5.1)$$

where E_{bond} describes the energy associated with bond order and bond energy, E_{over} and E_{under} is the energy associated with over and under coordination respectively, E_{lp} is an energy contribution from atoms which contain lone pairs, E_{val} is the energy from individual atomic valency, E_{pen} is the energy penalty associated with double bonded atomic valency, E_{tors} for torsional angles, E_{conj} for conjugation, E_{vdw} Van der Waals energy contribution and finally $E_{Coulomb}$ for coulombic energy terms. This work compares results with published data which is available for a number of models specifically SPC/E, TIP4P, TIP4P/Ew, TIP4P/ice and TIP4PQ.

For all investigations within this study, the LAMMPS molecular dynamics code

has been used[64]. Before any elasticity and EoS calculations were carried out, ice Ih was equilibrated using the force field of interest at zero pressure and 200 K in NpT for up to 0.5 ns with production runs of up to 0.5 ns using the Nose-Hoover thermostat and barostat with a dampener of 100 time-steps. Averages were calculated from the production runs with errors determined from standard deviation of the averages. The time step for ReaxFF is chosen to be 0.2 fs due to the increased complexity of the force calculation per time step. Periodic boundaries are applied in all directions. For elastic and EoS studies where specific temperatures and pressures are of interest, the structure was first equilibrated at zero pressure before being run at the desired pressure and temperature combination.

In this work heat capacities were measured at constant pressure and temperature NpT at each corresponding temperature via following relationship:

$$C_p = \left(\frac{\partial H}{\partial T} \right)_p \quad (5.2)$$

The thermal expansion coefficient was measured via NpT simulations using the following equation:

$$\alpha_T = -\frac{1}{\rho} \left(\frac{\partial \rho}{\partial T} \right) \quad (5.3)$$

The elastic constants C_{ijkl} of a material relate stress σ_{ij} to strain ϵ_{kl} :

$$\sigma_{ij} = C_{ijkl}\epsilon_{kl} \quad (5.4)$$

To calculate the elastic constants in a molecular dynamics simulation finite deformations are applied at zero temperature in each direction to a fully equilibrated simulation cell. After each deformation, the structure is energy minimized. The elastic constants were measured by modifying and implementing the LAMMPS elastic constants script for the system in question. To measure the elastic constants, the system was altered using the `changebox` command in LAMMPS to create a strain, followed by an energy minimization step, and measuring the resulting stress.

The bulk modulus K and shear modulus G were calculated according to the

Voigt-Reuss-Hill[135–137] approximation as follows:

$$K_V = \frac{1}{9}[(C_{11} + C_{22} + C_{33}) + 2(C_{12} + C_{23} + C_{31})] \quad (5.5)$$

$$\frac{1}{K_R} = \frac{1}{9}[(s_{11} + s_{22} + s_{33}) + 2(s_{12} + s_{23} + s_{31})] \quad (5.6)$$

$$K_{VRH} = \frac{1}{2}(K_V + K_R) \quad (5.7)$$

$$G_V = \frac{1}{15}[(C_{11} + C_{22} + C_{33}) - (C_{12} + C_{23} + C_{31}) + 3(C_{44} + C_{55} + C_{66})] \quad (5.8)$$

$$\frac{15}{G_R} = \frac{1}{9}[4(s_{11} + s_{22} + s_{33}) - 4(s_{12} + s_{23} + s_{31}) + 3(s_{44} + s_{55} + s_{66})] \quad (5.9)$$

$$G_{VRH} = \frac{1}{2}(G_V + G_R) \quad (5.10)$$

where K_V and G_V are the Voigt averaged bulk and shear modulus respectively, K_R and G_R are the Reuss averaged bulk and shear modulus respectively, K_{VRH} and G_{VRH} are the Voigt-Reuss-Hill averaged bulk and shear modulus respectively and s_{ij} is the compliance tensor which is the inverse relation between stress and strain.

5.4 Results and Discussion

5.4.1 Unit Cell Predictions and EoS

The most common form of ice is known as ice Ih, or ordinary ice, and exists at ambient pressures below 0°C. Neutron diffraction studies have shown that the structure of ice Ih consists of a network of hydrogen bonded water molecules where the oxygen atoms are arranged in a tetrahedral geometry with O-O-O bond angle of 109.47°, an O-O equilibrium distance of 2.76 Å where the central oxygen atom forms a tetrahedral structure with 4 neighbouring oxygen atoms. The overall crystal structure is a hexagonal prism with an aspect ratio (length

of c axis/ a axis) that is shorter than is normally seen with a purely tetrahedral structure. Each molecule in the network participates in four hydrogen bonds — two donor hydrogen bonds and two acceptor hydrogen bonds illustrated in Figure 5.2. Whilst the oxygen atoms are strictly ordered, the water hydrogen atoms contain a degree of disorder as a result of natural crystal defects.

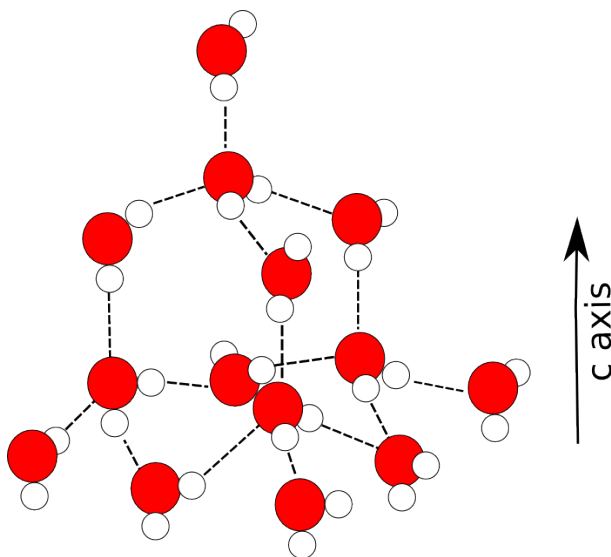


Figure 5.2: Structure of hexagonal ice Ih. Hydrogen (white), oxygen (red).

According to Röttger et al., ice Ih experimental lattice constants, derived from synchrotron X-ray powder diffraction, are observed to be $a = 4.515 \text{ \AA}$ and $c = 7.350 \text{ \AA}$ at 235 K and ambient pressure[111]. Figure 5.3 displays the temperature dependence of the lattice constants and unit cell volume of ice Ih by ReaxFF compared to the synchrotron X-ray diffraction experiment by Röttger et al.[111]. At 237 K, ReaxFF predicts lattice constants of $a = 4.520 \text{ \AA}$ and $c = 7.361 \text{ \AA}$ and are found to differ from experiment by less than 0.2%. The volume predicted by ReaxFF deviates slightly below temperatures of 150 K and is associated with shrinkage of the a and c axis. This may be attributed to the fact that at lower temperatures, quantum effects become more significant and thus will not be captured in a purely classical simulation.

The influence of temperature on the lattice constants of ice Ih was measured experimentally and found to be non-linear from 0 K to 250 K with a minimum of

4.496 Å being observed at 70 K for a and a minimum of 7.312 Å at 85 K for c [111]. For the lattice parameters a and c , ReaxFF results in greater thermal expansion than seen in experiment but not more than 1.1% difference from experimental results. ReaxFF, however, fails to predict the minimum value of the a and c . Volume expansion using ReaxFF shows accurate reproducibility at temperatures above 245 K. The ReaxFF simulation shows deviation from the experimentally observed minimum volume which predicts a minimum volume of 128.15 K at 70 K. The minimum volume of ReaxFF deviates by approximately 2% at 70 K from experiment. At low temperature, quantum effects become increasingly important and structural softening occurs due to the lower attraction of the quantum system. In a classical simulation however, the attraction remains constant due to the force field parameters and thus the volume decreases with temperature, a result of the inability of classical simulations to capture quantum effects in all phases of water[138, 139].

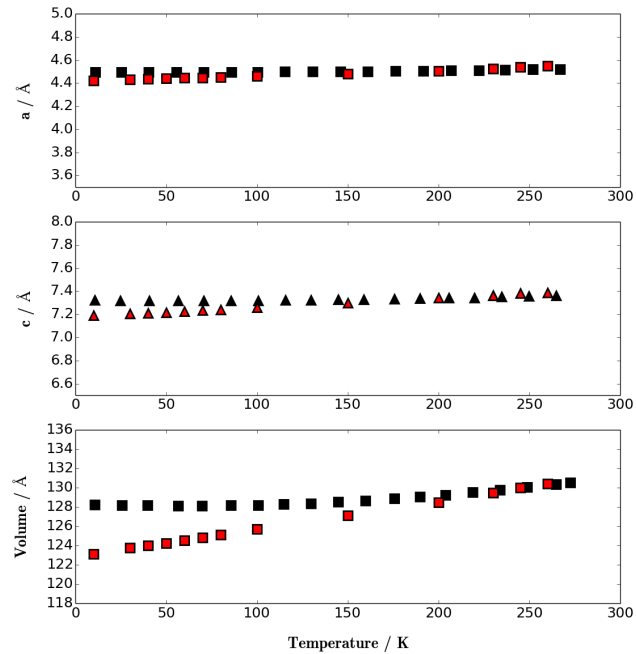


Figure 5.3: Comparison of thermal expansion of lattice constants a (top), c (middle) and volume (bottom) of ice Ih as predicted by ReaxFF and Neutron diffraction experiments. ReaxFF simulations (red), Expt. Ref. [111] (black).

Figure 5.4 compares ReaxFF ice Ih $T - \rho$ EoS with an experimental study by Feistel et al. and a number of simulation studies with common rigid potentials by Noya et al.[73, 140]. ReaxFF shows reasonable predictions of the T - ρ and P - ρ EoS for ice Ih and shows improvements upon some of the rigid potentials[73, 140]. At 250 K, ReaxFF outperforms TIP5P, SPC/E and TIP4P. At temperatures above 200 K TIP4P/ice predicts a density closer to experiment than ReaxFF, however, in the range of 100-200 K ReaxFF shows a slightly enhanced performance compared to TIP4P/ice. At temperatures above 150 K, TIP4P/2005 makes an excellent prediction of the density, however, at lower temperatures the same trend in densities by ReaxFF and TIP4P/2005 is seen and deviation from experiment is evident. As stated earlier, the quantum effects on the volume, and therefore the density, cannot be replicated in a classical simulation. Nonetheless, TIP4P/ice compares well at temperatures approaching 0 K however this is related to the parametrisation of the force field, evidenced by deviation of density at high temperatures followed by volume contraction as temperature decreases which results in a closer approximation of the density. Interestingly, the zero temperature density of ice Ih by ReaxFF matches closely to density of ice XI (0.92 g/cm^{-3}), a low temperature phase of ice (see Figure 3.4 in Chapter 3 for the phase diagram of water which depicts the location of ice XI). Note that this zero temperature run was not used as part of the fitting of the ice Ih T - ρ EoS.

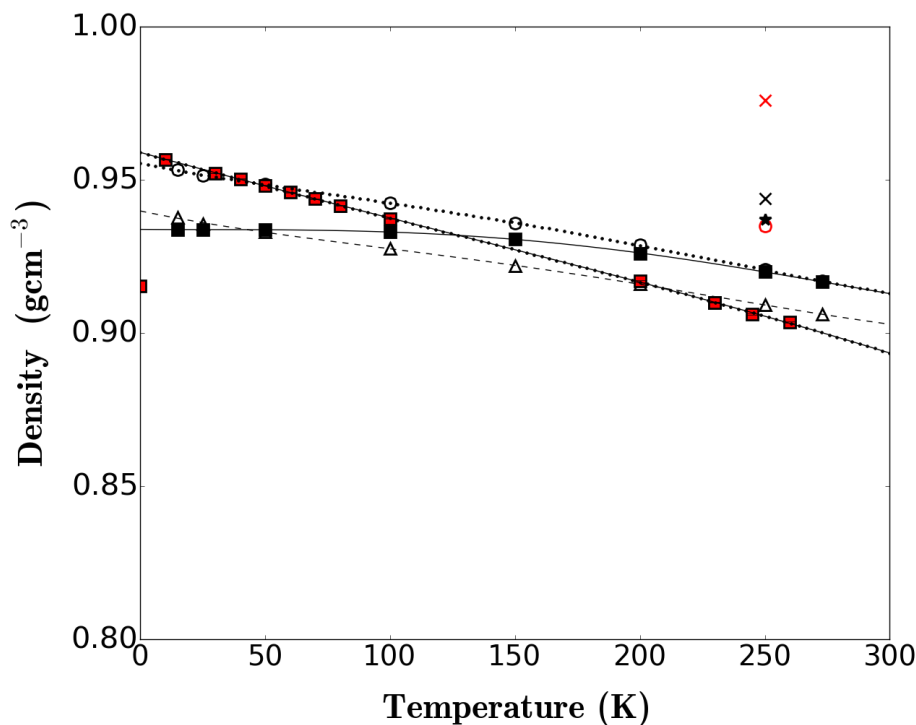


Figure 5.4: Comparison of dependence of density on temperature for common water potentials. Expt 1 bar Ref. [140] (solid black squares), TIP4P/2005 1 bar Ref. [73] (black unfilled circles), TIP4P/ice 1 bar Ref. [73] (black unfilled triangles), ReaxFF (red squares), SPC/E 0 bar Ref. [141] (black cross), TIP5P 0 bar Ref. [142] (red cross), TIP4P/Ew 0 bar Ref. [142] (red circle), TIP4P 0 bar Ref. [142] (black star). Note that ReaxFF is carried out at zero pressure above 70 K and 1 bar pressure below 70 K.

A comparison of experimental and predicted thermal expansion coefficient of ice Ih is displayed in Figure 5.5. Thermal expansion coefficients were not published for TIP4P/ice and TIP4P/2005 at the given temperatures therefore the values presented in Figure 5.5 result from our own fitting procedures from the published data given in Figure 5.4. In both cases, the thermal expansion coefficient, α_T is calculated from equation 5.3 by fitting to a 3rd degree polynomial. At

Table 5.1: Comparison of the predicted density of ice Ih for a number of water potentials at 250 K and 0 bar pressure

Potential	$\rho / \text{g cm}^{-3}$	Ref.
TIP5P	0.976	[97]
SPC/E	0.944	[97]
TIP4P	0.937	[97]
TIP4P/Ew	0.935	[97]
TIP4P/Ice	0.909	[73]
ReaxFF	0.905	—
Expt.	0.920	[140]

temperatures below 50 K, a negative thermal expansion is observed by Röttger et al. At temperatures greater than 50 K, the thermal expansion coefficient increases, becoming positive, and continues to increase to a value of $5 \times 10^{-5} \text{ K}^{-1}$. ReaxFF predicts higher thermal expansion coefficients than the other models in Figure 5.5, associated with the greater density change in Figure 5.4. At lower temperatures, there is a slight increase in the expansivity as the temperature lowers towards 0 K.

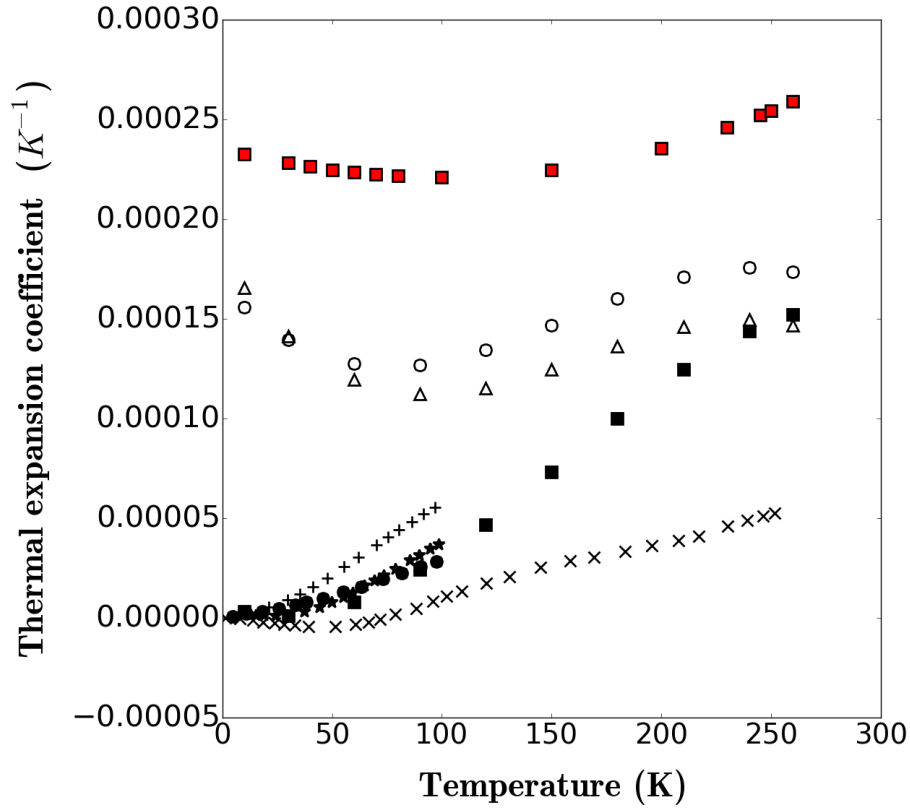


Figure 5.5: Dependence of thermal expansion coefficient α_T with T for common water potentials. Expt 1 bar Ref. [73] (solid black squares), TIP4P/2005 1 bar Ref. [73] (black unfilled circles), TIP4P/ice 1 bar Ref. [73] (black unfilled triangles), Röttger Expt. Ref. [111] (black crosses), ReaxFF 0 bar (red squares), TIP5P 0 bar Ref. [142] (black plus), TIP4P 0 bar Ref. [73] (black stars), Strassle Expt. Ref.[143] (solid black circles)

The ρ - p EoS is displayed in Figure 5.6. Note that the data in Figure 5.6 has been collected at different temperatures. For ρ - p EoS, ReaxFF compares reasonably well with single crystal ice Ih pressure experiments, with a difference of approximately 1.5% [81]. Based on the thermal expansion data in Figure 5.5, the data measured at 237 K should have a smaller density than that at 145 K. This is not the case for TIP4P/ice which has a higher density at 145 K than the experimental data at 237 K. Given that ReaxFF has a greater expansion at 237 K

than seen in experiment, it is expected that the predicted density of ice Ih is less than the experimental value (0.904 gcm^{-3} and 0.922 gcm^{-3} for ReaxFF and Expt. respectively).

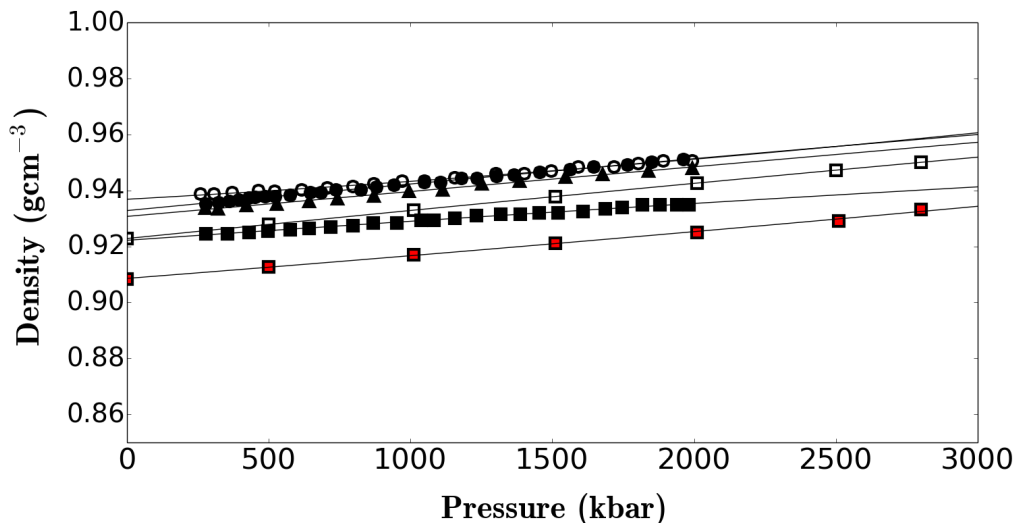


Figure 5.6: Comparison of dependence of density on pressure for common water potentials. Note that temperature differs. Gagnon Expt. [81] 237 K (unfilled squares), ReaxFF 237 K (red filled squares), Strassle Expt. 145 K Ref. [143] (black filled circles), FWEoS Ref. [140] (black filled triangles), TIP4P/2005 145 K Ref. [73] (unfilled circles), TIP4P/ice 145 K [73] (black filled squares). Where FWEoS is a prediction for the EoS based on thermodynamic modelling by Feistel and Wagner.

5.4.2 Heat Capacity Calculations

Classical potentials traditionally have failed to reproduce experimental heat capacities (C_p) for water and ice Ih. The 3rd Law of thermodynamics states that as temperature approaches 0 K, C_p tends to zero, however, this effect is quantum mechanical in nature therefore classical simulation predictions are unable to adhere to this trend. The TIP4P/2005 water model was re-parametrised into TIP4PQ/2005 by changing the dipole moment and, via the path integral method (a method which combines aspects of the theories of quantum and classical me-

chanics), was able to reproduce the experimental heat capacities of water and ice Ih down to 0 K[144]. A comparison of ReaxFF to experimental and simulation data is found in Figure 5.7.

ReaxFF predicts a C_p that is more than double the FWEoS and TIP4PQ/2005 predictions. Despite showing a poorer prediction of C_p when compared to the other literature data in the figure, ReaxFF still makes a reasonable prediction given the complexity and advantages of the ReaxFF model over other models such as flexibility and the ability to describe chemical reactions.

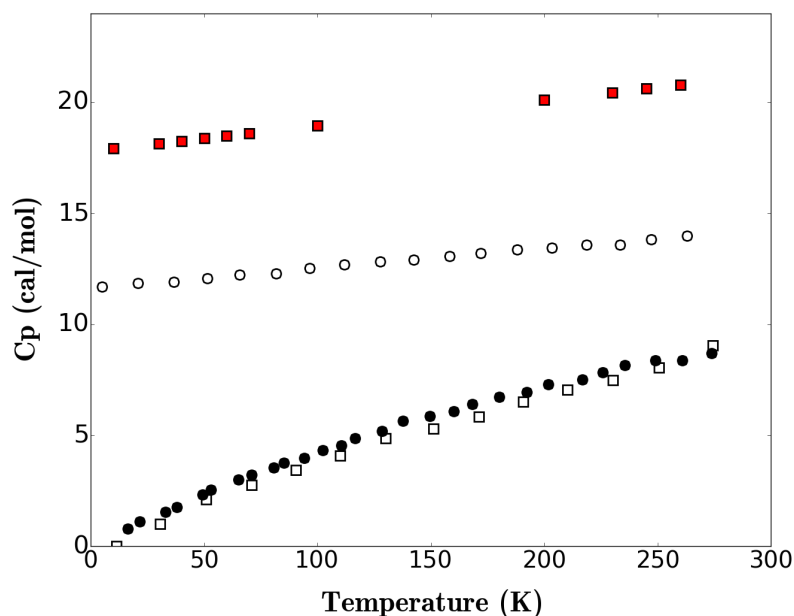


Figure 5.7: Change in C_p with temperature for Ice Ih. FWEoS Ref. [140] (unfilled black squares), ReaxFF 0 bar fit (red squares), TIP4PQ/2005 Ref. [110] (black circles), TIP4P/2005 Ref. [110] (open circles).

5.4.3 Elasticity

Ice Ih, a hexagonal crystal, has 5 independent elastic constants (C_{11} , C_{12} , C_{13} , C_{33} , and C_{44}) which relates to the x , xy , xz , z , yz directions respectively). The

first determination of single crystal elastic constants was carried out by a theoretical calculation based upon the experimentally measured Young's modulus and Poisson's ratio of polycrystalline ice[145]. This was followed by experimental measurement by Jona and Scherrer and further work measuring elastic wave velocities via an ultrasonic pulse method by Green and Mackinnon [146, 147]. Further work was carried out by Gagnon et al. to determine the effect of pressure on the elastic properties of ice[81]. Although a number of experimental determinations of the elastic constants of the various ice structures have been carried out, the number of molecular dynamics simulations of ice is surprisingly low. High pressure elastic constants were calculated in a molecular dynamics simulation using the TIP4P water model to explain the mechanical affect of pressure-induced amorphization, a phenomenon in which crystalline ice spontaneously changes to an amorphous solid[148]. By measuring the elastic constants of ice Ih using ReaxFF, it enables a check on the ability of ReaxFF to describe mechanical properties of ice Ih in the linear regime before applying ReaxFF to a fracture simulation. The ability of ReaxFF to reproduce the experimental elastic constants of ice Ih is tested and compared with those calculated by the SPC/E water potential and experimental results by Gagnon et al.[81]. In addition, the pre-pressure induced amorphization elastic constants at 8 kbar is also compared[148]. The results are summarised in Table 5.2 and Figure 5.8. ReaxFF is a clear improvement on SPC/E and presents a reasonable estimate of the experimental elastic constants which includes a purely theoretical prediction[145]. C_{11} , C_{12} and C_{44} compare well to experiment for ReaxFF although the C_{44} prediction of SPC/E also compares well to experiment. The C_{13} and C_{33} elastic constants of ReaxFF however over-predict by approximately 8 GPa and 6 GPa respectively.

Table 5.2: Elastic constants ReaxFF, SPC/E compared to theoretical and experimental results

C_{ij}	SPC/E (GPa)	ReaxFF (GPa)	TIP4P [149] (GPa)	Theory[145] (GPa)	Expt. [146] (GPa)	Expt.[81] (GPa)
T	200 K	200 K	80 K	—	—	237 K
C_{11}	24.73 ± 2.9	15.07 ± 0.38	17.35	15.2	13.33 ± 1.98	14.49
C_{33}	22.62 ± 2.3	19.66 ± 1.66	15.47	16.2	14.28 ± 0.54	15.63
C_{12}	17.30 ± 1.5	10.27 ± 3.28	11.67	8.0	6.03 ± 0.72	7.35
C_{13}	13.80 ± 1.4	11.63 ± 5.22	12.37	7.0	5.08 ± 0.72	5.97
C_{44}	2.36 ± 0.9	3.36 ± 1.78	1.64	3.2	3.26 ± 0.08	3.15

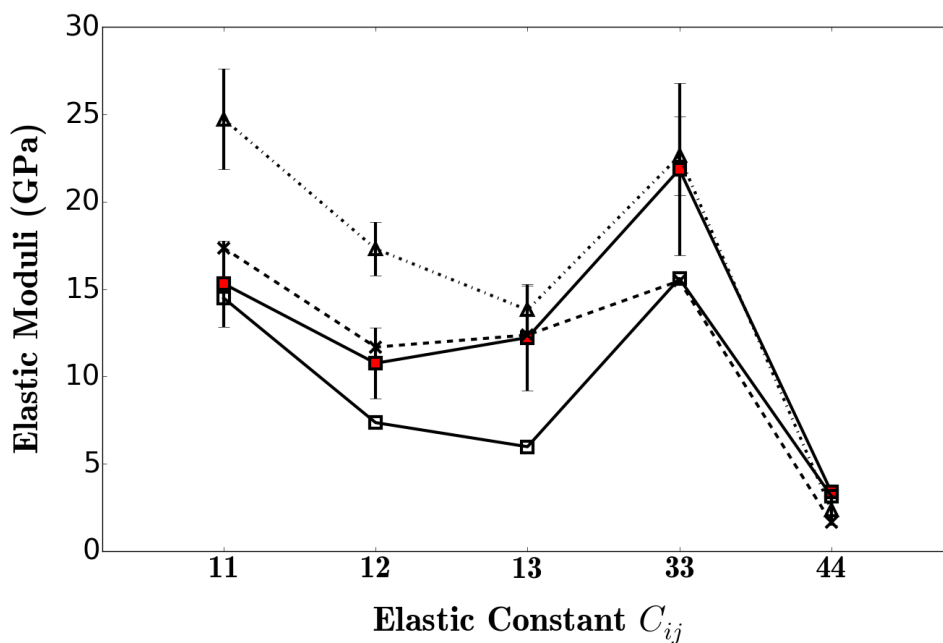


Figure 5.8: Comparison of Expt. Ref. [81] (237 K, 0 bar, open squares), SPC/E (200K, 0 kbar, triangles) and ReaxFF (200 K, 0 kbar, red squares) and TIP4P (80 K, 8 kbar black crosses) elastic constants prediction

Bulk modulus, K and shear modulus, G are calculated by Voigt-Reuss-Hill averaging method as described in the Section 5.3 above. Table 5.3 shows that the simulated bulk modulus K for ReaxFF at 230 K compares very well to the experimental value of Ref. [81]. Note that the experimental results by Gagnon et al. were collected at 237 K whereas simulations are carried out at 200 K as the low melting point (215 K) of the SPC/E potential has to be taken into consideration[150]. ReaxFF makes a fair comparison to the experimental K and shows an improvement over TIP4P and SPC/E potentials.

Table 5.3: Bulk modulus K and shear modulus G of ReaxFF and SPC/E compared to experiment.

T/K	Potential	K/GPa	G/GPa
200	SPC/E	13.39	7.52
80	TIP4P	13.66	2.14
200	ReaxFF	12.25	4.81
230	ReaxFF	10.76	4.45
237	Expt.[81]	9.24	—

Temperature dependence of elastic constants and bulk and shear modulus are presented in Figures 5.9 and 5.10 respectively. As the temperature increases, the value of elastic constants and moduli tend to decrease. This trend is expected as at higher temperatures as the structures will have more expansion due to the increase in the atomic kinetic energy, thus allowing the structures to be less resistant to compression. As was seen in Figure 5.4.1, the density decreases with temperature for the ice Ih phase and as a result, it is likely that hydrogen bonds will become longer, and therefore weaker resulting in reduced mechanical properties. This will in turn cause a decrease in the overall elastic properties.

From Figure 5.10 it can be seen that both K and G tend to fall as temperature increases. The bulk modulus K is a measure of the compressibility and as temperature increases, the density increases, resulting in the material becoming more compressible. Similarly the increase in temperature causes lengthening of the intermolecular bonds and therefore the shear strength of the ice will decrease.

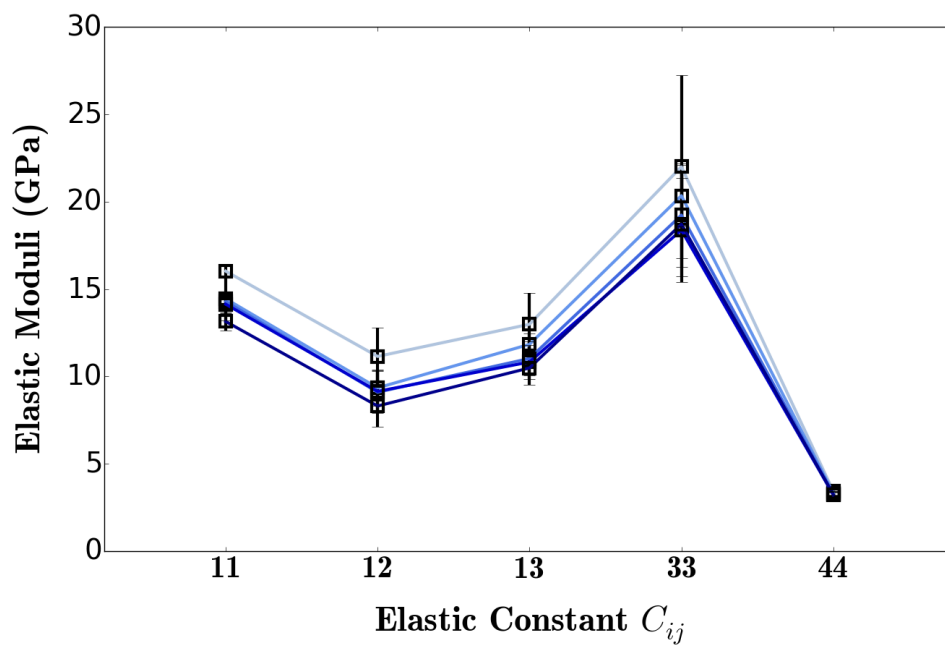


Figure 5.9: Temperature dependence on ice Ih elastic constants as predicted by ReaxFF at 0 kbar. 200 (grey)–260 (darkblue)

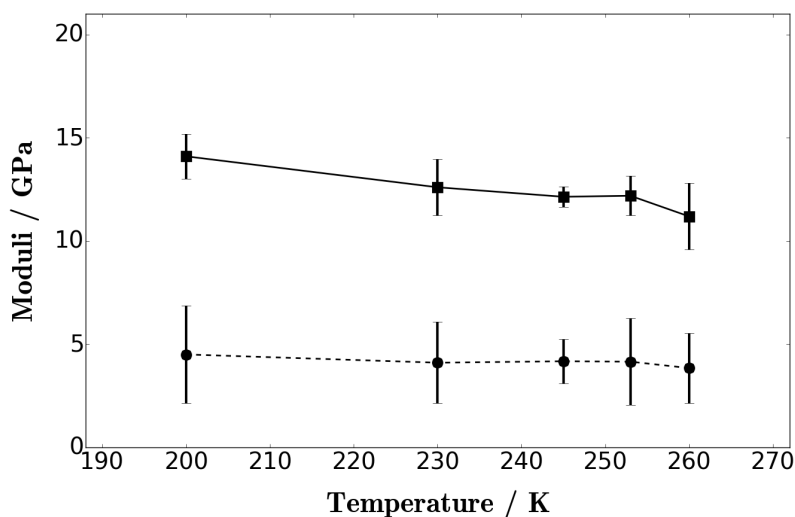


Figure 5.10: Temperature dependence of bulk modulus K (black squares) and shear modulus G (black circles) for ReaxFF.

Lastly, pressure dependence of the elastic properties was simulated using ReaxFF and compared with experimental data found in Ref. [81]. The results are found in Figures 5.11 and 5.12. As expected, as the pressure increases the elastic properties increase slightly due to the hydrogen bonds within the network being shortened and thus the attraction becomes stronger. As was observed earlier with the ambient pressure elastic constants prediction, C_{11} and C_{44} are close to experimental values at all pressures tested however there is a large difference for C_{33} and C_{13} which could be related to less compressibility in the c axis in the simulation compared to experiment however experimental data was not found to support this. Calculation of bulk and shear moduli for the ReaxFF simulations compare well to the experimental results.

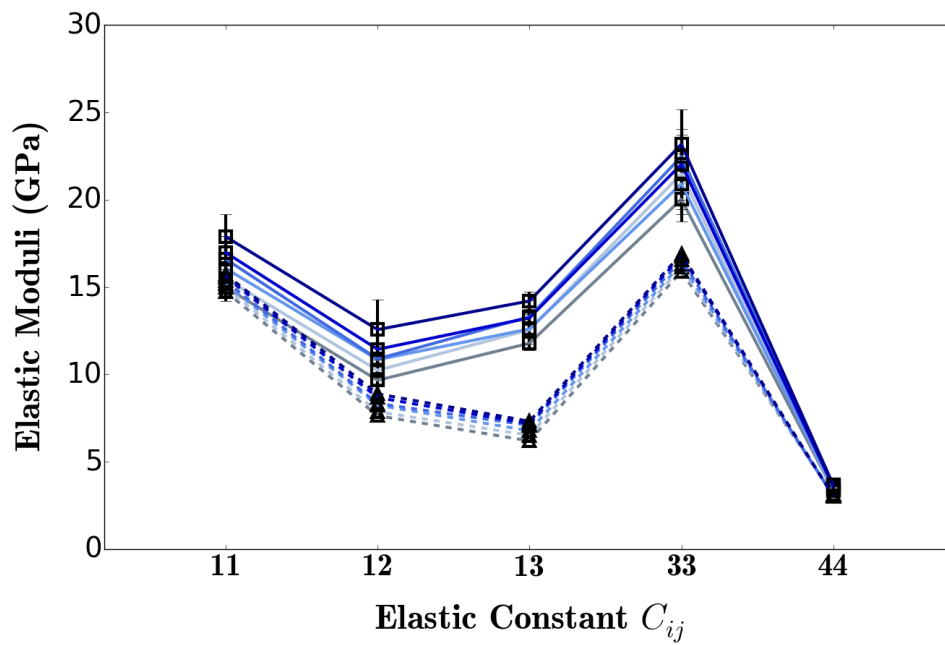


Figure 5.11: Pressure dependence C_{ij} ice Ih 0.5–1.51 kbar at 237 K. ReaxFF (squares). Expt. (triangles), 0.5 kbar (grey)–2.8 kbar (darkblue)

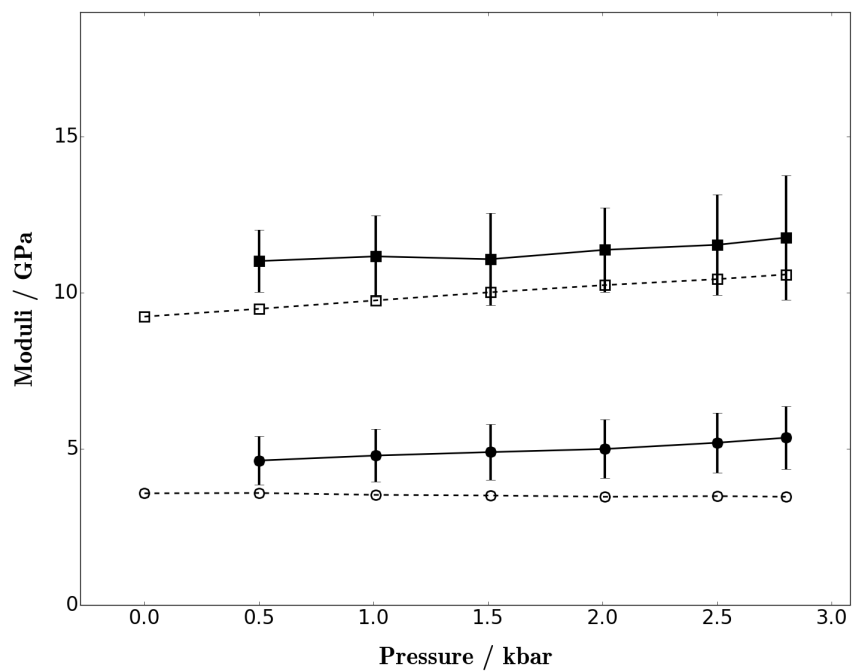


Figure 5.12: Comparison of ReaxFF and Experimental[81] pressure dependence on K and G at 237 K. ReaxFF K (black squares), ReaxFF G (black circles), Gagnon 1983 K (open squares), Expt. ref. [81] G (open circles)

5.5 Conclusions

ReaxFF is shown to give a good description of the ice Ih phase over the range of temperatures and pressures tested. Using ReaxFF, an improvement in the density prediction over all the potentials compared with the exception of TIP4P/ice is observed. Whilst no improvements compared to existing potentials are observed for thermal expansion and heat capacity, ReaxFF makes satisfactory predictions of these properties, and with the added flexibility and ability to undergo chemical reactions, ReaxFF has been shown to be a promising force field for the prediction of ice Ih. Compared to SPC/E, ReaxFF agrees better with experimental data for the elastic constants, bulk modulus and shear modulus validating the model and method. This indicates that ReaxFF is capable of describing the linear elastic properties of ice Ih and can now be tested beyond the linear regime in a fracture simulation. Nonetheless, the flexibility of the ReaxFF model and its reactive nature gives additional scope for the adoption of ReaxFF to describe the ice phases of water.

Lastly, although ice XI was not simulated, the interesting finding regarding the zero temperature density closely matching the density of ice XI could lead to future work which could give insight into planetary ice models.

Chapter 6

Fracture Simulations of the ice Ih Phase of Water

6.1 Overview

The deformation and mechanical properties of ice Ih is of great interest in fields such as cold climate engineering, polar exploration and planetary studies. Better understanding of the process of failure of ice is important in many global, academic and industrial contexts. For example, it is of global interest for rigorous understanding of ice fracture to help impede the deterioration of ice in Arctic regions and aid in slowing the fracture propagation of shelf ice to help protect and prolong the glacial environment[151–153]. From a civil engineering viewpoint, marine concrete structures for oil and gas exploration are susceptible to abrasion by drifting sea ice and, in areas of low temperature and variable water heights, adequate design of structures is critical to ensure longevity and safety of the structure. In particular, one of the most important aspects in design is not only understanding the behaviour of the building materials in such conditions but also understanding the mechanical properties and likely failure mechanisms of the ice drifts to assess collision impact[154]. Similarly, hull design of ice breaker ships could be further optimised if the mechanical properties of ice were better understood[155]. Lastly, high velocity ice impacts can disrupt and damage Earth

observation and communication satellites and as such, understanding of fracture mechanics of ice is critical to ensure damage limitation of these structures[156]. Therefore, in addition to being an appropriate validation structure for fracture simulations, mastering the fracture properties of ice is of global importance.

It was demonstrated in Chapter 5 that ReaxFF was capable of making satisfactory predictions for the physical and elastic properties of ice Ih. In this chapter, ReaxFF and MD is used to predict nanoscale fracture properties of ice. Fracture phenomena of ice at large scales reasonably well understood, however, the properties are complex and are often influenced by trace contaminants, such as salt and particulates which are found in natural environmental ice. Ice is known to have complex fracture behaviour, where high strain rates result in brittle fracture and low strain rates result in yielding. Similarly to C-S-H, it is widely accepted that to understand the fracture of ice, studies must be conducted at the fundamental nanoscale level where fracture stems from atomic scale defects and processes. For ice, however, there is a lack of published data regarding investigations at this scale. Using a reactive force field such as ReaxFF, fracture processes can be described by MD techniques, and the fundamental fracture processes can begin to be unravelled.

This chapter aims to design and validate a tensile failure MD test method by comparing to available experimental results of ice Ih. After validation of the method, this work looks to determine the process that drives fracture propagation in nanoscale ice Ih by studying crack tip formation, the influence of direction and the influence of properties such as temperature and strain rate.

This chapter begins with a general introduction to fracture behaviour in ice and discusses how the mechanical properties are affected by factors such as temperature, strain rate and direction. Next, previous experimental and theoretical studies of fracture are reviewed. The fracture simulation designed and used within this chapter is then described in detail explaining how fracture properties are determined. Effect of notch size, tension direction, temperature and strain rates on crack speeds and fracture properties are investigated and compared with experiment before overall evaluation of the method takes place.

6.2 Introduction

Investigations into ice fracture have predominantly focused on experimental studies of both polycrystal and single crystal test samples and have included both environmental ice fracture monitoring in Arctic glacial environments and lab based studies[88, 157, 158]. The large scale fracture behaviour of pure ice is generally well understood and as a result, few recent studies can be found in the literature. The compressive strength of ice is in the range of 5-25MPa[159]. The tensile strength of ice is much weaker in comparison to the compressive strength and is in the range of 0.7-3.1 MPa[159]. The tensile strength of ice is has been shown to have only a very weak dependence on temperature and studies have shown that both the compressive and tensile stress increases with decreasing temperature as shown in Figure 6.1. The weak temperature dependence of tensile strength is a result of the stress being concentrated at pre-existing crack tips, which is in contrast to the dislocations and sliding mechanisms which are influenced by increasing temperature when under compressive stress[159]. Additionally, Petrovic demonstrated that the tensile stress increases exponentially with decreasing ice grain diameter. i.e. a diameter of 5.9 mm results in a tensile strength of ≈ 0.8 MPa whereas a diameter of ≈ 0.8 mm results in tensile strength of ≈ 0.28 MPa 263K with a strain rate of $1 \times 10^{-5} s^{-1}$. Furthermore, the tensile strength of ice has been found to be largely independent to the strain rate as strain rate of $1 \times 10^{-7} s^{-1}$ to $1 \times 10^{-3} s^{-1}$ give a tensile stress of around 1.5 MPa as shown in Figure 6.2.

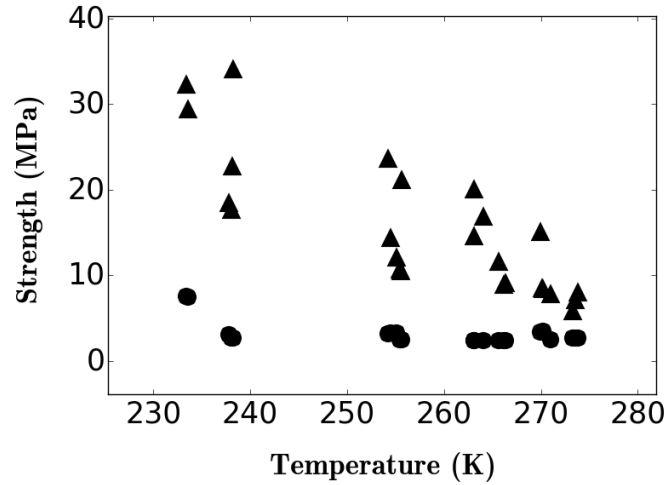


Figure 6.1: Variation of compressive strength (triangles) and tensile strength (circles) with temperature from Ref. [159, 160].

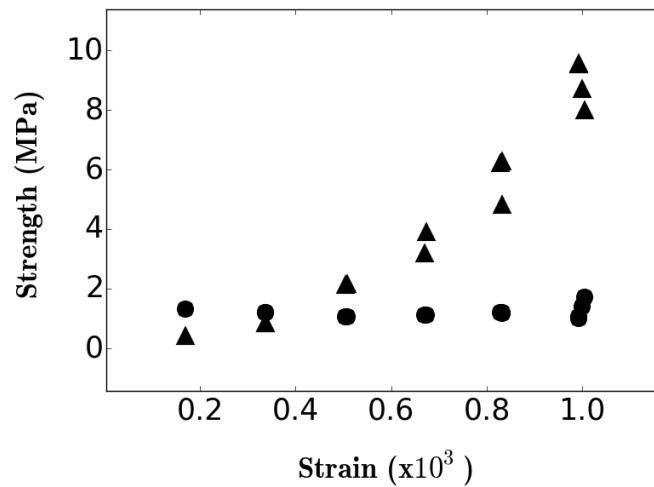


Figure 6.2: Variation of compressive strength (triangles) and tensile strength (circles) with strain rate at 263 K from Ref. [159, 160].

The fracture toughness of ice has been studied experimentally and is generally found to be in the region of $50\text{-}150\text{kPam}^{1/2}$ [109]. Whilst no obvious trend relating fracture toughness to temperature or loading rate, there is a trend in the fracture toughness with ice grain size where the fracture toughness decreases from approximately $80\text{-}100\text{kPam}^{1/2}$ to $70\text{-}80\text{kPam}^{1/2}$ at 1.4 mm and 9 mm respectively. [159]

Similar to cement, ice displays ductile to brittle transition and can be described as a non-linear visco-elastic material.[161] Although ice is not strictly a linear elastic material, linear elastic fracture mechanics has been applied to describe the fracture behaviour by assuming that the fracture length is much greater than the plastic region surrounding the crack tip.[162]

The macroscale structure of ice is complex and differs depending on the environment in which it is located. For example, when ice forms naturally in Arctic or glacial conditions, the ice is polycrystalline in nature and results from the random compaction of snow. This random compaction leads to polycrystals with grain sizes of 1-20 mm where random orientation of the crystal c axis occurs (refer to ice structure in Figure 3.2 in Chapter 2 for c axis)[158]. Arctic sea ice forms in columns and the crystal c axis lies in the plane of the ice sheet[158]. Furthermore, incorporation of salts, brine pockets and embedded CO_2 are found in natural ice and are known to affect fracture and mechanical behaviour[106, 157]. This complex macroscale environment results in a fracture behaviour that is variable and often unpredictable presenting a significant challenge to study.

In comparison to polycrystalline ice Ih, the single crystal structure of ice is less variable with a smaller range of defects, and as a result, the fracture propagation processes are somewhat simpler where fracture in the crystal basal direction, also known as basal slippage, is the predominant process[84, 163]. Jones and Glen demonstrated a temperature and strain rate dependence for single crystal ice where a decrease in temperature resulted in a slight increase in fracture tensile strength and that the fracture tensile stress increased with increasing strain-rate[164]. Plastic deformation is observed at lower strain rates and is normally associated with shear stress upon the basal plane and results in basal slip[84].

Despite the differences in the structural form of the poly and single crystal, their mechanical behaviour is rather similar. In both instances, the ice is loaded slowly resulting in plastic deformation/creep. If the the poly or single crystal is loaded rapidly, brittle failure of the ice is observed. This type of behaviour is also observed with cementitious materials. However, at very high strain rates, brittle failure of ice results in shattering. Ice has been shown to undergo a brittle to ductile transition under tensile load at a strain of 10^{-7} at 263 K[157].

Studying fracture using MD has been rising in popularity since the development of reactive force fields such as ReaxFF and the Tersoff potential allowing probing of atomic scale fracture mechanisms[60, 130, 165]. The methods predominantly consist of applying tensile stress along a plane until material failure. In some cases, initial cracks are added to allow fracture to stem from a controlled point[66, 112, 166]. Production of stress-strain curves in this manner can lead to calculations of fracture speeds, fracture toughness and fracture mechanisms. Two molecular simulations of ice Ih fracture have been found in the literature where tensile tests have been carried out using MD and ReaxFF[106, 107]. The focus of these studies of ice fracture are predominantly focused upon the effect of embedded carbon dioxide. Both studies centre their discussions of fracture perpendicular to the basal plane, in contrast to what is normally seen as the common failure plane experimentally[84, 163]. This work will compare fracture properties with the two published simulation studies, but will give additional insight into the parameters which affect the simulation model and the properties which affect fracture with overall aim of defining nanoscale fracture processes in ice.

6.3 Methods

MD simulations studies in this chapter have been carried out using LAMMPS [64]. The fracture methodology was developed based on work in references [67, 112, 167]. These MD simulations make the assumption that the material is defect free (with the exception of an central crack) and is a single crystal with no boundary effects.

6.3.1 System Preparation

The ice Ih crystal was rotated 30° clockwise around the z-axis (*c*-axis) from the original structure to ensure that fracture would propagate through the hydrogen bonded network vertically to avoid shear stresses associated with navigating the point of the hexagonal structure. The geometry of the system was chosen to resemble a thin sheet as described in reference [112] to maximise the distance

in which the fracture can propagate. By making the the simulation cell only 1 unit cell thick in the plane perpendicular to the applied tension, it allows maximum length in the direction of propagation to enable steady crack speeds to form. Additionally, with this thin geometrical set-up, the number of atoms in the simulation can be kept to a minimum, thus lowering the overall computational expense of the simulation. The systems contained approximately 21000 atoms for fracture propagation through the basal plane and approximately 29000 atoms for fracture propagation in the basal plane. The system was first equilibrated at 200 K and zero pressure in the NpT ensemble for up to 1 ns using Nose-Hoover thermostat and barostat with a dampener of 100 time steps before any pulling tests were carried out.

An initial crack was placed in the centre of the simulation cell after the equilibration stage to encourage controlled fracture propagation. This initial crack was produced by removing water molecules from a diamond shaped volume in the centre of the face perpendicular to the direction of tension as illustrated in Figure 6.3.

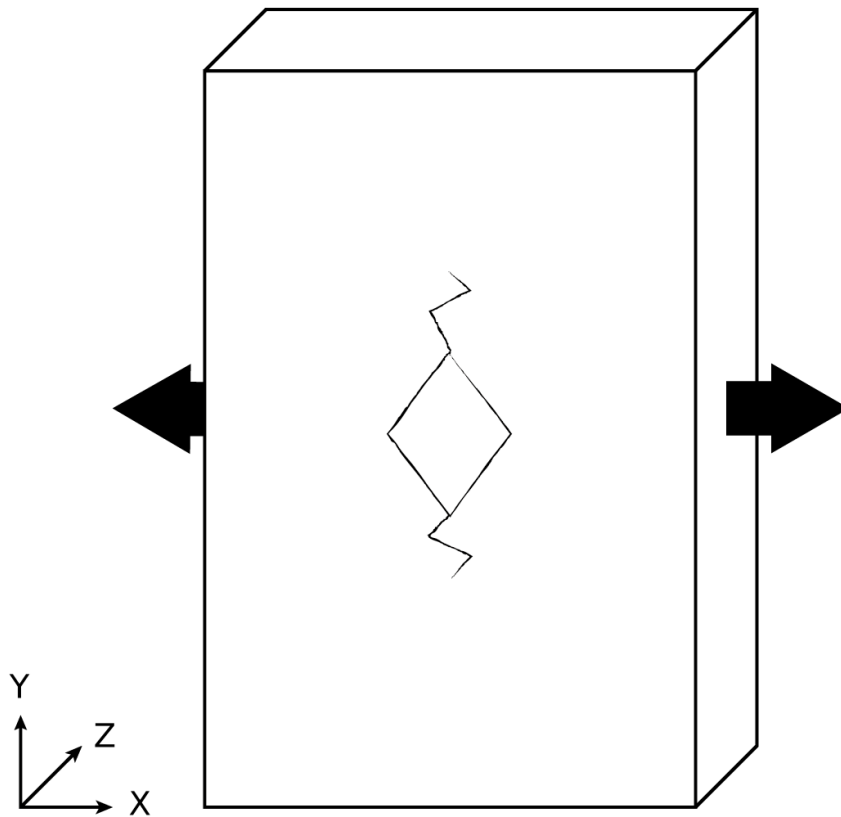


Figure 6.3: Illustration of ice Ih tensile test set-up.

The diamond shape was chosen over an ellipse or circle as reported in some previous methods as it was found that in the case of the ellipse, closure at low strains was observed[67, 167]. The diamond shape allowed a stress concentration to build up at the sharp point, enabling controlled fracture from an exact point. This was required to capture more accurately the speed as a clear fracture pathway was observed. In addition, the sharp point meant that less yielding was likely to occur. A circular notch was not used as the the notch would have to have a significant radius to prevent collapse of the ice structure into the vacuum space, which would result in non controlled fracture. This approach was an alternative

to removing interactions between molecules to create the initial crack as seen in some published work[168]. It was deemed that removing interactions may influence the crack healing behaviour and this, combined with the complexity of the ReaxFF simulation parameters, removal of interactions could lead to artefacts in the simulation[168]. According to reference [61], the crack should be the smallest possible size with respect to the length of the cell to ensure that the periodic images are not affected by the defect and to ensure that the properties determined are independent of the initial crack size. As such, after some notch size validation tests, the size of the initial crack is 45 Å in length, compared to 268 Å for the y-direction for the hexagonal faced pull test, unless stated otherwise.

6.3.2 The Tensile Fracture Method

The fracture test involved extending the length of the box in the direction of interest at a constant strain rate until failure and this was implemented by using the `fixdeform` command in LAMMPS[64]. The time step of 0.2 fs was used and periodic boundary conditions were applied in all directions. In the method found in reference [112], periodic boundaries are only applied in the direction which is one unit cell thick, however, when only applying periodic boundaries to the 1 unit cell dimension in the simulation of ice Ih, collapse of the non-periodic edges was observed. Thus, full periodic boundaries were implemented, as also done in references [61, 166]. Furthermore, the initial crack was chosen to be in the centre of the cell, in contrast with the method used in reference [112] which used an initial crack at the cell edge. Firstly, edge cracks could not be used with periodic boundaries due to cross image atoms affecting the crack and creating undesired crack geometries. Secondly, due to the computational expense of ReaxFF and the large system size required to maximise fracture propagation, having two crack tips allows some statistics to be gathered when calculating fracture speeds — two fracture pathways could be studied per simulation, reducing the total number of repeat runs for crack speed measurements.

Throughout the tensile test, the directions which are not under tension are kept at zero pressure to encourage realistic propagation of the fracture and to prevent non-physical deformation which was observed in *NVT* simulations. This work

predominantly focuses on fracture perpendicular to the basal plane due to clear crack progression through the hexagonal structure. This was in line with two other studies of ice Ih reported in recent literature[106, 107]. However, since basal slip is predominant in experiments, comparisons are also made between basal plane and basal face strength and failure processes as part of this work.

Strain rates for molecular simulations tend to be higher than those used in macroscale experiments due to the time limitations of MD[169]. As a result, the limitations in calculating the fracture properties using MD have to be considered carefully and cannot always be directly compared to experiment. The high strain rates required in MD is the equivalent of creating a shock load scenario on a macroscale system[169]. The highest strain rate employed in this work is $5 \times 10^{-5} \text{ fs}^{-1}$, compared to a typical fracture experimental strain rate being in the range of 10^{-5} s^{-1} to 10^{-1} s^{-1} [109].

The average stress of the entire system was calculated at every step. Note that this stress was directly related to stress as a result of the tension since the other dimensions were kept at zero pressure. The tests were run until complete failure was observed. The fluctuations of stress caused a large amount of noise in the stress-strain curves therefore for visual purposes only, noise was reduced in each stress-strain curve by applying a time series filter as implemented in SciPy.

Crack speed work was calculated by distance time relations of the crack tip at specified time intervals. The fracture toughness is calculated by means of the stress intensity factor, K_{IC} , based upon the theory as described in reference [61] and in Chapter 4. The stress intensity factor specifies the maximum value of stress which a material can sustain and defines the point in which the material can no longer resist fracture. Stress intensity is related to the critical energy release rate G_C by:

$$K_{IC} = \sqrt{\frac{G_C}{H_I}} \quad (6.1)$$

where G_C can be calculated by:

$$G_C = \frac{\Delta F}{\Delta A} = \frac{L_x L_y}{\Delta A_\infty} \int_{L_z0}^{L_{max}} \sigma_Z dL_Z \quad (6.2)$$

and H_I is calculated using the material elastic constants:

$$H_I = \frac{1}{2} \sqrt{\frac{C_{11}}{C_{11}C_{33} - C_{13}^2} \left(\frac{1}{C_{44}} + \frac{2}{C_{13} + \sqrt{C_{11}C_{33}}} \right)} \quad (6.3)$$

where L_x and L_y is the length in the x and y direction respectively. Ovito[170] and VMD[171] were used for visualisation of the of the trajectories and the crack surface area was measured using ImageJ[172, 173].

6.4 Results and Discussion

One of the main aims of this chapter is to compare fracture properties of molecular dynamics simulations to experimental fracture properties of ice Ih to enable validation of the method before applying to C-S-H. As discussed in the previous section, the concept of fracture is incredibly complex and many factors have to be considered when trying to predict realistic failure. In addition, the differences in fracture related properties between atomic scale and macroscale make validation of simulated properties even more complicated. It is known that strain rates used in simulations are generally much higher than those of experiment due to the very short time scales of MD[169]. Moreover, the atomic scale system tends to be defect free and often modelled as a single phase with no grain boundaries or pre-existing flaws, resulting in a much higher strength and toughness. As such, comparing molecular simulations directly to the experimental data for ice is not without limitations. Here, we attempt a systematic approach by checking parameters such as initial crack size, temperature and direction to quantify their effect and determine if they have a significant influence on the prediction of fracture properties at the nanoscale.

6.4.1 Simulating Fracture Under Plane Strain Conditions

When simulating fracture, the body under tension can be in one of two conditions - plane stress or plane strain. Plane stress occurs on samples which are not sufficiently thick and can result in undesired shear stresses occurring within the sample and thus, the energy increase throughout the simulation cannot be attributed to stress in the direction of tension. Plane strain occurs when the sample is of adequate thickness where the surrounding medium effectively holds the structure in place. In plane strain conditions the stress within the sample is a result of direct tension. This must be considered when measuring the fracture toughness. In plane strain conditions, at sufficient thickness B , the fracture toughness is independent of B . As B is reduced, the fracture toughness becomes dependent on B and plane stress conditions are observed as illustrated in Figure 6.4.

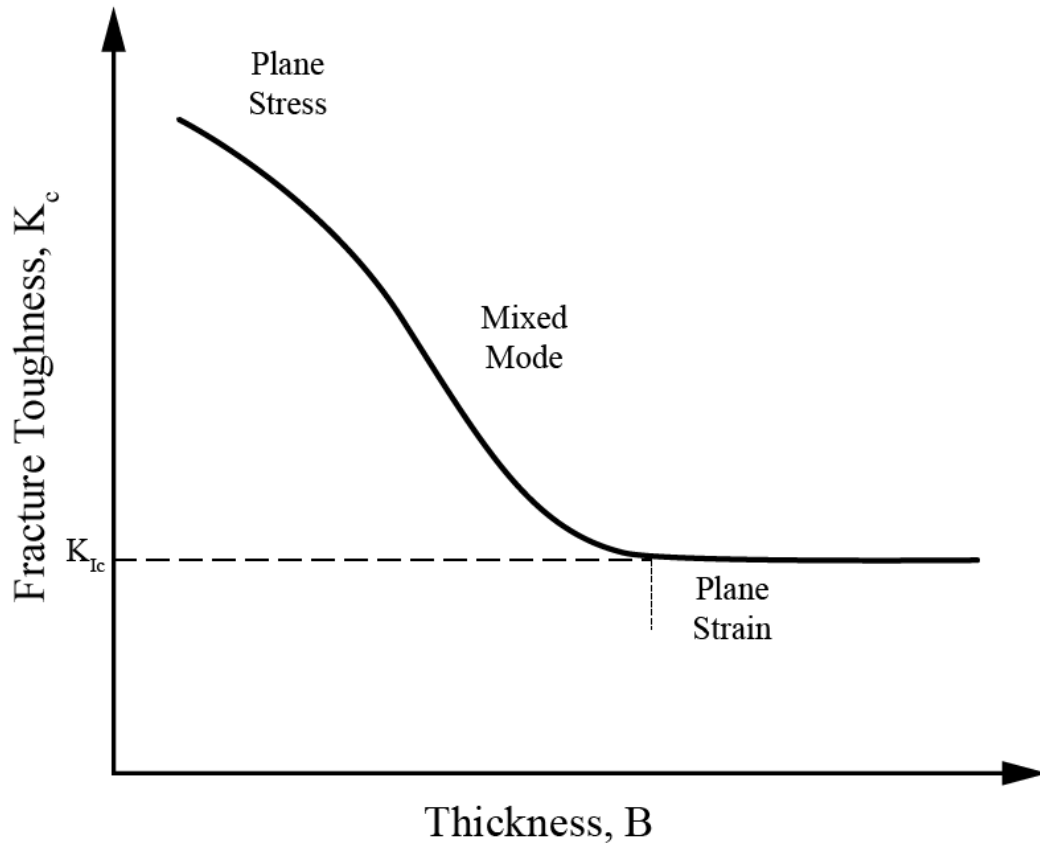


Figure 6.4: Relation of fracture toughness, K_{IC} to thickness, B .

Although the thickness of the samples carried out in this chapter are one unit cell thick (approximately 7 \AA), it is possible to overcome the issue of plane stress conditions by incorporating periodic boundary conditions. Figure 6.5 compares a simulation with and without periodic boundary conditions. It can be seen that without periodic boundaries, the simulation cell starts to shear, causing undesired stresses on the $x-y$ face. By including periodic boundaries, no shearing is observed; therefore, the simulation can be assumed to be under plane strain conditions.

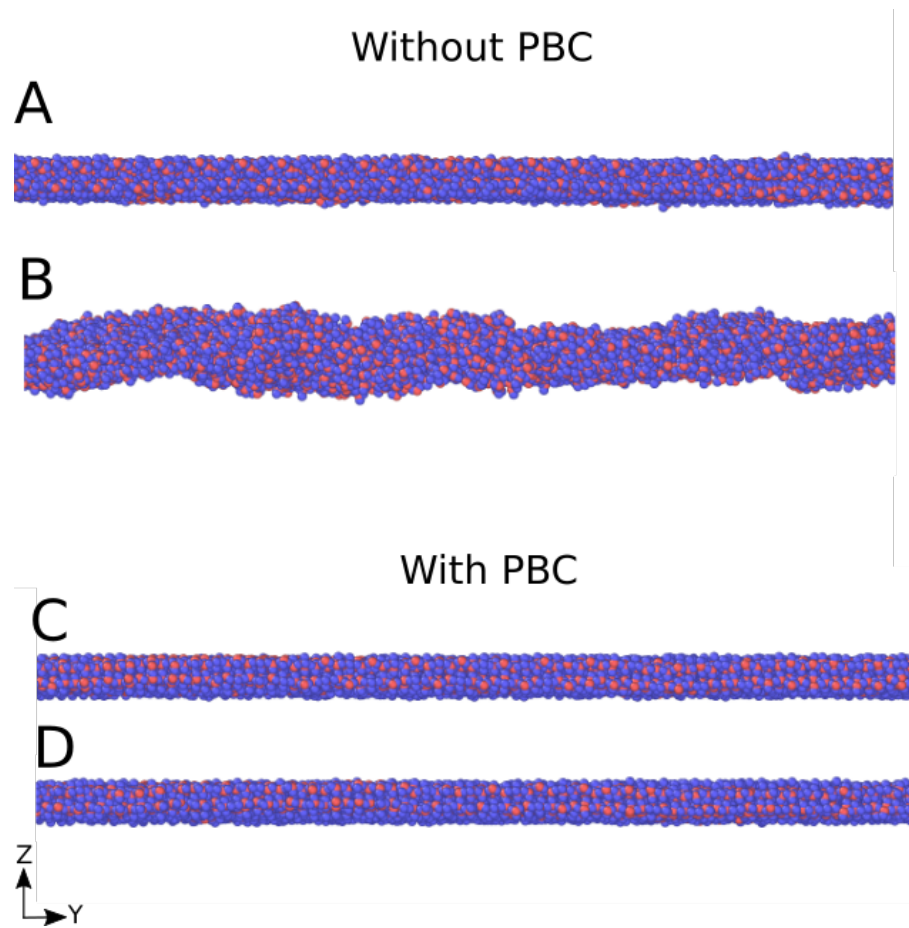


Figure 6.5: Fracture test carried out with and without PBC to compare plane stress and plane strain conditions. A and B correspond to before and after tensile testing without PBC respectively. C and D correspond to before and after testing with PBC respectively.

6.4.2 Effect of initial crack size

In MD fracture simulations, fracture initiation is usually achieved by creating an initial crack to provide a point of increased stress at the crack tip from where the fracture will propagate. Careful consideration of the size of the initial crack relative to the simulation cell is required for a number of reasons. First of all, an initial crack which is too large may cause undesired cross periodic image interactions. Secondly, the large initial crack sizes may influence the fracture properties. Finally, Brochard et al. demonstrated that the influence of the periodic images

becomes significant when the ratio of crack length to simulation cell length is greater than 0.5 ($2a/L > 0.5$), where a is half the length of the initial crack and L is the length of the cell)[166].

The literature varies in the size and shape of initial cracks: from central cylindrical holes and ellipses to triangular edge cracks[67, 112, 167]. In this study, initial cracks are placed in the centre of the simulation cell to allow periodic boundaries to be incorporated, and as described above, by using periodic boundaries, surface effects are reduced[166]. In this work, the initial cracks were chosen to be a rhombus/diamond shape as it was observed that at the very early stages of the simulation where the overall stress of the system was at zero, the initial cracks deviated from their initial geometries, and closure of the cracks occurred when not under the influence of stress due to the natural dynamics of the ice Ih structure. For the same reason, when calculating fracture toughness, the initial crack size was taken after the shape stabilised at 2 ps.

Brochard et al. has demonstrated that aspect ratios (length of initial crack/height of crack) of less than 0.5 are required to produce crack propagation whereas higher aspect ratios than this resulted in yield-type deformation[166]. Three initial cracks that consisted of decreasing aspect ratios, listed in Table 6.1 and illustrated in Figures 6.6, 6.7 and 6.8 were compared. One of the most important criteria for the initial crack was stability. It can be seen from Figure 6.6 that the smallest initial crack size became unstable as the simulation progressed as is evident by the healing of the ice structure. This healing is unlikely to produce a high stress concentration at the tip and therefore may result in further yielding before crack propagation. The medium crack size overcame this issue and no self healing across the breadth of the crack was observed. Lastly, the large crack saw very limited healing of the crack and the surfaces remained stable. In some early test studies, melting of the ice Ih into the vacuum space created by the initial crack was observed for large crack sizes (not pictured).

Table 6.1: Dimensions of initial crack sizes

Size	L (Å)	b/a	b/a at 2 ps
large	72	0.42	0.48
medium	45	0.22	0.25
small	36	0.15	—

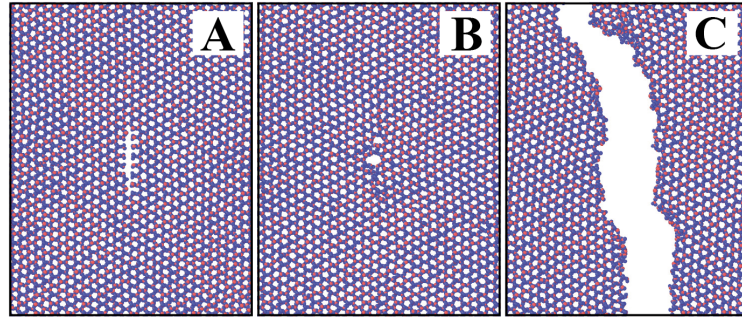


Figure 6.6: Fracture propagation using small initial crack ($b/a=0.15$) at 200 K, strain rate of $5 \times 10^{-6} \text{ fs}^{-1}$. (A) initial crack (B) crack healing occurring after 8 ps (C) fully propagated fracture.

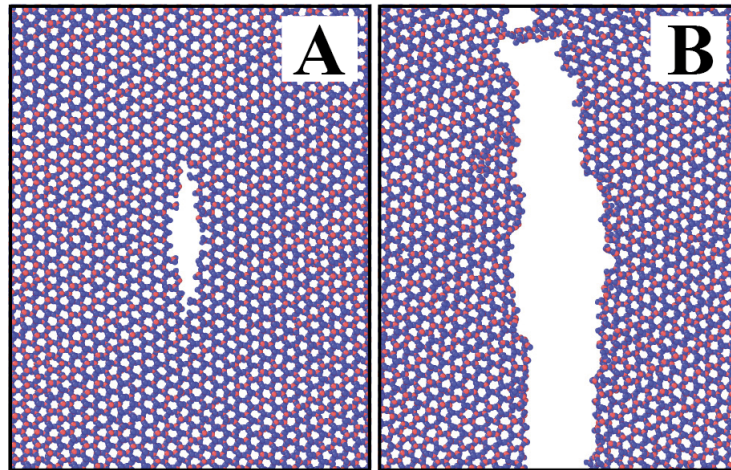


Figure 6.7: Fracture propagation using medium initial crack ($b/a=0.22$) at 200 K, strain rate of $5 \times 10^{-6} \text{ fs}^{-1}$. (A) initial crack (B) fully propagated fracture.

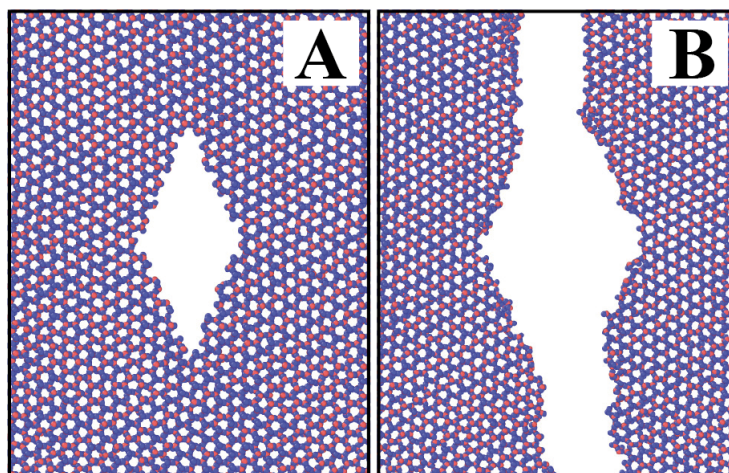


Figure 6.8: Fracture propagation using large initial crack ($b/a=0.42$) at 200 K, strain rate of $5 \times 10^{-6} \text{ fs}^{-1}$. (A) initial crack (B) fully propagated fracture.

During propagation, as is evident in Figure 6.6, it was noted that the surface roughness increases with decreasing initial crack aspect ratio which may be a direct result of crack tip stress concentrations; however, this was not investigated further.

Figure 6.9 shows the stress strain curves produced by different initial crack aspect ratios. The stress was calculated as an average over the entire x component of the stress, recall that the other directions were set to zero stress. At strains below 0.05, very little difference is seen between the three different initial crack sizes. As strain increases, deviation between the different systems is visible, reaching slightly different maximum stresses. The greatest tensile stress is seen with the smallest initial crack and the lowest tensile stress stems from large crack size. The most likely cause of this is demonstrated in Figure 6.6 where at small initial crack sizes, the ice Ih tries to heal itself by reforming the hydrogen bond network to minimize the open space. The closure of the crack results in reduced point stresses at the edge points of the crack and the resulting crack propagation is less controlled and more erratic as seen in the figure. In contrast, the large initial crack creates a significant defect, and whilst greater point stresses will be created at the y poles of the initial crack i.e. the propagation points, a more controlled propagating fracture is produced. The lower tensile stress is most likely due to

Table 6.2: Tensile strength at different initial crack sizes

L (Å)	b/a	Tensile Strength (GPa)	Fracture Toughness ((kPa.m ^{1/2}))
70	0.42	0.40	247
45	0.22	0.54	158
36	0.15	0.58	109

the significant defect, the initial crack takes up a larger percentage of the material surface creating a significant defect and therefore lowering the tensile strength. The medium crack size lies in between the results and gives benefits of both systems - a controlled fracture is seen but no closure and healing of the initial crack is evident. This medium sized crack is used for further investigations.

The tensile stress for the ReaxFF MD simulation is in the range of 0.4-0.6 GPa which is two orders of magnitude greater than the experimental tensile stress of 0.003 GPa. This is a common occurrence in MD fracture simulations and is linked to the high strain rates used[169]. Furthermore, the lack of defects in the system compared to experiment will contribute to a higher tensile strength. This value of tensile strength is comparable to a MD fracture study by Qin et al. as they calculate the tensile stress as being ≈ 0.3 GPa and therefore is in the same order of magnitude as the data presented in this study[107].

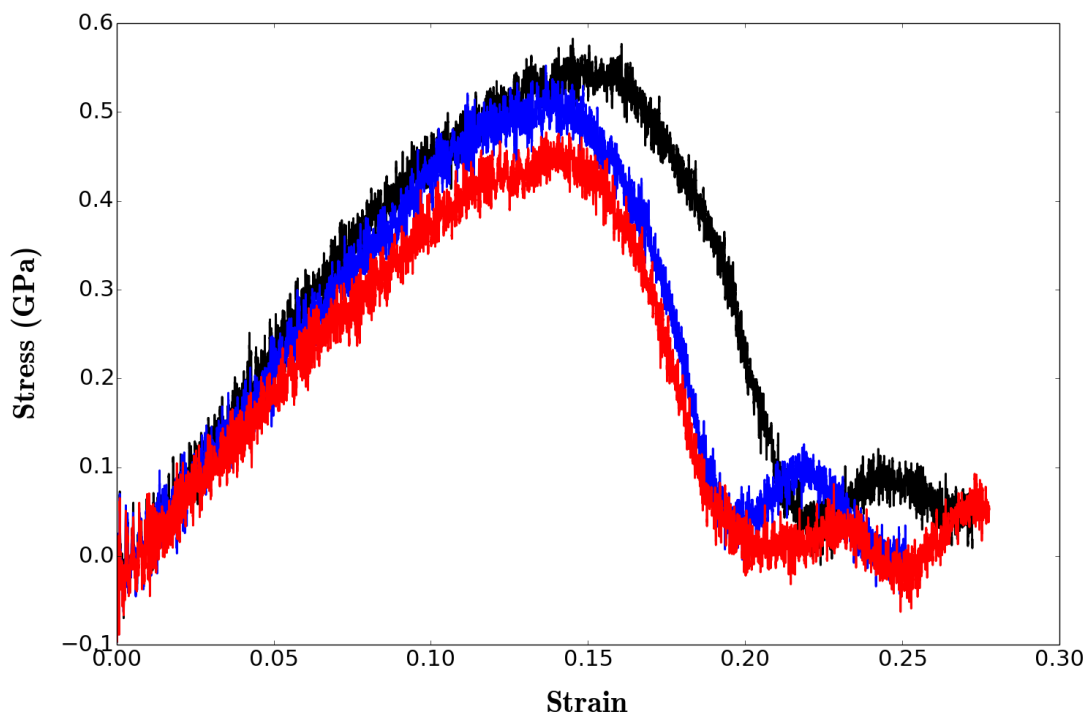


Figure 6.9: Stress strain curve for different initial crack sizes, strain rate $5 \times 10^{-6} \text{ fs}^{-1}$, x-direction, 200K. small (black), medium (blue) and large (red).

6.4.3 Failure of Ice Ih Under Tension at Different Strain Rates

The effect of strain rate on the nanoscale fracture of ice Ih is examined in this section. It has been shown that experimental strain rates have little effect on the fracture toughness of polycrystalline ice[159, 163, 174]. With respect to single crystal ice, according to Schulson and Duval[88], fracture toughness and tensile strength are not affected by strain rate or temperature. The strain rates were chosen to be of a similar magnitude to previous MD fracture simulations[169].

Figure 6.10 shows the difference in stress strain curve produced at different strain rates. At the highest strain rate tested ($5 \times 10^{-5} \text{ fs}^{-1}$), an increase in tensile strength is seen compared to the lower strain rates tested. Furthermore the strain at which failure occurs is much greater at the highest strain rate studied. The

mechanism of deformation at high strain rates does not produce a single crack but fails at multiple points throughout the structure as shown in Figure 6.11. As a result this strain rate was unsuitable for simulating fracture toughness and crack speed analysis. The lowest strain rate tested, $1 \times 10^{-6} \text{ fs}^{-1}$, added significant computation time therefore it was deemed infeasible to use this strain rate in further studies.

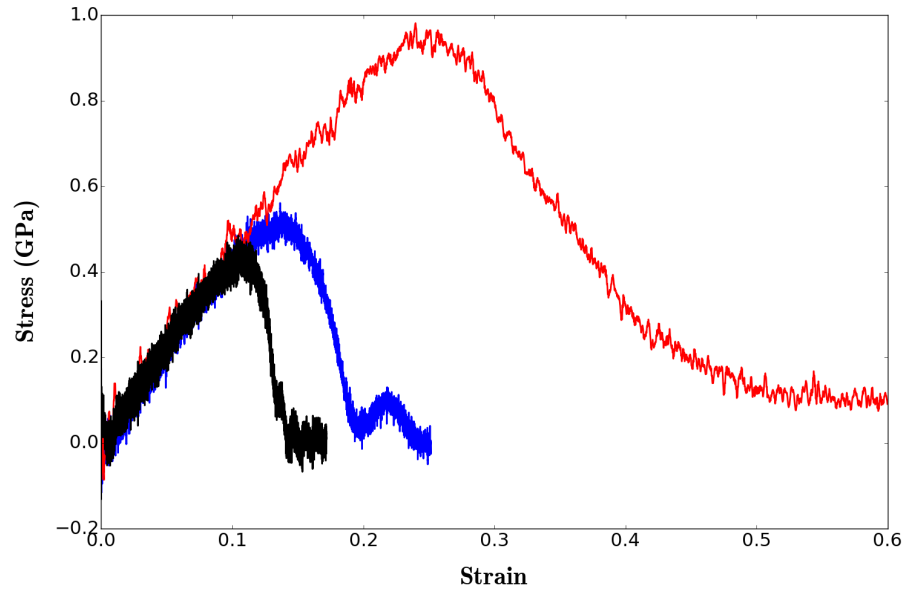


Figure 6.10: Stress strain curve for normal structure, strain rate $1 \times 10^{-6} \text{ fs}^{-1}$ (black), $5 \times 10^{-6} \text{ fs}^{-1}$ (blue), $5 \times 10^{-5} \text{ fs}^{-1}$ (red), strain applied perpendicular to basal plane direction, 200K

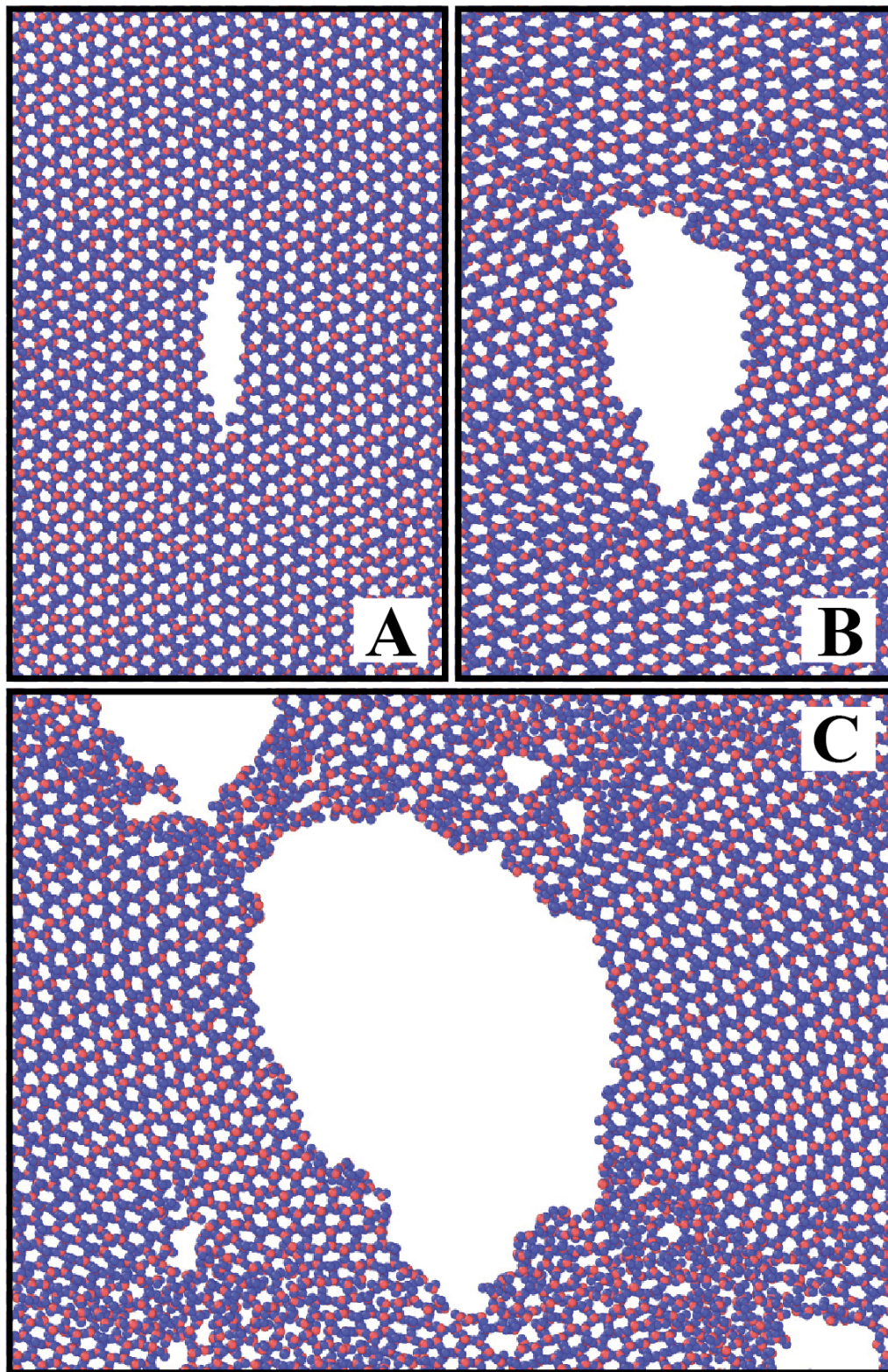


Figure 6.11: Visual of extreme brittle fracture and deformation at strain rate 5×10^{-5} , x-direction, 200K.

For the 5×10^{-6} strain rate simulation, the crack propagates predominantly down the central line of hydrogen bonded hexagons, and deviations from this are infrequently observed. Where possible, the fractured surface tried to maximise the number of hydrogen bonds including at the crack tip until the stress concentration overcomes the energy of the hydrogen bond. At high strain rates however, a single crack starts to propagate, but this is quickly followed by significant deformation in the hexagonal structure with defects opening up right across the structure as illustrated in Figure 6.11.

Table 6.5 displays the fracture data measured for the three strain rates tested. It can be seen that tensile strength increases with increasing strain rate which differs from the polycrystalline experimental data as described earlier. The value of tensile strength determined by MD is much higher than the values measured by experiment (170.02 GPa), however, this is expected as the simulations are for defect free structures and, therefore, the strength should be higher than seen in experiment[109].

Fracture toughness calculated experimentally by three point bending tests are in the range of 80-120 kPa.m^{1/2}[109]. The simulations carried out here show that for the 5×10^{-5} fs⁻¹ strain rate, the fracture toughness is close to this range with a value of 56 kPa.m^{1/2} for final failure and 158 kPa.m^{1/2} at peak strength. One thing which is not clear from the literature is whether the fracture toughness should be reported from the first point of failure or from the full stress strain curve.

A thorough search of the literature has revealed that only one other study of fracture toughness using MD has been reported[107]. This study, by Qin et al., uses ReaxFF but differs from this study by the simulation cell geometry and fracture method. Qin et al. use a simulation cell of $44 \times 44 \times 44 \times 44 \text{ \AA}$ geometry whereas this work uses a plate like geometry of $265 \times 130 \times 7 \text{ \AA}$ which can almost be considered as a 2D structure. The fracture method by Qin et al. also includes relaxation between every increase in strain, unlike the method devised in this thesis, and therefore it is expected that the results may differ. The fracture toughness data measured in this thesis appears to be an improvement over work by Qin et al. who calculate a fracture toughness of 22 kPa.m^{1/2}, however it must

Table 6.3: Fracture toughness and tensile strength data measured under different strain rates at 200 K.

Strain Rate (fs ⁻¹)	Tensile Strength (GPa)	Failure Strain	Tensile G_c (J/m ²)	Final G_c (J/m ²)	Final K_{IC} (kPa.m ^{1/2})	Tensile KIC (kPa.m ^{1/2})
1x10 ⁻⁶	0.434	0.106	2.63 ±1.84	0.11 ±0.10	32.97 ±16.95	162.36 ±73.12
5x10 ⁻⁶	0.509	0.136	0.275 ±0.08	2.21 ±0.128	55.95 ±9.57	158.47 ±4.54
5x10 ⁻⁵	0.944	0.250	—	—	—	—

be noted that the experimental value in which they compare to, 24.5 kPa.m^{1/2}, is close to their value, although this is from a report in 1969, much older work than the experimental value which this thesis uses as the experimental fracture toughness (80-120 kPa.m^{1/2})[175]. The value by Qin et al seems rather low as the simulation fracture toughness is expected to be greater than the experimental value due to natural defects which will weaken the ice structure. The difference in value between the fracture toughness calculated in this work for ice Ih versus the value by Qin et al. can most likely be attributed to difference in the method, highlighting the difficulty in drawing conclusions from MD fracture studies. Qin et al. use a simulation temperature of 250 K and a smaller system size (44Å × Å × 44Å). Furthermore, the authors implement an energy minimization step after each increase in strain as seen in [67] but not in [112]. Due to the vast differences in method, the exact cause of the difference in fracture toughness magnitude cannot be pin-pointed however it can be concluded that the method in this work provides a better representation of the most recent experimental experimental measurements of fracture toughness.

6.4.4 Effect of Temperature on the Fracture Properties of Ice Ih

It has been shown experimentally that fracture toughness of ice shows a slight dependence on temperature where there is a small increase in fracture toughness at lower temperatures for polycrystalline material, however, no such dependence is

observed for single crystal ice[88]. To test this hypothesis at the nanoscale, tensile tests were carried out at three different temperatures (175 K, 200 K and 215 K) using a strain rate of 5×10^{-6} . The effect of temperature on tensile strength, fracture toughness and crack propagation speed is assessed in this section.

Figure 6.12 displays the stress-strain curve at different simulation temperatures. The tensile curves show very little deviation as the stress is increased until a strain of 0.01, where the lowest temperature of 175 K continues on a steeper gradient path than the 200 K and 215 K tests. The curve at 225 K shows a slowing rate of change of stress-strain. While all temperatures reach a similar tensile strength, the point of failure is slightly varied. At lower temperatures, the ice Ih molecules/atoms will have a lower kinetic energy and therefore less thermal motion, making the structure more rigid. This rigidity means less movement of the water molecules and a slight contraction of the hydrogen bonded network, resulting in structure which is less susceptible to deformation. The softening curve differs for the temperature at 225 K only and this corresponds to the larger fracture toughness associated with this temperature as shown in Table 6.4.

Table 6.4: Fracture toughness and tensile strength data measured under different temperatures at a strain rate of $5 \times 10^{-6} \text{ fs}^{-1}$

Temp. (K)	Tensile Strength (GPa)	Failure Strain (GPa)	Tensile Gc (J/m^2)	Final Gc (J/m^2)	Final K_{IC} ($\text{kPa}\cdot\text{m}^{1/2}$)	Tensile KIC ($\text{kPa}\cdot\text{m}^{1/2}$)
175K	0.547	0.133	0.288 ± 0.0014	1.653 ± 0.151	57.23 ± 1.02	137.074 ± 6.39
200K	0.510	0.138	0.275 ± 0.08	2.21 ± 0.128	55.95 ± 9.57	158.47 ± 4.54
225 K	0.531	0.148	0.417 ± 0.151	2.455 ± 0.205	68.25 ± 12.57	167.11 ± 6.80

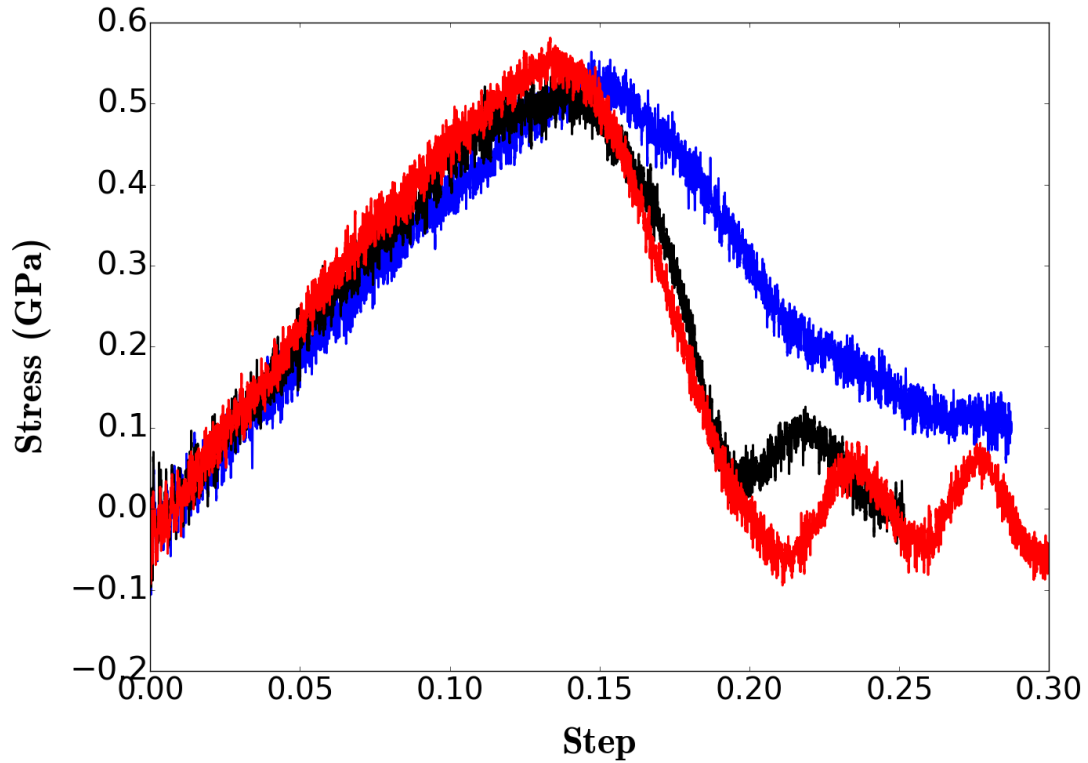


Figure 6.12: Stress strain curve for fracture tests at different temperatures. 175 K (red), 200 K (black), 225 K (blue), strain rate $5 \times 10^{-5} \text{ fs}^{-1}$, x-direction.

This increase in fracture toughness with decreasing temperature at the nanoscale contrasts with polycrystalline crystalline ice in experiment.[84]

6.4.5 Direction of Loading

It has been reported that fracture predominately occurs as basal plane slippage in ice Ih[84, 88]. The propagation of fracture was assessed as separation of the basal layers, as the original structure, and as the 30° rotated structure. All tests were conducted at 200 K and at a strain rate of 5×10^{-6} and 200 K. Stress-strain curves are displayed in Figure 6.13 and calculated fracture toughness values are given in Figure 6.5. The MD fracture tests back up experimental findings in that the basal plane is the weakest direction and fails at a lower strain than the other faces (≈ 0.098 strain for basal plane compared with 0.104 and 0.203 for the 30° rotated structure and the normal structure, respectively). The normal structure fails last as the water molecule at the peak of the hexagon, and therefore the crack tip, prevents the structure breaking apart which also prevents fast propagation as the path of least resistance is through the hydrogen bonds, which are at 30° relative to the direction of stress resulting in the creep effect displayed in the stress-strain curve prior to failure. Although the 30° rotated structure is the weakest in terms on the tensile strength, the hexagonal hydrogen bonded network is more resistant to stress than the distorted structure seen perpendicular to the basal plane.

Table 6.5: Fracture toughness and tensile strength data measured under different temperatures at a strain rate of $5 \times 10^6 \text{ fs}^{-1}$

Direction (K)	Tensile Strength (GPa)	Failure Strain (GPa)	Tensile Gc (J/m^2)	Final Gc (J/m^2)	Final K_{IC} ($\text{kPa}\cdot\text{m}^{1/2}$)	Tensile KIC ($\text{kPa}\cdot\text{m}^{1/2}$)
basal	0.77	0.10	2.27 ± 0.83	0.33 ± 0.12	60.64 ± 10.97	172.87 ± 31.33
30°	0.510	0.138	0.275 ± 0.08	2.21 ± 0.128	55.95 ± 9.57	158.47 ± 4.54
normal*	0.78	0.23	3.52	0.16	43.16	199.86

1

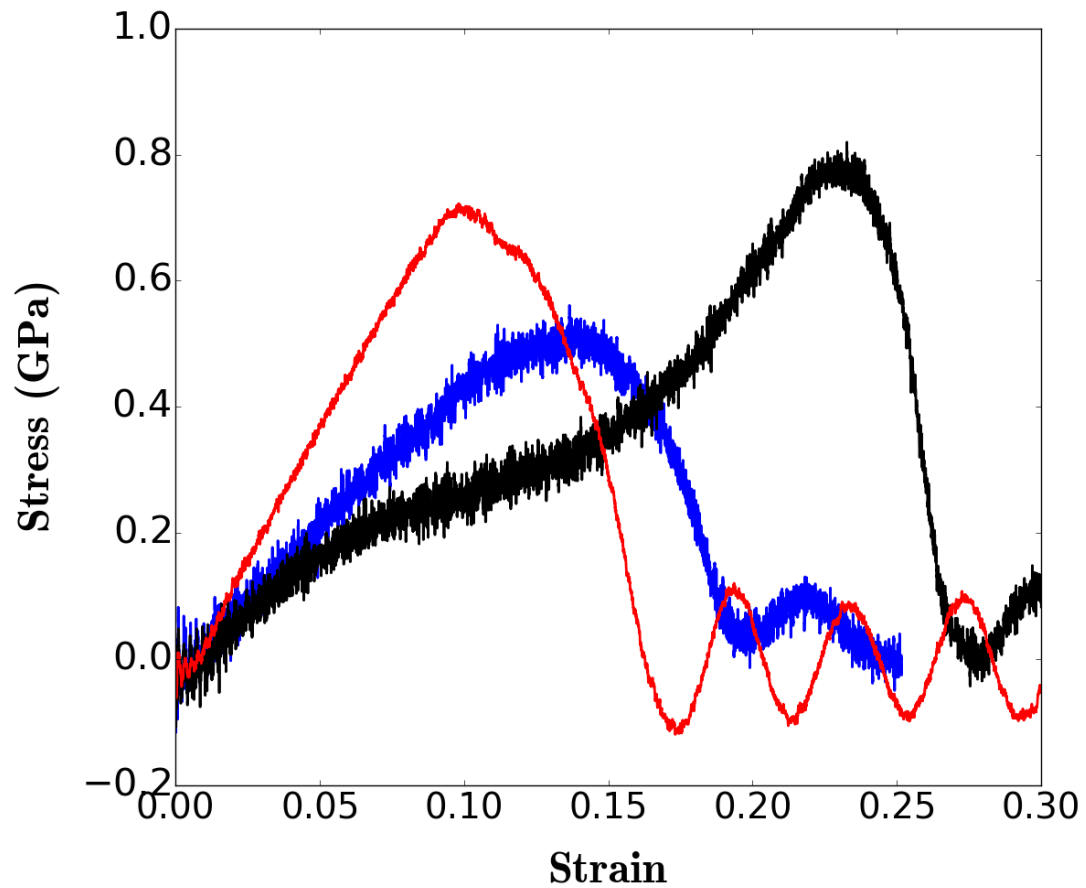


Figure 6.13: Effect of pulling direction on stress-strain curve at strain rate $5 \times 10^{-6} \text{ fs}^{-1}$, 200 K. Original structure (black), rotated by 30° (blue), basal plane (red).

6.4.6 Measurement of the Crack Speed of Ice Ih

As highlighted in Section 2, experimental crack speeds have been reproduced for silicon using MD and ReaxFF[112]. Experimental crack speeds of ice for lab grown, freshwater and sea ice are in the range of 100 m/s to 1300 m/s[176, 177]. Measurements of crack speeds can give information about failure rate which is especially important for Arctic ice shelves. Here, the crack speed in ice Ih is calculated and compared to available experimental data.

For the first part of the test, the resistance to fracture is high and no crack propagation occurs. At 0.0015 ns, the stress ahead of the crack tip is large enough to propagate the fracture, and the crack speed jumps from 0 to 200 ms^{-1} rapidly. As the simulation continues, the speed increases to over 600 ms^{-1} . Thereafter the speed drops due to failure of the material. Note that the speed does not reach zero as the simulation is stopped before complete failure due to the boundary effect. No reports have been made of single crystal ice fracture speeds, and as such the crack speeds of polycrystalline experiments as the benchmark as indicated in the figure.

As a result of the spread of deformation with high strain rates, as discussed in the previous section, it was not possible to measure speed further than the initial propagation. It can be seen, however, that under higher strain rates, erratic high fracture speeds occur, indicated by an increase in noise prior to 0.04 ns in Figure 6.14. At high strain rates, the speed is much greater than the Rayleigh wave speed (the speed of a wave which travels over the surface of a solid) of ice (1700 ms^{-1} for sea ice).

Experiments on Arctic sea ice found that the fracture travelled in one direction, and the speed varied from 100 ms^{-1} to 1100 ms^{-1} . [176] Another study on ice crack speeds has demonstrated that polycrystalline lab grown ice reaches speeds of 100-1300 ms^{-1} , but that saline ice has speeds as low as 10 ms^{-1} [177] It has been shown that the fracture propagation of ice is slowed by blunting of the crack tip [178]. In this study, it is observed that the hydrogen bond which bridges the gaps elongates right before fracture. No increase in the H-O-H bond angle is seen. The hydrogen bond bridging angle increases to around 140° whilst the vertical

bridging atom reduced to between 90° and 100° to resist fracture. It is significant extension in one of the hydrogen bond bridging angles which leads to break down of the ice structure. Two hexagons ahead of the crack tip have resulting extension in the O-O distance from 2.8 \AA at equilibrium to 3.0 \AA two hexagons away from fracture.

Figure 6.14 below compares the distance travelled by the fracture at different strain rates, the derivative being the speed. The sudden many point failure of the simulation carried out at $5 \times 10^{-5} \text{ fs}^{-1}$ strain rate could only have distance-time measurements up until a strain of 0.27 since after this point, single fracture propagation did not occur. From the slope of each curve in Figure 6.14, it can be seen that the initial speed is relatively constant until the point of sudden fracture propagation. At this point, the speed is much higher for the $5 \times 10^{-5} \text{ fs}^{-1}$ strain rate. The lowest strain rate, $1 \times 10^{-6} \text{ fs}^{-1}$ has a delay in steady crack propagation until around 0.1 ns and shows much slower fracture speed than the higher strain rates, which is to be expected. Note that the apparent difference in distance is a consequence of the noise during the measurement.

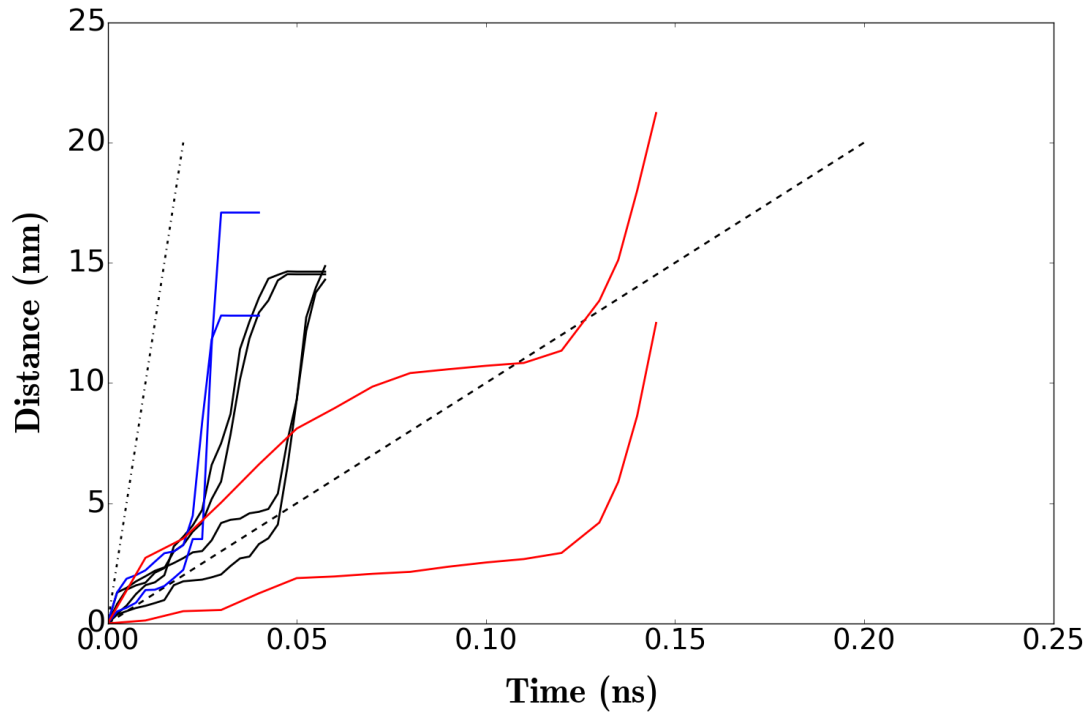


Figure 6.14: Speed time curve for ice Ih, strain rate 5×10^{-5} (blue), strain rate 5×10^{-6} (black), 1×10^{-5} (red), x-direction, 200 K. The lines represent 100 ms^{-1} (—) and 1000 ms^{-1} (---).

Figure 6.15 shows the effect of temperature on fracture propagation. The rate of change of distance with time is relatively constant over the temperature range studied indicating that temperature has little effect on fracture speed within the range of 175-225 K, although it is clear that lower temperatures cause a delay in the final crack speed. This supports the conclusion that lower temperatures help with fracture resistance as described earlier. This temperature range, however, is rather narrow and further work should be carried over over a wider temperature range to determine if fracture speeds changes further at the nanoscale at extremely low temperatures. It should be noted that the delay associated with the low temperature run (175 K) is observed in two out of the four runs tested, highlighting the probabilistic nature of modelling fracture.

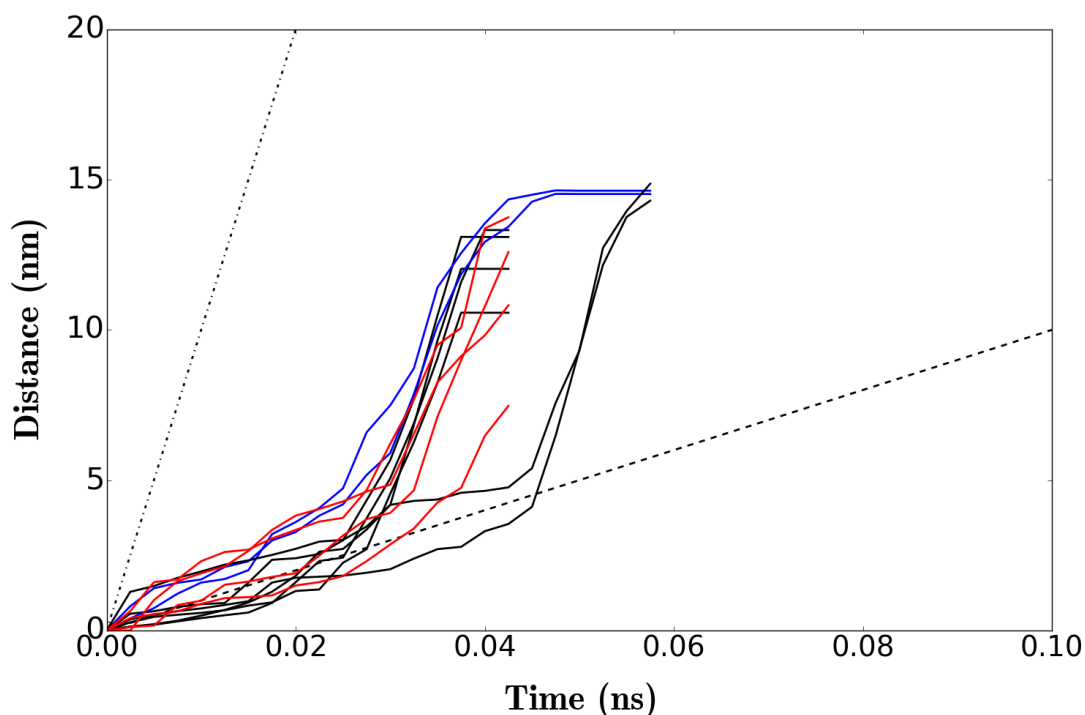


Figure 6.15: Speed time curve for ice Ih, strain rate 5×10^{-6} , x direction, 200 K (blue), 175 K (black), 225 K (red). The lines represent 100 ms^{-1} (—) and 1000 ms^{-1} (-.-).

6.4.7 Crack tip analysis

Analysis of crack propagation is carried out by studying deformation around the crack tip at 200 K and strain rate of $5 \times 10^{-6} \text{ fs}^{-1}$. From a single simulation, it is clear that two different deformation mechanisms occur in the $+y$ and $-y$ directions. Figure 6.16 shows the differences between the upper and lower notch before and after propagation. The lower and upper initial crack tips are shown in A and B respectively. Although slight differences occur initially due to the removal of water molecules to generate the initial crack, these differences were found to be negligible and soon disappeared upon kinetic vibration of the structure. Images C and D show the upper and lower crack tip right before fracture. The upper crack tip develops a more rounded geometry compared to the lower tip. The increased stress concentration on the lower crack with narrower radius

will help guide the fracture to propagate in a straight line. Immediately before propagation, the crack tip radius in both cases is approximately 5.7 \AA .

When the upper fracture is almost fully propagated, the fracture becomes erratic and larger rings are produced just ahead of the crack tip. This, however, is not observed by the lower fracture, and it seems to be a cleaner crack with less surface roughness as is visible from E and F in Figure 6.16. Formation of such rings has been reported in other materials such as silicon[112].

Fracture direction seems to be governed by extension of the angle and bond lengths of one of the hydrogen bonds. Fracture then proceeds by breaking of the hydrogen bonds as it extends beyond the limit of bonding. Two types of fracture are seen, depending on the radius of the crack tip. One method of crack resistance is by forming a large ring, similar to that seen in silicon which slows the fracture[112]. The other is where rapid progression of the fracture is seen.

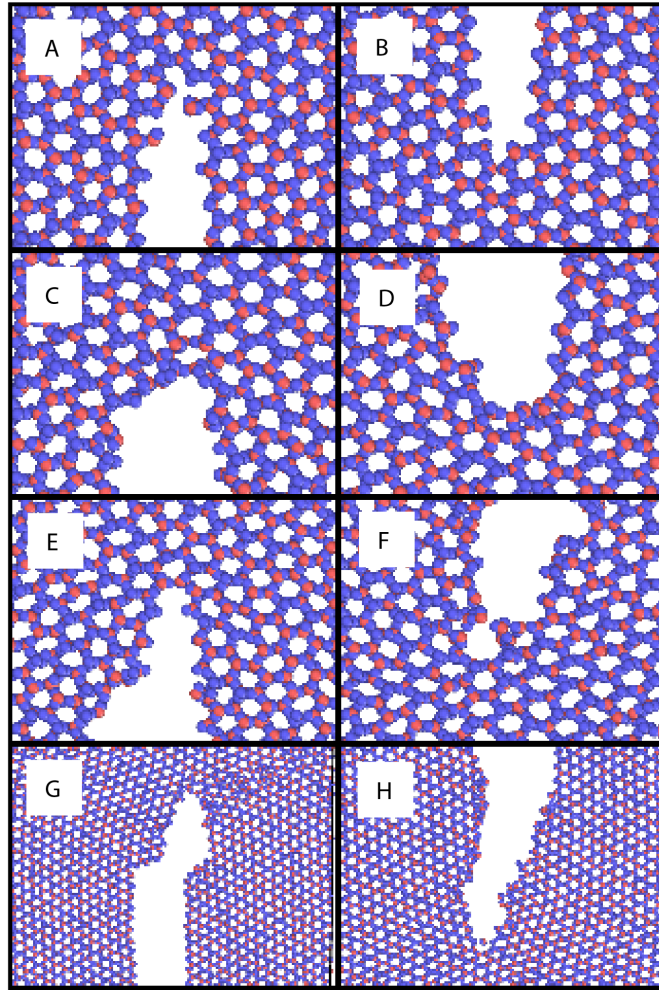


Figure 6.16: Crack tip shapes of ice Ih, strain rate 5×10^{-6} , x-direction, 200K.

6.5 Conclusions

In this chapter, validation of fracture initiation and propagation has been achieved by determining a reasonable aspect ratio relative to system size for ice. It has been demonstrated that the methodology here is able to produce a reasonable value of fracture toughness and shows an improvement over previous simulation work in the literature. The advantage of using the method devised in this work where continuous loading and using a maximum crack surface area is that both

fracture toughness and stress-strain relationships can be calculated from the one simulation. Despite the success of this method, there are some limitations of the model. Firstly, boundary effects will occur due to the use of periodic boundaries and therefore interacting images could have an effect. Furthermore, the method does not account for grain boundaries or natural crystal defects. Nonetheless the method is reasonable for predicting stress-strain relations and fracture toughness values for ice and can now be tested for the purposes of nanoscale fracture in cementitious materials such as C-S-H.

It was concluded that the proposed fracture method is capable of describing fracture phenomena, and experimental claims are supported by demonstrating the weakness in the basal direction. Additionally, the atomic scale crack speeds are within the range measured experimentally and the ReaxFF simulated fracture toughness values calculated by this method produce a realistic value and show improvement over existing simulation studies confirming that the proposed method is valid and can be applied to calcium silicate hydrates.

Chapter 7

Equilibrium Simulations of Calcium Silicate Hydrates - Validation of ReaxFF

7.1 Overview

In Chapters 5 and 6, the validation of the ReaxFF and the simulation methods were presented for condensed water giving insights into mechanisms of calculating elastic and fracture properties at the nanoscale using molecular simulation methods. In this chapter, some of the methods are applied to cementitious calcium silicate hydrates (C-S-H) and natural mineral calcium silicate hydrates (mC-S-H). To understand the physical and mechanical behaviour of C-S-H, it is important to first study mC-S-H structures with known crystal structure and well understood properties. By comparing ReaxFF predicted crystal structures and basic thermodynamic data to experimental results of mC-S-H, the force field and method can be validated, which gives confidence in the prediction of the behaviour of the hypothetical C-S-H models. In this chapter, equilibrium simulations using ReaxFF are carried out on a variety of mC-S-H and C-S-H samples to measure properties such as the crystal unit cell, chemical bond lengths and radial distribution functions (RDF) and the results are compared to experimental data where

available. In this chapter, the mineral and synthetic calcium silicate hydrates which are used for study are described alongside the hypothetical calcium silicate hydrate models. Simple validation of crystal structure is then carried out by checking ReaxFF predicted lattice parameters and bond distances of the mC-S-H models before using ReaxFF to model the crystal properties of hypothetical C-S-H structures. It is demonstrated that ReaxFF makes satisfactory structural predictions of mineral calcium silicate hydrates with solved chemical structures. Additional physical properties such as heat capacity, thermal expansion coefficient and constant pressure equation of state are measured and compared to available experimental and other simulation data in the published literature. This chapter demonstrates that ReaxFF reproduces well the crystal structure of mineral calcium silicate hydrates however some inadequacies are seen with heat capacity and thermal expansion coefficients. This chapter begins with a review of the previous experimental and simulation work that has been carried out in an attempt to understand the structure of C-S-H. A discussion of the limitations of both experimental and simulation work and how they can be used to compliment each other then follows. The methods are then described, giving more details about the C-S-H and mC-S-H structures which are modelled in this work. Validation of ReaxFF for C-S-H phases is carried out by bench-marking mineral C-S-H (mC-S-H) phases against available experimental crystal data and predictions are made for hypothetical C-S-H structures and is compared with available experimental data of similar Ca/Si ratio. Lastly, heat capacity and thermal expansion coefficients are carried out and compared with experimental data.

7.2 Introduction and Review of Previous Work

The nano-crystalline nature of C-S-H presents a significant challenge for solid state characterisation methods like X-ray diffraction (XRD) to capture a defined diffraction pattern and as a result, the exact chemical crystal structure of C-S-H has not been solved[6]. In addition, the variable nature of the cement composition results in many inconsistencies in the crystal structure meaning that quantifying a single crystal structure comes with great difficulty, and in fact, is far from real-

ity[27]. Advancements in lab based synthesis of C-S-H, as discussed in Chapter 2, has allowed more accurate knowledge of the composition and morphology of synthetic calcium silicate hydrates[27, 31]. Much work in this area has focused on creating synthetic C-S-H with controllable composition to enable further investigation of properties such as variability in Ca/Si ratio, density and nature of the silicate chains[6, 25].

It was recently confirmed that C-S-H forms a defective tobermorite structure, where the calcium silicate chains resemble the calcium silicate chains of tobermorite; but in contrast to the infinite chains found in tobermorite, defects in the chain are likely to occur in C-S-H and result in shorter calcium silicate chains[6, 27]. Work carried out using ^{29}Si NMR, has given an insight into the length of these polymeric chains demonstrating that low Ca/Si ratio C-S-H contain high numbers of silicate tetrahedra bound to two and three other tetrahedra resulting in bridged and branched tetrahedra respectively, indicating that the chains are infinite and therefore free of defects, such as those found in tobermorite. As Ca/Si ratio increases, ^{29}Si NMR data has shown that an increasing number of defects in the silicate chain results. A structure with defective chains means that the chain is no longer linear and infinite, but instead, is missing some bridging silicate tetrahedra. These shortened silicate chains have an irregular order and results in average chain lengths of 2-3 tetrahedra at Ca/Si ratios above 1.0.[6, 39, 40, 57] At the highest Ca/Si ratios, NMR data indicates that the sample is largely made up of dimeric chains.[6, 39, 40, 57]

The lack of crystal structure elucidation of C-S-H has led to development of hypothetical C-S-H models. Several computational C-S-H models have been derived from tobermorite and have aimed to reproduce the C-S-H chemical environment as inferred from experimental data[4, 14, 28, 39]. A frequently used hypothetical C-S-H model in computational work is Pellenq's C-S-H model which is derived from an early crystal refinement of a 11 Å tobermorite structure by removing bridging silicates to create a defective structure[14, 53]. This model was one of the first computational C-S-H models to be proposed; however, it has been criticised due to its lack of consistency with experimental data. Whilst the model reproduces the mean Ca/Si ratio of 1.7 and density of 2.6 gcm^{-3} of C-S-H as measured by Allen et al., the calcium environments in the model are unrealistic[28,

32]. In C-S-H, calcium ions are normally coordinated to 6 or 7 oxygens, however, in Pellenq's C-S-H model, calcium ions with coordination numbers as low as 3 and 4 are observed[28, 56]. Despite the inconsistencies in the model, many authors have continued to use the model in simulation studies to understand structure-property relationships[15, 66].

To overcome the drawbacks in Pellenq's model and provide more detailed structural information for C-S-H, Richardson developed hypothetical models and demonstrated their relation to experimental results derived from crystal geometrical reasoning[28]. These models demonstrated a number of principles which are consistent with experimental data including a decrease in basal spacing with increasing Ca/Si ratio, an increase in H₂O/Si ratio with increasing Ca/Si ratio and were able to reproduce the similar XRD patterns as seen in experimental C-S-H. Richardson produced double and single chain structures with varying Ca/Si ratio and silicate chains lengths.

Similarly, Rejmak et al. derived C-S-H structures from jennite and tobermorite 14 Å by removing bridging tetrahedra from the infinite silicate chains to create dimeric and pentameric silicate chain models. To balance the residual charge, either Ca²⁺ ions or H⁺ ions were added. This resulted in various models which were derived from tobermorite or jennite, had either pentameric or dimeric silicate chains and which had different Ca/Si and H₂O/Si ratios. By comparing theoretical NMR predictions of the models to that of experiment, the authors were able to rule out jennite type models, which is consistent with recent work by Grangeon et al.[31].

Most recently, Kumar et al. successfully produced a hypothetical model directly from NMR data of a single phase synthetic C-S-H. The authors balanced charges in a similar manner to those used by Rejmak where H⁺ and CaOH⁺ were used to balance the residual charge. The models from Rejmak and Kumar created systematic defects, in contrast to the random defect creation as seen in Pellenq's model.

Alongside advancing experimental work and the development of hypothetical structural models, MD simulation studies of mC-S-H and hypothetical calcium silicate hydrates C-S-H have increased in popularity, commonly with the aim of

quantifying material mechanical properties[14, 62]. Such simulation studies often employ tobermorite and jennite as crystal structural analogues for C-S-H as their crystal structures are readily available and can give an insight into the nanoscale behaviour of hydrated calcium silicates. Additional work has been carried out on hypothetical models in order to make predictions about the C-S-H structure and properties[4, 15].

The range of MD force fields for studying calcium silicate hydrate materials is narrow and in the earlier simulation studies, this was limited to CLAYFF and COMPASS[58, 59]. COMPASS is a general force field for use with a vast array of organic and inorganic small molecules[59]. CLAYFF, also a general force field, is parametrised specifically for studying clay-type minerals with complex layered structures[58]. CLAYFF uses a Lennard-Jones SPC model to describe water for use in hydrated clays. In contrast to common classical potentials, the non-aqueous phases are described by non-bonded interactions. This makes implementation of the force field to molecular dynamics codes such as LAMMPS much more straight forward as detailed bonding specifications are not required. In addition, it is easier to transfer between a number of mineral structures without significant modification of the input parameters.

Pellenq et al. modified the CLAYFF to be more akin to cementitious calcium silicate hydrate materials by more accurate parametrisation of the non-bonded parts, leading to the development of the CSHFF[14]. The CSHFF force field has been used for number of simulation studies since and shows reasonable reproducibility of the unit cell parameters of tobermorite and jennite with deviation of less than 3%[52]. Moreover, heat capacities and thermal expansion coefficients have been determined for unhydrated cement silicates from simulations using CSHFF and the comparisons are within an error margin of 20% for heat capacity[179]. However, it must be noted that the reliability of the experimental heat capacity is not clear due to outdated and inaccurate measurement protocols. Experimental values for thermal expansion could not be found for comparison.

One particular force field which has been rapidly increasing in popularity in C-S-H modelling in the literature is ReaxFF[60]. ReaxFF is simple to implement as no bonding configuration is required and has modelling capabilities of interest

to the cement industry which includes the ability to model chemical processes such as hydration and fracture[50, 61, 62, 131]. Although ReaxFF has been used in recent MD simulation studies in the literature, evidence of simple force field bench marking has not been included in any of the reports. In fact, with regards to CLAYFF and CSHFF, minimal validation with respect to thermodynamic and physical properties exists, however, this is unsurprising as the field is focused upon the engineering application of MD simulations as opposed to the fine chemical and crystal details. At this point, it is important to comment on the reproducibility of the common mC-S-H structures with CLAYFF and CSHFF. Despite lengthy attempts in this work to simulate tobermorite with CLAYFF and CSHFF, no stable structure could be produced. The reason for this could not be specifically identified however it is hypothesised that there may be some problems with the implementation of the force field whilst running dynamics — the validation paper by Shahsavari et al. uses energy minimization techniques as opposed to molecular dynamics and it is possible that this could be the reason for the structural instability when trying to implement CSHFF and CLAYFF[52].

The remainder of this chapter aims to describe in detail the structures studied and validate ReaxFF for use with C-S-H by comparing mC-S-H simulated crystal structural parameters with experimentally calculated structural parameters where experimental data is available. The work in this chapter aims to rigorously assess the capabilities of ReaxFF for use in cementitious materials.

7.3 Simulation details

Mineral calcium silicate hydrates (tobermorite 14Å , tobermorite 9Å , jennite and betawollastonite) were built from crystallographic information files retrieved from the ICSD database (icsd.cds.rsc.org) and as found in references [12, 13, 30, 180]. Model C-S-H structures (T5Ca1, T5H1, T2Ca1, T2H1, where T relates to a tobermorite starting structure and H/Ca refer to the charge balance method using H⁺ or Ca²⁺ ions respectively) were built from crystallographic information files as found in reference [39].

The computational expense of ReaxFF had to be considered when choosing ap-

appropriate system sizes. Firstly, relatively small system sizes had to be used to enable timely data collection. Larger system sizes were used for C-S-H structures as the effect of shortened silicate chains was one of the was dependent on the individual structure. mC-S-H structures consisted of systems sizes around $3 \times 3 \times 3$ unit cells which equated to around 1800 atoms. For C-S-H structures, the minimum system size was around 4000 atoms.

Table 7.1: System sizes for ReaxFF simulations

Structure	Crystal System	Chemical Formula	Ca/Si ratio	W/Si ratio	No. of Atoms	Unit Cell Replications	Ref.
Tobermorite 14 Å	monoclinic	$\text{Ca}_5\text{Si}_6\text{O}_{16}(\text{OH})_2(\text{H}_2\text{O})_7$	0.83	1.17	1872	$3 \times 3 \times 2$	[13]
Tobermorite 9 Å	monoclinic	$\text{Ca}_5\text{Si}_6\text{O}_{16}(\text{OH})_2$	0.83	0	1674	$3 \times 3 \times 3$	[30]
Jennite	triclinic	$\text{Ca}_9\text{Si}_6\text{O}_{18}(\text{OH})_6(\text{H}_2\text{O})_8$	1.5	1.33	1863	$3 \times 3 \times 3$	[12]
β wollastonite	—	CaSiO_3	1.0	0	1920	$4 \times 4 \times 4$	[180]
T5Ca1	NR	$\text{Ca}_{22}\text{Si}_{20}\text{O}_{60}(\text{OH})_4(\text{H}_2\text{O})_{28}$	1.1	1.4	4656	$6 \times 4 \times 1$	[39]
T5H1	NR	$\text{Ca}_{20}\text{Si}_{20}\text{O}_{60}(\text{OH})_4(\text{H}_2\text{O})_{28}$	1.0	1.4	6272	$4 \times 4 \times 2$	[39]
T2Ca1	NR	$\text{Ca}_{24}\text{Si}_{16}\text{O}_{56}(\text{H}_2\text{O})_{28}$	1.5	1.75	4320	$4 \times 3 \times 2$	[39]
T2H1	NR	$\text{Ca}_{20}\text{Si}_{16}\text{O}_{48}(\text{OH})_8(\text{H}_2\text{O})_{28}$	1.25	1.75	4416	$4 \times 3 \times 2$	[39]

Structures were energy minimised and equilibrated using the Velocity-Verlet integration algorithm as implemented in LAMMPS in NVT ensemble for 20 ps at 298 K and 0 bar pressure with 0.2 fs time step. Structures were then equilibrated at the desired temperature and pressure using ReaxFF with a time step of 0.2 fs in NpT ensemble for 0.7 ns to using the Nose-Hoover barostat and thermostat followed by a 0.25 ns production run. Reported values and errors are averages and standard deviations respectively as calculated from the production runs.

Visualisation of structures were carried out using the software packages VMD (<http://www.ks.uiuc.edu/Research/vmd/>) and OVITO (<https://ovito.org/>).[170, 171]. Crystal structure images were created using the crystal software VESTA (<http://jp-minerals.org/vesta/>)[181].

Heat capacities (C_p) were calculated using constant pressure simulations by fitting 3rd order polynomial curves to enthalpy (H) and temperature (T) data according to the following relationship:

$$C_p = \left(\frac{\partial H}{\partial T} \right)_p \quad (7.1)$$

The thermal expansion coefficient, α , was also calculated using constant pressure simulations by fitting 3rd order polynomials to density (ρ) temperature curves as follows:

$$\alpha_T = -\frac{1}{\rho} \left(\frac{\partial \rho}{\partial T} \right) \quad (7.2)$$

7.3.1 Measuring the Radial Distribution Function

The radial distribution function (RDF) describes how the density of a sample changes with radiating distance from a central point as illustrated in Figure 7.1.

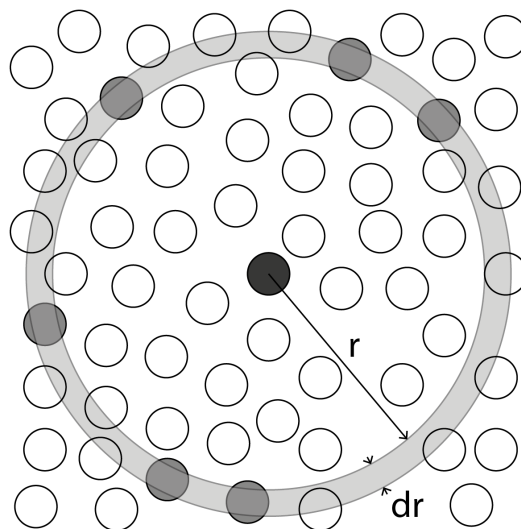


Figure 7.1: Measurement of the radial distribution function

The local density ρ_{local} of a material is related to the density of the bulk ρ_{bulk} through the RDF $g(r)$:

$$\rho_{local}(\vec{r}') = \rho_{bulk}g(r) \quad (7.3)$$

The RDF is calculated from an atomic trajectory by counting all of the pair distances and normalising by distances in uniform spheres:

$$dn(r) = \frac{N}{V}g(r)4\pi r^2 dr \quad (7.4)$$

The RDF was calculated from ReaxFF relaxed structural trajectories using VMD, averaged over 200 frames (4000 fs) by histogramming instances of interactions at given intervals to produce a graphical representation of RDF. The experimental equivalent of RDF is the pair distribution function (PDF) which can be measured using XRD.

7.4 Structures studied

The calcium silicate hydrates studied within this thesis are a mix of naturally occurring calcium silicate hydrates which have structural similarities to cemen-

titious calcium silicate hydrates (mC-S-H), and hypothetical structures (C-S-H) proposed by Rejmak et al.[39]. The structures were chosen to cover a range of Ca/Si ratios, H₂O/Si ratios, silicate chain lengths and densities so that trends in these properties could be assessed. The following sections describe each structure in turn, starting with β -wollastonite. For each structure, the ReaxFF relaxed crystal structures are presented and compared the simulated RDF to experimental data where available.

7.4.1 β Wollastonite

β wollastonite (bW), CaSiO₃, is often considered alongside C-S-H discussions as it is this final phase which is formed upon heating tobermorite and C-S-H to temperatures above 800°C[23, 182, 183]. Wollastonite type chains are also present in mC-S-H and C-S-H structures and therefore it is worthwhile to discuss this structure first. The structural properties are closely linked to the dreirketten chains of both tobermorite and jennite. The cell is triclinic with a space group of P1 and lattice parameters $a=7.94 \text{ \AA}$ $b=7.32 \text{ \AA}$ $c=7.07 \text{ \AA}$ $\alpha = 90.03^\circ$, $\beta = 95.37^\circ$ and $\gamma = 103.43^\circ$. The chains are infinite with rotated tetrahedral silicates as can be seen in Figure 7.2. The radial distribution function (RDF) is found in Figure 7.3. $g(r)$ has been shifted vertically for clarity. The chains are infinite and the interlayer contains no water or hydroxyl groups. The infinite silicate chains are very closely compacted and the interlayer distance is around 7 \AA . This can be seen in the global and Si-Si RDF at 7.1 \AA . The first peak in the Si-O RDF corresponds to the interaction between the central silicon and the four oxygen atoms which make up the the corners of the tetrahedron. The next peak, $r \approx 3 - 4 \text{ \AA}$ corresponds to the interaction between a central silicon on one tetrahedron and the closest oxygen on the adjoining tetrahedron. The peak at 4.3 \AA corresponds to silicon interacting with an oxygen on a neighbouring chain. In the Ca-O RDF, there are two prominent peaks – one at 2.3 \AA and the other at 4.5 \AA . These correspond to nearest neighbour Ca-O coordination on the closest silicate chain and a calcium interacting with an oxygen on the second closest silicate chain respectively. The first peak in the Ca-Ca RDF corresponds to neighbouring intralayer Ca-Ca interactions. The peak at 5 \AA corresponds to

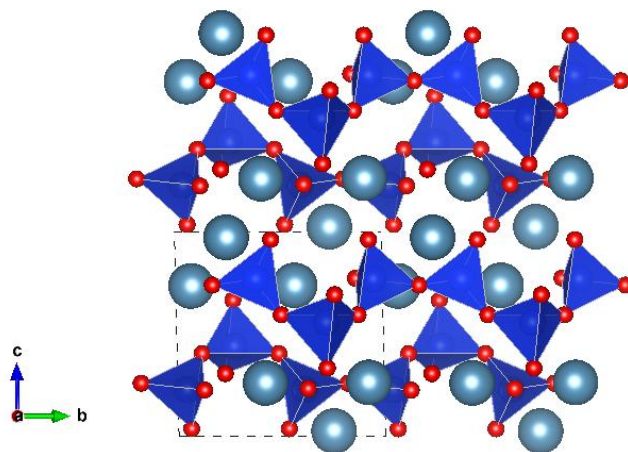


Figure 7.2: Crystal structure of β wollastonite, Ca^{2+} (green spheres), SiO_4^- (blue tetrahedra), O^{2-} (red spheres). The unit cell is identified by dashed lines.

a Ca ion in one intralayer interaction with a Ca in the next intralayer which is separated by two silicate chains where the lower intensity may be due to slight disorder in the placement of the Ca ions relative to one another. The first two peaks in the Ca-Si RDF correspond to nearest neighbour Ca-Si interactions 3.5 - 3.8 Å – the splitting of the peaks are due to the staggered nature of the silicate chains. For the Si-Si RDF, again the first peak represents nearest neighbours, however the lack of intensity in the remainder of the RDF pattern suggests that ReaxFF predicts some disorder of the wollastonite chain structure.

7.4.2 The Tobermorite Family

The tobermorite family is a class of calcium silicate hydrates defined by their dreiketten structure[184]. The family is known to be made up of three different structures each with a different interlayer spacing, dictated by their degree of hydration – tobermorite 14 Å tobermorite 11 Å and tobermorite 9 Å . For this study, tobermorite 11 Å was not chosen as a mineral calcium silicate hydrate as tobermorite 14 Å and tobermorite 9 Å provided more variation in structure which enabled more scope in determining structure-property relationships. As

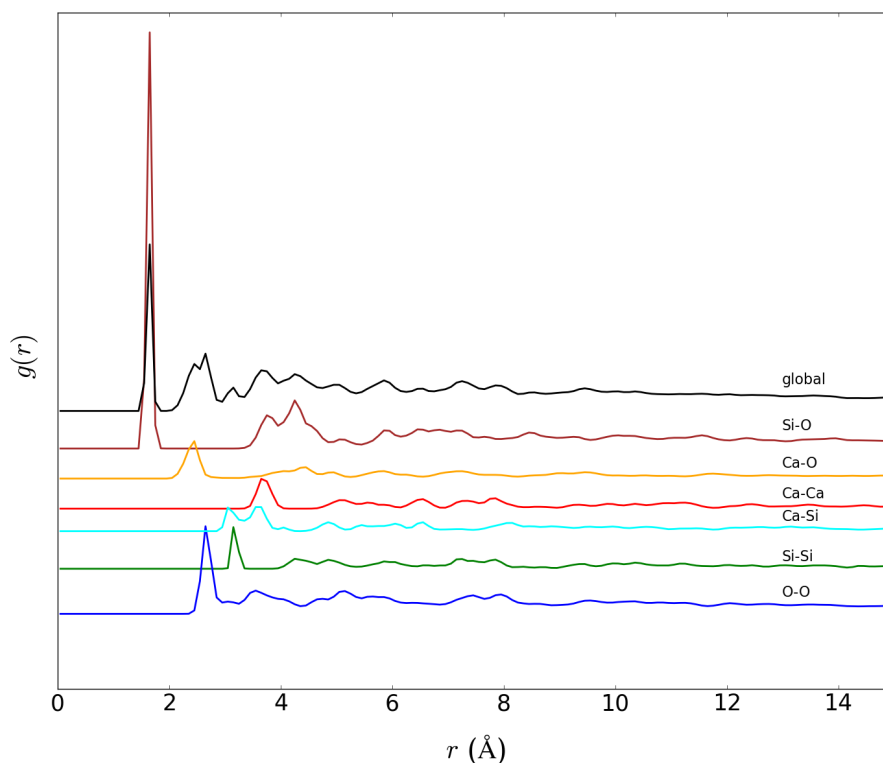


Figure 7.3: Radial distribution function of β wollastonite, ReaxFF (solid lines). Simulation values calculated from equilibrated structure at 298 K and zero pressure

the number of structures had to be limited due to time and cost, it was decided that tobermorite 11 Å gave the least in terms of structural and compositional variance compared to the other tobermorites.

Tobermorite 14 Å (T14), also known as plombierite, has the largest basal spacing of the tobermorite family and can be found in Ballycraigy N Ireland, Fuka Japan and the Urals mountains Russia[13]. The crystal structure was solved in 2005, and it was concluded that the crystal structure consisted of wollastonite like single chains sandwiched between alternating stacks of calcium containing water layers with basal spacing of 14 Å [13]. The layers are C-centred and staggered with C2m(b) symmetry. The unit cell is monoclinic and of space group B11b. The average chemical formula is $\text{Ca}_5\text{Si}_6\text{O}_{16}(\text{OH})_2 \cdot 7\text{H}_2\text{O}$ and each unit cell has lattice parameters $a = 6.375 \text{ \AA}$, $b = 7.425 \text{ \AA}$, $c = 27.987 \text{ \AA}$, $\gamma = 123.25^\circ$, $V = 1170.4 \text{ \AA}^3$

³[13]. Experimental work has shown, through XRD and NMR, that tobermorite very closely resembles low Ca/Si ratio synthetic C-S-H[6, 25, 28]. The crystal structure is illustrated in Figure 7.4. It can be seen that the silicate chains are infinite and are linked by bridges. Calcium ions can be found in interlayer spaces, coordinating predominantly to 7 oxygens and can also be found in the intralayer space bonding to the oxygens of the silicate tetrahedra.

The simulated RDF and the XRD determined PDF are displayed in Figure 7.5. The first peak in the global RDF calculated by ReaxFF MD simulation at $r \approx 0.9$ Å corresponds to the O-H coordination which is not normally picked in experiments due to the weak X-ray scattering. The weak scattering is a result of the proton only having one electron. Oxygen, with 14 electrons scatters more intensely followed by Si and Ca with 20 electrons scatters very intensely. This is not a factor when calculating the RDF from a set of simulated coordinates. Whilst the experimental global PDF shows that the tobermorite 14 Å sample is crystalline with long range order, as indicated by the sharpness of the peaks in the RDF; the apparent lack of crystallinity in the ReaxFF simulated structure is due to the relatively small sample size compared with experiment and so it appears that long range order is lost although this is known not to be the case.

The intense peak at $r \approx 1.64$ Å corresponds to the Si-O bond within the Si tetrahedra, and the bond length matches that of experiment. Furthermore, the lower intensity peaks of the Si-O RDF at $r \approx 3.7$ Å and $r \approx 4.3$ Å compare well to observations in experiment. The peaks corresponding to the first near neighbour in all cases compare well to experiment, with the exception of the Si-Si interaction where the nearest neighbour is out by approximately 3%; however, this is still well within a satisfactory limit. It can be concluded from the RDF and PDF analysis that ReaxFF reproduces the crystal structure of tobermorite 14 Å with reasonable accuracy.

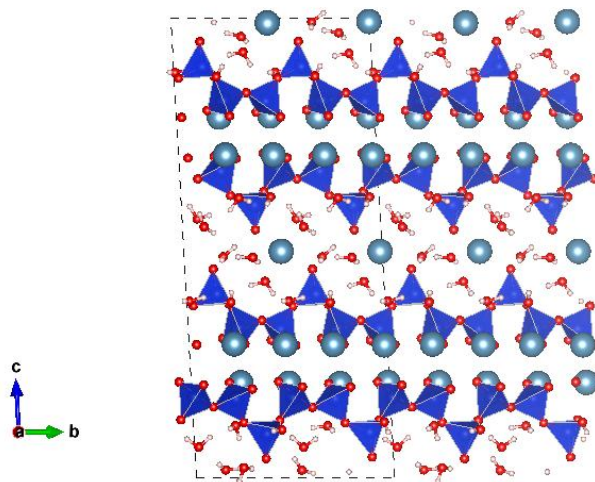


Figure 7.4: Crystal structure of tobermorite 14 Å, Ca^{2+} ions (green spheres), SiO_4^- (blue tetrahedra), O^{2-} (red spheres), and H^+ (white spheres). The unit cell is identified by dashed lines.

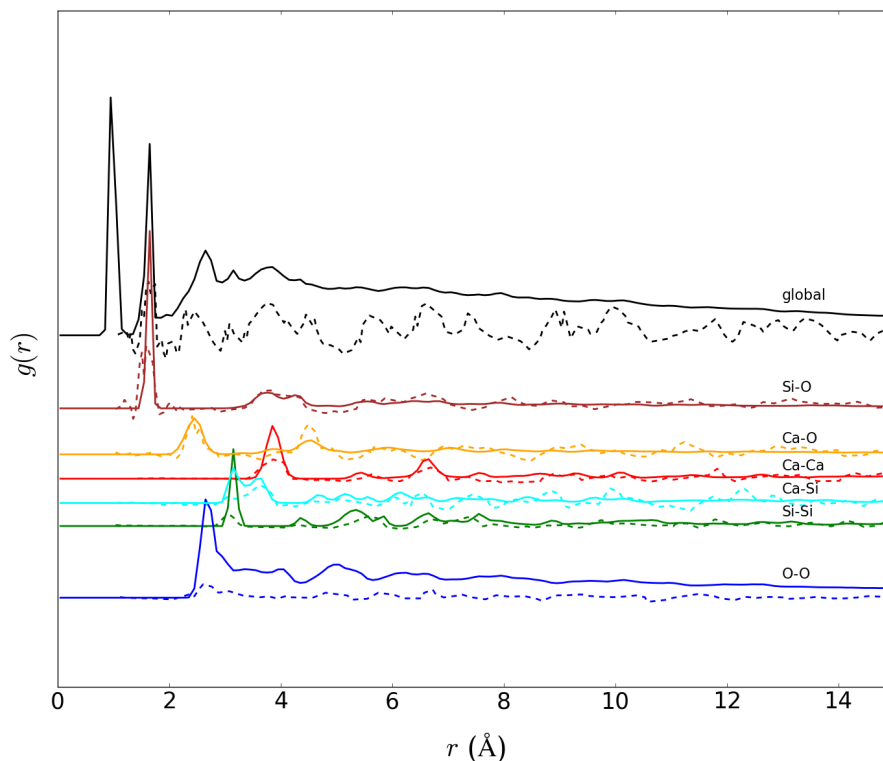


Figure 7.5: Radial distribution function of tobermorite 14 Å, expt. (dashed lines), ReaxFF (solid lines). Simulation values calculated from equilibrated structure at 298 K and zero pressure.

The least hydrated phase of tobermorite is the 9 Å (T9) phase and has the chemical formula $\text{Ca}_5\text{Si}_6\text{O}_{16}(\text{OH})_2$ and is produced by heating a normal 11 Å tobermorite phase to 573 K[30]. Tobermorite 9 Å is known as riversidite. Natural occurrences have not been fully confirmed[184]. The wollastonite chains present in tobermorite 14 Å are also present in tobermorite 9 Å. The space group is $A2/m$ with lattice parameters $a = 11.156 \text{ \AA}$ $b = 7.303 \text{ \AA}$ $c = 9.566 \text{ \AA}$ $\alpha = 101.08^\circ$, $\beta = 92.83^\circ$ and $\gamma = 89.84^\circ$. No experimental RDF data could be found in the literature for comparison to the ReaxFF simulations for T9 therefore Figure 7.7 consists of ReaxFF structural predictions only. The RDF data appears to hold more long range crystallinity than was seen with tobermorite 14 Å and this is due to the closer compaction of the crystal creating more long range order.

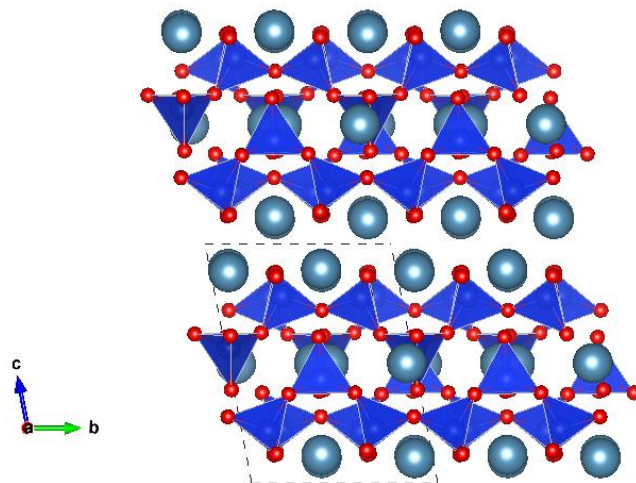


Figure 7.6: Crystal structure of tobermorite 9 Å, Ca^{2+} (green spheres), SiO_4^- (blue tetrahedra), O^{2-} (red spheres) and H^+ (white spheres). The unit cell is identified by dashed lines.

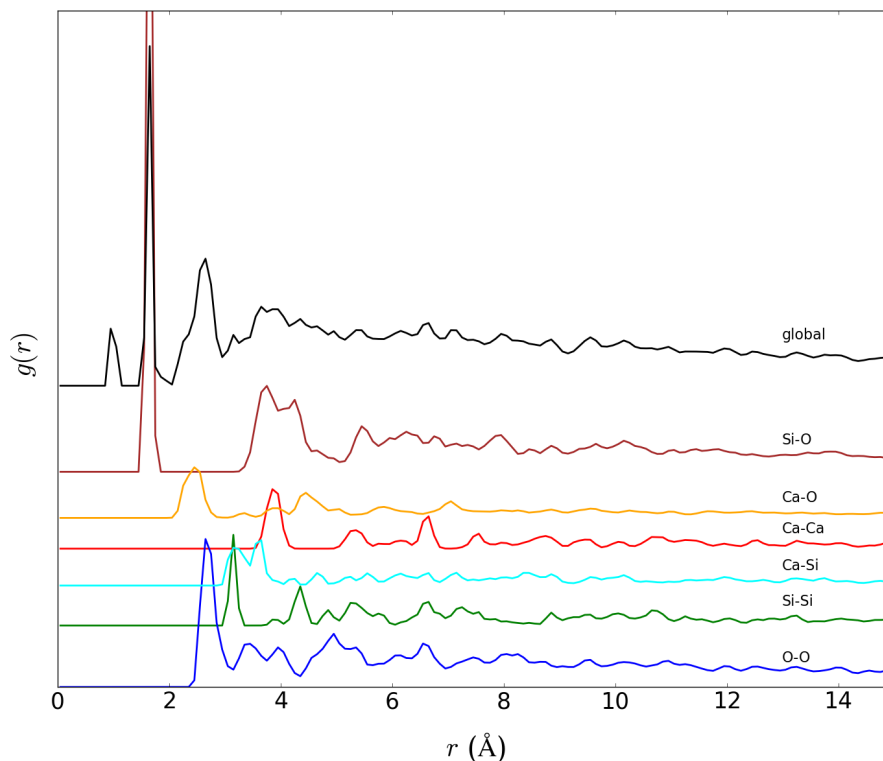


Figure 7.7: Radial distribution function of tobermorite 9 Å, ReaxFF. Simulation values calculated from equilibrated structure at 298 K and zero pressure.

7.4.3 Jennite

Jennite (J) is a naturally occurring mineral found in similar locals to tobermorite such as Crestmore and Fuka, Japan[12]. With a Ca/Si ratio of 1.5 it is much higher than that of the tobermorite counterpart. Belonging to the family of calcium silicate hydrates, the structure was previously thought to resemble high Ca/Si ratio C-S-H[28]. Similar to tobermorite, the silicate chains resemble wollastonite type chains with a basal spacing of approximately 10.45 Å which shrinks in the c -direction to 8.69 Å upon heating[12]. Again, similar to tobermorite, the wollastonite chains are of single form. The chemical formula is $\text{Ca}_9\text{Si}_6\text{O}_{18}(\text{OH})_6 \cdot 8\text{H}_2\text{O}$ with lattice parameters $a = 10.576$ Å $b = 7.265$ Å $c = 10.931$ Å $\alpha = 101.30^\circ$, $\beta = 96.98^\circ$ and $\gamma = 109.65^\circ$ and is a triclinic crystal with space group P1. The crystal structure of jennite is shown in Figure 7.8 and

the corresponding ReaxFF calculated RDF is found in Figure 7.9. Again, no experimentally determined RDF data was found in the literature for jennite.

Compared to tobermorite 14 Å, the Ca/Si ratio of jennite is much higher and this different Ca environment is reflected in the Ca-Ca RDF for jennite whereby more intense peaks are observed. The Ca-Ca peak at $r \approx 4.0$ Å is split into two peaks for jennite whereas in tobermorite 14 Å this is represented as one single peak. This peak splitting is directly related to the double Ca layer residing in the interlayer of the jennite structure whereas in tobermorite 14 Å, only a single layer exists, giving rise to only 1 Ca-Ca neighbour pair interaction peak.

Additionally, the Si-O environment is different between the jennite and tobermorite 14 Å crystal structures which is reflected in the difference in intensity between jennite and tobermorite 14 Å. A peak is observed in the Si-Si PDF at $r \approx 5.0$ Å for jennite which is not seen in T14.

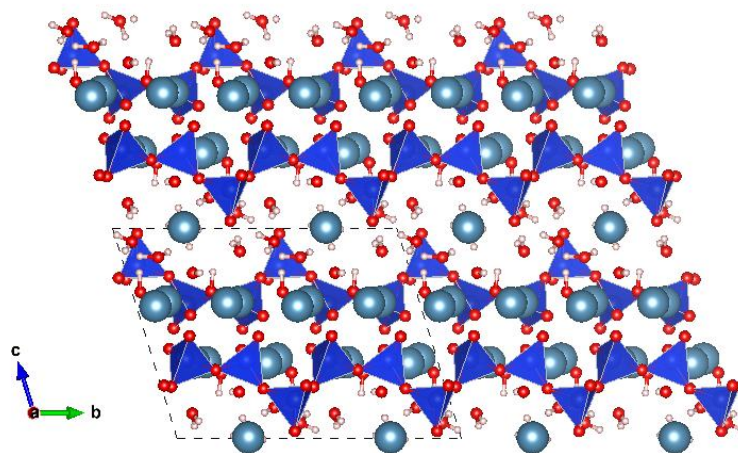


Figure 7.8: Crystal structure of jennite, Ca^{2+} (green spheres), SiO_4^- (blue tetrahedra), O^{2-} (red spheres), H^+ (white spheres). The unit cell is identified by dashed lines.

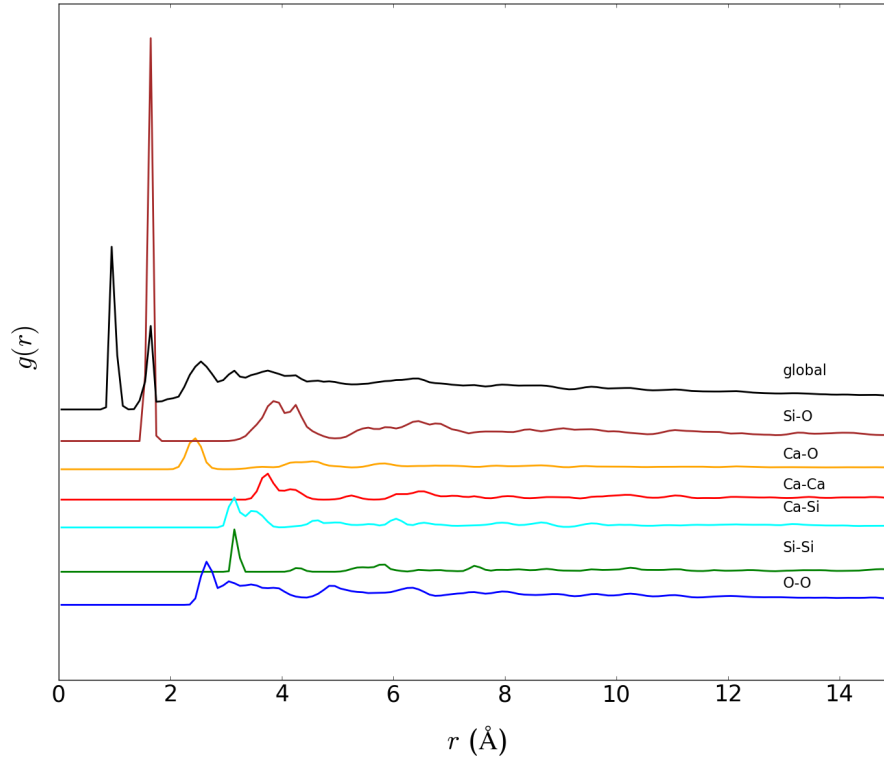


Figure 7.9: Radial distribution function of jennite, ReaxFF. Simulation values calculated from equilibrated structure at 298 K and zero pressure.

7.4.4 Rejmak Structures

The Rejmak C-S-H model structures are derived from tobermorite 14 Å and jennite and consist of pentameric and dimeric silicate chains[39]. These shortened chains come about by the removal of bridging tetrahedra as also seen in models by Pellenq, Manzano and Richardson[4, 14, 28]. Since a number of experimental C-S-H studies have shown that jennite phases are not present in cementitious calcium silicate hydrates, C-S-H models in this study have been restricted to tobermorite derived models. Pentameric and dimeric chains are produced by removing $\text{SiO}(\text{OH})^+$ and adding H^+ , Ca^{2+} or $\text{Ca}(\text{OH})^+$ to balance the residual charge. With regards to the Rejmak structures, the naming system is kept consistent with the original publication where T denotes tobermorite derived, 5 or 2 represents pentameric or dimeric silicate chains respectively and Ca or H rep-

resents the charge balance method. Choosing four C-S-H models (Figure 7.14, Figure 7.10, Figure 7.12, Figure 7.16) allows a number of comparisons to be made such as Ca/Si ratio, MCL and H₂O/Si ratio to be made. Mechanical properties are often thought to be linked to the number of defects in the silicate chain, often the result of a change in Ca/Si ratio. Rejmak's structures show that even with differing defects, the Ca/Si ratio is not always directly correlated due to the possibility of different charge balancing methods. Here, the effect of Ca/Si ratio and polymer chain length on the RDF is discussed and compared to experimentally derived RDFs of matching Ca/Si ratio.

For T5Ca1 (Figures 7.10 and 7.11), with a Ca/Si ratio of 1.1, no experimental PDF data was found for comparison. Comparing the T14 and T5Ca1 RDF data, no obvious differences exist in the peak shapes and locations suggesting that the removal of a bridging tetrahedron doesn't affect the interaction distances. Like previous structures, the first peak in the Si-O RDF represents Si-O bonding with a each individual tetrahedra. The peaks at $r \approx 4 \text{ \AA}$ represents the interaction between a Si on one tetrahedron and the oxygen atoms on the adjoining tetrahedra. The first peak on the Ca-O RDF corresponds to the Ca-O coordination in the interlayer. The Ca-Ca first peak is the intralayer and interlayer nearest neighbour Ca. The intense peak at around 6.8 \AA represents the diagonal near neighbour Ca ions in the intralayer. Although not evident from the RDF pattern, the removal of a bridging tetrahedron results in a slight lengthening of the distance between the now end chain Si tetrahedra (4.34 \AA becomes 4.43 \AA upon removal).

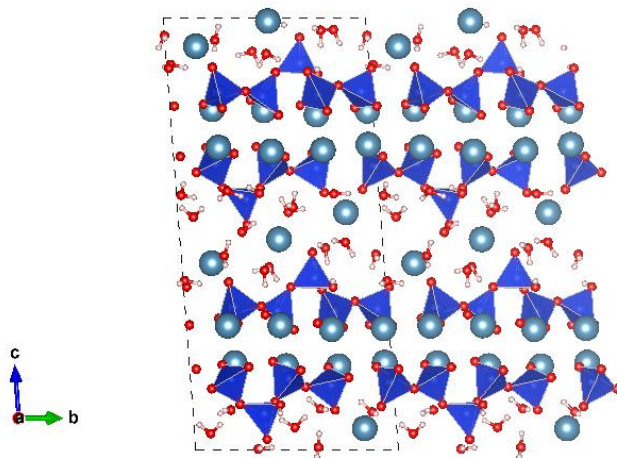


Figure 7.10: Crystal structure of T5-Ca1, Ca^{2+} (green spheres), SiO_4^- (blue tetrahedra), O^{2-} (red spheres), H^+ (white spheres). The unit cell is identified by dashed lines.

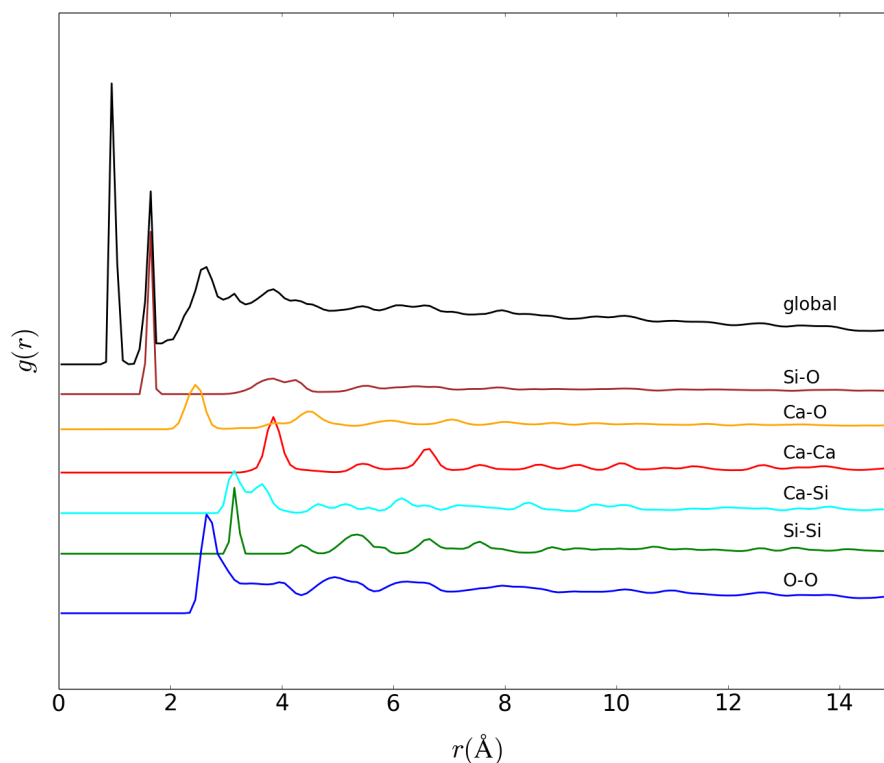


Figure 7.11: T5Ca1 radial distribution function, ReaxFF (solid lines). Simulation values calculated from equilibrated structure at 298 K and zero pressure.

Figures 7.12 and 7.13 display the crystal structure and RDF data for T5H1. The Ca/Si ratio is 1.0 and was compared with synthetic C-S-H with a C/S ratio of 1.04. The Si-O PDF matches very well with the ReaxFF predicted T5H1 RDF suggesting that the Si-O bond length of this model is consistent with synthetic C-S-H of a similar Ca/Si ratio. Similarly the first and second peak of the Ca-O RDF also compares very well with the experimentally calculated data for Ca/Si ratio 1.04. However, the Si-O peak at 1.6 \AA is much broader for experimental than as predicted by ReaxFF suggesting that in fact the experimental structure is more disordered than is predicted by simulation. This finding is important as, when considered alongside tobermorite 14 \AA and tobermorite 9 \AA , it is clear that ReaxFF fails to describe the disorder which has been discussed in experimental findings, backing up that the experimental C-S-H can be thought of as a disordered C-S-H as ReaxFF demonstrates that a more ordered structure, with

a more defined Si) peak suggests that the tetrahedra are more regular in simulation, proving that the Si-O bonds in the tetrahedra are less regular. Ca-Ca and Si-Si peaks appear in the experimental data, suggesting similar environments with the exception of relatively intense peak at $r \approx 5.2\text{\AA}$ which is not seen in the global RDF from the experimental data - in fact it seems that in the experimental data this peak is shifted to the right suggesting that the interlayer distance may be longer in experiment. Looking at the Si-Si RDF data, the first peak refers to the neighbour Si within the chains, this should be more intense for pentamers than dimers and this can be seen by comparing the Si-Si RDF from Figure 7.13 and 7.17. The next peak, $r \approx 5.4\text{\AA}$ corresponds to the break in the polymer chain i.e. from the end member Si of one pentamer and the first Si on the next pentamer. The next peak corresponds to the distance between Si1 and Si3 is a pentamer chain however this peak appears as a shoulder in the global RDF of the experimental data peak $r \approx 5.9\text{\AA}$ is suggesting that this distance is longer than in the simulated model. If this is the case, a larger angle would be expected between Si1 and Si3 than is seen in the T5H1 model however this experimental data is not available to compare. The next peak in the Si-Si $r \approx 6.9\text{\AA}$ corresponds to the bridging silica to bridging Si suggesting that the bridging Si environment matches that of experiment. Between 4 and 6 \AA , the for the pentameric structures a 3rd peak is observed in the Ca-Si chain. Again, it is not explicitly clear whether these peaks are observed in the experimental data due to lack of separation of the peaks which suggests there is more disorder in the silicate chains than is possible to simulate. Furthermore, the interlayer spacing is approx 12.9\AA and this is consistent with shorter chains and increasing Ca/Si from experiment[28].

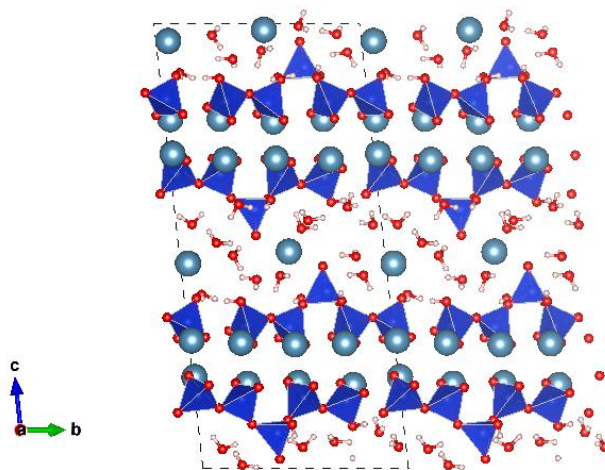


Figure 7.12: Crystal structure of T5-H1, Ca^{2+} (green spheres), SiO_4^- (blue tetrahedra), O^{2-} (red spheres), H^+ (white spheres). The unit cell is identified by dashed lines.

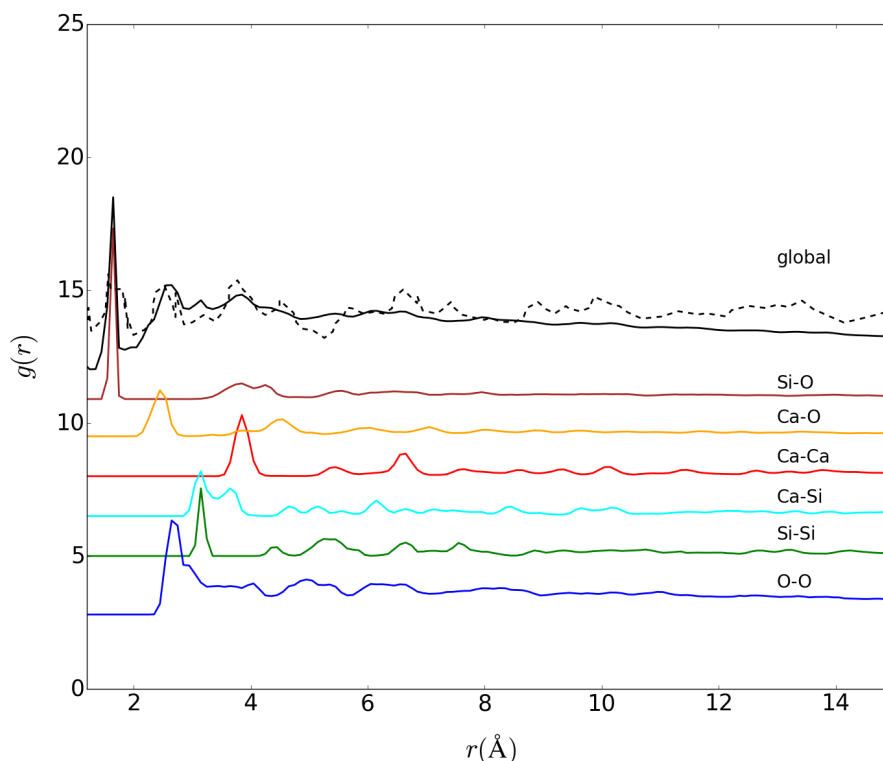


Figure 7.13: T5H1 radial distribution function, expt. (dashed lines), ReaxFF (solid lines). Simulation values calculated from equilibrated structure at 298 K and zero pressure.

The crystal structure and RDF data for the T2Ca1 structure is found in Figures 7.14 and 7.15. The global RDF matches reasonably well with the experimental data with a Ca/Si ratio of 1.47 (note that the Ca/Si ratio of T2Ca1 is 1.5 and is the highest Ca/Si ratio studied of the hypothetical C-S-H structures). Whilst there is a larger discrepancy with the global simulated and experimental RDF pattern, the individual simulated RDF peaks do seem to compare reasonably well with the global experimental RDF. Like seen with the T5H1 structure, the experimental global RDF, the Si-O peak is broader than is predicted with ReaxFF suggesting the silicate tetrahedra are more disordered in experiment. The overall RDF patterns however are less defined in T2Ca1 than in the T5Ca1, tobermorite 14 Å and tobermorite 9 Å models suggesting dimeric structures are less ordered which is due to the lack of rigidity holding the chains in place. The Ca-O peaks matches well to experiment suggesting that the Ca-O distances in

C-S-H must be around 2.7 Å which is slightly longer than is seen in the mC-S-H structures. The simulated Ca-Ca distance is approximately 0.2 Å longer than is seen in experiment indicated by the small shift to the right in the simulated RDF compared to the experimental global PDF. The first peak (at around 3 Å) in the simulated Ca-Si PDF is not seen in the experimental RDF, however there is evidence of a slight shoulder and this could suggest this Ca-Si environment is different in experiment from Rejmak's model however it is difficult to draw any conclusions from this. Similarly the first Si-Si peak at around 3.2 Å is not seen experimentally, again with the exception of a small shoulder, and this could be an indication that the Si-Si distance is much longer or that the experimental sample at 1.47 has a different silicate chain structure than Rejmak's T2Ca1 model.

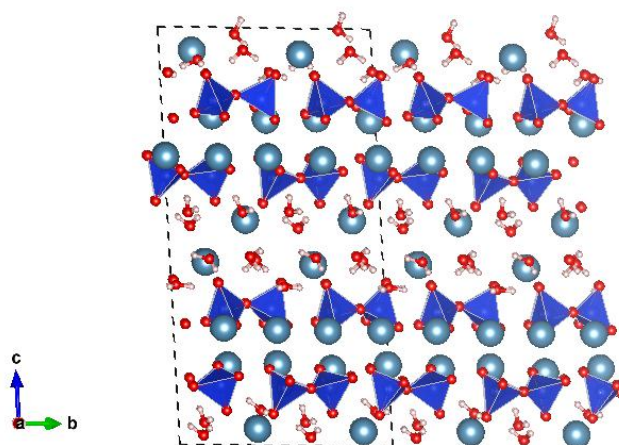


Figure 7.14: Crystal structure of T2-Ca1, Ca^{2+} (green spheres), SiO_4^- (blue tetrahedra), O^{2-} (red spheres), H^+ (white spheres)

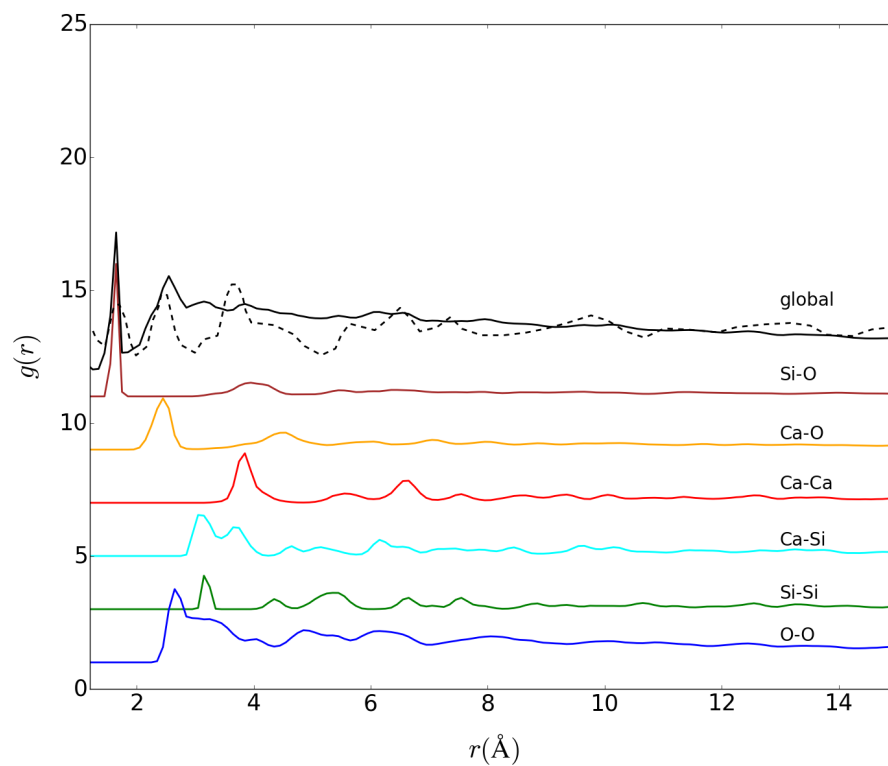


Figure 7.15: T2Ca1 radial distribution function, expt. (dashed lines), ReaxFF (solid lines). Simulation values calculated from equilibrated structure at 298 K and zero pressure.

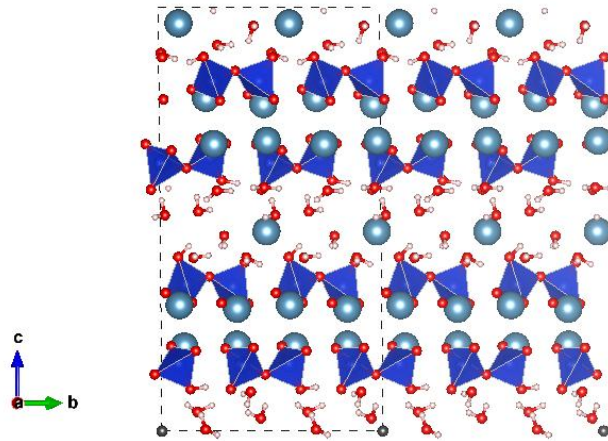


Figure 7.16: Crystal structure of T2-H1, Ca²⁺ (green spheres), SiO₄⁻ (blue tetrahedra), O²⁻ (red spheres), H⁺ (white spheres)

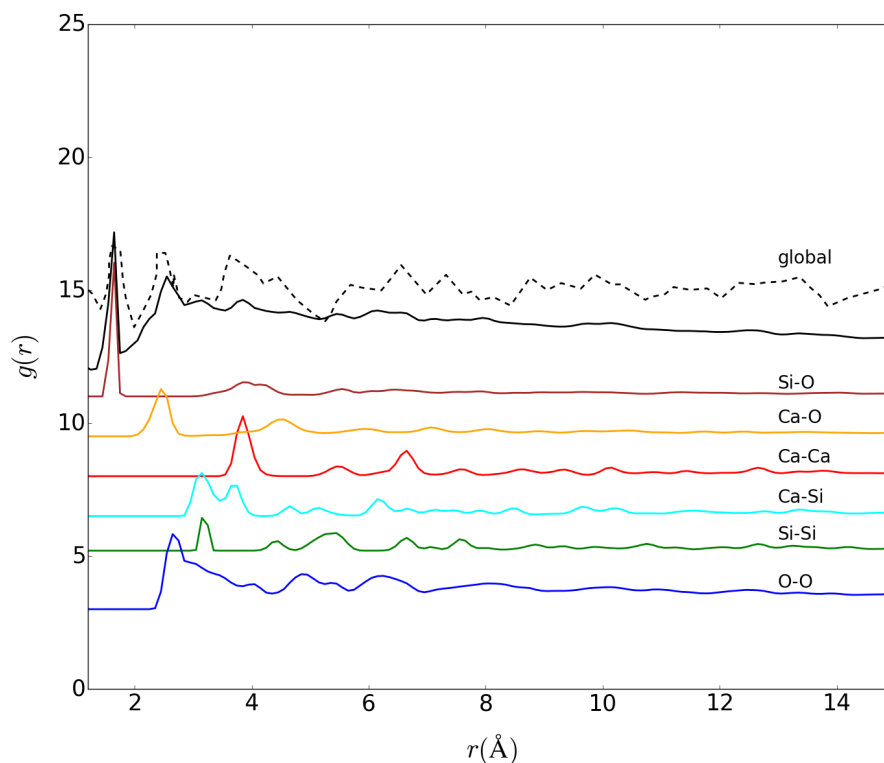


Figure 7.17: T2H1 radial distribution function, expt. (dashed lines), ReaxFF (solid lines). Simulation values calculated from equilibrated structure at 298 K and zero pressure.

The crystal structure and RDF data for the T2H1 structure is found in Figures 7.16 and 7.17. The global RDF matches reasonably well with the experimental data with a Ca/Si ratio of 1.22 (the Ca/Si ratio of T2H1 is 1.25). The experimental RDF compares well with the simulated ReaxFF prediction and the Si-O, Ca-O global experimental RDF. Again, as was seen in the T2Ca1 structure, the Ca-Si and the Si-Si environments seem to differ between the Rejmak structure and the experimental data suggesting that the silicate environment in reality may be different to the simulated model. Despite the apparent inability of ReaxFF to model the disorder in C-S-H, the models are clearly similar to experimental C-S-H.

7.5 Validating ReaxFF using tobermorite 14 Å and jennite

ReaxFF prediction of structural properties at 298 K and zero pressure were checked against experimental crystal XRD data. Unfortunately no bond data was available for the other mC-S-H and C-S-H structures in this study. Comparisons of tobermorite 14 Å and jennite ReaxFF predicted lattice parameters with XRD experimental and alternative potentials are found in Table 7.2.

Table 7.2: Lattice parameters for ReaxFF compared to experiment

Structure	Method	a (Å)	%Error	b(Å)	%Error	c(Å)	%Error	ref.
T14	XRD	6.69	—	7.39	—	27.99	—	[13]
T14	ReaxFF	6.65	0.6	7.51	1.62	28.22	0.82	—
T14	DFT-GGA	6.87	2.69	7.43	0.54	28.49	1.79	[52]
T14	Core-shell	6.94	3.74	7.35	0.54	28.35	1.29	[52]
T14	ClayFF	6.87	2.69	7.37	0.27	28.55	2.0	[52]
T14	CSHFF	6.70	0.15	7.41	0.27	28.70	2.54	[52]
T9	XRD	11.16	—	7.30	—	9.57	—	[30]
T9	ReaxFF	10.83	2.96	7.56	3.52	9.53	0.42	—
J	XRD	10.58	—	7.27	-	10.93	—	[12]
J	ReaxFF	10.22	0.03	7.49	3.0	11.18	2.23	—
J	DFT-GGA	10.70	1.13	7.34	0.9	10.89	0.37	[52]
β W	XRD	7.94	—	7.32	—	7.07	—	[180]
β W	ReaxFF	7.82	1.51	7.48	2.19	7.17	1.41	—

For tobermorite 14 Å ReaxFF predicts the lattice constants well overall. The a parameter as predicted by ReaxFF has an error of 0.6% compared to experiment, beaten only by CSHFF. Similarly ReaxFF performs well in predicting the c parameter and in this case, CSHFF performs the worst out of the potentials available. In the b direction however, ReaxFF has more deviation from the experimental lattice parameter than the other potentials however this is still within an acceptable value. In the case of jennite, ReaxFF displays a poorer performance compared to tobermorite but still within a satisfactory limit. Bond distance

results predicted by ReaxFF are shown in Table 7.3.

Table 7.3: Average Bond Distances for tobermorite 14 Å and jennite

Structure	Method	Si-O (Å)	Ca-O (Å)
T14	Expt.	1.63	2.43
T14	ReaxFF	1.63	2.46
J	Expt. [12]	1.64	2.42
J	ReaxFF	1.63	2.45

Average bond distances predicted by ReaxFF show very good reproducibility to experiment. The greatest error is in the Ca-O distance in jennite at 1.2% error when compared to the XRD data.

From simple comparisons of lattice constants and bond distances, it can be concluded that ReaxFF makes a reasonable prediction of the crystal structure for the calcium silicate hydrate mineral phases of tobermorite and jennite under the conditions tested.

7.5.1 Variation of Lattice Parameters with Temperature for (m)C-S-H

Calcium silicate hydrates are known to have interesting thermal properties where interlayer structure changes due to loss of interlayer water at around 80 °C. These thermal properties, in the case of tobermorite, allow the production of tobermorite 11 Å and tobermorite 9 Å by subsequent heating. MD simulations of the type studied within this thesis require a constant number of particles and therefore it is not possible to simulate the loss of water in this way. As a result, thermal studies have been restricted to a narrow range (273-323 K).

Temperature dependence on lattice parameters and density are found in Figures 7.18 and 7.19. It can be seen that over such narrow temperature ranges, mC-S-H and C-S-H shows almost no response in the lattice parameters to increasing temperature.

Similarly, the density remains relatively constant over the temperature range studied.

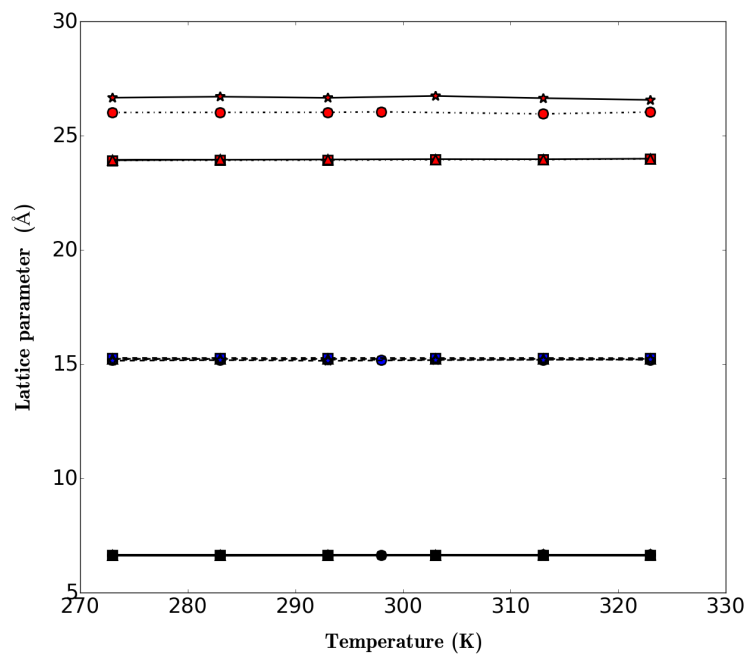


Figure 7.18: Dependence of lattice parameters on temperature at temperatures ranging from 273-323 K for C-S-H structures. T5Ca1 (circles), T2Ca1 (squares), T2H1 (triangles), T5H1 (stars), a (black), b (blue), c (red).

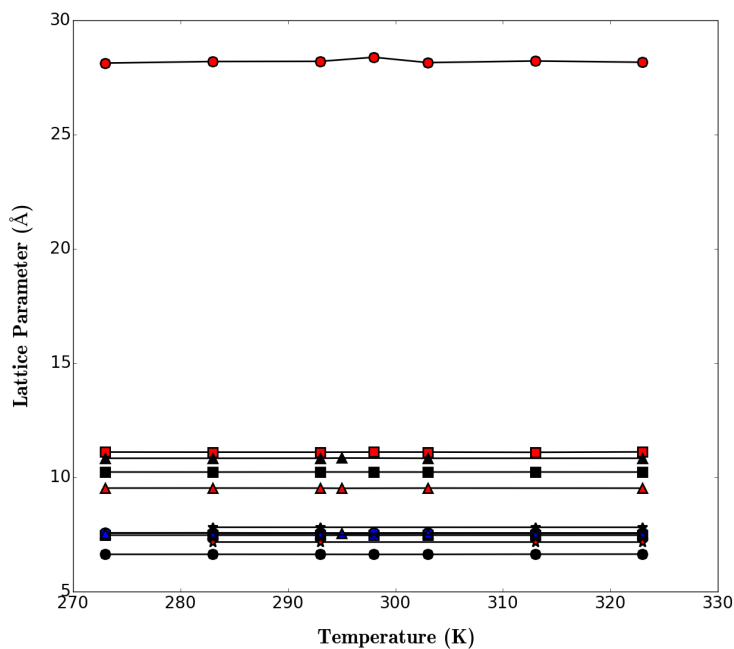


Figure 7.19: Dependence of lattice parameters on temperature at temperatures ranging from 273-323 K for mC-S-H structures. T14 (circles), T9 (triangles), J (squares), bW (stars), a (black), b (blue), c (red).

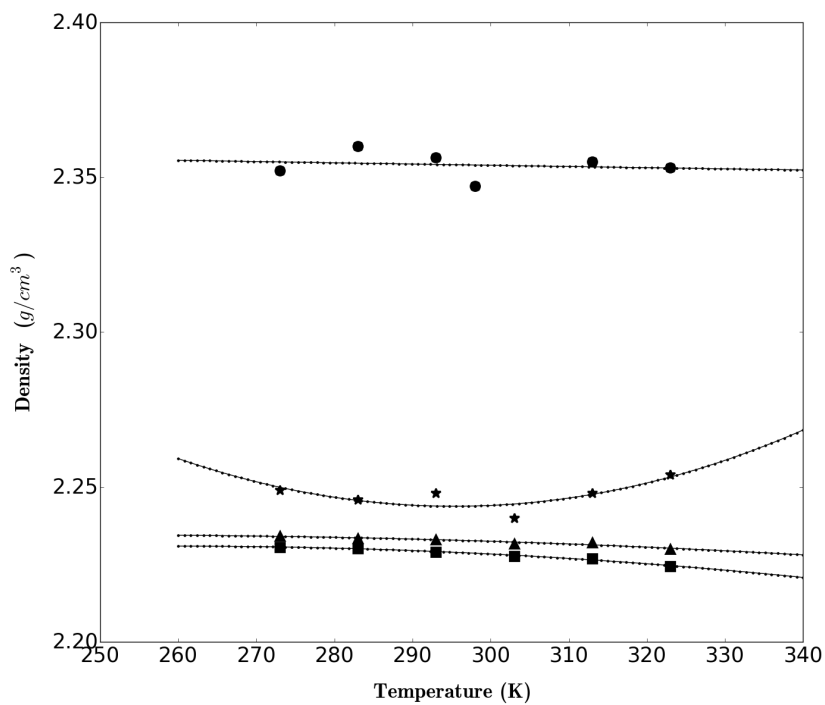


Figure 7.20: Dependence of density on temperature at temperatures ranging from 273-323 K for C-S-H structures. T5Ca1 (circles), T2Ca1 (squares), T2H1 (triangles), T5H1 (stars).

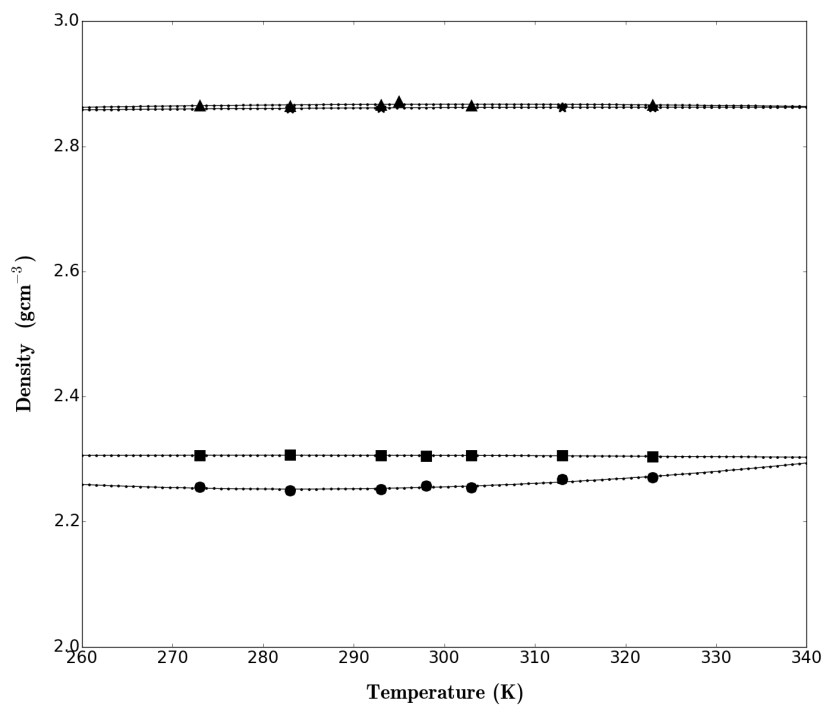


Figure 7.21: Dependence of density on temperature at temperatures ranging from 273-323 K for mC-S-H structures. T14 (circles), T9 (triangles), J (squares), bW (stars).

7.5.2 Heat Capacity

Heat capacity data for pure cement minerals and synthetic counterparts are lacking in the literature for both experimental work and simulated predictions. Qomi et al. made predictions using CSHFF for some common cement related materials such as Portlandite and for Pellenq's C-S-H model and further hypothetical structures derived from the model. It was demonstrated that hydrated C-S-H models in all cases had a higher C_p than the corresponding water free equivalent and that C_p increased with increasing Ca/Si ratio. A simulation study by Mutisya et al. has shown that constant volume C_V heat capacities increase from tobermorite 9 Å to tobermorite 14 Å which supports the finding that calcium silicate hydrates have larger heat capacities than their non-hydrated counterparts. Rodriguez et al (2017) observed a relationship between the change in C_p between the high temperature C-S-H configuration and β Wollastonite at the transformation temperature and Ca/Si ratio where higher Ca/Si ratios resulted on a lower change in the heat capacity before and after the transition. Here, C_p at 298 K is predicted by ReaxFF for mC-S-H and C-S-H models used within this study and are compared to experimental and simulated data in the literature where possible. The results are shown in Table 7.4.

Table 7.4: Heat capacities of mC-S-H and C-S-H at 298 K

Structure	Method	Ca/Si ratio	C_p (J/g/K)	Ref.
C-S-H	Expt	0.64	0.91	[185]
C-S-H	Expt	1.06	0.77	[185]
C-S-H	Expt	1.23	0.82	[185]
C-S-H	Expt	1.47	0.91	[185]
cement paste	Expt	NR	1.4-1.7	[186]
T14	CLAYFF	0.83	0.89	[187]
T14	ReaxFF	0.83	2.1	—
T9	CLAY	0.83	0.76	[187]
T9	ReaxFF	0.83	1.7	—
J	ReaxFF	1.5	1.77	—
bW	Expt	1.0	0.65	[188]
bW	ReaxFF	1.00	1.0	—
T5Ca1	ReaxFF	1.1	1.41	—
T5H1	ReaxFF	1.0	1.62	—
T2Ca1	ReaxFF	1.5	1.61	—
T2H1	ReaxFF	1.25	1.9	—

The ReaxFF predicted C_p tend to be much higher than predictions by CSHFF and CLAYFF however the unreliability in the experimental work means that reliable comparisons cannot be made. The ReaxFF results are more akin to cement paste C_p than experimental C-S-H data. Although it cannot be known for sure, the higher ReaxFF results may be due to the limited temperature range in which the simulations were carried out. Rodriguez et al., amongst other authors, had demonstrated through Differential Scanning Calorimetry and Thermogravimetric Analysis experiments that the weight loss occurs from loss of water from room temperature but dramatically increases above 323 K therefore the simulations were not carried out above this temperature. Additionally this helped with efficiency as the aim was to assess structure-property relationships and therefore it was in the interest of the research to cover as many structures as was feasible.

7.5.3 Thermal Expansion Coefficient

Thermal expansion coefficients measure at 298 K are shown in Table 7.5. As no thermal expansion is seen in the density and the lattice parameters at this temperature, it is unsurprising that the expansion parameters are very low. Furthermore, the noise associated with the short temperature range and this is reflected in the apparent fluctuation in the the thermal expansion coefficients. By simulating over a wider range of temperatures, the thermal expansion coefficients may improve.

Table 7.5: Thermal Expansion coefficients of mC-S-H and C-S-H at 298 K

Structure	$\alpha \times 10^{-5}$ ReaxFF
T14	-16.7
T9	-0.91
J	1.48
bW	-1.85
T5H1	-5.12
T2H1	3.54
T5Ca1	1.67
T2Ca1	4.64

7.6 Conclusions

In this chapter it has been demonstrated that ReaxFF reproduces with reasonable accuracy the crystal structure of the mC-S-H crystals studied at ambient temperatures and pressures and compares well to experimental XRD data. Predictions have been made for hypothetical C-S-H structures using ReaxFF at ambient pressure and a range of different temperatures. In addition, the use of ReaxFF has enabled comparison of predicted structures with experimental RDF values and has aided understanding of the structure and shown some similarities in the C-S-H structures of Rejmak, demonstrating the difficulty in identifying differences in structures from RDF data alone. It was shown that ReaxFF predicts higher heat capacities than is measured experimentally under the conditions tested however limited heat capacity data is available for comparison and the heat capacity is notoriously difficult to measure by experimentally. Thermal expansion coefficient

data confirms that the over the range of temperatures tested, (m)C-S-H lattice parameters show little movement. This chapter has demonstrated that ReaxFF shows promise for simulating calcium silicate hydrates and has shown sufficiency accuracy to be used to predict the mechanical properties using MD.

Chapter 8

Elastic Properties of Calcium Silicate Hydrates

8.1 Overview

In the previous chapter, the use of ReaxFF was validated for calcium silicate hydrates and the ability of ReaxFF to predict accurate crystal structure. Having confirmed that ReaxFF is capable of modelling (m)C-S-H, the focus is now on delivering insights into structure-property relationships. By determining the elastic properties of mC-S-H and C-S-H, it is possible to determine how the materials responds to an applied load. To improve the properties of cement, it is possible to study the elastic behaviour of (m)C-S-H and determine trends relating to the structure and composition of the material associated with reversible deformation. In this chapter, elastic constants are measured and compared with available experimental data before going on to predict the elastic constants of some hypothetical structures. Furthermore, the isothermal equation of state of each structure was modelled using the Birch-Murnaghan equation of state (BMEoS) to calculate the bulk modulus and the behaviour of each structure was studied. It was revealed that differences are found in the bulk modulus depending on whether the simulation method was zero temp elastic constants method or the BMEoS method. When compared to other elastic constants and moduli simulation results from

the literature, ReaxFF compares better with experiment than force fields such as CLAYFF and CSHFF. Of great significance, it is shown that there is vast spread in the data depending on the method and force field and method used, highlighting that further assessment and computations are required in this area before conclusive experimental predictions can be made. By review of the measured data, it is evident that C-S-H with high density, low water content and long polymeric chains give rise to materials with a greater bulk and shear modulus and greater resistance to applied loads.

8.2 Introduction

The elastic properties of a material can give an indication of how the material behaves when under stress[65]. This is extremely important for performance materials and construction materials as an understanding of their response to load can influence their application[189, 190]. While the compressive and elastic properties of macroscale cement and concrete structures is an area which is well studied, the mechanical properties at the molecular scale is much less understood.

In Chapter 2 it was discussed how the mechanical properties of cement material stem from C-S-H at the nanoscale and thus one possible way of improving mechanical properties is by focusing on the material composition and structure. One of the simplest ways to investigate mechanical properties with molecular simulations is by modelling the elastic tensor of the material. Elastic properties of minerals are often calculated experimentally through direct measurement by techniques such as ultrasonic time measurements, interferometry impulsively stimulated laser scattering and Brillouin scattering[65].

For mC-S-H and C-S-H phases, experimental determination of the full elastic tensor has not been carried out, most likely as a result of the nanocrystalline nature of the materials. Instead, some experimental elastic moduli have been determined from alternative methods such as nanoindentation and high pressure XRD experiments.[15, 51, 191, 192]. Nanoindentation involves using an indenter to load and unload a sample where the gradient of the unloading curve corresponds to the elastic modulus of the material or grain in question. High pressure

XRD experiments involve placing single crystals in a diamond anvil cell, applying a pressure and measuring the relative strain. Nanoindentation techniques have measured the elastic modulus of pure C-S-H to be around 40 GPa[43] Other studies, however, other deviate from this and have been reported to be 57 GPa and 60 GPa[Pellenq'van'damme'2004, 45]. This variation makes comparison of simulations to experimental data difficult, highlighting the need for sufficient validation of the method to a well studied material such as ice Ih. In addition, nanoindentation does not explicitly describe the Young's Modulus (relation of tensile stress to tensile strain) or the bulk modulus (relation of volumetric stress to volumetric strain) therefore absolute comparisons cannot be made.

Many computational simulation studies have focused on the elastic properties of mineral analogues (mC-S-H) such as tobermorite and jennite, however, a growing number of studies have used a variety of hypothetical C-S-H models to predict the elastic properties of cementitious C-S-H[4, 5, 14, 52, 193]. Manzano et al. calculated the elastic constants of tobermorite, jennite and a number of tobermorite and jennite derived C-S-H models using MD[4, 194]. Similarly, using a combination of DFT and MD, Shahsavari et al. calculated the elastic tensor and corresponding elastic moduli of tobermorite structures producing comparable results to Manzano's simulation data[5, 52, 193]. Despite the progress in simulation of elastic properties of both mC-S-H and C-S-H, there is still a disagreement in the value of the bulk modulus. The spread in tobermorite 14 \AA bulk modulus is shown in Figure 8.1 and is in the range of 32-180 GPa and shows that, in many of the reported cases, there is still disagreement in the data. This has highlighted a real need for a better understanding in how these simulations are run between different methods and how the parameters are set up.

Additionally, errors in this type of simulation data are rarely reported making comparison and analysis difficult. Here, to add to the growing number of elastic simulations and to gain some insight into the possible differences in the methods, we use ReaxFF to calculate the elastic tensor and elastic moduli predictions. The aim is to critically assess ReaxFF elastic predictions and where possible, determine trends based on physical data that can indicate which structure and composition is most desirable and can lead to a suggested structure for target synthesis.

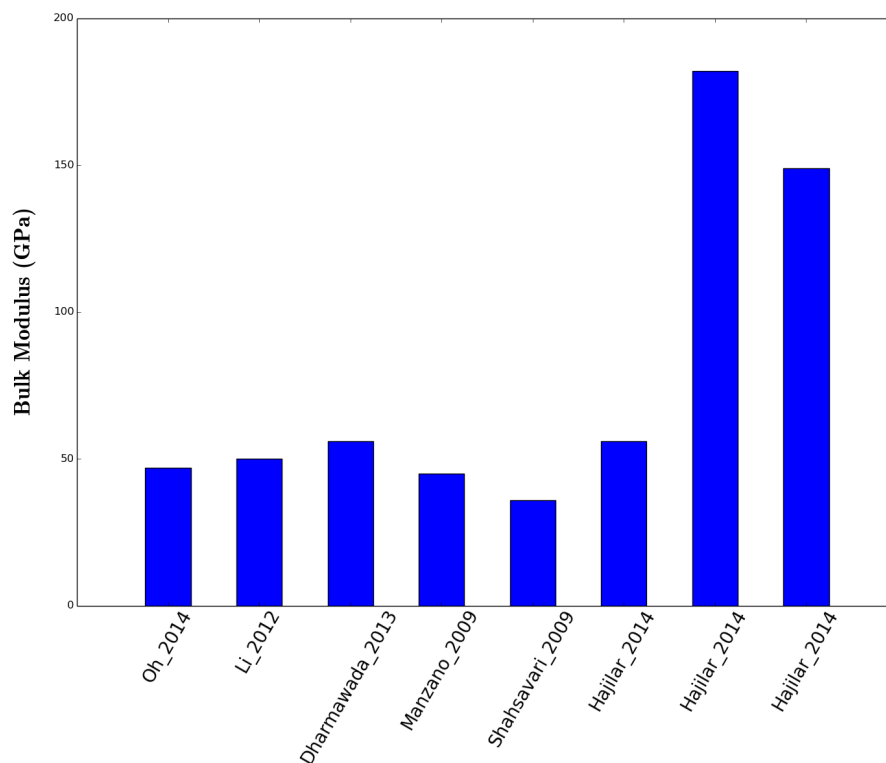


Figure 8.1: Simulated values of bulk modulus for tobermorite 14 Å from the recent literature compared to high pressure XRD experimental value (Oh₂014)[192]

8.3 Simulation Details

The LAMMPS molecular dynamics code was used to carry out all of the molecular simulations in this chapter. Structures were built from the corresponding crystallographic information as described in Chapter 7. Structures were equilibrated in the NpT ensemble using the Nose-Hoover barostat and thermostat with a time step of 0.2 fs with ReaxFF at the temperature and pressure of interest for up to 1 ns until the structure had reached equilibrium.

To calculate the elastic constants, 10 structures were sampled from the equilibrated trajectory and these equilibrated coordinates were used for a zero temperature elastic constant calculation. Elastic constants are calculated by applying a strain in each direction with energy minimization between each deformation as

described in Chapter 4. The elastic constants are then calculated from the corresponding stress/strain tensor. It is widely accepted that finite temperature elastic constants do not give a greater worth compared to zero temperature due to the increased difficulty and much larger expense in calculating them[195]. Therefore simulation results of elastic constants in the literature are most commonly from zero temperature calculations. As ReaxFF is already a computationally intensive force field this, combined with the expense of the finite temperature calculation, made it impossible to calculate finite temperature elastic constants with the available computational resources. Bulk modulus K , shear modulus G and Young's modulus E were calculated from zero temperature elastic constants using Voigt-Reuss-Hill averaging of elastic constants as described in Chapter 4[137].

For equation of state calculations, equilibrium simulations in the NpT ensemble were carried out at the desired temperature and pressure. Resulting equilibrated volumes were plotted against pressure and fitted to a 3rd order BMEoS (Equation 8.1). The model of the calculated ReaxFF employed the Scipy python library and EoSFit7.

$$p(V) = \frac{3K}{2} \left[\left(\frac{V_0}{V} \right)^{1/3} - \left(\frac{V_0}{V} \right)^{2/3} \right] \left\{ 1 + \frac{3}{4}(K' - 4) \left[\left(\frac{V_0}{V} \right)^{2/3} - 1 \right] \right\} \quad (8.1)$$

where V is the volume resulting from compression, V_0 is the original volume, p is the pressure and K is the bulk modulus and K' is the derivative of the bulk modulus.

8.4 Results and Discussion

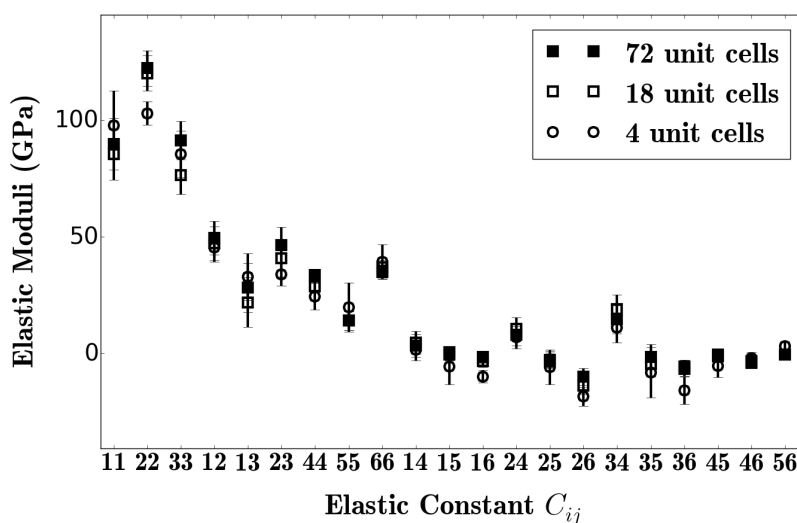
The results of the simulations are presented in the following sections. Firstly the confirmation of appropriate system size is shown followed by simulated elastic constants for the calcium silicate hydrates studied within this thesis. Thereafter the structure-property relationships and equation of state are discussed.

8.4.1 System Size Effects in the Elasticity Calculation

Prior to the parametric study of elasticity in calcium silicate hydrates the size effect of the elastic constants and bulk modulus of tobermorite 14 Å was checked. Due to the number of structures and parameters required to give an overview of material properties and the computational expense of ReaxFF, it is in the interest of this work to run systems of the smallest possible size to ensure timely data acquisition. The size of published data varies from only a few hundred atoms to several thousand atoms[62, 67]. Figure 6.1 displays ReaxFF predictions of the elastic tensor of tobermorite 14 Å at different system sizes. Comparison of the elastic tensor at 4, 18 and 72 replications of the crystal unit cell shows that the system size has a very minimal effect of the prediction of the elastic properties. Systems with 18 and 72 unit cell replications are very comparable within the error limit of each other. The smallest system checked with 4 replicates shows a difference out-with the error limit for the C_{22} only. Table 8.1 contains the calculated elastic moduli for the different system sizes under study. For K , G and E , the 72 unit cell system predicted higher values than the 4 and 18 unit cell system sizes. However, since there is no overall increasing trend with of moduli with system size and that the elastic constants are within statistical error, it is deemed that the size effect is negligible. As a result, the 18 unit cell system size is chosen for future calculations. For other mC-S-H structures, a comparable system size to the 18 unit cell was used. For C-S-H models however, a larger system size was used (approximately 4000 atom simulations) to account for the shortened polymeric chains.

Table 8.1: Comparison of Voigt-Reuss-Hill averaged elastic moduli for tobermorite 14 Å at different system sizes

No. of Unit Cells	Number of Atoms	K (GPa)	G (GPa)	E (GPa)
4	416	52.2 ± 4.7	32.0 ± 9.7	91.8 ± 17
18	1872	49.8 ± 6.0	35.7 ± 8.2	86.3 ± 16.9
72	7488	58.3 ± 3.1	38.2 ± 9.7	94.0 ± 14

Figure 8.2: Elastic constants (C_{ij}) for tobermorite 14 Å at different system sizes

8.4.2 Comparing ReaxFF predicted elastic properties of tobermorite and jennite to Available Data

To further validate ReaxFF, the elastic constants and Voigt-Reuss-Hill averaged moduli were compared to the literature values from experiment and simulations. However, since the full elastic tensor has not been carried out experimentally, most likely due to poor crystallinity, this study is limited to comparing ReaxFF

Table 8.2: Comparison of ReaxFF Voigt-Reuss-Hill Bulk Modulus K , Shear Modulus G and Young’s Modulus E

Structure	Method	K (GPa)	G (GPa)	E (GPa)	Ref.
T14	exp	47	—	—	[192]
T14	ReaxFF	49.8	35.7	86.4	—
T14	DFT-GGA	35.9	20.6	51.87	[52]
T14	ClayFF	35.6	18.5	48.07	[52]
T14	CSH-FF	42.4	19.2	50.0	[52]
J	exp	64	—	—	[51]
J	ReaxFF	62.6	37.1	93.0	—
J	DFT-GGA	31.8	22.0	53.6	[52]

with other simulation results in the literature. This makes validation of the elasticity data difficult as it relies upon accurate predictions of other simulation studies. The elastic constants of tobermorite 14 Å and jennite have been calculated in the literature by force field and quantum mechanical methods[5, 52]. To compare results, structures are equilibrated at 298 K and zero pressure in NpT ensemble to ensure full relaxation of the cell before carrying out zero temperature elastic constants calculation. Results are shown in Figure 8.3. In both cases, the elastic constants as predicted by ReaxFF are comparable to the other methods however some differences appear in the earlier elastic constants as ReaxFF overpredicts these individual moduli. A possible reason for these differences could be caused by the level of disorder in the structure predicted by each of the force fields, however without RDF patterns of structures by the other force field this cannot be compared. In the case of this work, a structure which has been equilibrated at temperature has been used – this was not clear for the other literature data. In addition, no statistical errors were reported was found in the other studies therefore difference in error margins could also cause slight differences when compared with the calculated results herein.

From the elastic constants calculated in Figure 8.3, the Voigt-Reuss-Hill averaged bulk modulus K , shear modulus G and Young’s modulus E) were calculated for the ReaxFF predictions and compared to available literature studies. The results are found in Table 8.2.

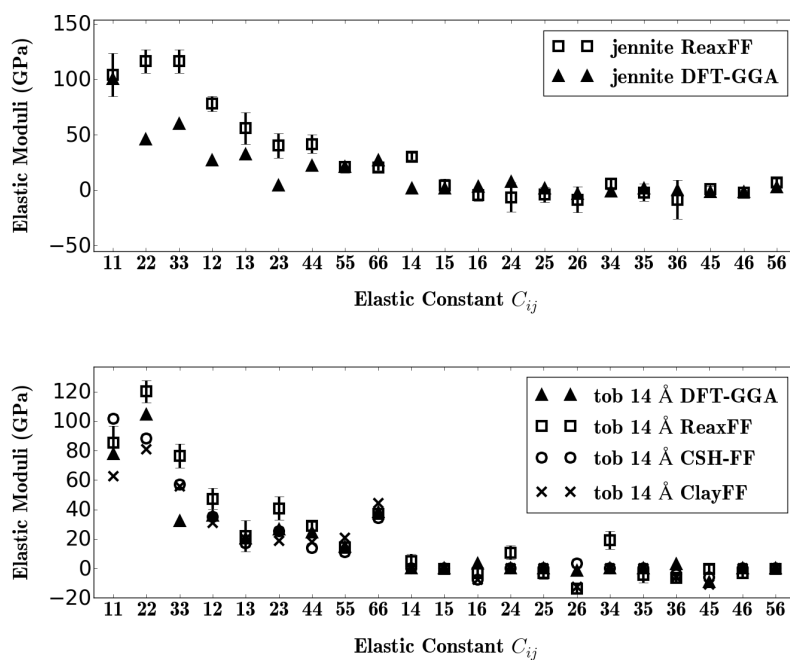


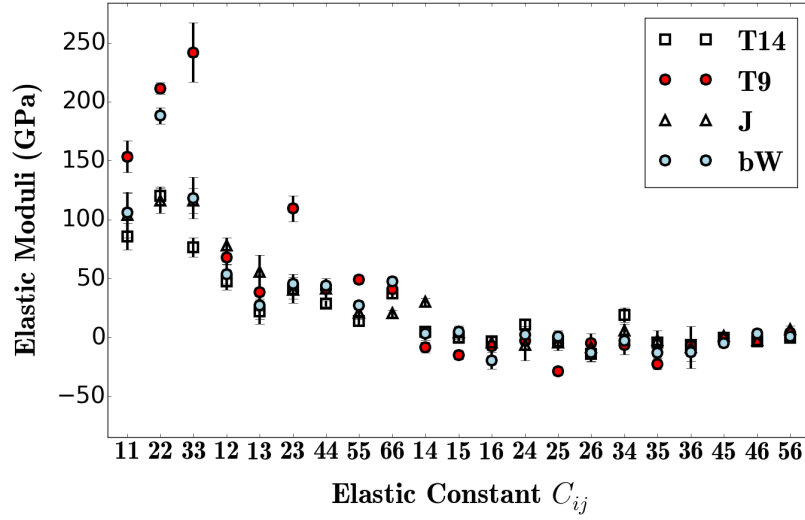
Figure 8.3: Elastic constants (C_{ij}) for tobermorite and jennite as predicted by ReaxFF compared to other simulation studies. CSHFF, CLAYFF and DFT-GGA data taken from Ref. [52]. Note that error bars were not provided for the literature data.

For both tobermorite 14 Å and jennite, ReaxFF predicts higher values than the other methods for K . When compared to experimental high pressure XRD BMEoS values, it can be seen that ReaxFF predicts closer to experimental values than the other methods. This validates our zero temperature method and validates the use of ReaxFF for predicting compressive elastic properties of mineral calcium silicate hydrates. With regards to G and E , ReaxFF predicts a higher modulus than other force field methods however it is not possible to comment upon the validity of these values due to lack of experimental data. Without experimental evidence it is not possible to conclude if ReaxFF predicts better E and G values than the other force field based methods.

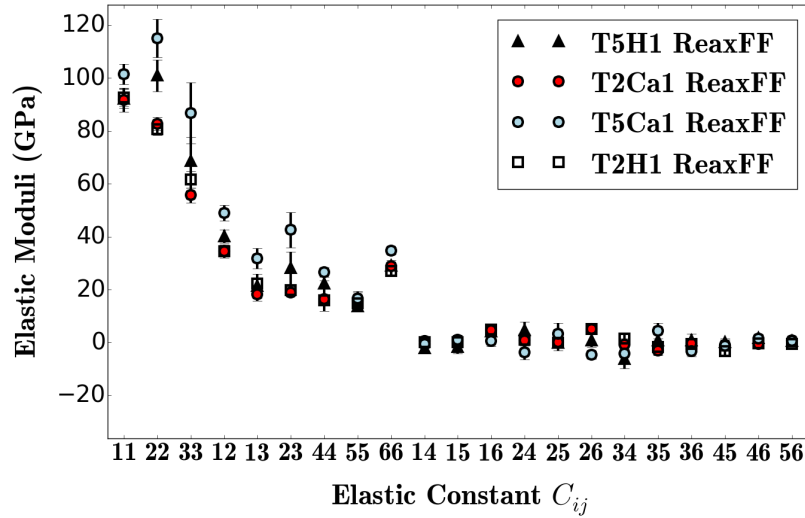
8.4.3 Predicted Elastic Constants of Mineral Calcium Silicate Hydrates

ReaxFF has been used to predict the elastic properties of mC-S-H. These values can be used as predictions and can be compared to experimental data once available. Figure 8.4 displays the mC-S-H results as predicted by ReaxFF. For the first 6 C_{ij} values, β wollastonite and tobermorite 9 Å have greater values. In the case of β wollastonite and tobermorite 9Å the structures are completely water free indicating that the presence of water reduces the elasticity.

Table 8.3 displays the measured Voigt-Reuss-Hill averaged elastic moduli for mC-S-H structures. The trend is similar to that seen with the C_{ij} elastic moduli in that the mC-S-H structures with lower water content have larger K , G and E values. mC-S-H with larger basal spacing such as tobermorite 14 Å and jennite have a smaller bulk modulus and therefore a lower ability to resist compression. Hydrated interlayer spacing allows rearrangement of the water molecules under compression allowing a reduction in the basal spacing. Minerals with the highest water content show lower shear modulus which is unsurprising as the weak interlayer hydrogen bonding will create a slip effect. These findings indicate that for mC-S-H structures, higher resistance to deformation occurs with low water contents and small basal spacings.

Figure 8.4: Elastic constants (C_{ij}) for mCSH structuresTable 8.3: Voigt-Reuss-Hill Bulk modulus K , Shear modulus G and Young's modulus E averages for mC-S-H structures Structure

Structure	Method	K (GPa)	G (GPa)	E (GPa)
T14	ReaxFF	49.8 ± 6.0	35.7 ± 8.2	86.3 ± 16.9
T9	ReaxFF	105.6 ± 9.6	74.1 ± 21.9	180.2 ± 37.3
J	ReaxFF	62.61 ± 1.4	37.12 ± 10.9	92.99 ± 9.3
bW	ReaxFF	57.64 ± 6.1	57.23 ± 14.5	133.92 ± 24.6

Figure 8.5: Elastic constants (C_{ij}) for C-S-H

8.4.4 Predicted Elastic Constants for Hypothetical Calcium Silicate Hydrates

Analysis of hypothetical C-S-H models, combined with the results of mC-S-H. C-S-H can give an overall prediction of how synthetic C-S-H products behave under finite strains. By this process, it is possible identify trends in chemical composition and material properties to understand the origin of strength in C-S-H based on suggested models. Elastic properties of hypothetical C-S-H models from Rejmak et al. are found in Figure 8.5 and Table 8.4.

It is clear that C-S-H structures with dimeric C-S-H chains have lower K , G and E values, most likely due to the lower rigidity in the silicate chain structure. In addition, the charge balance method appears to have an effect on the values of the elastic moduli. When comparing charge balance methods, the structures with additional calcium ions for charge balancing have higher values of elastic moduli when a pentameric chain is used but seems to have little effect in the dimeric

Table 8.4: Voigt-Reuss-Hill Bulk Modulus K , Young's Modulus E and Shear Modulus G and Young's Modulus E averages for C-S-H

Structure	K (GPa)	G (GPa)	E (GPa)
T5Ca1	59.6 ± 1.5	38.6 ± 11.0	95.2 ± 9.4
T5H1	47.1 ± 1.9	34.7 ± 10.3	63.5 ± 11.0
T2Ca1	39.7 ± 1.7	32.1 ± 9.4	76.0 ± 10.0
T2H1	41.8 ± 1.3	31.5 ± 9.4	75.6 ± 8.1

Table 8.5: Nanoindentation Hardness H and Modulus M data of synthetic C-S-H

Ca/Si	M	H (GPa)	Ref
<1	20	0.8	[46]
>1	31	0.9	[46]

structures.

8.4.5 Overall Analysis of Mechanical Properties for mC-S-H and C-S-H

The elastic properties depend on both the composition of each mineral and on the crystal structure. As such, relating elasticity of calcium silicate hydrate minerals to their chemical and physical structure is complex. Nonetheless, observing general trends and identifying structure-property relationships is achievable within the limits of MD. As discussed earlier, experimental data is severely lacking in this area, especially for the mechanical properties of mC-S-H and C-S-H due to the poorly crystalline nature. Experimental studies have focused instead on the hardness H and indentation modulus M which is more achievable with powder-like crystals[46].

Acker et al. showed that the hardness and indentation modulus of C-S-H was greater for C-S-H with Ca/Si ratio greater than 1 which indicates a relation of the structure and composition to mechanical properties as shown in Table 8.5[46].

Similarly, Geng et al. has calculated bulk moduli of synthetic C-S-H samples using

Table 8.6: Variation of K with Ca/Si ratio for C-S-H in High Pressure XRD experiments

Ca/Si	K (GPa)	Ref.
0.8	58.3	[191]
1.0	69.4	[191]
1.3	77.4	[191]

high pressure XRD in a diamond anvil cell and subsequent fitting of pressure-volume data to the BMEoS. The results are displayed in Table 8.6.

The work of Geng et al. (see Figure 8.6) shows that K increases with increasing Ca/Si ratio[191]. This finding was in agreement with a simulation study by Dharmawardhana et al., however, it was in contrast to simulation work by Qomi et al. where K decreases with increasing Ca/Si ratio. Other work by Manzano et al. and Shahsavari et al. show no overwhelming trend of bulk modulus with Ca/Si ratio. While the structures of the tested C-S-H models are developed through similar process from the same starting material, it is unsurprising that a trend exists. Figure 8.6 compares ReaxFF predictions to other literature studies of K to Ca/Si ratio. It is clear that from all of the C-S-H models proposed and different calculation methods, be that experimental or simulation, there is no agreeing trend linking Ca/Si ratio to K except in isolated cases. This is most likely due to differences in structure, force field and experimental conditions.

Based upon the total bond order density (TBOD) as a description of crystal cohesion in calcium silicate hydrate classification proposed by Dharmawardhana et al. A general trend exists with TBOD and Ca/Si where TBOD decreases with increasing Ca/Si ratio. Although no link between TBOD and mechanical properties was quantified by Dharmawardhana et al., ReaxFF was used to test the hypothesis. Based on already quantified TBOD of tobermorite 14 Å, β wollastonite, jennite and tobermorite 9 Å any effect of TBOD on K , G and Y was checked. The results are shown in Figure 8.6. Note that mC-S-H compared here belong to the medium and high TBOD categories in the paper. It may also be noted that cement gel has an average Ca/Si ratio of 1.7 and therefore is expected to be in the medium TBOD category.

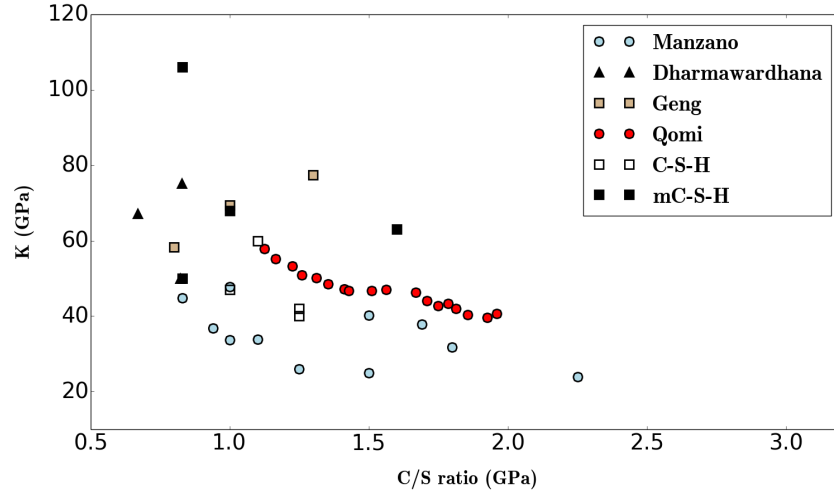


Figure 8.6: Variation of K with Ca/Si ratio

Interestingly, as TBOD increases for the tobermorite-like species with TBOD less than $0.235 \text{ e}/\text{\AA}^3$, an increase in elastic moduli is observed. This proves that, for species of similar silicate chain structure, the internal bonding structure has a small effect on the mechanical properties of the structure of interest.

By adopting a grouped strategy, similar to the TBOD method, and rather than purely taking into account individual properties such as Ca/Si ratio, combinations of structural and physical properties and their effect on elastic properties are now assessed. Figure 8.8 shows a clear relation of K , E and G for mC-S-H and C-S-H structures in that those with high K are more likely to have high E and G . When considered alongside Table 8.7, it can be seen that the highest elastic properties are achieved by a combination of low Ca/Si ratio, high density, and longer silicate chains. Jennite, with a subtly different silicate chain structure than the other minerals studied, is an exception to this trend. It can be concluded that for calcium silicate hydrates, physical properties such as $\text{H}_2\text{O/Si}$ ratio, Ca/Si ratio and MCL can give an indication of elastic behaviour. From this it can be inferred that for pure synthetic C-S-H it is likely of a low Ca/Si ratio with high density and low water content will produce an increase in bulk and shear modulus.

Figure 8.9 shows variation in moduli against measurable physical properties. Generally speaking, as mean silicate chain length increases, the values of K , G and E increase. This effect is most likely due to rigidity of the silicate chains and the fact

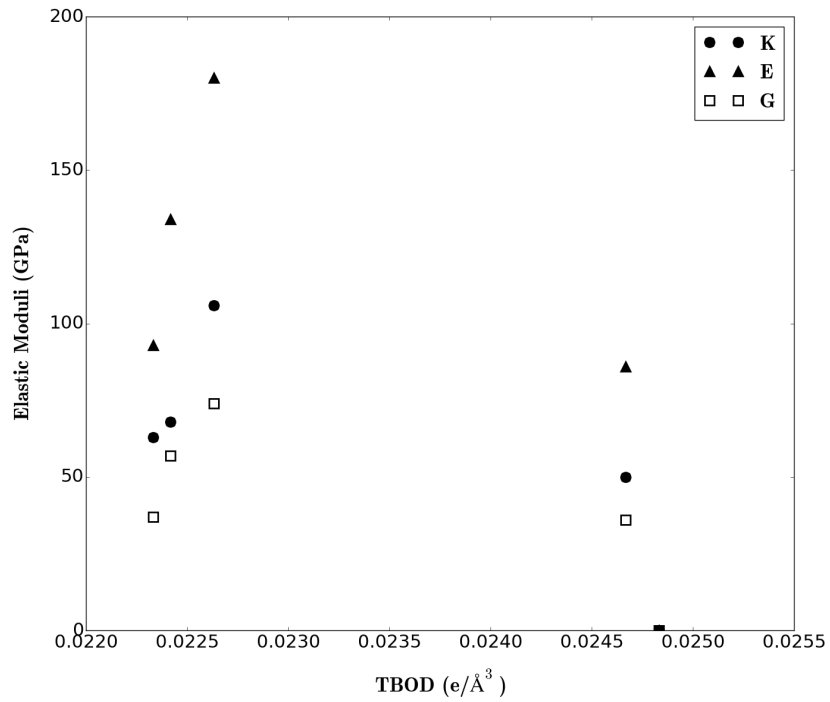


Figure 8.7: Variation of Elastic Moduli with TBOD ratio

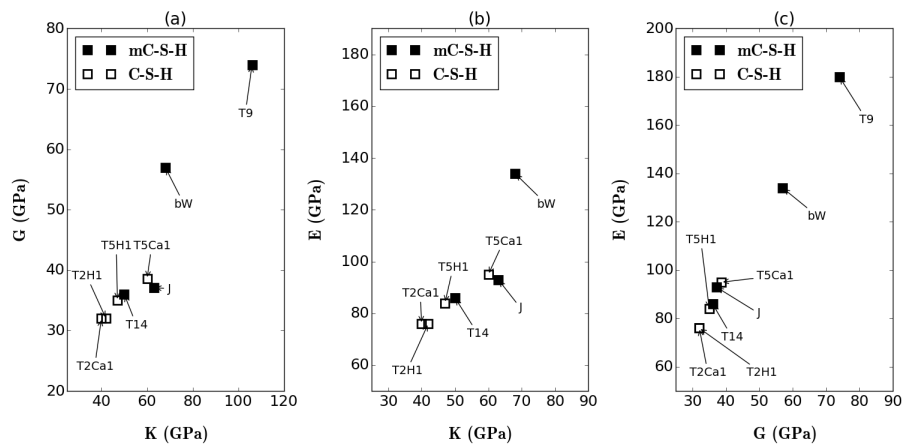


Figure 8.8: Variation of elastic moduli K , G and E for mC-S-H and C-S-H using ReaxFF

Table 8.7: Measurable Physical Properties of mC-S-H and C-S-H by simulation

Structure	Ca/Si ratio	Density (gcm^{-3})	H ₂ O/Si ratio	MCL
T9	0.83	2.87	0	inf
bW	1.0	2.87	0	inf
T5Ca1	1.1	2.34	1.4	5
J	1.6	2.31	1.33	inf
T14	0.83	2.26	1.16	inf
T5H1	1.0	2.25	1.0	5
T2H1	1.25	2.23	1.75	2
T2Ca1	1.5	2.25	1.75	2

that they are less likely to deform under compression or tension. No overall trend is seen throughout all calcium silicate hydrates tested. With regards to H₂O/Si ratio, a water free structure leads to much greater mechanical properties. As the water content increases, there is a slight rise in mechanical properties however at a H₂O/Si ratio of 1.75 there is a drop in the elastic moduli. Lastly, an increase in density results in an increase in mechanical properties with increasing density.

8.4.6 Isothermal Equation of State of Calcium Silicate Hydrates

The behaviour of building materials under pressure is important to understand deformation mechanisms and ultimately understand how they behave under load as this is their intended use. It is possible to do this experimentally via XRD experiments by introducing pressure into the system at constant temperature and monitoring the response of the unit cell volume. By determination of the equation of state, the bulk modulus can be calculated. Moreover, simulations can be used to determine equation of state to compare with experiment, or as a simple prediction in place of experimental determination. Simulations can also give an insight into atomic deformation mechanisms.

The BMEoS, as described earlier, is often used to describe the response of minerals with pressure at constant temperature, or depth, in the case of deep earth minerals[196]. It is intuitive to assume that density increases with increasing pressure,

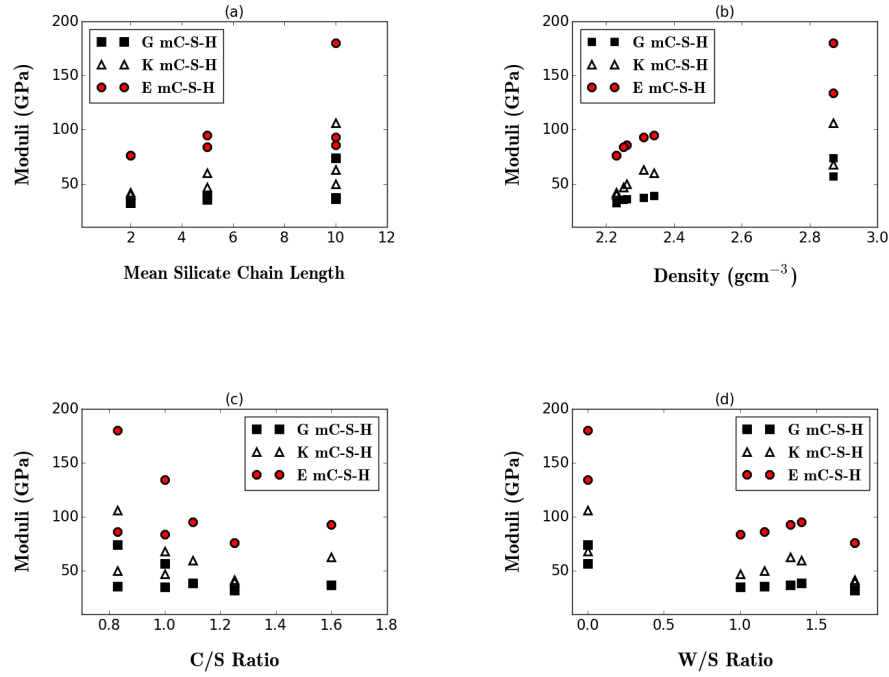


Figure 8.9: Variation of elastic moduli with measurable physical properties using ReaxFF

Table 8.8: Voigt-Reuss-Hill Bulk Modulus K and Shear Modulus G for C-S-H and mC-S-H structures

Structure	Method	K (GPa)	G (GPa)	Ref (Ref.)
T14	ReaxFF	49.8	35.7	—
T14	DFT-GGA	35.9	20.6	[52]
T14	exp	47	[192]	
T14	ClayFF	35.6	18.5	[52]
T14	CSH-FF	42.4	19.2	[52]
J	ReaxFF	62.6	37.1	—
J	exp	64	[51]	
J	DFT-GGA	31.8	22.0	[52]
T9	ReaxFF	105.6	74.1	[52]
bW	ReaxFF	67.6	57.23	—
T5Ca1	ReaxFF	59.6	38.6	—
T2Ca1	ReaxFF	39.7	32.1	—
T5H1	ReaxFF	47.1	34.7	—
T2H1	ReaxFF	41.8	31.5	—

however, this process is often non-linear for complex solids. The volume compression from pressure-volume equation of state accumulates from independent response of each lattice parameters to pressure. As calcium silicate hydrates are largely anisotropic, the overall volume compression stems from the ability of the a , b and c parameters to respond independently and is directly related to structure. Here, some insights into the behaviours and relationships of structure and compression is discussed. While the bulk modulus can be calculated by means of fitting to an BMEoS or be determined from elastic constants from zero temperature as discussed earlier, each method has its advantages and limitations. One advantage of the BMEoS method is that a fit can be performed at a specific temperature meaning that the calculation is more representative of a bulk modulus calculation via experiment. However, this method requires multiple runs and therefore is more time consuming and more demanding of computational resources. On the other hand, zero temp elastic constants calculation requires only a single simulation at the temperature and pressure of interest before performing the computationally inexpensive energy minimization calculation. As this is a static calculation, vibrational contributions to the elasticity are neglected and as a result, the bulk modulus tends to be higher than the value produced by BMEoS method. In addition, the strains applied for elastic constants method are small and finite to ensure that irreversible deformation is avoided. This is not always the case for BMEoS methods. In this section we determine K by fitting to the BMEoS and compare the values to experiment for a selection of calcium silicate hydrates. Moreover it is demonstrated that BMEoS fitting can give information about specific deformation processes within the crystal unit cell – something which zero temperature elastic constants cannot provide.

Firstly, comparisons are made between MD ReaxFF simulated BMEoS and experimentally derived BMEoS for tobermorite 14 Å and jennite. Figure 8.10 displays the ReaxFF BMEoS fitted P-V equation of state for tobermorite 14 Å compared to a recently published XRD study by Oh et al.[192]. As can be seen in the figure, ReaxFF predicts overall a greater increase in volume compression compared to experiment and is reflected in the bulk modulus value. ReaxFF undershoots the experimental bulk modulus value by 9 GPa (see Table 8.9). The value seems somewhat surprising as it is normally the case that simulated mechanical prop-

erties are higher than their experimental counterparts due to lack of structural defects. It can be seen from Figure 8.29 that in tobermorite 14Å the c direction is the softest and this is due to the large interlayer water-filled spacing. Looking at the RDF at 4.8 GPa for tobermorite 14Å, the biggest shift towards shorter r values is in the Ca-Ca and Si-Si RDF data. The peak at $r \approx 7.6$ Å represents the distance between the Si1 and Si4 in the silicate chain showing that, under pressure, the arch of the silicate chains is compressed somewhat. Similarly this is also seen by the reduction of distance in the Si1 to Si3 distance. The nearest neighbour Ca ions within the same interlayer are also brought closer together under pressure which is shown by a slight shortening of $r \approx 7.6$ Å. This suggests that the interlayer spacing reduces the amount of deformation elsewhere in the crystal structure.

Crystal deformations is depicted in Figure 8.12. As is seen with the RDF pattern, the compression of the interlayer distance of tobermorite 14 Å is seen within the crystal structure and measured distances show clearer compression than the RDF pattern by reducing the interlayer spacing by 1.3 Å. There is also a slight reduction in Ca-Ca intralayer distance of around 0.1 Å in the z -direction (equivalent to the c axis, not shown in figure).

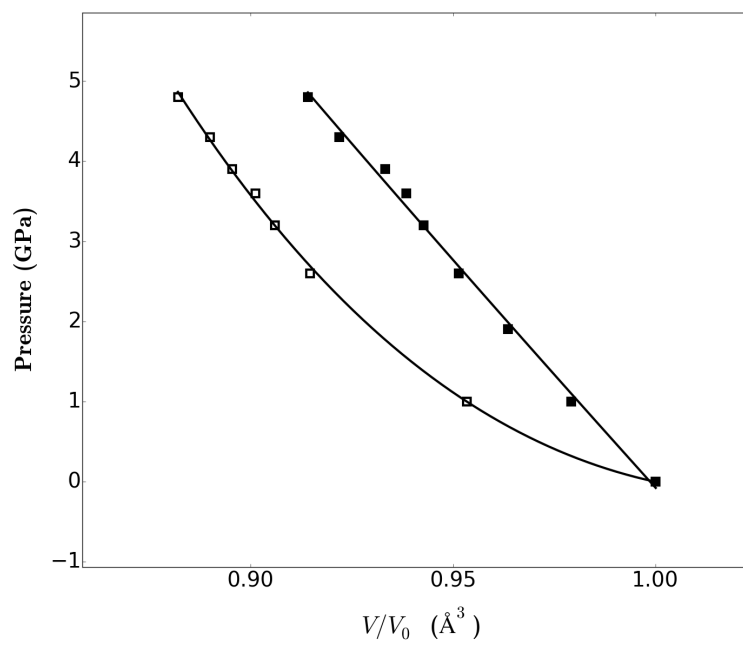


Figure 8.10: Tobermorite 14 Å BMEoS comparison of experimental (black squares) and simulation (white squares). Experimental data taken from Ref. [192].

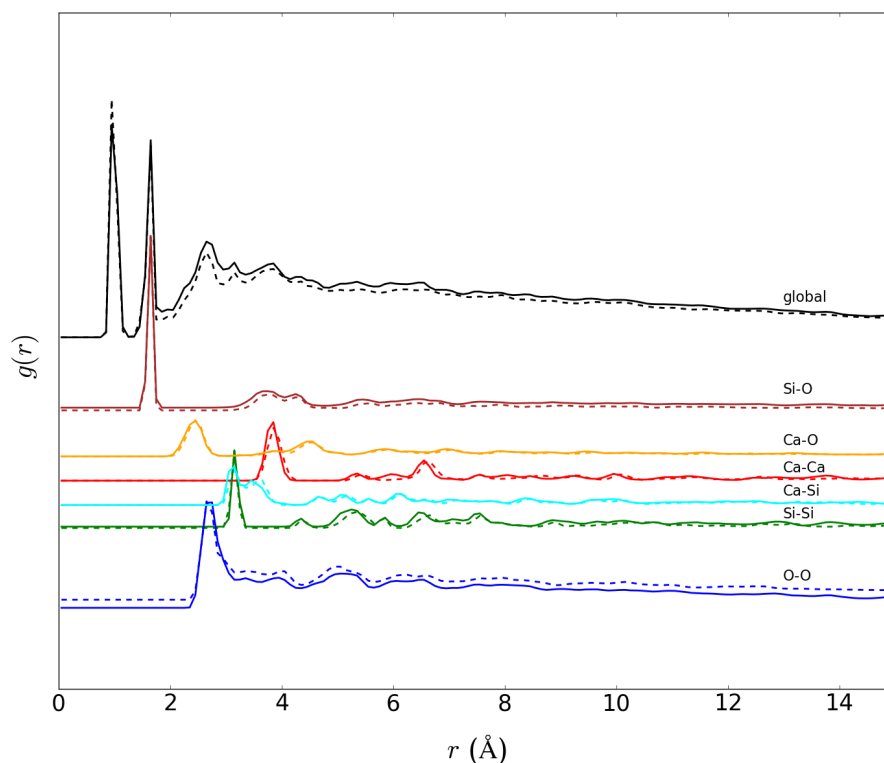


Figure 8.11: RDF of tobermorite 14Å at 0 GPa(dashed lines) and 4.8 GPa (solid lines)

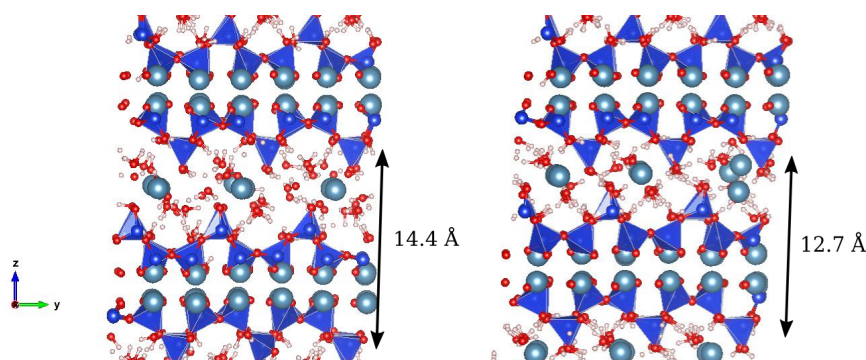


Figure 8.12: Comparison of crystal interlayer of tobermorite 14Å at 0 GPa (A) and 4.8 GPa (B) pressure

A similar trend is seen for jennite (Figure 8.13) whereby the ReaxFF predicted BMEoS differs from the XRD P-V curve as ReaxFF predicts a slower response

of jennite to pressure. Very little movement in the RDF function is seen at short distances however it is evident that the interlayer spacing reduces from 11.1 Å to 10.0 Å whilst there is little movement in other parts of the structure again suggesting that the interlayer compression may prevent deformation of the silicate chain structure. This shortening of the interlayer distance can be seen in the Si-Si RDF where the peak at $r \approx 10$ Å and $r \approx 11$ Å shift to smaller distances. Subtle difference can be seen in the jennite RDF data with regards to shortening of bond and interaction distances. For jennite RDF, a shift in the first peak is observed where Si-O is the most prominent suggesting that the polymer chains play a role in the contraction of the crystal under pressure. It is noted that the RDF pattern at 4.8 GPa has broader peaks than at 0 GPa indicating that the structure becomes more disordered at higher pressure.

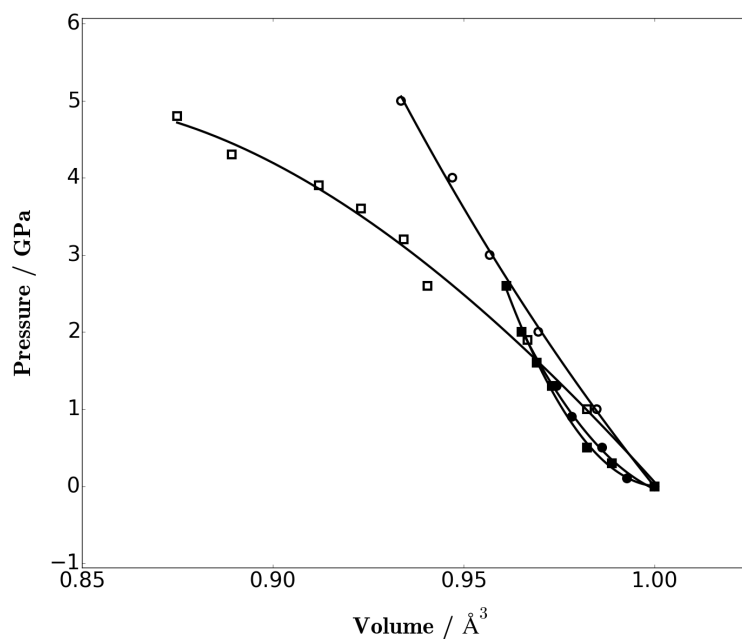


Figure 8.13: Jennite BMEoS comparison of experimental (black squares), ReaxFF simulation (white squares) and DFT simulations (white circles). Experimental data taken from Ref. [51]

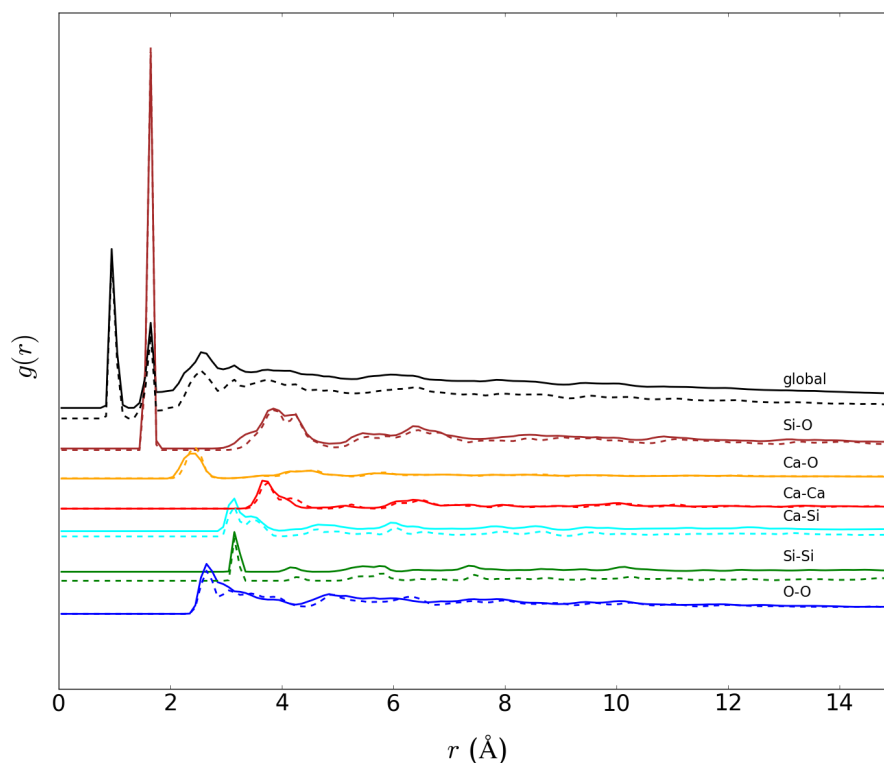


Figure 8.14: RDF of jennite at 0 GPa(dashed lines) and 4.8 GPa (solid lines)

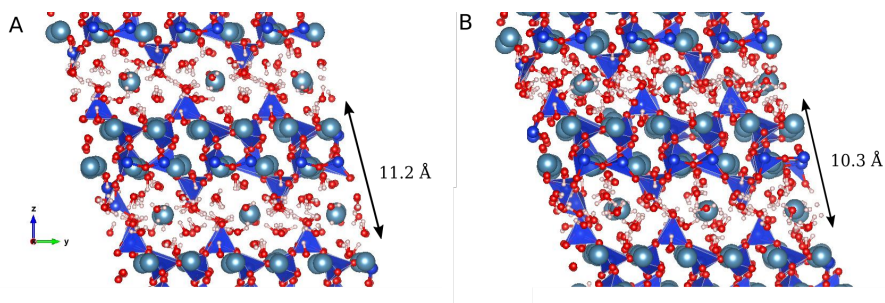


Figure 8.15: Comparison of crystal interlayer of jennite at 0 GPa (A) and 4.8 GPa (B) pressure

Tobermorite 9 Å is the least compressive of the mC-S-H and this is reflected in the BMEoS through a steep gradient between P and V . Surprisingly, the tobermorite 9 Å RDF pattern shows a greater shortening in Ca-Ca RDF compared to jennite and tobermorite 14 Å, which have been shown to be more compressive than

tobermorite 9 Å . As seen in Figure 8.18, the Si-Si distance between silicate chains contracts under pressure (indicated by green circles) and more shifts are seen in the Ca and silicate oxygens which suggests that when the interlayer is unable to compress, distortion occurs in the calcium silicate structure itself. It is observed that tobermorite 9 Å at high pressure has more features from $r < 6$ Å and less features at $r > 6$ Å compared to the structure simulated at zero pressure, suggesting that at high pressure, tobermorite 9 Å has more short range order than at zero pressure whereas at low pressure the system has more long range order than at zero pressure.

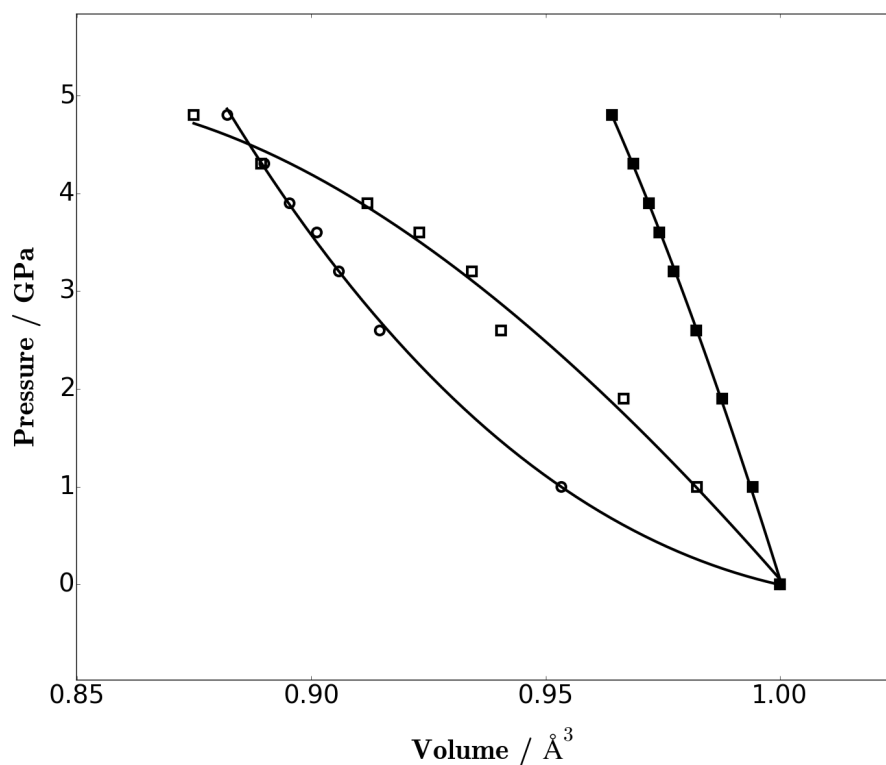


Figure 8.16: mC-S-H BMEoS, tobermorite 14 Å (circles), tobermorite 9 Å (black squares), jennite (white squares)

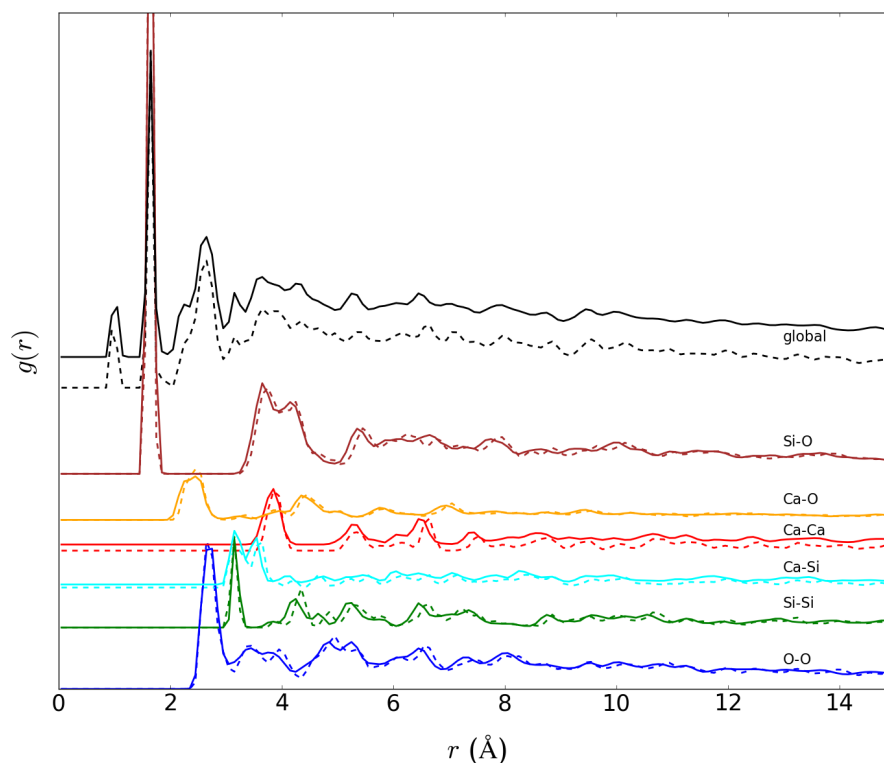


Figure 8.17: RDF of tobermorite 9Å at 0 GPa(dashed lines) and 4.8 GPa (solid lines)

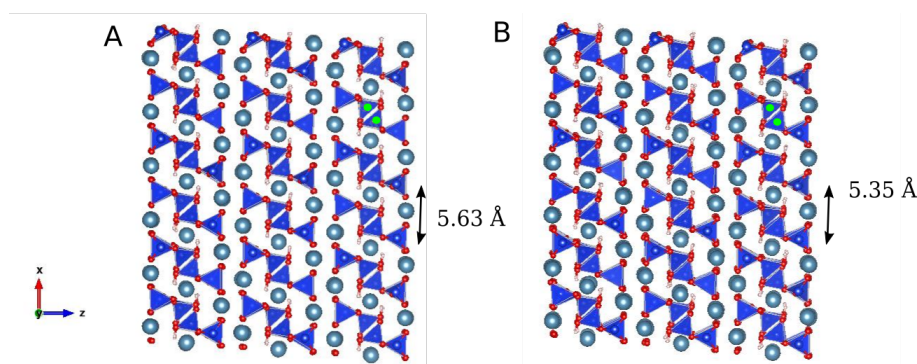


Figure 8.18: Comparison of crystal interlayer of tobermorite 9 Å at 0 GPa (A) and 4.8 GPa (B) pressure. Green circles represents compression of Si atoms – distance between green circles in A is 4.32 Å distance between green circles in B is 4.11 Å

With the C-S-H BMEoS, a similar volume response to pressure is observed, how-

ever, the structures with pentameric silicate show a greater resistance to compression under pressure. Like the mC-S-H structures, the Ca-Ca RDF shows the biggest shift suggesting that the layered nature of C-S-H allows for compression without significantly affecting the internal silicate chain structure. A slightly greater shift is seen in Ca-Ca RDF with the dimeric structures than is seen with the pentameric C-S-H however the effect is almost negligible. Figures 8.23 and 8.21 illustrate the compression of the interlayer in the crystal structure of T2Ca1 and T5Ca1 respectively.

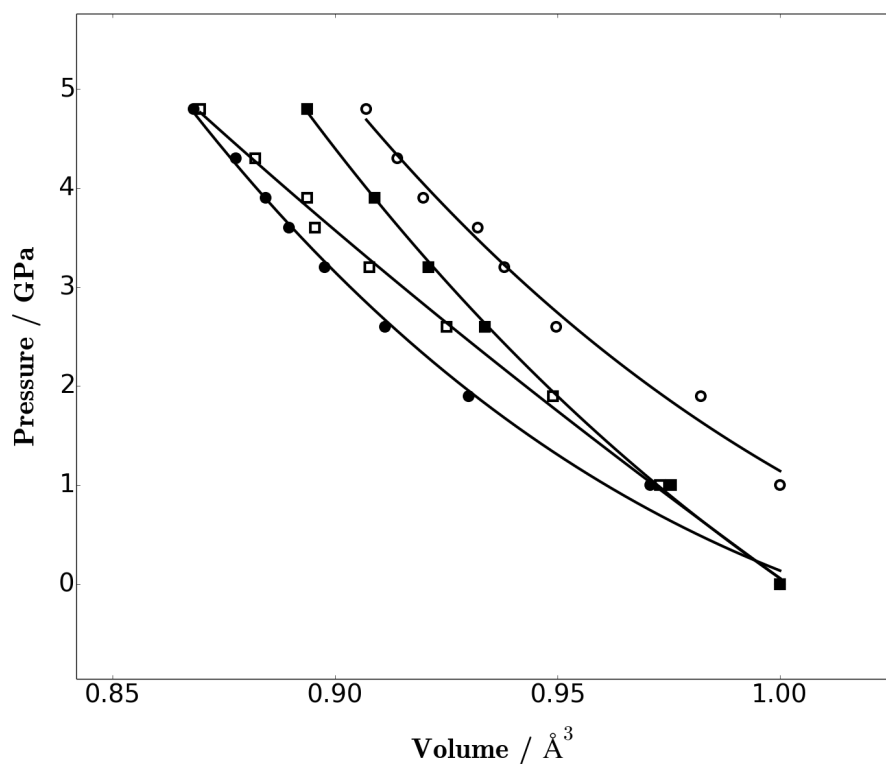


Figure 8.19: C-S-H BMEoS, T5Ca1 (black squares), T2H1 (white circles), T2Ca1 (white squares), T5H1 (black circles)

Figures 8.20 and 8.21 compare the RDF and crystal structure of the T5Ca1 structure under pressure respectively. It can be seen that in general, applying an isotropic pressure of 4.8 GPa leads to a slight shortening of interaction distances in all of the RDF functions as indicated by a slight shift to lower r values. The first interaction peak in the Ca-O RDF shows the most dramatic shift however this

is still only by approximately 0.15 \AA . Compared to the mC-S-H RDF patterns at 4.8 GPa, there seems to be less disorder caused in T5Ca1 (and for the other C-S-H patterns). From the crystal structure in Figure 8.21, it can be seen that the basal spacing is reduced by 0.71 \AA , which is significantly less than the 1.7 \AA compression seen for tobermorite 14 \AA basal spacing and 0.1 \AA more compression than is seen with jennite.

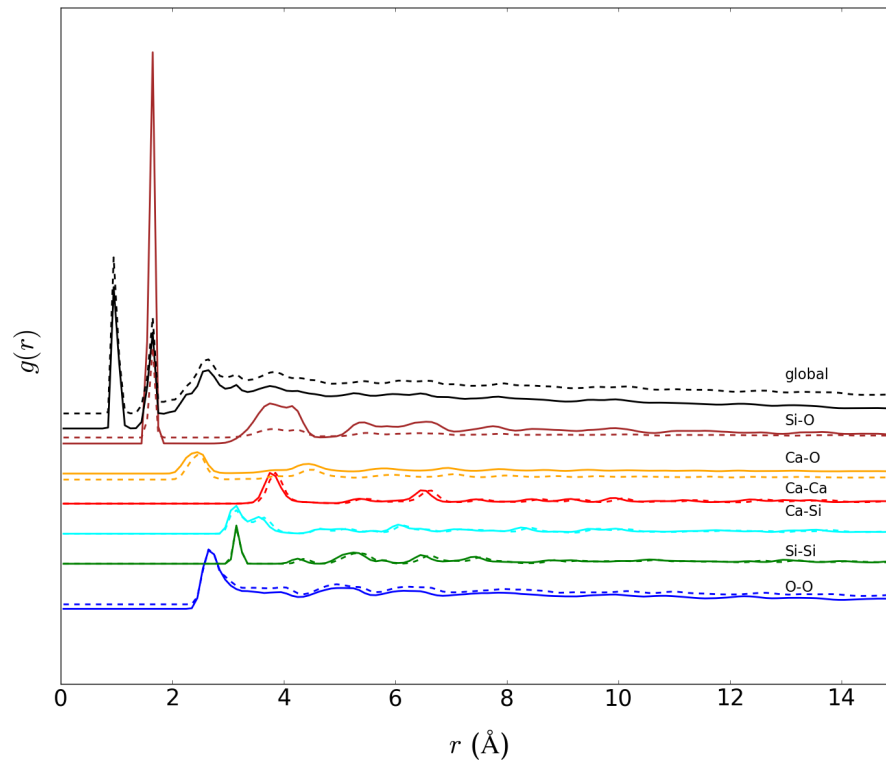


Figure 8.20: RDF of T5Ca1 at 0 GPa and 4.8 GPa

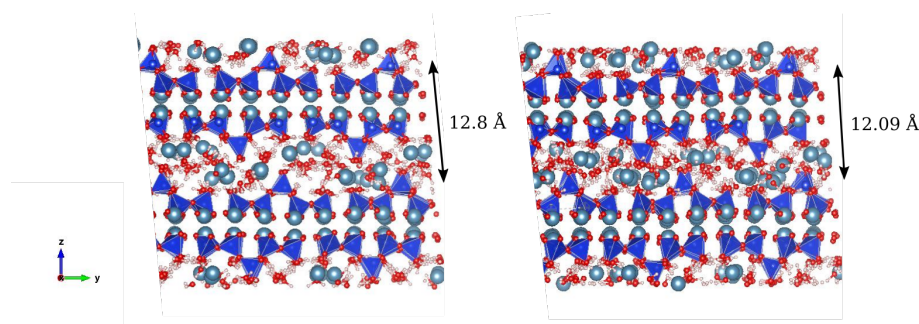


Figure 8.21: Comparison of crystal interlayer of T5Ca1 at 0 GPa (A) and 4.8 GPa (B) pressure

Figures 8.22 and 8.23 show the RDF and crystal structure of T2Ca1 under pressure. Compared to T5Ca1, the difference between the RDF pattern at 0 GPa and 4.8 GPa is more dramatic. Interestingly, the first interaction peak of the Ca-Ca RDF pattern shows the greatest difference between 0 GPa and 4.8 GPa with a shift to lower r values of the 4.8 GPa by approximately 0.2 \AA . No shift is seen with the first Si-Si interaction peak suggesting that there is no compression of the dimeric intra molecular bonds. There is, however, a slight downward shift in the other Si-Si interaction peaks indicating that the dimers move closer together. The first Si-O interaction peak indicates more disorder in the Si-O bonds, as is evident by the slight broadening of the peak at 4.8 GPa. Figure 8.23 shows the compression of the basal spacing from 13.6 to 12.4 \AA when 4.8 GPa pressure is applied. It is evident that under compression, the interlayer Ca ions become significantly more disordered.

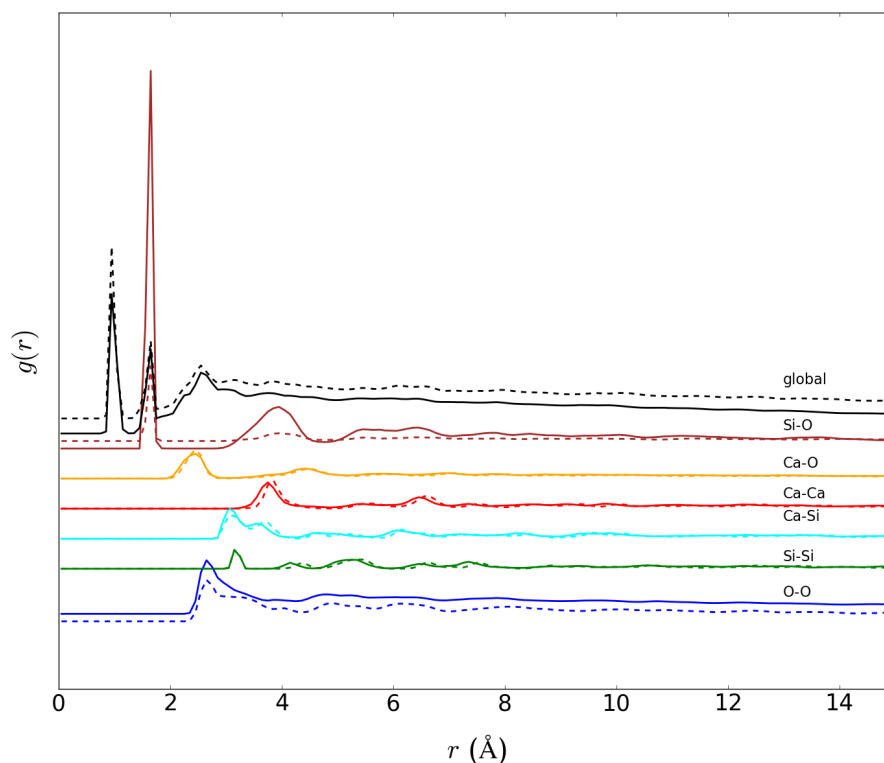


Figure 8.22: RDF of T2Ca1 at 0 GPa (dashed lines) and 4.8 GPa (solid lines)

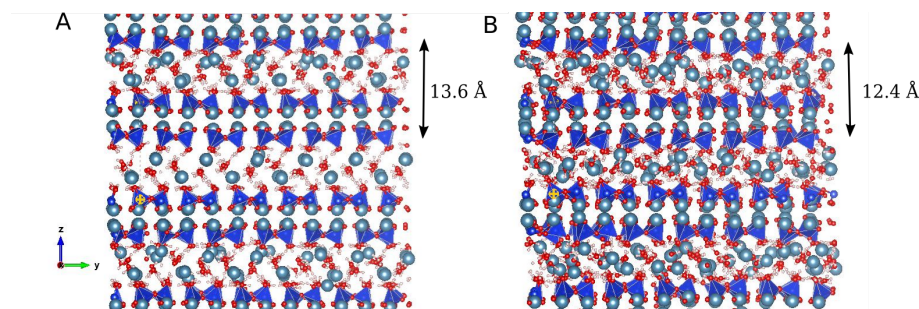


Figure 8.23: Comparison of crystal interlayer of T2Ca1 at 0 GPa (A) and 4.8 GPa (B) pressure

Figures 8.24 and 8.27 shows the RDF and crystal structure of T5H1 under pressure. A similar scenario is seen with T5H1 where the Ca-Ca peaks show the most compression as indicated by a small shift of approximately 0.1 \AA to lower values of r . Similarly, more disorder is seen in the Si-O RDF at short distances. The

Si-Si RDF indicates that no disorder occurs within the pentamer chains but increasing disorder is seen at longer Si-S- interaction distances. Figure 8.27 shows that more disorder occurs in the interlayer spacing when increasing the pressure from 0.0 GPa to 4.8 GPa and that the interlayer spacing reduces by 0.96 \AA which is less than is seen with T2Ca1 but more than is seen by T5Ca1.

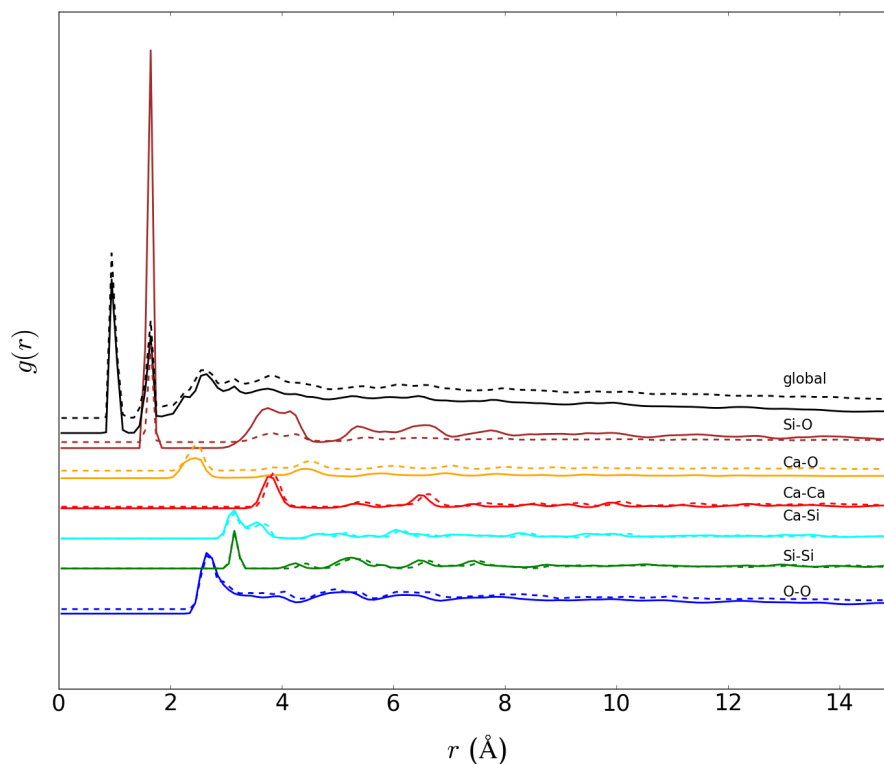


Figure 8.24: RDF of T5H1 at 0 GPa(dashed lines) and 4.8 GPa (solid lines)

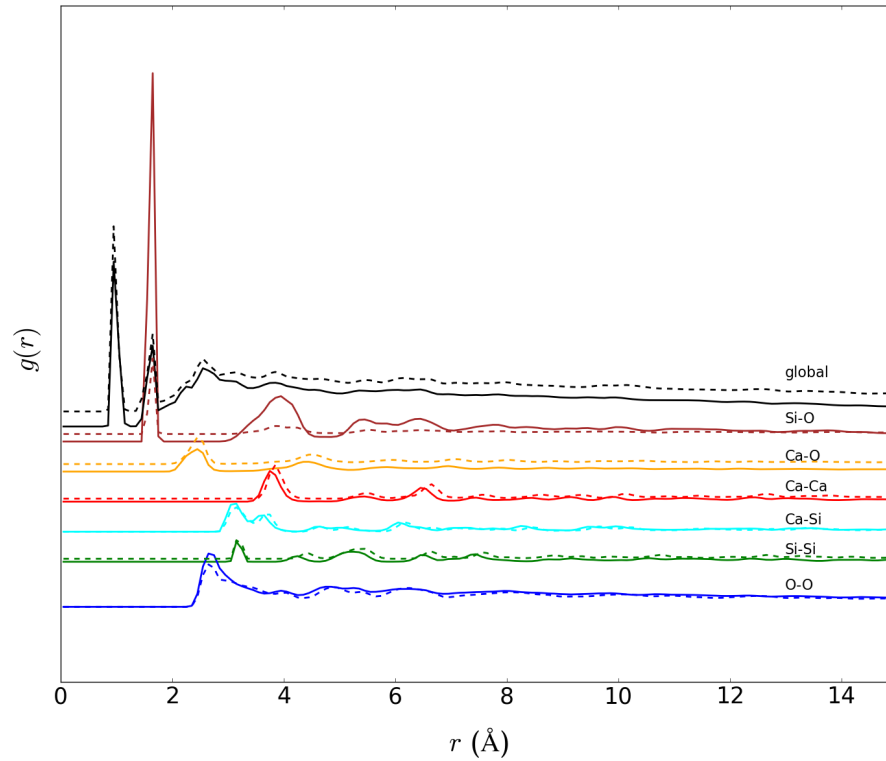


Figure 8.25: RDF of T2H1 at 0 GPa(dashed lines) and 4.8 GPa (solid lines)

Figures 8.25 and 8.26 shows the RDF and crystal structure of T5H1 under pressure. Like seen with previously discussed C-S-H RDF patterns, it is evident that the structure becomes more ordered under pressure. The basal spacing reduces by 0.81 \AA upon going from 0 to 4.8 GPa. Interestingly, the basal spacing compresses less in the T2H1 structure than is seen in the T2Ca1 structure (1.2 \AA reduction in basal spacing). This was not evident in the comparison of basal spacing compression for T5Ca1 and T5H1 and therefore it cannot be inferred that the compression is necessarily related to the charge balance method.

Table 8.9: Comparison of BMEoS at zero temperature elastic constant method mC-S-H and C-S-H structures

Structure	BMEoS (GPa)	Elastic Constants (GPa)
T14	38	55
J	57	71
T9	168	105
T5Ca1	38	59
T2Ca1	36	39.7
T2H1	29	41.8

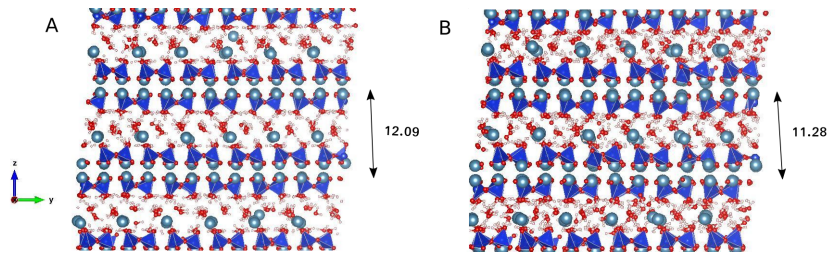


Figure 8.26: Comparison of crystal interlayer of T2H1 at 0 GPa (A) and 4.8 GPa (B) pressure

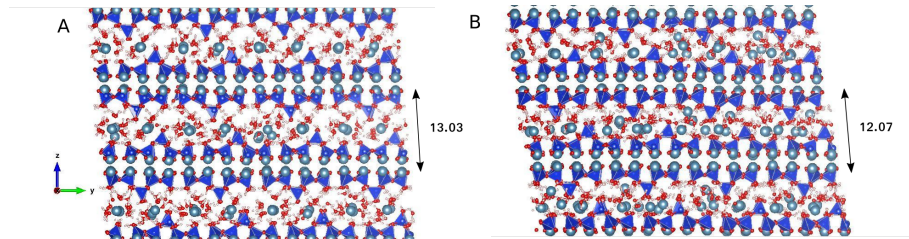


Figure 8.27: Comparison of crystal interlayer of T5H1 at 0 GPa (A) and 4.8 GPa (B) pressure

8.4.7 Anisotropy in Calcium Silicate Hydrates

The anisotropy in calcium silicate hydrates is clearly demonstrated in Figures 8.28 and 8.29 which show the relative compression of C-S-H and mC-S-H lattice parameters respectively. For all C-S-H structures tested, the c direction shows the

most compression. The c direction contains repeating units of water layers and since the water molecules have a greater degree of flexibility in how they align themselves with each other and with other surrounding species and can accommodate the rise in pressure resulting in compression of the interlayer spacing. Furthermore, from Figure 8.28, dimeric polymer chain structures shows less resistance to compression in the c direction. This may be due less restriction and angle constraints with the polymeric chain compared to a pentameric structure. The compression in a and b directions is significantly less as compression in this direction would rely on twisting and deformation of the silicate chains but due to the compaction of the calcium silicate layers this is more difficult. Again in both cases, increased compression as seen for the dimeric silicate chains and will be due to the lower resistance and the inability to resist deformation. Similar trends are seen in mC-S-H structures whereby the c axis shows the most compression due to this being the interlayer water filled space. With tobermorite 9 Å, the overall density of the structure and the interlayer is high therefore compression is difficult. In the a direction, tobermorite 14 Å shows the most compression.

It can be seen for C-S-H structures that there is a small effect on how much compression occurs under pressure in the b direction with decreasing chain length. The dimeric structures display more compression in the x -direction (a -axis) compared with pentamers which subsequently show more compression in the b direction. This is directly related to the manoeuvrability of the structure and the flexibility in which it can adopt. The high compressive strength in cement could be related to this ability to adapt rather than restriction causing brittle compressive failure, however, more tests are required to confirm this. For C-S-H models it is shown that pentameric chains show least compression in the c direction as well as the b direction. Overall, the C-S-H models are softer in all directions as a result of the reduced rigidity in the structure than mC-S-H models. Specifically, the polymerisation has an effect on the compression along the b axis where, the compression is greater for dimeric chains, followed by pentameric chains followed by infinite chains. The softest layer of all, the c direction, relates directly to the basal spacing. Geng et al. has related the bulk modulus directly to the length of the basal spacing where large basal spacings were associated with smaller bulk moduli. This is in fact contrary to the findings using a selection of calcium sil-

icates. With mC-S-H, this finding holds true. However, with the basal spacing being around 11 Å for the C-S-H structures, the findings of Geng do not completely hold true as K is much less for the C-S-H structures and the mC-S-H structures.

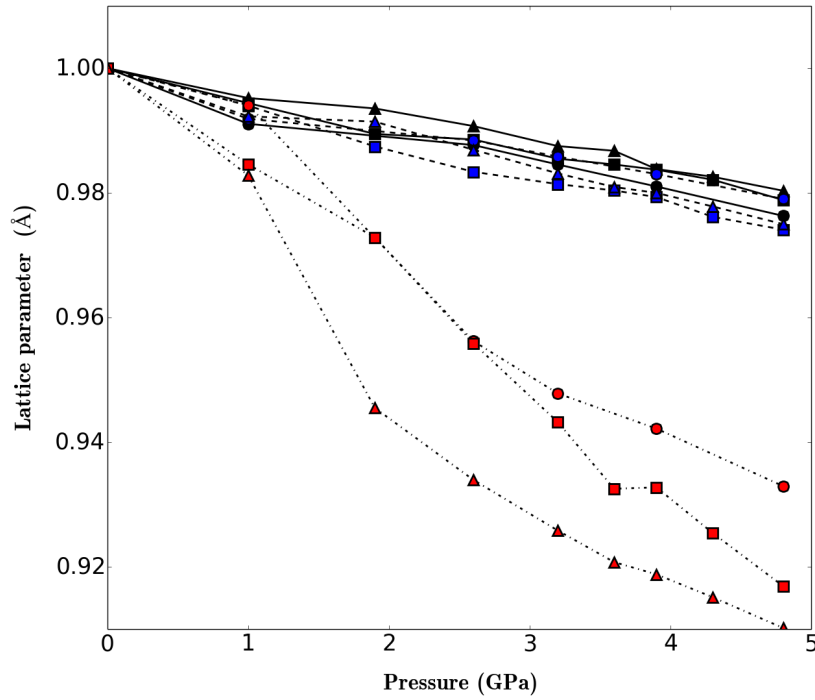


Figure 8.28: Lattice constant dependence on pressure for C-S-H, REAXFF, 298K, T5Ca1 (circles), T2H1 (triangles), T2Ca1 (squares), a (black), b (blue), c (red)

Table 8.10: Percentage compression at 4.8 GPa for mC-S-H and C-S-H structures

Structure	a (Å)	b (Å)	c (Å)	V (Å ³)	ρ
T14	2.51	-0.30	8.52	12.12	-13.76
J	1.72	1.50	9.56	12.59	-13.06
T9	1.88	1.66	-0.05	3.72	-3.60
T5Ca1	2.36	2.07	6.63	10.65	-11.94
T2Ca1	2.29	3.28	8.06	13.07	-14.87
T2H1	2.01	2.57	9.87	15.17	-13.17

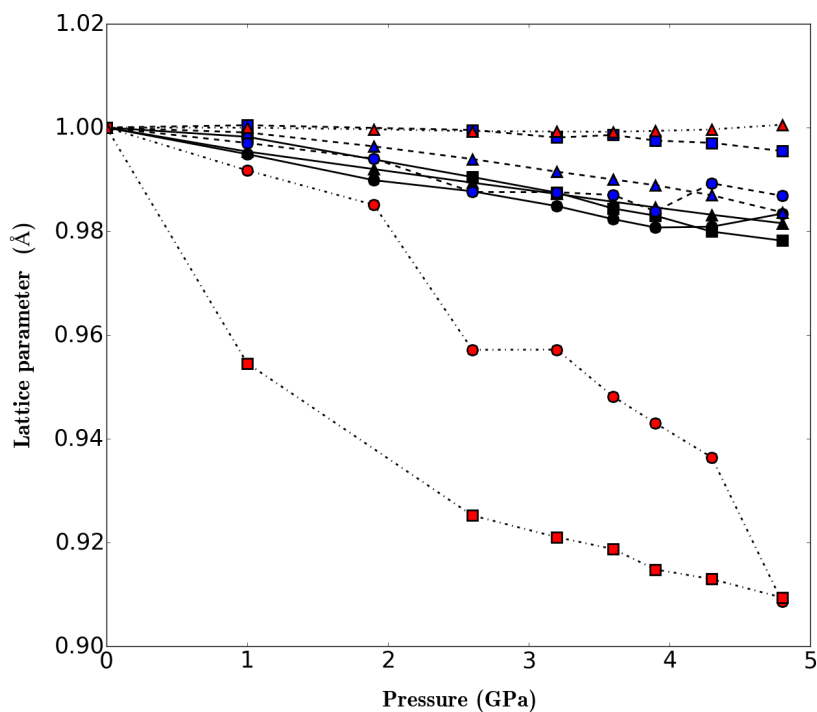


Figure 8.29: Lattice constant dependence on pressure for mC-S-H, tobermorite 14 Å (circles), tobermorite 9 Å (black squares), jennite (white squares).

8.5 Summary

In this chapter it has been shown that of the two most common simulation methods for elastic constants, the zero temperature elastic constants produce a higher value but seem more akin to experimental results. For known mineral structures, ReaxFF reproduces with reasonable accuracy the elastic constants and elastic moduli. Based upon a rigorous assessment this study has backed up findings in the literature whereby the density of the interlayer increases the bulk modulus of the structure. Additionally, this study has provided evidence that a number of factors come into play together to increase the bulk modulus and therefore increase the overall compressive strength of the material. From the findings, the recommended structure to cementitious calcium silicate hydrate that can resist compression is that with a high density, low water content and a silicate chain with a high degree of polymerisation. It has also been demonstrated that there is an inconsistency with simulating the value of bulk modulus where the elastic constant and BMEoS method produce a different value of the modulus, however, both methods predict the same trend in structure property relations. Lastly, insights into deformation mechanisms have been shown that the interlayer plays a role in protecting the silicate chains from deformation.

Chapter 9

Nanoscale Fracture Processes of Calcium Silicate Hydrates

9.1 Overview

In Chapter 8, it was concluded that ReaxFF MD simulations were capable of capturing the nanoscale structure-property relationships of (m)C-S-H and that the structure and composition of (m)C-S-H have an influence on the resulting elasticity. In this chapter, the fracture protocol is applied to two hypothetical C-S-H structures (T5Ca1 and T2Ca1) using the fracture methodology designed and validated in Chapter 6. Since it was demonstrated that the methodology could reproduce experimental fracture toughness and crack speeds for ice Ih, the method can now be applied to C-S-H with reassurance that the fracture method is realistic, and therefore is capable of making reliable predictions.

This chapter begins with a review of previous MD fracture simulations of C-S-H, comparing the methods used and the results of C-S-H fracture data in the literature. The simulation method is then presented indicating how the fracture method from Chapter 6 has been modified to simulate C-S-H. The effect of the direction of the applied tension is investigated using the pentameric structure as an example. Finally, the effect of polymer chain length is investigated, highlighting the limitations in the method. The chapter ends with a discussion on the

usefulness of fracture data of C-S-H determined from molecular simulations and the future work which must be done to improve upon the current predictions.

9.2 Introduction

Due to the structural complexity of cementitious building materials, there is a general consensus in the cement field that in order to improve the toughness of cementitious materials, the properties of C-S-H, the most mechanically influential component of cement, must be understood. As was highlighted in Chapter 2, producing pure C-S-H samples which can be mechanically tested is a challenge therefore the field has turned to molecular simulations to investigate the fracture properties of C-S-H[66, 67, 197, 198]. By simulating the fracture of C-S-H using MD, insights into the behaviour of C-S-H at the nanoscale can be gained and will allow the structure-property relationships to be determined beyond the elastic regime.

Since direct tensile tests of nanoscale C-S-H are not feasible due to poorly crystalline nature of C-S-H, nanoindentation has proven to be a useful tool to measure the fracture toughness of nanoscale C-S-H as was discussed in Chapters 2 and 8[199, 200]. Nanoindentation tests can be carried out on a compacted, synthetic C-S-H sample to determine deformation behaviour. A combination of nanoindentation tests and FEM modelling have estimated the tensile strength of C-S-H to be around $0.15 \text{ MPa}\cdot\text{m}^{0.5}$ which was found to be approximately half the value calculated for cement ($0.3\text{-}0.5 \text{ MPa}\cdot\text{m}^{0.5}$)[199, 201, 202].

Microscale tensile bending tests have shown that outer product C-S-H tensile strength is around $264.1 \pm 73.4 \text{ MPa}$ and that inner product C-S-H is around $700.2 \pm 198.5 \text{ MPa}$ [203]. Within the same experiment, the Young's modulus was found to be 23 GPa for the outer product and 34 GPa for the inner product[203]. Given that the inner product is more dense than outer product C-S-H, and since in the previous chapter it was concluded that C-S-H structures with a higher density had increased bulk, shear and elastic modulus, it is reasonable that the inner product would have a higher tensile strength and Young's modulus when compared to the outer product.

By using a hypothetical C-S-H model, it is possible to predict how C-S-H will behave under uniaxial tension at the nanoscale, and by testing a variety of structures, a structure-property relationship specifically linked to fracture behaviour can be determined. Recently, a number of studies in the literature have utilised MD and Pellenq’s C-S-H model to determine stress-strain relationships and fracture toughness of C-S-H[62, 67, 204–207]. These studies, however, show little consistency with each other in the measure of tensile stress and failure mechanisms. Recent simulation studies of the tensile strength of Pellenq’s C-S-H model have measured the tensile stress to be in the range of 3-6 GPa, which is ten times larger than that of experimental C-S-H. Furthermore, the Young’s modulus is in the range of 30-60 GPa from simulations compared to 75 GPa as found by experiment. It is expected that these values should be higher than seen by experiment as the structures are defect free in simulations therefore a higher toughness, tensile stress and Young’s modulus is expected. A summary of the results is displayed in Table 9.1. Note that the z-direction is equivalent to the c axis i.e. the crystal axis with alternating layers of calcium silicate chains and interlayer water and the x-direction is equivalent to the crystal a axis.

Table 9.1: Fracture properties from simulation studies in the literature of Pellenq’s C-S-H model

Force Field	Direction	Strain Rate 1/ps	E (GPa)	Tensile Stress (GPa)	Strain at Tensile Stress	Strain at Complete Failure	Ref.
ReaxFF	x	0.08	58	6.9	0.2	0.79	[62]
ReaxFF	z	0.08	35	2.8	0.1	0.32	[62]
CSHFF	x	0.008	61	3.94	0.08	0.58-0.8	[66]
CSHFF	z	0.008	44	2.2	0.05	0.58-0.8	[66]
ReaxFF	z	—	—	1.4	0.06	0.25	[67]

It is clear that variation in the measured fracture properties exist, even when the same hypothetical C-S-H model is simulated. Despite the differences in the data, both studies by Hou et al. are in agreement that the z-direction is the weakest direction, where the tensile stress is approximately half of the tensile stress in the x-direction and the failure occurs at a lower strain than in the x-direction. It is

understood that both studies by Hou et al. have been carried out using the same fracture protocol and system set up therefore the difference in force field and strain rate is most likely the cause of the difference in results. In Chapter 6, it was demonstrated with ice Ih that a strain rate of 5×10^{-5} versus 5×10^{-6} caused the tensile stress to increase from approximately 0.5 GPa to approximately 0.9 GPa and therefore it is likely that the 10 fold increase of strain between the two studies has a role to play in the difference in tensile stress. Furthermore, the force field is likely to have an effect upon the measurement of mechanical properties as it was evident from work carried out in Chapter 8 that CSHFF and ReaxFF differ in the prediction of the elastic properties of C-S-H. Lastly, it should also be noted that CSHFF is not parametrised to break bonds and therefore should not be used for the description of fracture processes.

The deformation patterns also varied between the work of Bauchy and Hou[66, 67]. Bauchy et al. was able to calculate the fracture toughness due to the propagation of a single fracture which is in contrast to the deformation seen in studies by Hou and Ding et al.[66, 208] In the latter studies, failure was seen at multiple points, much like the deformation pattern seen with high strain rates of ice Ih in Chapter 6, however, it cannot be inferred that a high strain rate was to blame from the data given. These findings highlight the need for a more critical review of simulation methods to ensure that the data gathered from simulations can be useful predictions.

This short chapter begins the process of working towards making realistic predictions of C-S-H fracture properties. It aims to compare the fracture protocol designed in this thesis with existing fracture simulations in the literature. It is expected that this work will lead to an understanding of the structure-property relationships of C-S-H beyond the elastic regime.

9.3 Methods

Molecular dynamics simulations studies in this chapter have been carried out using LAMMPS [64]. This chapter employs the use of T5Ca1 and T2Ca1 as hypothetical structures to model the fracture properties of C-S-H. Due to the

high computational cost of running the fracture simulations, only two structures were simulated. Due to the time constraints, T5Ca1 and T2Ca1 were chosen to represent C-S-H.

The fracture methodology was developed based on work in references [67, 112, 167] and is described in detail in the following sections.

9.3.1 System Preparation

The system preparation followed a similar path to the method developed for ice Ih in Chapter 6. Like ice, the geometry of the system was chosen to resemble a thin sheet as described in reference [112] to maximise the distance in which the fracture can propagate. The thickness of the plate for C-S-H was thicker than ice due to the larger repeating unit of the C-S-H structures. Table 9.2 contains the geometry for the C-S-H simulation cells used in this chapter. The systems contained approximately 24000 atoms, around 3000 more atoms that was simulated for ice, therefore incurring a greater computational cost. Due to the increased thickness of the the simulation cell, the other dimensions were reduced in length as otherwise the number of atoms would significantly affect the simulation time. This is critical when equilibrating the structure as a system this large takes around two weeks to equilibrate on ARCHIE-West (high performance computing facilities at Strathclyde) using 12 cores. The system was first equilibrated at 300 K and zero pressure in the NpT ensemble for up to 1 ns using Nose-Hoover thermostat and barostat with a dampener of 100 time steps before any pulling tests were carried out. For the T2Ca1 system, the x-dimension was 75% greater than in the T5Ca1 system due to instabilities during the equilibration. The dimeric model was found to be unstable at small thickness therefore the thickness was increased. Due to the significant rise in the number of atoms associated with the thicker cell, the other cell dimensions had to be reduced to lower the computational expense.

An initial crack was placed in the centre of the simulation cell after the equilibration stage to encourage controlled fracture propagation. This initial crack was produced by removing molecules from a diamond shaped volume as shown in Figure 9.1. The notch and system sizes are displayed in Table 9.2. The residual

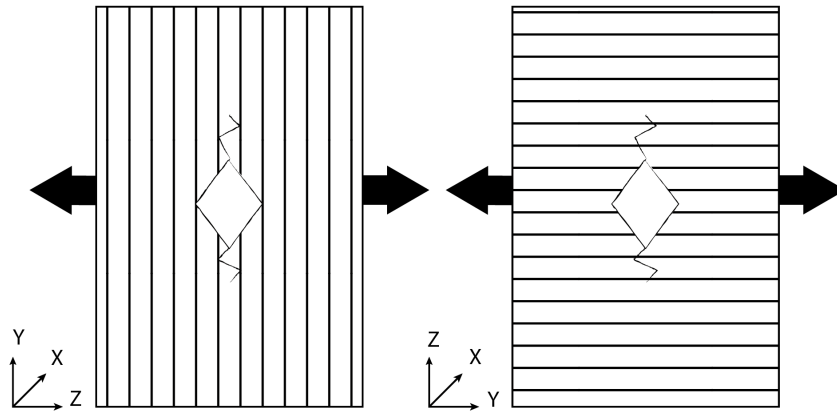


Figure 9.1: Tensile pulling directions. Through the chains and with the chains where the lines represent the direction of the silicate chains.

charge was balanced by adding H^+ or OH^- ions. The notch was made larger than required for ice as early tensile tests revealed that C-S-H fracture was reluctant to propagate directly from the notch tip.

Table 9.2: Dimensions of Simulation Cells and Initial Cracks for T2Ca1 and T5Ca1

Structure	Loading Direction	Cell Size (\AA)	Initial Crack (\AA)
T5Ca1	y	$10 \times 100 \times 210$	20×40
T5Ca1	z	$10 \times 200 \times 100$	20×40
T2Ca1	y	$30 \times 60 \times 120$	12×24

9.3.2 The Tensile Fracture Method

The fracture test involved extending the length of the box in the direction of interest at a constant strain rate until failure and this was implemented by using the `fixdeform` command in LAMMPS[64]. The strain rate used in all tests in this chapter was 1×10^{-6} . A time step of 0.2 fs was used and periodic boundary conditions were applied in all directions. Throughout the pulling simulation run,

the directions which are not under tension are kept at zero pressure to encourage realistic propagation of the fracture.

The global stress was calculated at every step via the pressure change in the system. The tests were run until complete failure was observed or no further stress reduction was evident. The fluctuations of stress results in a large amount of noise in the stress-strain curves therefore for clarity only, noise was reduced in each stress-strain curve by applying a IIR filter which reduces noise and smooths the curve as implemented in Scipy.

Tensile tests were carried out in two different directions as outlined in Figure 9.1. For the T5Ca1 structure, investigations through the silicate chains (tension in the y-direction) and in the plane of the silicate chains (tension in the z-direction) were carried out. For T2Ca1, only through chain fracture propagation tests were carried out.

9.4 Results and Discussion

To investigate the effect of the loading direction on C-S-H, the T5Ca1 structure was loaded in two different directions. The first test involved pulling in the z-direction to investigate fracture between the silicate chains. The second involved loading in the y-direction where the fracture pathway would propagate through the silicate chains. Although the x-direction was not tested, it was assumed that little difference would be observed between y-direction and x-direction tests. In agreement with the work by Hou et al., the z-direction is shown to be weaker in terms of the tensile strength. Results comparing the direction of loading are displayed in Figure 9.2. In the z-direction, bonding primarily consists of hydrogen bonds between the water and the oxygens of the silicate chains. Hydrogen bond energies are in the order of 20 kJ/mol, compared to covalent bond energies which can be up to 400 kJ/mol[209]. In the z-direction, the strain at the initial failure is 0.06 compared to an initial failure strain of 0.09 in the y-direction suggesting that the hydrogen bonded layer fails earlier and at a lower strain, and therefore lower load, than in the x-direction. The tensile stress for failure in the z-direction is much lower than in the x-direction and is 1.25 GPa and 2.3 GPa respectively,

indicating that that the most likely failure direction is the z-direction. In the y-direction, the bonding is predominately covalent bonding giving rise to the higher tensile strength.

By comparing the softening curves in Figure 9.2, qualitative information can be gained. The softening curve in the z-direction tensile test has a sharp fall in stress with increasing strain indicating that the failure is more rapid in nature when compared to the y-direction failure. Observations of deformation reveals that two different fracture processes occur depending on the direction of loading. Figure 9.3 shows that the fall in the stress is associated with the initial separation of the layers. The gradual reduction in the gradient is a result of the bending of the silicate chains with increasing strain which prevents further propagation of the fracture. On the other hand, the softening curve of the y-direction fracture has a slower gradient suggesting that more resistance to fracture occurs when the fracture propagates through the chains. Figure 9.4 shows the failure process of T5Ca1 in the y-direction. The figure shows that the fracture has to navigate through the silicate chains which slows the fracture propagation. Image C in Figure 9.4 shows a bridging silicate chain which is helping to resist fracture. This resistance is the reason behind the slow softening stress-strain curve.

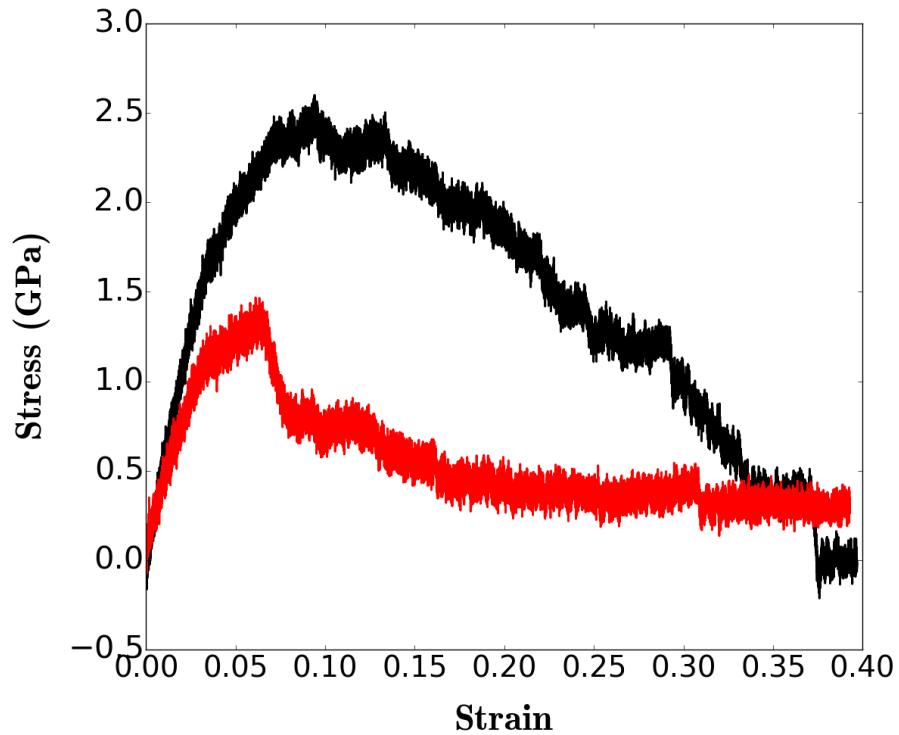


Figure 9.2: Effect of loading direction on stress-strain curve of T5Ca1, y-direction(black), z-direction(red), 300 K, 1×10^{-6} .

Although it was proven that the fracture protocol resulted in comparable experimental data for ice Ih, the implementation of the method for C-S-H came with a number of challenges. While the method was still suitable for determining the tensile strength and stress-strain relation of C-S-H, the method was unable to produce a single fracture pathway stemming entirely from the initial notch, and as a result, the fracture toughness could not be calculated. The failure to produce a single fracture is consistent with a number of other literature studies[62, 66, 208].

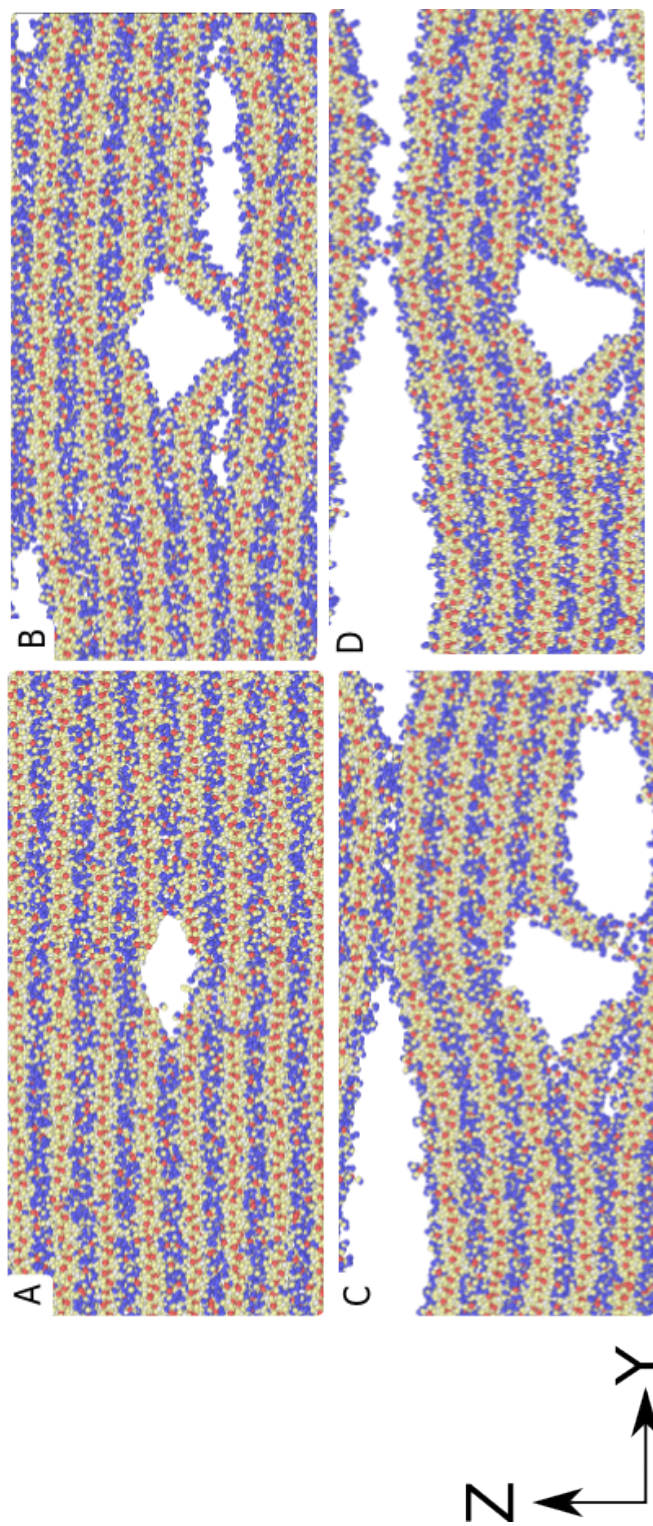


Figure 9.3: Deformation of T5Ca1 in the z-direction

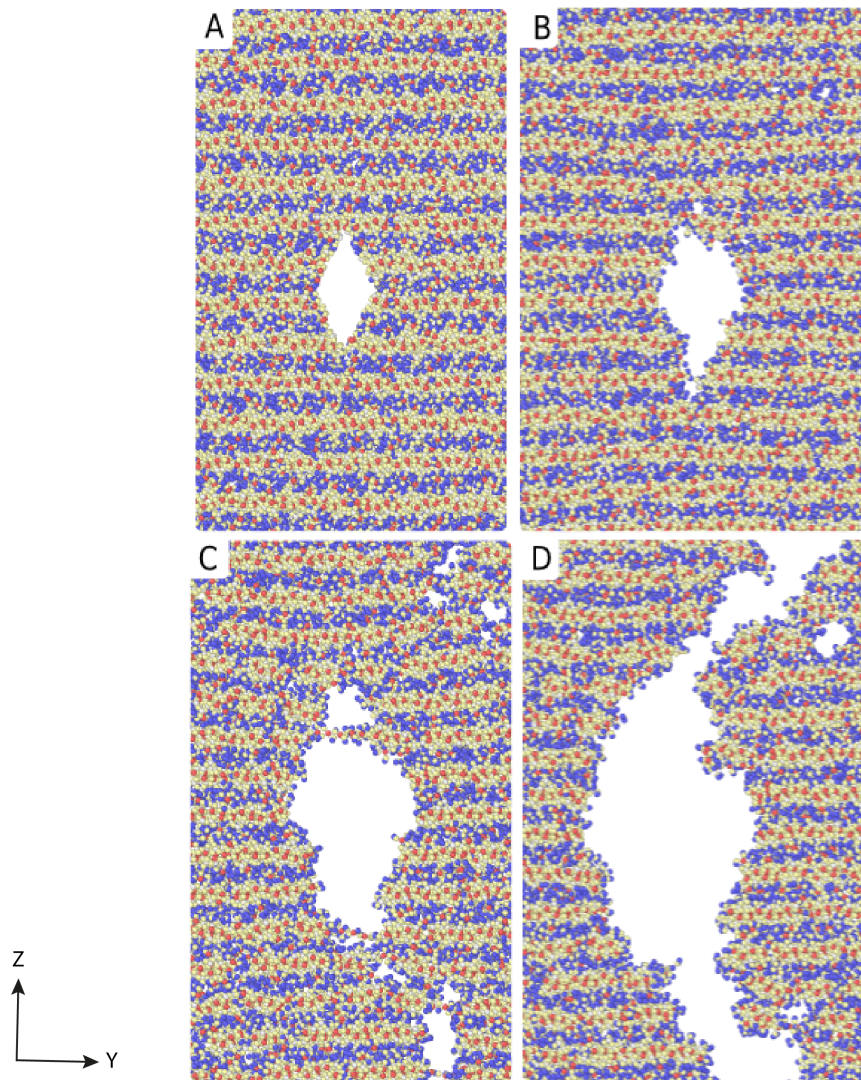


Figure 9.4: Deformation of T5Ca1 in the y-direction

To assess the effect on silicate chain length on the strength and fracture properties of C-S-H, T5Ca1 was compared with T2Ca1 in the y-direction at 300 K and a strain rate of 1×10^{-6} . The results are compared in Figure 9.5. While it appears that T2Ca1 has a higher tensile stress than T5Ca1, it is of the opinion that this is an artefact of the different simulation sizes. As mentioned in the methods section above, the T2Ca1 structure was unstable when the x-direction therefore a thicker sample had to be used. As it was expected that pentameric silicate chains would

provide more resistance to fracture and a greater tensile stress, further work must be carried out to confirm the effect of the silicate chain length on the fracture properties. Unfortunately, as a result, no conclusion can be drawn regarding the effect of polymer chain length on the fracture properties of C-S-H.

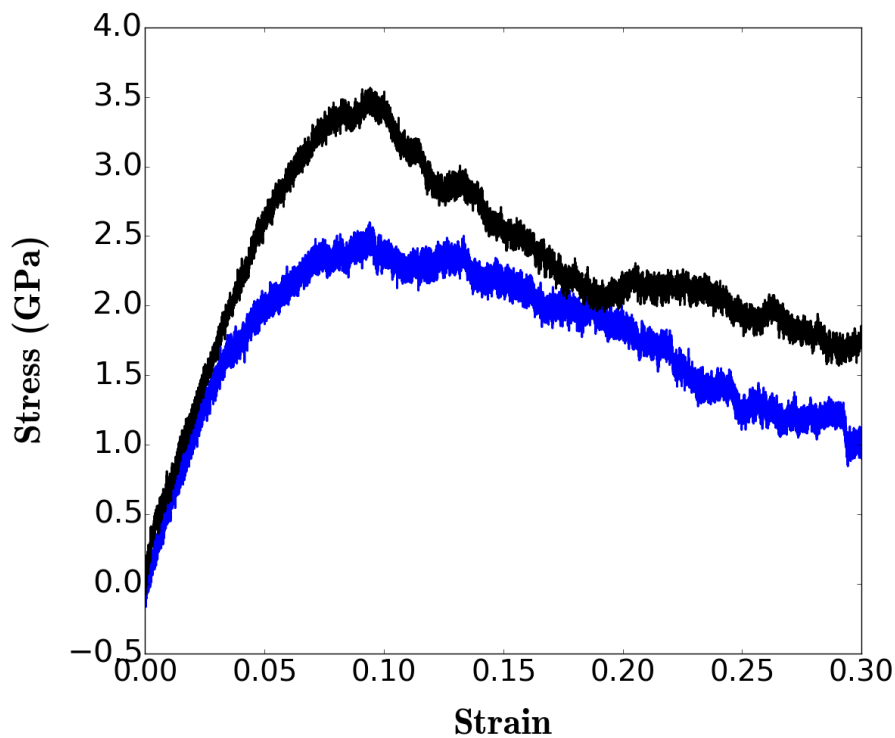


Figure 9.5: Comparison of stress-strain curve for T2Ca1 (black) and T5Ca1 (blue), 300K, 1×10^{-6}

Table 9.3: Fracture properties measured by ReaxFF for Rejmak structures

Structure	Direction	E (GPa)	C_{33}	Tensile Stress (GPa)	Strain at Tensile Stress
T5Ca1	z	40.6	86.6	1.25	0.06
T5Ca1	y	55.5	118.0	2.45	0.09
T2Ca1	y	64.0	82.0	3.5	0.11

9.5 Conclusions

In this final results chapter, preliminary simulations have been carried out with the aim of identifying nanoscale fracture properties of C-S-H. Stress-strain relationships of two hypothetical C-S-H models have been presented. It was confirmed that the z-direction, which is equivalent in this case to the crystal *c*-axis, was the weaker layer over the y-direction which involved generating a fracture pathway through the chains. While the presented method was able to predict the tensile stress and Young's modulus with reasonable accuracy, the method was unable to calculate fracture toughness due to the formation of multiple fracture points. Due to the limitations in the method, further work must be carried out to assess the effect of polymer chain length on the fracture and tensile properties for C-S-H.

Chapter 10

Conclusions and Future Work

This aim of this thesis was to determine if MD simulations can aid in the characterisation of C-S-H, determine any structure-property relationships in nanoscale C-S-H and to determine if realistic fracture properties can be inferred from MD simulations. In doing so, ice Ih was used as a proof of concept model due to the availability of experimental and simulation data for comparison.

This thesis was able to demonstrate that ReaxFF can describe the crystal structure of ice Ih well and is capable of describing a number of physical and mechanical properties such as density, heat capacity and elasticity. Similarly, by using ice Ih as a test model, this thesis was able to demonstrate that the macroscale experimental fracture toughness and fracture speeds could be reproduced in a MD simulation by using a plate-like structure and a diamond shaped initial crack, using the energy balance theory of fracture.

By using carefully validated MD methods, this thesis was able to give a new insight into the structure-property relationships of C-S-H. It was shown that by using MD in combination with ReaxFF, mC-S-H crystal structures could be produced with excellent accuracy and displayed improvements over other force fields. Over a narrow temperature range, heat capacities were measured and were in the same order of magnitude as experimentally measured heat capacities of C-S-H. Elasticity measurements of mC-S-H and C-S-H showed that the elastic properties of C-S-H depend on a number of factors including density and water

content. Finally, this thesis gave preliminary insights into fracture behaviour of a pentameric and dimeric C-S-H structure demonstrating the potential of MD to analyse and predict fracture behaviour which can be taken into consideration when synthesising C-S-H with the desired mechanical properties.

10.1 Key Findings

Despite the challenges encountered with modelling such complex materials, this thesis has made a number of contributions to the fields of cement and ice research. The contributions to the cement field are as follows:

1. Thermal expansion coefficients, heat capacity and equation of state has been quantified using ReaxFF for a number of C-S-H structures and ice Ih. None of which have been quantified before using ReaxFF, and in the case of C-S-H, only very limited studies have been carried out at all using MD to measure the thermodynamic properties.
2. A true validation has been carried out in terms of suitability of the simulation methods using ice Ih and careful consideration has been demonstrated throughout this thesis. In doing so, this thesis has presented useful and interesting data for the simulation of ice Ih demonstrating that the flexibility and reactive abilities of ReaxFF has additional benefits compared to the rigid models which are often used to describe water. There is the potential for ReaxFF to make significant impact in the literature of ice Ih modelling which could lead to the understanding of the properties of ice and water which cannot be inferred from experiment.
3. The elastic constants of C-S-H have been evaluated and available literature data has been considered. The elastic constants have been calculated for ReaxFF and C-S-H and structure-property relationships have been highlighted using a number of physical properties. Note that previous studies tend to focus only on the effect of individual properties on the elasticity. This thesis has concluded that the structure is related to composition of C-S-H and is influenced by a number of collated physical characteristics such as Ca/Si ratio, density and water content where C-S-H with the most resistant mechanical properties should have a high density, low water to silicate ratio and long silicate chains.

4. Insights into the atomic deformation behaviour of C-S-H which cannot be achieved by current experimental methods have been given. It has been shown that large interlayer spacings are reduced under isotropic pressure.
5. By combining a number of fracture methods from the literature, a method has been designed which enables the calculation of fracture speeds and fracture toughness from the same simulation and for ice Ih has shown improvements over other methods in the literature. This finding is significant and will have an impact amongst ice researchers and glaciologists as it has shown that there is potential for realistic fracture properties to be inferred from MD.
6. Fracture processes of Rejmak structures have been lightly explored, demonstrating that at the nanoscale, C-S-H does not produce a single fracture pathway, meaning that this method for calculating fracture toughness may not be used for C-S-H. From the results, it cannot be inferred if this is related to the C-S-H structure or if the method simply needs to be run with a much lower tensile strain rate.

10.2 Limitations of this Work

As is the case with every research topic, there are some limitations in this research. By identifying these limitations, the results and conclusions can become more meaningful and aspects of future work can be highlighted.

1. The first and most significant limitation is that MD is a method to *simulate* the properties of a material. While the methods can be validated, as done in the thesis, there will always be deviations from reality as force field methods can only provide simple descriptions of a material.
2. Classical simulations cannot take into account quantum effects which become significant with decreasing scale. Similarly, as is the case with any model, MD is only as good as the input parameters will allow.
3. While it has been shown that ReaxFF is capable of describing C-S-H and ice Ih, force field methods are only approximations therefore it is expected that the results will differ from experimental data to an extent. Furthermore, by using crystal structures derived from XRD, it is only possible to simulate an idealised,

averaged crystal structure, therefore the structure is only an estimate of the true crystal structure.

4. Although MD and statistical mechanics can relate to macroscale properties such as heat capacity, density and elasticity, it cannot describe the natural defects of an atomic structure unless defects are explicitly introduced. Another limitation of using MD to predict the properties of complex structures like C-S-H and ice Ih is that their properties are influenced by the hierarchical nature therefore the relation of nanoscale to macroscale properties must be considered carefully. This work compares to a number of simulation studies of ice Ih and C-S-H to benchmark ReaxFF predictions however it relies on other simulation studies being well validated which is not the case for C-S-H due to the lack of experimental data. However, it is hoped that the contributions in this thesis will be compared to experimental data when it becomes available.

5. Finally, although the method for calculating elastic properties having been rigorously validated in this thesis, there is much debate in the literature over the best fracture protocol. The method designed in this thesis has reproduced accurate fracture toughness and crack speeds for ice Ih and C-S-H tensile stresses, however, it is possible that the nanoscale fracture processes of real materials may differ from the predicted process in this thesis.

10.3 Conclusions and Future Work

The work in this thesis has answered a number of questions relating to the mechanical properties of ice Ih and C-S-H, however, along the way, further questions which lead on from the work of this thesis should be addressed in future work. This final section draws attention to some interesting work for future research.

In Chapter 3 and Chapter 5, it was mentioned that, despite the many force fields that have been devised to model the properties of ice and water, there is no single force field which can model the full phase diagram. In most cases, the coexistence curve and melting point of ice Ih have been incorrectly predicted by the current models. While checking the melting point of ice Ih was out of the scope of this work, it would be very interesting to identify the melting point as

predicted by ReaxFF. Melting point determinations by experiment are relatively simple, however, in MD simulations, measuring the melting point is a challenge.

In Chapter 6, tensile fracture processes were investigated for ice Ih. A size effect study was not carried out since such a large system was used. However, for optimisation purposes, a size effect study could identify a critical size and there is a possibility that smaller simulations could lead to the same conclusions. It would be interesting, and of great importance in glaciology, if fracture processes close to the melting point of ice could be predicted. Additionally, in the interest of multiscale modelling it would be interesting to see how the measured mechanical properties influence FEM if used as input parameters. This may aid in the development of a model which can describe ice fracture across multiple scales.

Chapter 7 exemplified equilibrium properties of a number of C-S-H models. Thermal properties of C-S-H are known to change at different temperatures due to the change in structure as a result of water evacuation from the interlayer. It was mentioned in Chapter 7 that Rodriguez et al. observed that the heat capacity changed between upon transformation into wollastonite at high temperatures. Further simulation work to determine the heat capacity at high temperatures could infer structural changes by changing the structure and measuring the response of the heat capacity. Additionally, free energy methods could be used to model phase changes which may give additional insights into the thermal behaviour of C-S-H and could provide useful data for the employment of C-S-H in extreme conditions such as in nuclear power plants.

The elastic properties of C-S-H were determined in Chapter 8, however, it was noted that the elastic properties change depending on the simulation method. By collaborating with experimentalists, it would be very interesting to see the effect of targeted synthesis of C-S-H to have a particular Ca/Si ratio, density and water content could effect the BMEoS. However, this relies upon the ability of current XRD methods to measure accurately the lattice constants of the C-S-H nanocrystals.

Finally, Chapter 8 introduced some preliminary fracture data for C-S-H. This chapter showed that the fracture protocol designed in this thesis may not be suitable for C-S-H as the method was unable to produce a single fracture pathway.

Further work is required at a lower strain rate to determine if the strain rate was too high or if multiple deformation points is the true failure response of C-S-H. This should be taken into consideration in the early project stages as significant computational resources will be required to run simulations of this size at a lower strain rate.

Overall, this thesis has highlighted the variability that exists in simulation outputs for both ice Ih and C-S-H. In particular, this thesis has shown the development and progress which has been made over the past four years in simulation methods of cementitious materials and with careful consideration of future methods, this thesis has shown the potential for MD methods to be revolutionary in cement research.

Bibliography

- ¹E. Benhelal, G. Zahedi, E. Shamsaei, and A. Bahadori, “Global strategies and potentials to curb co2 emissions in cement industry”, *Journal of Cleaner Production*, **51**, 142–161 (2013).
- ²J. F. Ouyang and R. P. A. Bettens, “Modelling water: a lifetime enigma”, *CHIMIA International Journal for Chemistry*, **69**, 3, 104–111 (2015).
- ³H. Taylor, *Cement chemistry*, 2nd edition (Thomas Telford Publishing, 1997).
- ⁴H. Manzano, J. S. Dolado, A. Guerrero, and A. Ayuela, “Mechanical properties of crystalline calciumsilicatehydrates: comparison with cementitious csh gels”, *physica status solidi (a)*, **204**, 6, 1775–1780.
- ⁵H. Manzano, J. Dolado, and A. Ayuela, “Elastic properties of the main species present in portland cement pastes”, *Acta Materialia*, **57**, 5, 1666–1674 (2009).
- ⁶S. Grangeon, F. Claret, C. Roosz, T. Sato, S. Gaboreau, and Y. Linard, “Structure of nanocrystalline calcium silicate hydrates: insights from xray diffraction, synchrotron xray absorption and nuclear magnetic resonance”, *Journal of Applied Crystallography*, **49**, 3, 771–783.
- ⁷M. Schneider, M. Romer, M. Tschudin, and H. Bolio, “Sustainable cement productionpresent and future”, *Cement and Concrete Research*, **41**, 7, Special Issue: 13th International Congress on the Chemistry of Cement, 642–650 (2011).
- ⁸G. VD, “Ancient, modern and future concretes”, *Proc. 1 st Int. Conf. on Alkaline Cements and Concretes, VIPOL, Kiev, Ukraine*, 1–9 (1994).

- ⁹E. Benhelal, G. Zahedi, E. Shamsaei, and A. Bahadori, “Global strategies and potentials to curb co2 emissions in cement industry”, *Journal of Cleaner Production*, **51**, 142–161 (2013).
- ¹⁰F. H. Wittmann, “Structure of concrete and crack formation”, *Fracture of non-metallic materials: proceeding of the 5th advanced seminar on fracture mechanics, joint research centre, ispra, italy, 14–18 october 1985*, edited by K. P. Herrmann and L. H. Larsson (Springer Netherlands, Dordrecht, 1987), 309–340.
- ¹¹K. E. Drexler, “Nanotechnology: from feynman to funding”, *Bulletin of Science, Technology & Society*, **24**, 1, 21–27 (2004).
- ¹²E. Bonaccorsi, S. Merlino, and H. Taylor, “The crystal structure of jennite, $\text{Ca}_9\text{Si}_6\text{O}_{18}(\text{OH})_6\text{H}_2\text{O}$ ”, *Cement and Concrete Research*, **34**, 9, H. F. W. Taylor Commemorative Issue, 1481–1488 (2004).
- ¹³E. Bonaccorsi, S. Merlino, and A. R. Kampf, “The Crystal Structure of Tobermorite 14 (Plombierite), a CSH Phase”, *Journal of the American Ceramic Society*, **88**, 3, 505–512 (2005).
- ¹⁴R. J.-M. Pellenq, A. Kushima, R. Shahsavari, K. J. Van Vliet, M. J. Buehler, S. Yip, and F.-J. Ulm, “A realistic molecular model of cement hydrates”, *Proceedings of the National Academy of Sciences*, **106**, 38, 16102–16107 (2009).
- ¹⁵M. Abdolhosseini Qomi, K. Krakowiak, M. Bauchy, K. Stewart, R. Shahsavari, D. Jagannathan, D. Brommer, A. Baronnet, M. Buehler, S. Yip, F.-J. Ulm, K. Van Vliet, and R.-M. Pellenq, “Combinatorial molecular optimization of cement hydrates”, *Nature Communications*, **5**, cited By 96 (2014) 10.1038/ncomms5960.
- ¹⁶P. D. Tennis and H. M. Jennings, “A model for two types of calcium silicate hydrate in the microstructure of portland cement pastes”, *Cement and Concrete Research*, **30**, 6, 855–863 (2000).
- ¹⁷H. M. Jennings, “Colloid model of csh and implications to the problem of creep and shrinkage”, *Materials and Structures*, **37**, 1, 59–70 (2004).

- ¹⁸H. M. Jennings, J. J. Thomas, J. S. Gevrenov, G. Constantinides, and F.-J. Ulm, “A multi-technique investigation of the nanoporosity of cement paste”, *Cement and Concrete Research*, **37**, 3, Cementitious Materials as model porous media: Nanostructure and Transport processes, 329–336 (2007).
- ¹⁹G. Constantinides, F. J. Ulm, and K. Van Vliet, “On the use of nanoindentation for cementitious materials”, *Materials and Structures*, **36**, 3, 191–196 (2003).
- ²⁰F. J. Ulm, G. Constantinides, and F. H. Heukamp, “Is concrete a poromechanics materials?—a multiscale investigation of poroelastic properties”, *Materials and Structures*, **37**, 1, 43–58 (2004).
- ²¹M. J. DeJong and F.-J. Ulm, “The nanogranular behavior of c-s-h at elevated temperatures (up to 700 c)”, *Cement and Concrete Research*, **37**, 1, 1–12 (2007).
- ²²S.-U. Sezen, C. S. Rosie, B. C. J., W. Hans-Rudolf, and M. P. J. M., “Compositional evolution of calcium silicate hydrate (csh) structures by total x-ray scattering”, *Journal of the American Ceramic Society*, **95**, 2, 793–798.
- ²³E. T. Rodriguez, K. Garbev, D. Merz, L. Black, and I. G. Richardson, “Thermal stability of c-s-h phases and applicability of richardson and groves’ and richardson c-(a)-s-h(i) models to synthetic c-s-h”, *Cement and Concrete Research*, **93**, 45–56 (2017).
- ²⁴L. B. Skinner, S. R. Chae, C. J. Benmore, H. R. Wenk, and P. J. M. Monteiro, “Nanostructure of calcium silicate hydrates in cements”, *Phys. Rev. Lett.*, **104**, 195502 (2010).
- ²⁵S. Grangeon, A. Fernandez-Martinez, A. Baronnet, N. Marty, A. Poulain, E. Elkam, C. Roosz, S. Gaboreau, P. Henocq, and F. Claret, “Quantitative xray pair distribution function analysis of nanocrystalline calcium silicate hydrates: a contribution to the understanding of cement chemistry”, *Journal of Applied Crystallography*, **50**, 1, 14–21.
- ²⁶G. Krassimir, B. Gnter, B. Marc, B. Leon, and S. Peter, “Cell dimensions and composition of nanocrystalline calcium silicate hydrate solid solutions. part 1: synchrotron-based x-ray diffraction”, *Journal of the American Ceramic Society*, **91**, 9, 3005–3014.

- ²⁷A. Kumar, B. J. Walder, A. Kunhi Mohamed, A. Hofstetter, B. Srinivasan, A. J. Rossini, K. Scrivener, L. Emsley, and P. Bowen, “The atomic-level structure of cementitious calcium silicate hydrate”, *Journal of Physical Chemistry C*, **121**, 32, Cited By :12, 17188–17196 (2017).
- ²⁸I. G. Richardson, “Model structures for C-(A)-S-H(I)”, *Acta Crystallographica Section B*, **70**, 6, 903–923 (2014).
- ²⁹N. C. M. Marty, S. Grangeon, F. Warmont, and C. Lerouge, “Alteration of nanocrystalline calcium silicate hydrate (c-s-h) at ph 9.2 and room temperature: a combined mineralogical and chemical study”, *Mineralogical Magazine*, **79**, 2, 437 (2015).
- ³⁰S. MERLINO, E. BONACCORSI, and T. ARMBRUSTER, “The real structures of clinotobermorite and tobermorite 9 a : od character, polytypes, and structural relationships”, *European Journal of Mineralogy*, **12**, 2, 411 (2000).
- ³¹S. Grangeon, F. Claret, Y. Linard, and C. Chiaberge, “X-ray diffraction: a powerful tool to probe and understand the structure of nanocrystalline calcium silicate hydrates”, *Acta Crystallographica Section B*, **69**, 5, 465–473 (2013).
- ³²A. J. Allen, J. J. Thomas, and H. M. Jennings, “Composition and density of nanoscale calcium–silicate–hydrate in cement”, *Nature materials*, **6**, 4, 311 (2007).
- ³³H F. W. Taylor and J W. Howison, “Relationship between calcium silicates and clay minerals”, **3**, 98–111 (1956).
- ³⁴J. J. Chen, J. J. Thomas, H. F. Taylor, and H. M. Jennings, “Solubility and structure of calcium silicate hydrate”, *Cement and Concrete Research*, **34**, 9, H. F. W. Taylor Commemorative Issue, 1499 –1519 (2004).
- ³⁵I. Richardson and G. Groves, “Models for the composition and structure of calcium silicate hydrate (csh) gel in hardened tricalcium silicate pastes”, *Cement and Concrete Research*, **22**, 6, 1001 –1010 (1992).
- ³⁶T. C. Powers and T. L. Brownyard, “Studies of the physical properties of hardened portland cement paste”, *Journal proceedings*, Vol. 43, 9 (1946), 101–132.

- ³⁷P. Bonnaud, Q. Ji, and K. Van Vliet, “Effects of elevated temperature on the structure and properties of calcium-silicate-hydrate gels: the role of confined water”, *Soft Matter*, **9**, 28, cited By 14, 6418–6429 (2013).
- ³⁸C. Roosz, S. Gaboreau, S. Grangeon, D. Prt, V. Montouillout, N. Maubec, S. Ory, P. Blanc, P. Vieillard, and P. Henocq, “Distribution of water in synthetic calcium silicate hydrates”, *Langmuir*, **32**, 27, PMID: 27281114, 6794–6805 (2016).
- ³⁹P. Rejmak, J. S. Dolado, M. J. Stott, and A. Ayuela, “²⁹Si NMR in Cement: A Theoretical Study on Calcium Silicate Hydrates”, *J. Phys. Chem. C*, **116**, 17, 9755–9761 (2012).
- ⁴⁰X. Cong and R. J. Kirkpatrick, “¹⁷O mas nmr investigation of the structure of calcium silicate hydrate gel”, *Journal of the American Ceramic Society*, **79**, 6, 1585–1592.
- ⁴¹E. Pustovgar, R. P. Sangodkar, A. S. Andreev, M. Palacios, B. F. Chmelka, R. J. Flatt, and J.-B. d. de Lacaillerie, “Understanding silicate hydration from quantitative analyses of hydrating tricalcium silicates”, *Nature communications*, **7**, 10952 (2016).
- ⁴²D. E. Macphee, K. Luke, F. P. Glasser, and E. E. Lachowski, “Solubility and aging of calcium silicate hydrates in alkaline solutions at 25c”, *Journal of the American Ceramic Society*, **72**, 4, 646–654.
- ⁴³C. Plassard, E. Lesniewska, I. Pochard, and A. Nonat, “Intrinsic Elastic Properties of Calcium Silicate Hydrates by Nanoindentation”, 12th International Congress on the Chemistry of Cement, edited by J. M. J.J. Beaudoin and L. Raki (July 2007), 44.
- ⁴⁴F. Pelisser, P. J. P. Gleize, and A. Mikowski, “Effect of the ca/si molar ratio on the micro/nanomechanical properties of synthetic c-s-h measured by nanoindentation”, *The Journal of Physical Chemistry C*, **116**, 32, 17219–17227 (2012).
- ⁴⁵G. Constantinides and F.-J. Ulm, “The nanogranular nature of c-s-h”, *Journal of the Mechanics and Physics of Solids*, **55**, 1, 64–90 (2007).

- ⁴⁶P Acker, “Micromechanical analysis of creep and shrinkage mechanisms”, **1**, 15–25 (2001).
- ⁴⁷J. J. Hughes and P. Trtik, “Micro-mechanical properties of cement paste measured by depth-sensing nanoindentation: a preliminary correlation of physical properties with phase type”, *Materials Characterization*, **53**, 2, EMABM 2003: 9th Euroseminar on Microscopy Applied to Building Materials, 223–231 (2004).
- ⁴⁸W. Zhu, J. J. Hughes, N. Bicanic, and C. J. Pearce, “Nanoindentation mapping of mechanical properties of cement paste and natural rocks”, *Materials characterization*, **58**, 11-12, 1189–1198 (2007).
- ⁴⁹M. Vandamme and F.-J. Ulm, “Nanogranular origin of concrete creep”, *Proceedings of the National Academy of Sciences*, **106**, 26, 10552–10557 (2009).
- ⁵⁰H. Manzano, R. J. M. Pellenq, F.-J. Ulm, M. J. Buehler, and A. C. T. van Duin, “Hydration of Calcium Oxide Surface Predicted by Reactive Force Field Molecular Dynamics”, *Langmuir*, **28**, 9, 4187–4197 (2012).
- ⁵¹J. Moon, S. Yoon, and P. J. Monteiro, “Mechanical properties of jennite: a theoretical and experimental study”, *Cement and Concrete Research*, **71**, 106–114 (2015).
- ⁵²R. Shahsavari, M. J. Buehler, R. J.-M. Pellenq, and F.-J. Ulm, “First-principles study of elastic constants and interlayer interactions of complex hydrated oxides: case study of tobermorite and jennite”, *Journal of the American Ceramic Society*, **92**, 10, 2323–2330 (2009).
- ⁵³S A. Hamid, “The crystal structure of the 11 natural tobermorite $ca_{2.25}[si_{3o}7.5(oh)1.5]1h_{2o}$ ”, **154**, 189–198 (1981).
- ⁵⁴H. F. TAYLOR, “Proposed structure for calcium silicate hydrate gel”, *Journal of the American Ceramic Society*, **69**, 6, 464–467.
- ⁵⁵J. D. Gale, “Gulp: a computer program for the symmetry-adapted simulation of solids”, *J. Chem. Soc., Faraday Trans.*, **93**, 629–637 (1997).
- ⁵⁶I. G. Richardson, “The importance of proper crystal-chemical and geometrical reasoning demonstrated using layered single and double hydroxides”, *Acta Crystallographica Section B*, **69**, 2, 150–162 (2013).

- ⁵⁷F. Brunet, P. Bertani, T. Charpentier, A. Nonat, and J. Virlet, “Application of ^{29}Si homonuclear and $^1\text{H}^{29}\text{Si}$ heteronuclear nmr correlation to structural studies of calcium silicate hydrates”, *The Journal of Physical Chemistry B*, **108**, 40, 15494–15502 (2004).
- ⁵⁸R. T. Cygan, J.-J. Liang, and A. G. Kalinichev, “Molecular models of hydroxide, oxyhydroxide, and clay phases and the development of a general force field”, *The Journal of Physical Chemistry B*, **108**, 4, 1255–1266 (2004).
- ⁵⁹H. Sun, “Compass: an ab initio force-field optimized for condensed-phase applications overview with details on alkane and benzene compounds”, *The Journal of Physical Chemistry B*, **102**, 38, 7338–7364 (1998).
- ⁶⁰A. C. T. van Duin, S. Dasgupta, F. Lorant, and W. A. Goddard, “Reaxff: a reactive force field for hydrocarbons”, *The Journal of Physical Chemistry A*, **105**, 41, 9396–9409 (2001).
- ⁶¹M. Bauchy, M. J. Abdolhosseini Qomi, C. Bichara, F.-J. Ulm, and R. J.-M. Pellenq, “Nanoscale Structure of Cement: the Viewpoint of Rigidity Theory”, *The Journal of Physical Chemistry C* (2014).
- ⁶²D. Hou, T. Zhao, H. Ma, and Z. Li, “Reactive molecular simulation on water confined in the nanopores of the calcium silicate hydrate gel: structure, reactivity, and mechanical properties”, *Journal of Physical Chemistry C*, **119**, 3, cited By 55, 1346–1358 (2015).
- ⁶³N. Zhang and R. Shahsavari, “Balancing strength and toughness of calcium-silicate-hydrate via random nanovoids and particle inclusions: atomistic modeling and statistical analysis”, *Journal of the Mechanics and Physics of Solids*, **96**, cited By 17, 204–222 (2016).
- ⁶⁴S. Plimpton, “Fast parallel algorithms for short-range molecular dynamics”, *Journal of Computational Physics*, **117**, 1, 1–19 (1995).
- ⁶⁵R. J. Angel, J. M. Jackson, H. J. Reichmann, and S. Speziale, “Elasticity measurements on minerals: a review”, *European Journal of Mineralogy*, **21**, 3, 525–550 (2009).

- ⁶⁶D. Hou, T. Zhao, P. Wang, Z. Li, and J. Zhang, “Molecular dynamics study on the mode I fracture of calcium silicate hydrate under tensile loading”, *Engineering Fracture Mechanics*, **131**, cited By 11, 557–569 (2014).
- ⁶⁷M. Bauchy, H. Laubie, M. Abdolhosseini Qomi, C. Hoover, F.-J. Ulm, and R.-M. Pellenq, “Fracture toughness of calcium-silicate-hydrate from molecular dynamics simulations”, *Journal of Non-Crystalline Solids*, **419**, cited By 39, 58–64 (2015).
- ⁶⁸P. G. Debenedetti, “Supercooled and glassy water”, *Journal of Physics: Condensed Matter*, **15**, 45, R1669 (2003).
- ⁶⁹S. Izadi, R. Anandakrishnan, and A. V. Onufriev, “Building water models: a different approach”, *The Journal of Physical Chemistry Letters*, **5**, 21, PMID: 25400877, 3863–3871 (2014).
- ⁷⁰W. F. Kuhs and M. S. Lehmann, “The structure of the ice Ih by neutron diffraction”, *The Journal of Physical Chemistry*, **87**, 21, 4312–4313 (1983).
- ⁷¹T. Bartels-Rausch, V. Bergeron, J. H. E. Cartwright, R. Escribano, J. L. Finney, H. Grothe, P. J. Gutiérrez, J. Haapala, W. F. Kuhs, J. B. C. Pettersson, S. D. Price, C. I. Sainz-Díaz, D. J. Stokes, G. Strazzulla, E. S. Thomson, H. Trinks, and N. Uras-Aytemiz, “Ice structures, patterns, and processes: a view across the icefields”, *Rev. Mod. Phys.*, **84**, 885–944 (2012).
- ⁷²C. Knight, S. J. Singer, J.-L. Kuo, T. K. Hirsch, L. Ojamäe, and M. L. Klein, “Hydrogen bond topology and the ice VII/VIII and Ih/XI proton ordering phase transitions”, *Phys. Rev. E*, **73**, 056113 (2006).
- ⁷³E. G. Noya, C. Menduía, J. L. Aragoñes, and C. Vega, “Equation of state, thermal expansion coefficient, and isothermal compressibility for ices Ih, II, III, V, and VI, as obtained from computer simulation”, *The Journal of Physical Chemistry C*, **111**, 43, 15877–15888 (2007).
- ⁷⁴C. Vega and J. L. F. Abascal, “Simulating water with rigid non-polarizable models: a general perspective”, *Phys. Chem. Chem. Phys.*, **13**, 19663–19688 (2011).
- ⁷⁵E. M. Schulson, “The structure and mechanical behavior of ice”, *JOM*, **51**, 2, 21–27 (1999).

- ⁷⁶R. B. Alley, “Flow-law hypotheses for ice-sheet modeling”, *Journal of Glaciology*, **38**, 129, 245–256 (1992).
- ⁷⁷A.-M. Kietzig, S. G. Hatzikiriakos, and P. Englezos, “Physics of ice friction”, *Journal of Applied Physics*, **107**, 8, 081101 (2010).
- ⁷⁸H. H. G. Jellinek and R. Brill, “Viscoelastic properties of ice”, *Journal of Applied Physics*, **27**, 10, 1198–1209 (1956).
- ⁷⁹R. Alizadeh, J. J. Beaudoin, and L. Raki, “Viscoelastic nature of calcium silicate hydrate”, *Cement and Concrete Composites*, **32**, 5, 369–376 (2010).
- ⁸⁰P. H. Gammon, H. Kiefte, and M. J. Clouter, “Elastic constants of ice samples by brillouin spectroscopy”, *The Journal of Physical Chemistry*, **87**, 21, 4025–4029 (1983).
- ⁸¹R. E. Gagnon, H. Kiefte, M. J. Clouter, and E. Whalley, “Elastic constants of ice Ih, up to 2.8 kbar, by brillouin spectroscopy”, *J. Phys. Colloques*, **48**, C1, 23–28 (1987).
- ⁸²B. Michel, *Ice mechanics* (Presses de l’université Laval, 1978).
- ⁸³R. J. Evans and N. Untersteiner, “Thermal cracks in floating ice sheets”, *Journal of Geophysical Research*, **76**, 3, 694–703 (1971).
- ⁸⁴M. Rist, “High-stress ice fracture and friction”, *The Journal of Physical Chemistry B*, **101**, 32, 6263–6266 (1997).
- ⁸⁵E. M. Schulson, S. G. Hoxie, and W. A. Nixon, “The tensile strength of cracked ice”, *Philosophical Magazine A*, **59**, 2, 303–311 (1989).
- ⁸⁶E. M. Schulson, P. N. Lim, and R. W. Lee, “A brittle to ductile transition in ice under tension”, *Philosophical Magazine A*, **49**, 3, 353–363 (1984).
- ⁸⁷S. A. Snyder, E. M. Schulson, and C. E. Renshaw, “Effects of prestrain on the ductile-to-brittle transition of ice”, *Acta Materialia*, **108**, 110–127 (2016).
- ⁸⁸J. Jacka, “E.m. schulson and p. duval. 2009. creep and fracture of ice. cambridge, etc., cambridge university press. 401 pp. isbn-10: 0-521806-20-6, isbn-13: 978-0-521-80620-6, hardback, 69/us134.”, *Journal of Glaciology*, **57**, 202, 385–386 (2011).

- ⁸⁹J. Barker and R. Watts, “Structure of water; a monte carlo calculation”, *Chemical Physics Letters*, **3**, 3, 144–145 (1969).
- ⁹⁰A. Rahman and F. H. Stillinger, “Molecular dynamics study of liquid water”, *The Journal of Chemical Physics*, **55**, 7, 3336–3359 (1971).
- ⁹¹B. Guillot, “A reappraisal of what we have learnt during three decades of computer simulations on water”, *Journal of Molecular Liquids*, **101**, 1, *Molecular Liquids. Water at the New Millenium*, 219–260 (2002).
- ⁹²T. R. Forester and W. Smith, “Shake, rattle, and roll: efficient constraint algorithms for linked rigid bodies”, *Journal of Computational Chemistry*, **19**, 1, 102–111.
- ⁹³J.-P. Ryckaert, G. Ciccotti, and H. J. Berendsen, “Numerical integration of the cartesian equations of motion of a system with constraints: molecular dynamics of n-alkanes”, *Journal of Computational Physics*, **23**, 3, 327–341 (1977).
- ⁹⁴H. J. C. Berendsen, J. P. M. Postma, W. F. van Gunsteren, and J. Hermans, “Interaction models for water in relation to protein hydration”, *Intermolecular forces: proceedings of the fourteenth jerusalem symposium on quantum chemistry and biochemistry held in jerusalem, israel, april 13–16, 1981*, edited by B. Pullman (Springer Netherlands, Dordrecht, 1981), 331–342.
- ⁹⁵H. J. C. Berendsen, J. R. Grigera, and T. P. Straatsma, “The missing term in effective pair potentials”, *The Journal of Physical Chemistry*, **91**, 24, 6269–6271 (1987).
- ⁹⁶W. L. Jorgensen, J. Chandrasekhar, J. D. Madura, R. W. Impey, and M. L. Klein, “Comparison of simple potential functions for simulating liquid water”, *The Journal of Chemical Physics*, **79**, 2, 926–935 (1983).
- ⁹⁷J. L. F. Abascal, E. Sanz, R. G. Fernandez, and C. Vega, “A potential model for the study of ices and amorphous water: tip4p/ice”, *The Journal of Chemical Physics*, **122**, 23, 234511 (2005).
- ⁹⁸W. L. Jorgensen and J. D. Madura, “Temperature and size dependence for monte carlo simulations of tip4p water”, *Molecular Physics*, **56**, 6, 1381–1392 (1985).

- ⁹⁹M. W. Mahoney and W. L. Jorgensen, “A five-site model for liquid water and the reproduction of the density anomaly by rigid, nonpolarizable potential functions”, *The Journal of Chemical Physics*, **112**, 20, 8910–8922 (2000).
- ¹⁰⁰M. A. Gonzalez and J. L. F. Abascal, “A flexible model for water based on tip4p/2005”, *The Journal of Chemical Physics*, **135**, 22, 224516 (2011).
- ¹⁰¹Y. Wu, H. L. Tepper, and G. A. Voth, “Flexible simple point-charge water model with improved liquid-state properties”, *The Journal of Chemical Physics*, **124**, 2, 024503 (2006).
- ¹⁰²D. Frenkel and A. J. C. Ladd, “New monte carlo method to compute the free energy of arbitrary solids. application to the fcc and hcp phases of hard spheres”, *The Journal of Chemical Physics*, **81**, 7, 3188–3193 (1984).
- ¹⁰³C. Vega, M. Martin-Conde, and A. Patrykiewicz, “Absence of superheating for ice ih with a free surface: a new method of determining the melting point of different water models”, *Molecular Physics*, **104**, 22-24, 3583–3592 (2006).
- ¹⁰⁴C. Vega, E. Sanz, and J. L. F. Abascal, “The melting temperature of the most common models of water”, *The Journal of Chemical Physics*, **122**, 11, 114507 (2005).
- ¹⁰⁵C. Vega, J. L. F. Abascal, E. Sanz, L. G. MacDowell, and C. McBride, “Can simple models describe the phase diagram of water?”, *Journal of Physics: Condensed Matter*, **17**, 45, S3283 (2005).
- ¹⁰⁶C. S. W, “Statistical nanomechanics of ice and effect of embedded carbon dioxide”, *International Conference on Offshore Mechanics and Arctic Engineering*, **8** 10.1115/OMAE2015-4102.
- ¹⁰⁷Z. Qin and M. J. Buehler, “Carbon dioxide enhances fragility of ice crystals”, *Journal of Physics D: Applied Physics*, **45**, 44, 445302 (2012).
- ¹⁰⁸H. Liu and K. Miller, “Fracture toughness of fresh-water ice”, *Journal of glaciology*, **22**, 86, 135–143 (1979).
- ¹⁰⁹M. Yasui, E. M. Schulson, and C. E. Renshaw, “Experimental studies on mechanical properties and ductile-to-brittle transition of ice-silica mixtures: young’s modulus, compressive strength, and fracture toughness”, *Journal of Geophysical Research: Solid Earth*, **122**, 8, 6014–6030.

- ¹¹⁰C. Vega, M. M. Conde, C. McBride, J. L. F. Abascal, E. G. Noya, R. Ramirez, and L. M. Ses, “Heat capacity of water: a signature of nuclear quantum effects”, *The Journal of Chemical Physics*, **132**, 4, 046101 (2010).
- ¹¹¹K. Röttger, A. Endriss, J. Ihringer, S. Doyle, and W. F. Kuhs, “Lattice constants and thermal expansion of H₂O and D₂O ice *Ih* between 10 and 265 K”, *Acta Crystallographica Section B*, **50**, 6, 644–648 (1994).
- ¹¹²M. J. Buehler, H. Tang, A. C. van Duin, and W. A. Goddard III, “Threshold crack speed controls dynamical fracture of silicon single crystals”, *Physical Review Letters*, **99**, 16, 165502 (2007).
- ¹¹³J. Weertman, “Creep deformation of ice”, *Annual Review of Earth and Planetary Sciences*, **11**, 1, 215–240 (1983).
- ¹¹⁴H. H. G. Jellinek and R. Brill, “Viscoelastic properties of ice”, *Journal of Applied Physics*, **27**, 10, 1198–1209 (1956).
- ¹¹⁵M. Vandamme and F.-J. Ulm, “Nanoindentation investigation of creep properties of calcium silicate hydrates”, *Cement and Concrete Research*, **52**, 38–52 (2013).
- ¹¹⁶A. Morshedifard, S. Masoumi, and M. A. Qomi, “Nanoscale origins of creep in calcium silicate hydrates”, *Nature communications*, **9**, 1, 1785 (2018).
- ¹¹⁷M. P. Allen and D. J. Tildesley, *Computer simulation of liquids* (Oxford university press, 2017).
- ¹¹⁸M. González, “Force fields and molecular dynamics simulations”, *École thématique de la Société Française de la Neutronique*, **12**, 169–200 (2011).
- ¹¹⁹B. Devine, T.-R. Shan, Y.-T. Cheng, A. J. H. McGaughey, M. Lee, S. R. Phillpot, and S. B. Sinnott, “Atomistic simulations of copper oxidation and cu/cu₂o interfaces using charge-optimized many-body potentials”, *Phys. Rev. B*, **84**, 125308 (2011).
- ¹²⁰J. Tersoff, “Modeling solid-state chemistry: interatomic potentials for multi-component systems”, *Phys. Rev. B*, **39**, 5566–5568 (1989).
- ¹²¹A. C. T. van Duin, A. Strachan, S. Stewman, Q. Zhang, X. Xu, and W. A. Goddard, “Reaxffsio reactive force field for silicon and silicon oxide systems”, *The Journal of Physical Chemistry A*, **107**, 19, 3803–3811 (2003).

- ¹²²A. C. T. van Duin, S. Dasgupta, F. Lorant, and W. A. Goddard, “Reaxff: a reactive force field for hydrocarbons”, *The Journal of Physical Chemistry A*, **105**, 41, 9396–9409 (2001).
- ¹²³L. Liu, A. Jaramillo-Botero, W. A. Goddard, and H. Sun, “Development of a reaxff reactive force field for ettringite and study of its mechanical failure modes from reactive dynamics simulations”, *The Journal of Physical Chemistry A*, **116**, 15, PMID: 22413941, 3918–3925 (2012).
- ¹²⁴K. Chenoweth, A. C. T. van Duin, and W. A. Goddard, “Reaxff reactive force field for molecular dynamics simulations of hydrocarbon oxidation”, *The Journal of Physical Chemistry A*, **112**, 5, PMID: 18197648, 1040–1053 (2008).
- ¹²⁵T. P. Senftle, S. Hong, M. M. Islam, S. B. Kylasa, Y. Zheng, Y. K. Shin, C. Junkermeier, R. Engel-Herbert, M. J. Janik, H. M. Aktulga, et al., “The reaxff reactive force-field: development, applications and future directions”, *NPJ Computational Materials*, **2**, 15011 (2016).
- ¹²⁶L. Brochard, G. Hantal, H. Laubie, F. J. Ulm, and R. J. M. Pellenq, “Fracture mechanisms in organic-rich shales: role of kerogen”, *Poromechanics v ()*.
- ¹²⁷M. Ceriotti, W. Fang, P. G. Kusalik, R. H. McKenzie, A. Michaelides, M. A. Morales, and T. E. Markland, “Nuclear quantum effects in water and aqueous systems: experiment, theory, and current challenges”, *Chemical Reviews*, **116**, 13, PMID: 27049513, 7529–7550 (2016).
- ¹²⁸Y. K. Shin, L. Gai, S. Raman, and A. C. T. van Duin, “Development of a reaxff reactive force field for the ptni alloy catalyst”, *The Journal of Physical Chemistry A*, **120**, 41, PMID: 27670674, 8044–8055 (2016).
- ¹²⁹N. Wang, J. Peng, A. Pang, T. He, F. Du, and A. Jaramillo-Botero, “Thermodynamic simulation of the rdxaluminum interface using reaxff molecular dynamics”, *The Journal of Physical Chemistry C*, **121**, 27, 14597–14610 (2017).
- ¹³⁰A. C. T. van Duin, C. Zou, K. Joshi, V. Bryantsev, and W. A. Goddard, “Chapter 6 a reaxff reactive force-field for proton transfer reactions in bulk water and its applications to heterogeneous catalysis”, *Computational catalysis* (The Royal Society of Chemistry, 2014), 223–243.

- ¹³¹Y. Zhang, C. Liu, Z. Liu, G. Liu, and L. Yang, “Modelling of diffusion behavior of ions in low-density and high-density calcium silicate hydrate”, *Construction and Building Materials*, **155**, Cited By :1, 965–980 (2017).
- ¹³²M. Sobrino Fernandez Mario, M. Neek-Amal, and F. M. Peeters, “Aa-stacked bilayer square ice between graphene layers”, *Phys. Rev. B*, **92**, 245428 (2015).
- ¹³³V. Satarifard, M. Mousaei, F. Hadadi, J. Dix, M. Sobrino Fernandez, P. Carbone, J. Beheshtian, F. M. Peeters, and M. Neek-Amal, “Reversible structural transition in nanoconfined ice”, *Phys. Rev. B*, **95**, 064105 (2017).
- ¹³⁴C. Anders and H. M. Urbassek, “Impacts into cosmic ice surfaces: a molecular-dynamics study using the reax force field”, *Nuclear Instruments and Methods in Physics Research Section B: Beam Interactions with Materials and Atoms*, **303**, Proceedings of the 11th Computer Simulation of Radiation Effects in Solids (COSIRES) Conference Santa Fe, New Mexico, USA, July 24-29, 2012, 200 –204 (2013).
- ¹³⁵W Voigt, “Lehrbuch der kristallphysik (teubner, leipzig, 1928)”, *Google Scholar*, **962** (1928).
- ¹³⁶A Reuss, “Berechnung der fließgrenze von mischkristallen auf grund der plastizitätsbedingung für einkristalle.”, *ZAMM-Journal of Applied Mathematics and Mechanics/Zeitschrift für Angewandte Mathematik und Mechanik*, **9**, 1, 49–58 (1929).
- ¹³⁷R. Hill, “The elastic behaviour of a crystalline aggregate”, *Proceedings of the Physical Society. Section A*, **65**, 5, 349 (1952).
- ¹³⁸L Hernández de la Peña, M. Gulam Razul, and P. Kusalik, “Quantum effects in ice ih”, *The Journal of chemical physics*, **123**, 14, 144506 (2005).
- ¹³⁹B. Pamuk, P. B. Allen, and M.-V. Fernandez-Serra, “Insights into the structure of liquid water from nuclear quantum effects on the density and compressibility of ice polymorphs”, *The Journal of Physical Chemistry B*, **122**, 21, PMID: 29490459, 5694–5706 (2018).
- ¹⁴⁰R. Feistel and W. Wagner, “A new equation of state for h2o ice ih”, *Journal of Physical and Chemical Reference Data*, **35**, 2, 1021–1047 (2006).

- ¹⁴¹S. C. Gay, E. J. Smith, and A. D. J. Haymet, “Dynamics of melting and stability of ice 1h: molecular-dynamics simulations of the spc/e model of water”, *The Journal of Chemical Physics*, **116**, 20, 8876–8880 (2002).
- ¹⁴²Y. Koyama, H. Tanaka, G. Gao, and X. C. Zeng, “Melting points and thermal expansivities of proton-disordered hexagonal ice with several model potentials”, *The Journal of Chemical Physics*, **121**, 16, 7926–7931 (2004).
- ¹⁴³T. Strssle, S Klotz, J. S. Loveday, and M Braden, “Equation of state of ordinary ice ih at 145 k under true hydrostatic pressure up to 5 kbar”, *Journal of Physics: Condensed Matter*, **17**, 40, S3029 (2005).
- ¹⁴⁴R. MacKenzie, “Path integral methods and applications”, arXiv preprint quant-ph/0004090 (2000).
- ¹⁴⁵A. H. A. Penny, “A theoretical determination of the elastic constants of ice”, *Mathematical Proceedings of the Cambridge Philosophical Society*, **44**, 3, 423439 (1948).
- ¹⁴⁶R. E. Green and L. Mackinnon, “Determination of the elastic constants of ice single crystals by an ultrasonic pulse method”, *The Journal of the Acoustical Society of America*, **28**, 6, 1292–1292 (1956).
- ¹⁴⁷F. J. P. Scherrer, “Die elastischen konstanten von eis-einkristallen”, *Helvetica Physica Acta*, **25**, 35–54 (1952).
- ¹⁴⁸J. S. Tse, “Mechanical instability in ice ih. a mechanism for pressureinduced amorphization”, *The Journal of Chemical Physics*, **96**, 7, 5482–5487 (1992).
- ¹⁴⁹J. S. Tse, V. P. Shpakov, and V. R. Belosludov, “Vibrational spectrum, elastic moduli and mechanical stability in ice viii”, *The Journal of Chemical Physics*, **111**, 24, 11111–11116 (1999).
- ¹⁵⁰C. Vega, J. L. F. Abascal, M. M. Conde, and J. L. Aragoes, “What ice can teach us about water interactions: a critical comparison of the performance of different water models”, *Faraday Discuss.*, **141**, 251–276 (2009).
- ¹⁵¹D. MacAyeal, O. Sergienko, A. Banwell, I Willis, G. Macdonald, and J Lin, “Can thermal bending fracture ice shelves?”, *Agu fall meeting abstracts* (2017).

- ¹⁵²K. E. ALLEY, T. A. SCAMBOS, R. S. ANDERSON, H. RAJARAM, A. POPE, and T. M. HARAN, “Continent-wide estimates of antarctic strain rates from landsat 8-derived velocity grids”, *Journal of Glaciology*, **64**, 244, 321332 (2018).
- ¹⁵³B. Chris, M. Daniel, and P. Allen, “Fracture propagation and stability of ice shelves governed by ice shelf heterogeneity”, *Geophysical Research Letters*, **44**, 9, 4186–4194.
- ¹⁵⁴A. T. Bekker, S. G. Gomolskiy, O. A. Sabodash, R. G. Kovalenko, T. E. Uvarova, E. E. Pomnikov, I. G. Prytkov, P. Anokhin, et al., “Physical and mechanical properties of modeling ice for investigation of abrasion process on ice-resistant offshore platforms”, *The twentieth international offshore and polar engineering conference (International Society of Offshore and Polar Engineers, 2010)*.
- ¹⁵⁵R. Lubbad and S. Lset, “A numerical model for real-time simulation of ship-ice interaction”, *Cold Regions Science and Technology*, **65**, 2, 111–127 (2011).
- ¹⁵⁶A. Rahnamoun and A. C. T. van Duin, “Study of thermal conductivity of ice clusters after impact deposition on the silica surfaces using the reaxff reactive force field”, *Phys. Chem. Chem. Phys.*, **18**, 1587–1594 (2016).
- ¹⁵⁷E. M. Schulson, “The fracture of water ice ih: a short overview”, *Meteoritics & Planetary Science*, **41**, 10, 1497–1508.
- ¹⁵⁸E. M. Schulson, “Brittle failure of ice”, *Engineering Fracture Mechanics*, **68**, 17, 1839–1887 (2001).
- ¹⁵⁹J. J. Petrovic, “Review mechanical properties of ice and snow”, *Journal of Materials Science*, **38**, 1, 1–6 (2003).
- ¹⁶⁰F. D. Haynes, *Effect of temperature on the strength of snow-ice*, tech. rep. (COLD REGIONS RESEARCH and ENGINEERING LAB HANOVER NH, 1978).
- ¹⁶¹L. Morland, “Non-linear viscoelastic response of ice”, *Applied Ocean Research*, **13**, 5, 254–261 (1991).

- ¹⁶²L. U. Arenson, W. Colgan, and H. P. Marshall, “Chapter 2 - physical, thermal, and mechanical properties of snow, ice, and permafrost”, *Snow and ice-related hazards, risks and disasters*, edited by J. F. Shroder, W. Haeberli, and C. Whiteman (Academic Press, Boston, 2015), 35–75.
- ¹⁶³E. M. Schulson, “Fracture of ice and other coulombic materials”, *Mechanics of natural solids*, edited by D. Kolymbas and G. Viggiani (Springer Berlin Heidelberg, Berlin, Heidelberg, 2009), 177–202.
- ¹⁶⁴S. J. Jones and J. W. Glen, “The mechanical properties of single crystals of pure ice”, *Journal of Glaciology*, **8**, 54, 463473 (1969).
- ¹⁶⁵S. J. Stuart, A. B. Tutein, and J. A. Harrison, “A reactive potential for hydrocarbons with intermolecular interactions”, *The Journal of Chemical Physics*, **112**, 14, 6472–6486 (2000).
- ¹⁶⁶L. Brochard, I. G. Tejada, and K. Sab, “From yield to fracture, failure initiation captured by molecular simulation”, *Journal of the Mechanics and Physics of Solids*, **95**, 632–646 (2016).
- ¹⁶⁷R. Abadi, R. Uma, M. Izadifar, and T. Rabczuk, “Investigation of crack propagation and existing notch on the mechanical response of polycrystalline hexagonal boron-nitride nanosheets”, *English, Computational Materials Science*, **131**, 86–99 (2017).
- ¹⁶⁸S.-H. Cheng and C. T. Sun, “Size-dependent fracture toughness of nanoscale structures: crack-tip stress approach in molecular dynamics”, *Journal of Nanomechanics and Micromechanics*, **4**, 4, A4014001 (2014).
- ¹⁶⁹C. Brandl, P. M. Derlet, and H. V. Swygenhoven, “Strain rates in molecular dynamics simulations of nanocrystalline metals”, *Philosophical Magazine*, **89**, 34–36, 3465–3475 (2009).
- ¹⁷⁰A. Stukowski, “Visualization and analysis of atomistic simulation data with ovitothe open visualization tool”, *Modelling and Simulation in Materials Science and Engineering*, **18**, 1, 015012 (2010).
- ¹⁷¹W. Humphrey, A. Dalke, and K. Schulten, “VMD – Visual Molecular Dynamics”, *Journal of Molecular Graphics*, **14**, 33–38 (1996).

- ¹⁷²C. A. Schneider, W. S. Rasband, and K. W. Eliceiri, “Nih image to imagej: 25 years of image analysis”, *Nature methods*, **9**, 7, 671 (2012).
- ¹⁷³J. Schindelin, C. T. Rueden, M. C. Hiner, and K. W. Eliceiri, “The imagej ecosystem: an open platform for biomedical image analysis”, *Molecular reproduction and development*, **82**, 7-8, 518–529 (2015).
- ¹⁷⁴M. A. Lange and T. J. Ahrens, “The dynamic tensile strength of ice and ice-silicate mixtures”, *Journal of Geophysical Research: Solid Earth*, **88**, B2, 1197–1208.
- ¹⁷⁵W. M. Ketcham and P. V. Hobbs, “An experimental determination of the surface energies of ice”, *The Philosophical Magazine: A Journal of Theoretical Experimental and Applied Physics*, **19**, 162, 1161–1173 (1969).
- ¹⁷⁶C. Stamoulis and I. Dyer, “Acoustically derived ice-fracture velocity in central arctic pack ice”, *The Journal of the Acoustical Society of America*, **108**, 1, 96–104 (2000).
- ¹⁷⁷V. F. Petrenko and O. Gluschenkov, “Crack velocities in freshwater and saline ice”, *Journal of Geophysical Research: Solid Earth*, **101**, B5, 11541–11551 (1996).
- ¹⁷⁸P. J. Donovan, M. Arakawa, and V. Petrenko, “Crack propagation in freshwater and saline ice”, **578** (1999).
- ¹⁷⁹M. Abdolhosseini Qomi, F.-J. Ulm, and R.-M. Pellenq, “Physical origins of thermal properties of cement paste”, *Physical Review Applied*, **3**, 6, cited By 34 (2015) 10.1103/PhysRevApplied.3.064010.
- ¹⁸⁰H. Zhu, R. C. Newton, and O. J. Kleppa, “Enthalpy of formation of wollastonite (casio₃) and anorthite (caal₂si₂o₈) by experimental phase equilibrium measurements and high-temperature solution colorimetry”, *American Mineralogist*, **79**, 1-2, 134 (1994).
- ¹⁸¹K. Momma and F. Izumi, “*VESTA* for three-dimensional visualization of crystal, volumetric and morphology data”, *Journal of Applied Crystallography*, **44**, 6, 1272–1276 (2011).
- ¹⁸²J. Tolliday, “Crystal Structure of β -Wollastonite”, **182**, 1012–1013 (1958).

- ¹⁸³S Shaw, C. Henderson, and B. Komarschek, “Dehydration/recrystallization mechanisms, energetics, and kinetics of hydrated calcium silicate minerals: an in situ tga/dsc and synchrotron radiation saxs/waxs study”, *Chemical Geology*, **167**, 1, 141 –159 (2000).
- ¹⁸⁴C. Biagioni, S. Merlino, and E. Bonaccorsi, “The tobermorite supergroup: a new nomenclature”, *Mineralogical Magazine*, **79**, 2, 485-495 (2015).
- ¹⁸⁵C. Roosz, P. Vieillard, P. Blanc, S. Gaboreau, H. Gailhanou, D. Braithwaite, V. Montouillout, R. Denoyel, P. Henocq, and B. Mad, “Thermodynamic properties of c-s-h, c-a-s-h and m-s-h phases: results from direct measurements and predictive modelling”, *Applied Geochemistry*, **92**, 140 –156 (2018).
- ¹⁸⁶D. Bentz, “A review of early-age properties of cement-based materials”, *Cement and Concrete Research*, **38**, 2, Special Issue The 12th International Congress on the Chemistry of Cement. Montreal, Canada, July 8-13 2007, 196 –204 (2008).
- ¹⁸⁷S. M. Mutisya, J. M. de Almeida, and C. R. Miranda, “Molecular simulations of cement based materials: a comparison between first principles and classical force field calculations”, *Computational Materials Science*, **138**, 392 –402 (2017).
- ¹⁸⁸V. Swamy and L. S. Dubrovinsky, “Thermodynamic data for the phases in the casio3 system”, *Geochimica et Cosmochimica Acta*, **61**, 6, 1181 –1191 (1997).
- ¹⁸⁹S. Tariq, A. Ahmed, S. Saad, and S. Tariq, “Structural, electronic and elastic properties of the cubic catio3 under pressure: a dft study”, *AIP Advances*, **5**, 7, 077111 (2015).
- ¹⁹⁰C. Hsieh and W. Tuan, “Elastic properties of ceramicmetal particulate composites”, *Materials Science and Engineering: A*, **393**, 1, 133 –139 (2005).
- ¹⁹¹G. Geng, R. J. Myers, M. J. A. Qomi, and P. J. M. Monteiro, “Densification of the interlayer spacing governs the nanomechanical properties of calcium-silicate-hydrate”, *Scientific Reports*, **7**, 1, Cited By :3 (2017).
- ¹⁹²J. E. Oh, S. M. Clark, H.-R. Wenk, and P. J. Monteiro, “Experimental determination of bulk modulus of 14 tobermorite using high pressure synchrotron x-ray diffraction”, *Cement and Concrete Research*, **42**, 2, 397 –403 (2012).

- ¹⁹³R. Shahsavari, R. J.-M. Pellenq, and F.-J. Ulm, “Empirical force fields for complex hydrated calcio-silicate layered materials”, *Phys. Chem. Chem. Phys.*, **13**, 1002–1011 (2011).
- ¹⁹⁴A. Gmira, “Gmira, tude texturale et thermodynamique d’hydrates modles du ciment, thesis”, University of Orleans (2003).
- ¹⁹⁵P. Steneteg, O. Hellman, O. Y. Vekilova, N. Shulumba, F. Tasnádi, and I. A. Abrikosov, “Temperature dependence of tin elastic constants from ab initio molecular dynamics simulations”, *Phys. Rev. B*, **87**, 094114 (2013).
- ¹⁹⁶F. Birch, “Finite elastic strain of cubic crystals”, *Phys. Rev.*, **71**, 809–824 (1947).
- ¹⁹⁷A. Picker, L. Nicoleau, Z. Burghard, J. Bill, I. Zlotnikov, C. Labbez, A. Nonat, and H. Cölfen, “Mesocrystalline calcium silicate hydrate: a bioinspired route toward elastic concrete materials”, *Science Advances*, **3**, 11 (2017) 10.1126/sciadv.1701216.
- ¹⁹⁸H. Manzano, E. Masoero, I. Lopez-Arbeloa, and H. M. Jennings, “Shear deformations in calcium silicate hydrates”, *Soft Matter*, **9**, 7333–7341 (2013).
- ¹⁹⁹E. M. Soliman, S. H. Aboubakr, and M. M. Reda Taha, “Estimating fracture toughness of c-s-h using nanoindentation and the extended finite element method”, *International Journal of Advances in Engineering Sciences and Applied Mathematics*, **9**, 3, 154–168 (2017).
- ²⁰⁰S. Aboubakr, E. Soliman, and M Reda Taha, *Fracture toughness of synthetic c-s-h using nanoindentation*, Sept. 2015.
- ²⁰¹J. Beaudoin, P Gu, and R. Myers, “The fracture of csh and csh/ch mixtures 1”, *Cement and concrete research*, **28**, 3, 341–347 (1998).
- ²⁰²S. P. Shah, “Fracture toughness of cement-based materials”, *Fracture of concrete and rock* (Springer, 1989), 1–12.
- ²⁰³J. Nmeek, V. Krlk, V. milauer, L. Polvka, and A. Jger, “Tensile strength of hydrated cement paste phases assessed by micro-bending tests and nanoindentation”, *Cement and Concrete Composites*, **73**, 164 –173 (2016).

- ²⁰⁴D. Hou, H. Ma, Y. Zhu, and Z. Li, “Calcium silicate hydrate from dry to saturated state: structure, dynamics and mechanical properties”, *Acta Materialia*, **67**, cited By 58, 81–94 (2014).
- ²⁰⁵D. Hou, Y. Zhu, Y. Lu, and Z. Li, “Mechanical properties of calcium silicate hydrate (c-s-h) at nano-scale: a molecular dynamics study”, *Materials Chemistry and Physics*, **146**, 3, cited By 29, 503–511 (2014).
- ²⁰⁶D. Hou, T. Zhao, P. Wang, Z. Li, and J. Zhang, “Molecular dynamics study on the mode i fracture of calcium silicate hydrate under tensile loading”, *Engineering Fracture Mechanics*, **131**, cited By 12, 557–569 (2014).
- ²⁰⁷D. Hou, J. Zhang, Z. Li, and Y. Zhu, “Uniaxial tension study of calcium silicate hydrate (csh): structure, dynamics and mechanical properties”, *Materials and Structures/Materiaux et Constructions*, **48**, 11, cited By 11, 3811–3824 (2015).
- ²⁰⁸D. Fan and S. Yang, “Mechanical properties of c-s-h globules and interfaces by molecular dynamics simulation”, *Construction and Building Materials*, **176**, cited By 0, 573–582 (2018).
- ²⁰⁹P. Atkins, P. Atkins, and J. de Paula, *Atkins’ physical chemistry* (OUP Oxford, 2014).